Characterization of Free and Wall-Impinging Fuel Spray under Cross-Flow Condition

（横風気流中での自由噴霧および壁面衝突噴霧の特性）

By

張 更新（ZHANG GENGXIN）

Dissertation

Submitted in Partial Fulfillment of the Requirements for the

Degree of Doctor of Engineering

at

Mechanical Power and Motor Systems Laboratory

Department of Mechanical Systems Engineering

Graduate School of Engineering

Doctor of Engineering

Hiroshima University

September 2022

ABSTRACT

Vehicle ownership and fossil fuel consumption are increasing annually worldwide. Meanwhile, emission regulations in various countries are becoming more stringent. Therefore, energy conservation and emission reduction have become important issues. Direct injection technology is widely used owing to its low fuel consumption and high thermal efficiency. The atomization, evaporation, and mixture formation of fuel spray significant affect the combustion and emissions of direct injection spark ignition (DISI) engines. However, the highly transient characteristics inside internal combustion engines (ICEs) can result in cycle-to-cycle variations (CCVs), which are reflected in various behaviors of fuel spray. All these CCVs are coupled with each other significantly during engine operation, and a significant CCV can results in low thermal efficiency, high fuel consumption, and exhaust emissions. It was discovered in a previous study that if most CCVs can be decreased, then the output power can be enhanced for the same amount of fuel consumed. Therefore, it is of great significance to investigate the spray CCVs inside the ICEs cylinder.

In addition, DISI engine has advantages such as good fuel economy and high thermal efficiency. However, it is known that a high fuel injection pressure and small cylinder volume result in the impingement of fuel spray on the surface of the piston and cylinder wall. Wall-impingement fuel spray usually affects atomization and combustion effectiveness, resulting in excessive hydrocarbons (HC) and soot emissions. It is difficult for DISI engines to satisfy future particle number (PN) requirements in this situation. ICEs have been developed to reduce pollutant emissions and fuel consumption. As various countries have recently pursued carbon neutrality targets, the mechanism behind the spray wall-impingement phenomenon and fuel adhesion characteristics requires further investigation.

Moreover, the airflow inside the cylinder has a direct impact on the fuel spray and in-cylinder combustion characteristics. The CCV characteristics and wall-impinging behaviors are inevitably affected by the in-cylinder airflow. Generally, cross-flow is applied to simulate the airflow movement in the cylinder. Therefore, it is necessary to study the cross-flow effect, which plays a significant role at the end of the exhaust period.

The novelty of this study is the characterization of free and wall-impinging fuel spray under cross-flow condition. At present, various research methods and evaluation principle, such as proper orthogonal decomposition (POD), presence probability image (PPI), intersection over union (IoU), and edge fluctuation lengths (EFL), have been applied to analyze spray CCVs in previous studies. However, there are few studies that have been performed to investigate the CCV of spray characteristics under cross-flow conditions so far. In addition, although several studies have been conducted on free spray under cross-flow conditions, but only a few studies have been conducted on wall-impingement spray, especially for the fuel adhesion characteristics. Meanwhile, there are no reports on the existence and propagation of the wall-jet vortex phenomenon at the wall-impinging spray tip region under cross-flow conditions. The experimental results can provide an insight into the operating conditions of air-flow inside the engine.

Spray images were obtained via high-speed photography using the diffused background illumination (DBI) method. The continuous wave (CW) laser sheet technology is used to perform high-speed photography on the vertical and horizontal planes to obtain wall-impingement spray images. Additionally, particle image velocimetry (PIV) technology was used to demonstrate the velocity distribution of wall-impingement spray. The sauter mean diameter (SMD) of spray droplets was obtained with laser diffraction spray analyzer (LDSA). The Mie scattering technique was used to perform high-speed photography on the vertical observation to obtain a side view of fuel spray. Meanwhile, the refractive index matching (RIM) technology was used for high-speed photography at the bottom of the observation section to obtain images of fuel adhesion. In addition, Numerical simulations are applied to investigate the characteristics of wall-impingement spray in a cross-flow flow field.

There are three main research part in the study. First is the CCV characteristics of free spray in the cross-flow flow field. The objectives include to quantitatively the CCV of spray characteristics, to observe droplet size distribution, and to clarify the effects of cross-flow/ injection and ambient pressure on the CCV of spray characteristics. Second is the characteristics of wall-impingement spray in the cross-flow flow field. The objectives include to quantitatively the wall-jet vortex characteristics, to evaluate the effects of cross-flow/ ambient pressure/ wall-impingement distance on the wall-jet vortex, and to clarify the effects of cross-flow

and wall-impingement degree on the fuel adhesion characteristics. Third one is the computational fluid dynamics (CFD) simulation of wall-impingement spray in the cross-flow flow field. The objective is to validate the CFD results with the detailed measurements and then mainly consider the cross-flow effect.

In summary, the objective of the present study is to experimentally investigate the CCV characteristics of free spray, structure of wall-impingement spray and the fuel adhesion characteristics of wall-impingement spray under cross-flow conditions, the results of which will provide data support to further improve the accuracy of empirical prediction equations and models.

NOMENCLATURES

D	nozzle exit diameter
H	vortex height
H_c	vortex core height
I	gray value of the spray image
I_0	gray value of the background light
I_c	contribution index
I_{ref}	surface brightness of the dried quartz
I_{wet}	surface brightness of the quartz after the fuel adherence to the flat-wall
Ins	dimensionless number that characterizes instability
L_c	vortex core distance
L_w	impingement distance
N	measurement number
P_v	vertical penetration
P_h	horizontal penetration
$\overline{P}$	average of penetration
P_σ	standard deviation of penetration
P_i	penetration of the experiment i
P_a	ambient pressure
P_{ing}	injection pressure
$P_{ara.}$	the parameter value of any spray characteristics
$P_{ara.i}$	any spray characteristic parameter at a certain timing
$\overline{P_{ara.}}$	the average value of any spray characteristics parameter
R_f	surface roughness

S	spray tip penetration
SS	spray area
t_{ing}	injection pulse
U_x	cross-flow velocity
m	Injection mass
ρ_l	fuel density
σ	surface tension
μ	absolute viscosity
τ	optical thickness
τ_{cov}	COV of optical thickness
τ_σ	standard deviation of optical thickness
$\bar{\tau}$	average of optical thickness
$\Delta I(x, y)$	reduction in the value of scattered light
$h(x, y)$	fuel adhesion thickness
AICE	Automotive Internal Combustion Engines
AMR	Adaptive mesh refinement
ASOE	After the Start of Energization
ASOI	After Start of Injection
CCD	Charge-Coupled Device
CCVs	cycle-to-cycle variations
CDF	Cumulative Distribution Function
CFD	Computational Fluid Dynamics
COV	Coefficient of Variation
CW	Continuous Wave

DBI	Diffused Background Illumination
DISI	Direct Injection Spark Ignition
ECU	Electronic Control Unit
EFL	Edge Fluctuation Lengths
EGR	Exhaust Gas Recirculation
EOI	End of Injection
GDI	Gasoline Direct Injection
HC	Hydrocarbons
HCCI	Homogenous Charge Compression Ignition
HSV	High-Speed Video
ICEs	Internal Combustion Engines
IoU	Intersection over Union
KH	Kelvin-Helmholtz
LDA	Laser Doppler Anemometry
LDV	Laser Doppler Velocimetry
LDSA	Laser Diffraction Size Analyzer
LED	Light Emitting Diode
LIEF	Laser-Induced Exciplex Fluorescence
MOI	Middle of Injection
PDA	Phase Doppler Analyzer
PDF	Probability Density Function
PDPA	Particle Droplet Particle Analyzer
PFI	Port Fuel Injection
PIA	Particle Image Analyzer
PIV	Particle Image Velocimetry

PLC	Programmable Logic Controller
PMF	Probability Mass Function
PN	Particle Number
POD	Proper Orthogonal Decomposition
PPI	Presence Probability Image
PTV	Particle Tracking Velocimetry
RANS	Reynolds-Averaged Navier–Stokes
RIM	Refractive Index Matching
RMS	Root Mean Square
SCSI	Stratified Combustion Spark Ignition
SMD	Sauter Mean Diameter
SOI	Start of Injection
UHC	Unburned Hydrocarbons
VCO	Valve Covered Orifice
WHO	World Health Organization

TABLE OF CONTENTS

CHAPTER 1 INTRODUCTION

1.1 Background and Motivation

1.1.1 Energy and environmental

Global warming is one of the most pressing challenges facing the world today. According to data surveys (Figure 1.1), the global average temperature has risen by more than 1°C since 1850 [1]. Greenhouse gas emissions from human activities, including economic development and population growth, are the primary drivers of this warming, with CO_2 is one of the main greenhouse gases.

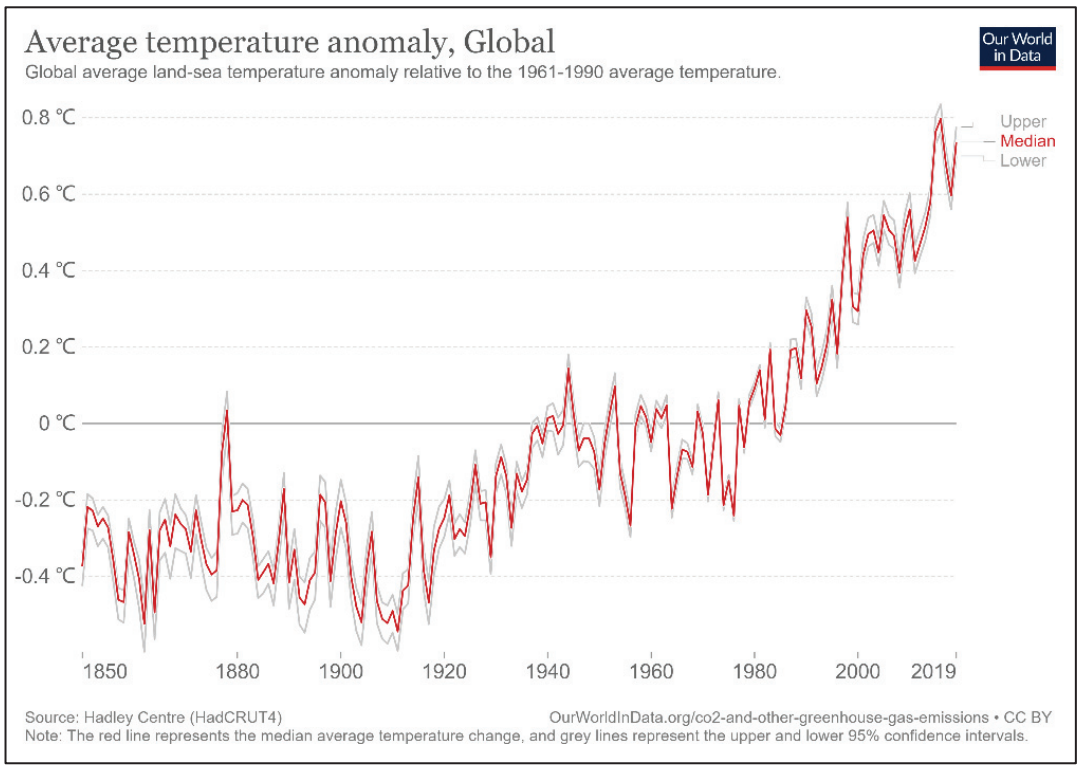

Figure 1.1 Global average temperature anomaly [1].

The 1°C rapid warming itself already has major impacts on climate and natural systems, and this average rise masks temperature changes around the world. In particular, it can be seen from Figure 1.2 that the temperature rise near the poles has exceeded 5°C [2]. Unfortunately, often these regions could experience the largest

impacts such as sea ice, permafrost and glacial melt. The Paris Agreement promises that the global average temperature increase will not exceed 2°C by the end of this century and should be kept below 1.5°C as much as possible [3]. As long as we emit greenhouse gases, their concentration in the atmosphere will increase. To end climate change, the concentration of greenhouse gases in the atmosphere needs to stabilize, and world greenhouse gas emissions must drop to net zero for achieving this target. Therefore, various countries have issued relevant laws and regulations [4]. For example, China has set emission reduction targets to achieve carbon peaking in 2030 and carbon neutrality in 2060 [5].

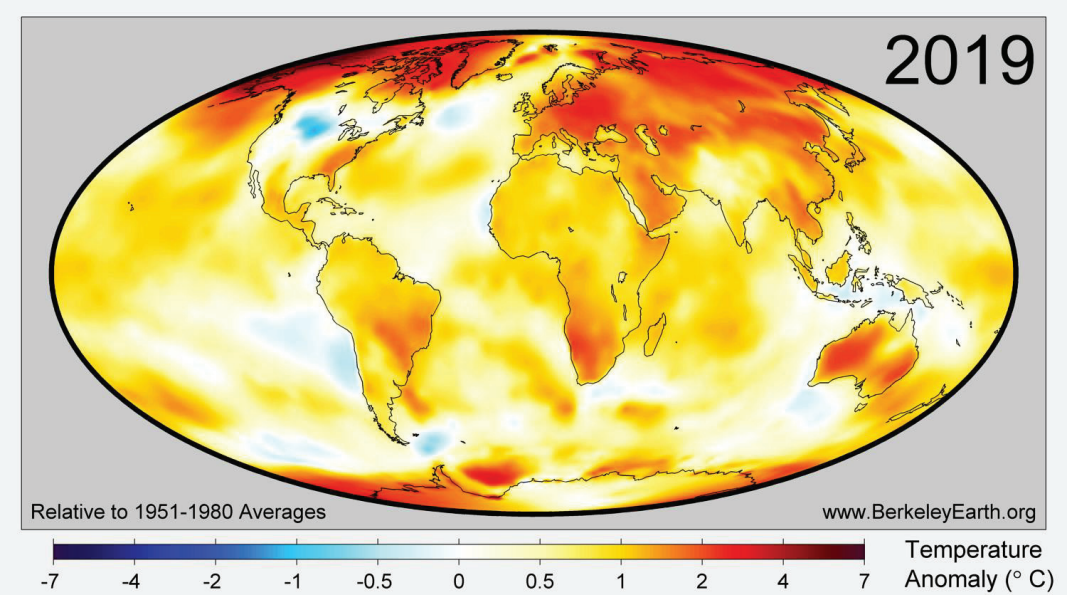

Figure 1.2 Local temperatures in 2019 relative to the average temperature in 1951-1980 [2].

From the mid-19th century to the present, fossil energy has supported human culture and social development for nearly 200 years. Fossil fuels are combustible minerals formed by long-term changes in geological conditions, temperature, pressure, and microorganisms of animals and plants in buried strata at various geological ages. Therefore, fossil fuels are non-renewable energy sources. Fossil fuels mainly include coal, oil and natural gas. They are mixtures of hydrocarbons or hydrocarbon derivatives, which contain a high percentage of carbon. Therefore, the consumption of

fossil fuels inevitably leads to the emission of CO_2, which is the biggest driver of global climate change. Despite the rapid growth of low-carbon energy consumption led by natural gas and renewable energy, historically, energy transformation requires a long transitional duration. At present, fossil energy still dominates energy consumption (as shown in Figure 1.3) [6].

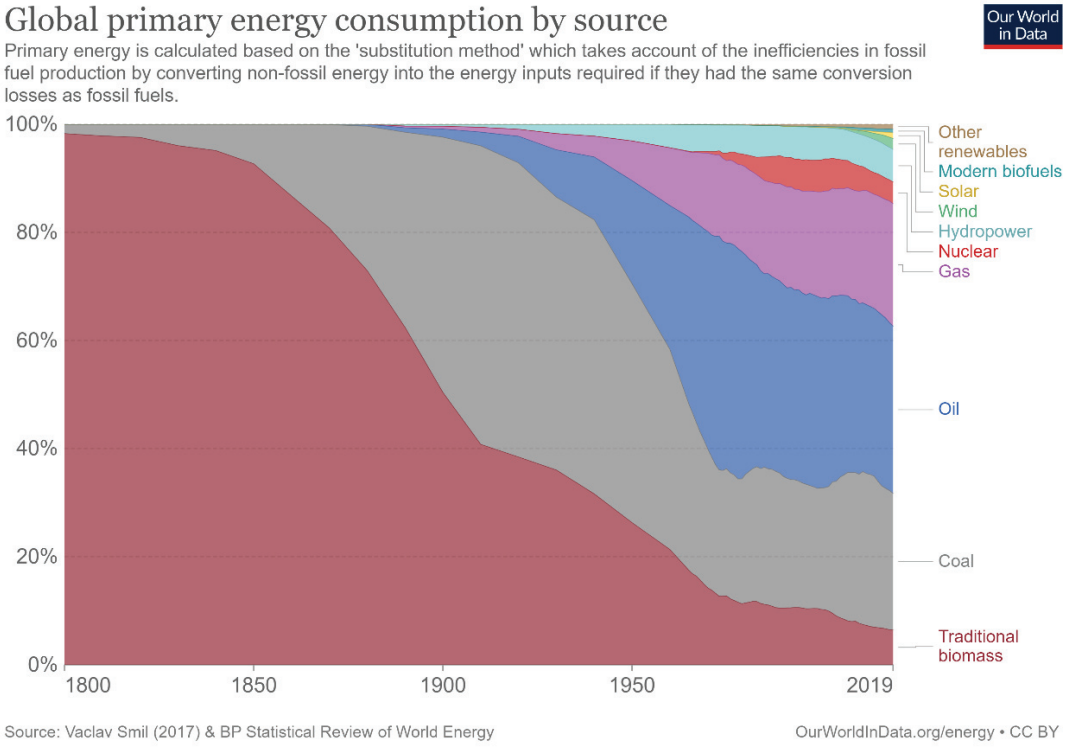

Figure 1.3 Global primary energy consumption by source [6].

With the increase of population and the further development of society, the demand for fossil fuels continues to rise, which in turn leads to the continuous increase of CO_2 emissions. In the situation of the COVID-19 epidemic, global fossil fuel consumption in 2020 reduced. As shown in Figure 1.4, CO_2 emissions from fossil fuel consumption have accounted for more than 80% of global CO_2 emissions by 2020 [7].

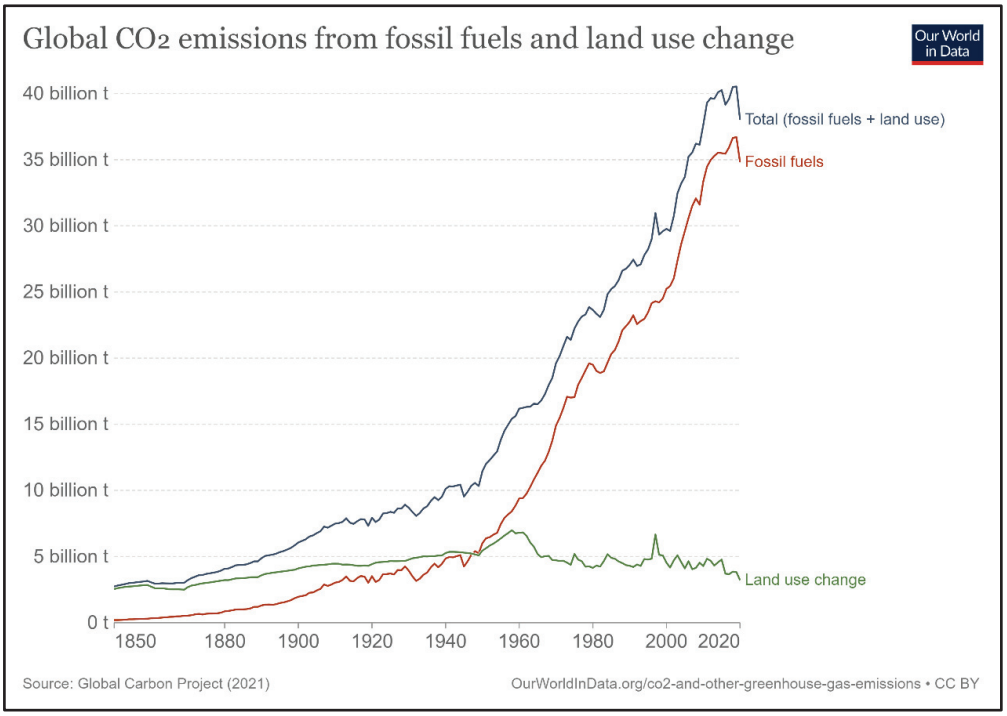

Figure 1.4 Global CO_2 emissions from fossil fuels and land use change [7].

In addition to CO_2 emissions that contribute to global warming, excessive use of fossil fuels produces sulfur dioxide and a lot of dust. The sulfur dioxide produced can form acid rain, and the resulting dust increases the respirable particles in the air. The World Health Organization (WHO) reports that excessive air pollution is often a by-product of unsustainable policies in sectors such as transport, energy, waste management, and industry [8]. As shown in Figure 1.5, around 3.6 million people worldwide died from air pollution caused by fossil fuels in 2015, which is six times the annual death toll from all murders, war deaths and terrorist attacks combined [9]. It confirms that air pollution is now the world's greatest environmental health risk. Reducing air pollution has the potential to save millions of lives. As a result, how to deal with the problem of energy production and emissions from fossil fuels, which is undoubtedly one of the most difficult energy problems in human history.

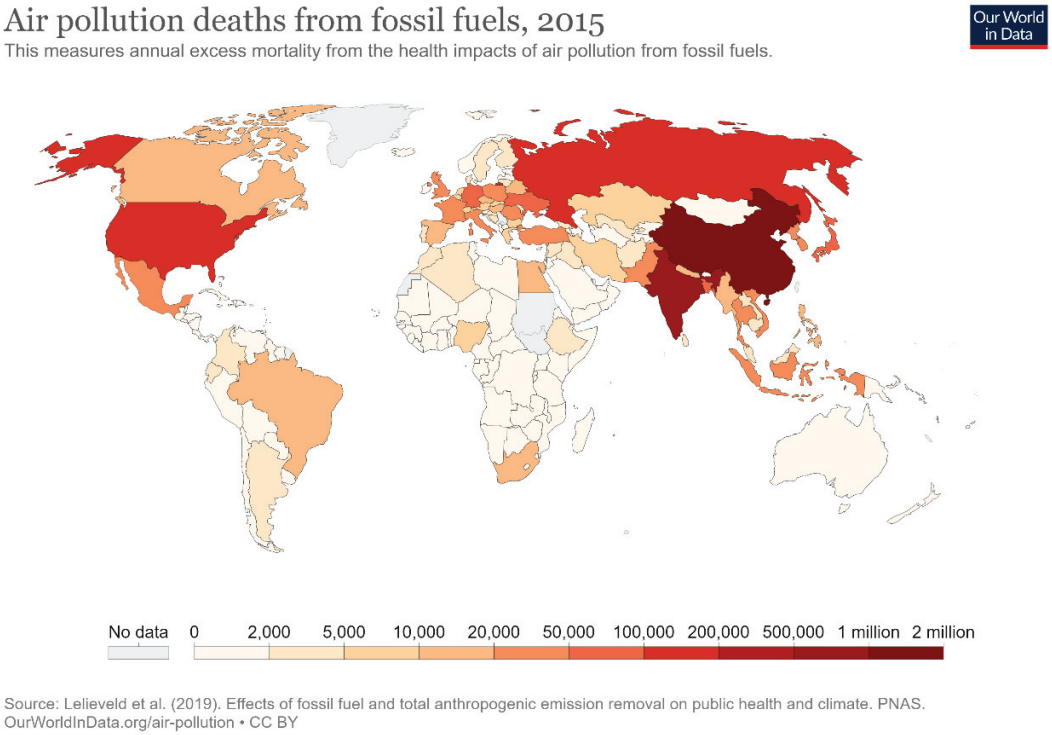

Figure 1.5 Air pollution deaths from fossil fuels [9].

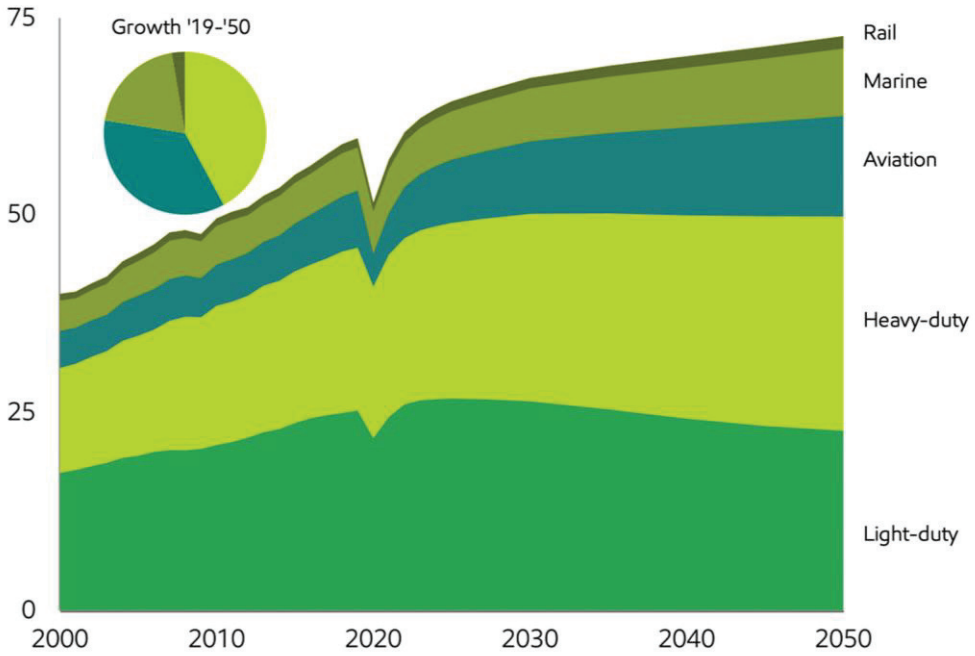

Fig. 1.6 Transportation energy demand growth [10].

As of the end of 2019, oil consumption accounted for 33% of total fossil fuel

consumption, which is the largest consumption part. The transportation sector has one of the fastest growing energy demands in the global economy. Transportation is inextricably linked to and associated with the oil sector. We can generate electricity from a variety of fuels, but oil fuel accounts for 96% of all transportation.

As depicted in Figure 1.6, the most energy-intensive transportation sectors are heavy- and light-duty vehicles [10]. It is evident that the auto industry's energy demand will stay high for an extended period of time. Diesel is primarily used for heavy-duty vehicles outside of Europe, while gasoline is typically utilized for light-duty vehicles such as passenger cars and motorbikes.

Figure 1.7 shows the energy demand and composition of light-duty vehicles over the near 30 years [10]. Full hybrids, as well as electric vehicles, are considered important in improving energy efficiency and reducing emissions. But gasoline will remain the main fuel for light-duty vehicles for a long time to come. The automotive industry urgently needs cleaner, more efficient technologies that can effectively improve ambient air quality, reduce greenhouse gas emissions, and help achieve energy security. Therefore, many technologies for improving engine performance, such as DISI technology, are being studied recently.

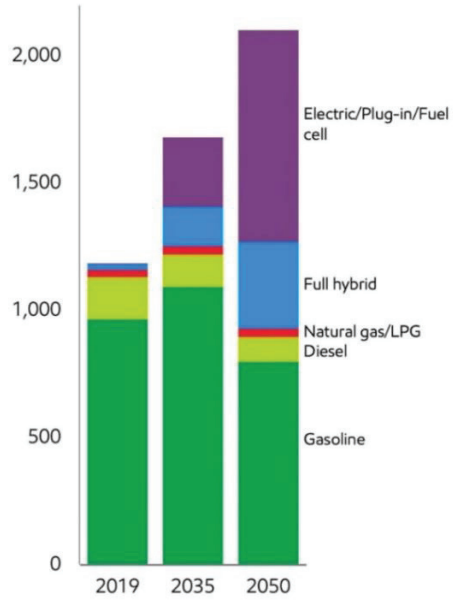

Fig. 1.7 Fuel used in light duty vehicles [10].

1.1.2 DISI engines

Unlike an external combustion engine, an internal combustion engine releases energy through the combustion of fuel within the engine. The actual working fluids are the fuel-air mixture and post-combustion products. The energy is transferred from the working fluids to the engine's mechanical components [11]. Otto invented the first spark-ignition engine in 1876, and Diesel invented the first compression-ignition engine in 1892 [12].

Otto developed an engine with four strokes in order to address the low thermal efficiency and high weight, which thermal efficiency rose to 14%. The two-stroke ICEs were future developed by Karl Benz and James Robson et al. The intake and exhaust processes occur during the beginning of the compression stroke and the end of the power stroke. Rudolf Diesel, a German engineer, obtained a patent by a new form of ICE in 1892. The ignition of fuel is heated only by compression, which would double the efficiency of other ICEs. Thereafter, a practical engine was developed in Augsburg by Diesel and the resources of M.A.N. combined. The first rotary engine was successfully tested in 1957 and was based on the concepts of German inventor Felix Wankel. One of the most significant advancements in the ICE area came with the introduction of the rotational ICE.

Gasoline was produced from lighter crude oil fractions in the late 1800s. After gasoline became available, technologies were developed to vaporize fuel for engines. After the quality of gasoline mixture was significantly enhanced in the late 1930s, compression ratios steadily increased, resulting in an increase in power and efficiency. The improvement in fuel consumption and reduction in air pollution influenced the engine's design and operation. As the use of ICEs increased, more fossil fuel was consumed, and enormous quantities of harmful gases were released into the atmosphere. In such a circumstance, fuel efficiency enhancement and emission reduction became the focus of the researchers.

Early gasoline engines formed the mixture with a carburetor, resulting in high emissions and fuel consumption. Consequently, port fuel-injection (PFI) systems replaced carburetors in automobiles because they were more efficient and required less maintenance [13]. Due to the relatively low injection pressure, a fuel film may form on the port wall and intake valves, which has negative effects during cold start. Interactions between the spray and airflow in the manifold will produce intense turbulence in the cylinder. To prevent cylinder knocking, the PFI compression ratio is capped at 10:1. Even though emissions can be controlled to an acceptable level, the exhaust after-treatment system barely meets the requirements [14].

To overcome the limitations of the PFI engine, two combustion technologies were developed: stratified combustion spark ignition (SCSI) [15] and homogeneous charge compression ignition (HCCI) [16-17] Compared to the PFI engine, the DI SCSI engine can achieve lower fuel consumption and NO emissions [18]. The HCCI technique reduces NO emissions significantly while increasing HC emissions compared to the PFI engine [19]. The limited speed/load (low to medium) range of the two technologies necessitates the operation of the engine in mixed combustion modes.

Figure 1.8 depicts the DISI engine's operational modes. The DISI engine's mixed mode operates in stratified charge and lean mode at low load/speed [20-21]. There are two portions to the engine when the load/speed is high: the medium load region and the higher load region [22]. For the former, the charge is overall lean, but rich in the latter. Exhaust gas recirculation (EGR) is applied to control nitrogen oxide emissions in the case of high load. The optimal fuel economy determines the level of excess air and EGR dilution utilization, and it keeps emission and combustion stability at an acceptable range.

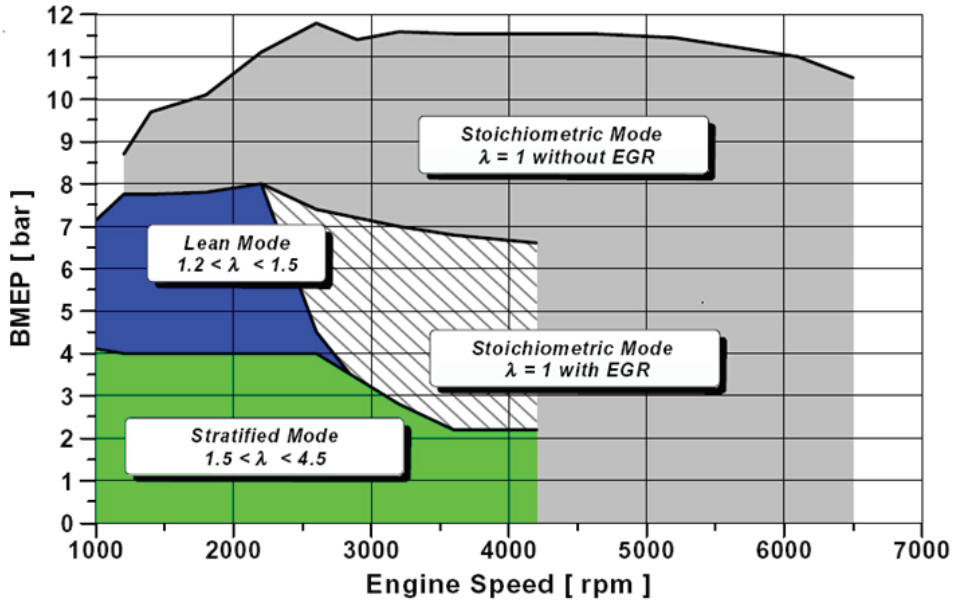

Figure 1.8 Operational modes for the DISI engines [14].

Combustion systems are divided into air, wall, and spray-guided categories in the DISI engines as indicated in Figure 1.9. Spray-guided combustion systems have their spark plugs near to the injector [23-25]. In the wall-directed system, the spray is guided to the spark plug by the airflow created by the interaction between the spray and the piston combustion cavity. Additional to that, a defined air motion in a cylinder blows the spray for an air-guided system [26-27]. The wall-guided combustion technology was widely used in the initial generation of DISI engines. In the second generation, the spray-guided combustion technology may be employed [28].

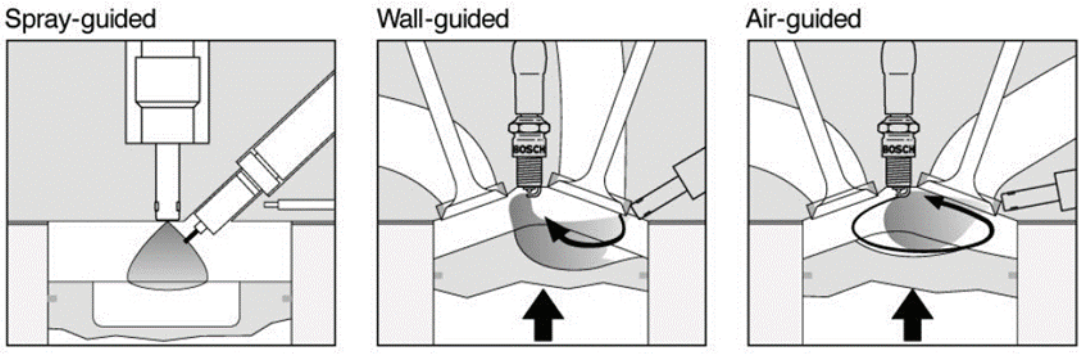

Figure 1.9 Classification of the GDI combustion systems [14].

Due to the GDI system's high injection pressure and small cylinder, fuel spray

may impinge on the piston cavity wall before vaporizing. Fuel spray impingement affects atomization and combustion process, and then increases HC and soot emissions [29]. Therefore, it is challenging for DISI engines to meet future PN requirements in this situation. Since of various countries are pursuing the carbon neutrality targets recently, ICEs have been developing to reduce pollutant emissions and fuel consumption.

1.2 Objectives and Approaches

This work was aimed at investigating the characterization of free and wall-impinging fuel spray under cross-flow condition, which plays a critical role at the end of the exhaust period. This investigation was a fundamental study for clarifying the effects of airflow on fuel spray inside cylinder of DISI engine. Several main objectives which were paid special attention are shown as follows:

(1) Research on the CCV characteristics of free spray in the cross-flow flow field. The objectives include to quantitatively the CCV of spray characteristics, to observe the CCV characteristics of near-field spray and droplet size distribution, and to clarify the effects of cross-flow/ injection and ambient pressure on the CCV of spray characteristics.

(2) Research on the characteristics of wall-impingement spray in the cross-flow flow field. The objectives include to quantitatively the wall-jet vortex characteristics, to evaluate the effects of cross-flow/ ambient pressure/ wall-impingement distance on the wall-jet vortex, and to clarify the effects of cross-flow and wall-impingement degree on the fuel adhesion characteristics.

(3) Research on the CFD simulation of wall-impingement spray in the cross-flow flow field. The objective is to validate the CFD results with the experimental measurements.

In this work, the free spray and wall-impingement spray characteristics were measured by DBI and Mie scattering methods. The velocity distribution of wall-

impingement spray was demonstrated using PIV technology. The LDSA was used to measure the SMD of spray droplets. Meanwhile, RIM technology was used for measuring the fuel adhesion characteristics. Furthermore, numerical simulations are used to investigate the characteristics of wall-impingement spray in a cross-flow flow field.

1.3 Outlines

To present this work, the dissertation is organized as follows:

Firstly, a review of the previous work such as the spray mixture formation under cycle-to-cycle conditions, the air-flow in cylinder, the spray/jet in cross-flow, the spray/wall interaction and the optical diagnostic techniques used in spray research field are introduced in Chapter 1.

Secondly, Chapter 2 introduces the experimental setups and the optical diagnostic technologies adopted in this work. The experimental setups mainly include the high-pressure wind tunnel, the trigger control system, the fuel supply system, the signal acquisition system, the images acquisition system, and the injection rate measurement system. The main optical diagnostic technologies mainly include DBI, Mie scattering, PIV, LDSA, and RIM.

Thirdly, the characteristics of free spray was measured by using DBI and LDSA method in Chapter 3 and 4. The effects of injection pressure and ambient pressure on the CCV characteristics of free spray under cross-flow conditions are statistically analyzed. Chapter 5 illuminates the structures of wall-impingement spray, especially the characteristics of wall-jet vortex under cross-flow conditions, which is measured by CW laser diagnostic method. Subsequently, the fuel adhesion characteristics is measured by RIM diagnostic method under cross-flow conditions in Chapter 6. In Chapter 7, the fuel adhesion characteristics under cross-flow conditions are investigated by numerical simulation.

Finally, general conclusions on the characterization of free and wall-impinging

fuel spray under cross-flow condition are summarized in Chapter 8.

1.4 Review of Previous Works

1.4.1 Spray mixture formation

When it comes to DISI engines, the fuel is injected directly into the combustion chamber, where it combines with air to produce a mixture that can be ignited. The ignition behavior, heat release, the formation of pollutants, and fuel economy are all affected by the formation of the spray mixture.

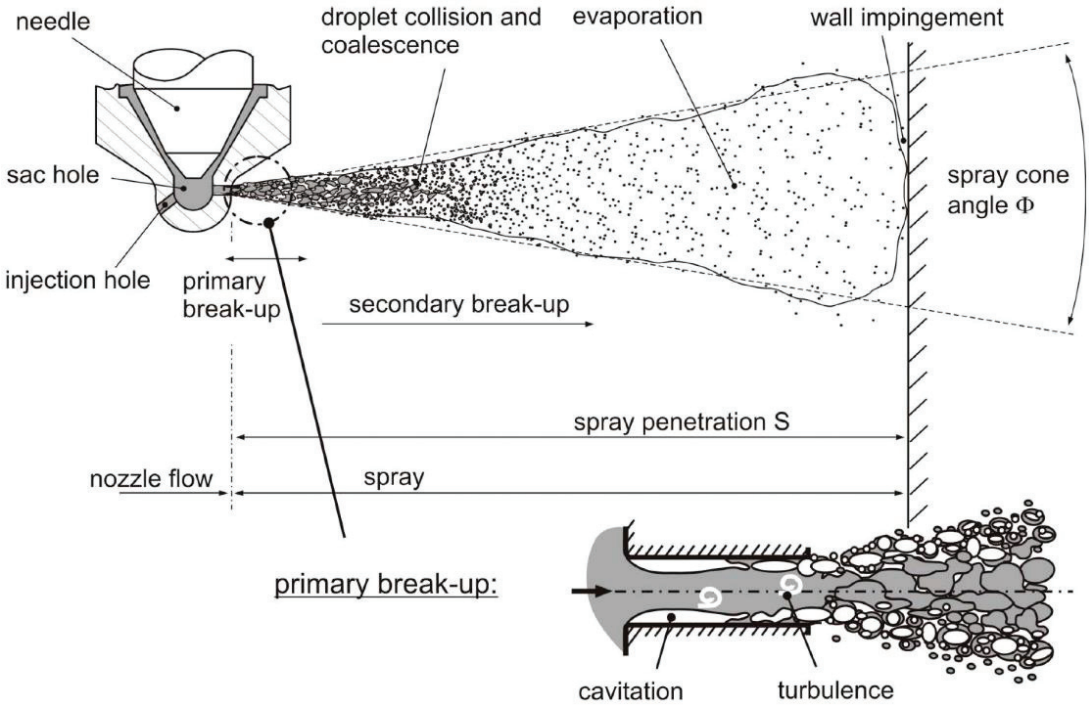

Figure 1.10 Spray breakup process from hole-injector [36].

The fuel jet immediately disperses and transforms into a conical spray following the injection of fuel under pressure. When the injection pressure is high, cavitation and turbulence inside the injection holes can enhance the breakup [30-31]. The dense spray is composed of large ligaments and droplets that result from the initial breakup, which occurs near the nozzle [32-35]. Secondary breakup refers to the subsequent processes of droplet fragmentation that result from primary fragmentation. The aerodynamic force, which is the result of the relative velocity between the droplets

and the surrounding gas, allows for the formation of smaller droplets. The resistance of the surrounding gas causes the droplets to decelerate. The strong drag force influences the spray tip droplets, causing them to lose momentum faster than droplets near the nozzle. As the penetration increases, the spray tip continuously replaces the existing droplets with new droplets. The spray's cone shape is formed by droplets that are stripped by airflow. The final shape of the fuel spray also depends on the wall-impingement or not (see Figure 1.10).

Dense droplets are concentrated near the nozzle, while entrainment air dilutes droplets downstream of the nozzle. Although some droplets and vapor exist the spray’s outer regions, most dense droplets are concentrated near the spray's axis. The interaction between the spray and the entrained gas produces these droplet distributions. Collisions are possible in the region of dense droplets, where the droplet size and velocity in that region are unstable. Meanwhile, coalescence is caused by collisions, so small droplets can collision into large droplets.

The dilution spray downstream of the nozzle is affected by boundary conditions such as injection pressure and temperature, ambient pressure and temperature, and in-cylinder airflow intensity. In further decomposition and evaporation, droplets are sensitive to the boundary conditions. In addition, , wall-impingement phenomenon may occur when the injection pressure is high and the injection duration is long, especially in the case of a small cylinder of DISI engines. In this case, it is difficult for the fuel adhesion to evaporate, so ineffective combustion will occur, and then resulting in reduced fuel economy and increased emissions.

Numerous fundamental experimental and semi-empirical studies have been done and published regarding relevant spray parameters. A wide range of boundary conditions were tested to determine the spray parameters such as cone angle, penetration depth, breakup length, and average droplet diameter [37-47]. In addition, the fuel spray characteristics can be affected by the airflow movement in the cylinder of a DISI engine significantly, which should be further studied.

1.4.2 Cycle-to-cycle variation caused by air-flow

The complex physico-chemical in-cylinder processes have a direct impact on engine dynamics, fuel economy, and emission levels. These in-cylinder processes, such as the formation of the fuel spray structure [48,49], the spray breakup and evaporation process [50], and the combustion process [51,52], are all significantly influenced by the in-cylinder flow field. Optimizing the flow field in the cylinder can accelerate spray breakup and evaporation, prepare the high-quality fuel mixture, effectively accelerate combustion and reduce CCV variation, and play a significant role for the ICEs to adapt the burn combustion. Therefore, a comprehensive understanding of the airflow characteristics within the cylinder is necessary.

Larger-scale flow fields, such as tumble, swirl, or squish flow [53-56], are often used in modern DI gasoline engines, which can be generated by modifying the intake system's (intake port, shape of intake valve, etc.) and combustion chamber's structures. Microscopically, these airflow movements accelerate the process of fuel spray breakup and evaporation by transporting the fuel mixture to form the desired homogeneous or stratified mixture. Before ignition (the late compression stroke), the piston squeezes and breaks these flow field structures into smaller-scale structures. Improve combustion stability, speed up combustion, reduce knocking, and reduce unburned hydrocarbon and soot emissions by using these microscopic turbulences.

In addition to the above-mentioned large-scale airflow movements in the cylinder, another very important flow in gasoline engines is turbulence [57, 58]. Turbulence is the small-scale, unsteady, and irregular airflow movement in a cylinder. There are many ways to form turbulence. The friction between different airflow structures during the intake process can generate turbulence; the airflow interacts with the surface of the combustion chamber during the compression process can generate turbulence; larger-scale organized motion fragmentation can generate turbulence; even combustion also can generate turbulence. Because the main characteristics of turbulent flow are randomness and irregularity, statistical methods are usually needed

to study turbulent flow characteristics [59]. For gasoline engines, turbulent flow effectively promotes various exchange processes between the unburned mixture and the combusted mixture before and after the flame front, increasing the flame front and increasing the combustion speed.

It should be emphasized that the above-mentioned various flow field structures have strong cyclic variability, that is, any two engine cycles under the same operating conditions have different flow field structures or kinetic energy at the same time [60-64]. Because the gasoline engine is ignited by a single-point spark, and then the flame spreads from a fixed single point to the entire combustion chamber, the strong cyclic variation and turbulent characteristics of the flow in the cylinder can easily lead to the instability of the flame propagation process [51, 52]. As a result, it directly leads to the fluctuation of in-cylinder pressure and the fluctuation of engine torque, which leads to the deterioration of vehicle drivability, the increase of engine noise, fuel consumption, and the emissions [65].

Nevertheless, studies regarding the effect of in-cylinder airflows on fuel spray CCVs are scarce. According to Wieske et al., cyclical variations that exist during the formation of a mixture are primarily driven by the airflow in a cylinder [66]. Goryntsev et al. proposed that the CCV phenomenon was affected by turbulence within a cylinder [67]. As shown in Figure 1.11, Qi et al. analyzed the CCV of a pulsing spray structure inside an optically accessible engine using the POD method; subsequently, they decomposed the spray structure into four different parts. It was found that large scale structure part has the largest CCV, which was mainly affect by the flow filed inside cylinder [68]. Although multiple injections per cycle can enhance the overall combustion stability, CCV can still be observed. According to Stiehl et al., this might be due to the effects of in-cylinder flows and turbulence induced by prior injections on the subsequent spray development and mixture formation. Therefore, PIV and Mie scattering were performed to measure the time evolution of the flow field and spray generation in the cylinder, and the effect of the in-cylinder flow field

of multiple injections on the CCV was investigated [69]. Zeng et al. performed a two-dimensional PIV measurement to understand the mechanism by which swirl decreases the CCV of a flow. The results show that the swirl produces flow patterns in each cycle that are like those of an ensemble-averaged cycle and low in variability [70]. Truffin et al. performed a large eddy simulation and a multivariate analysis to investigate the factor that contributed to combustion cycle variations in spark ignition engines, and the findings revealed that the cause of CCVs may vary depending on the engine type and combustion mode [71]. Riccardo et al. investigated the cycle variation of a multicycle engine using reynolds-averaged navier–stokes (RANS) modeling technology and discovered that CCVs are primarily driven by the variation in the flow field in the cylinder [72].

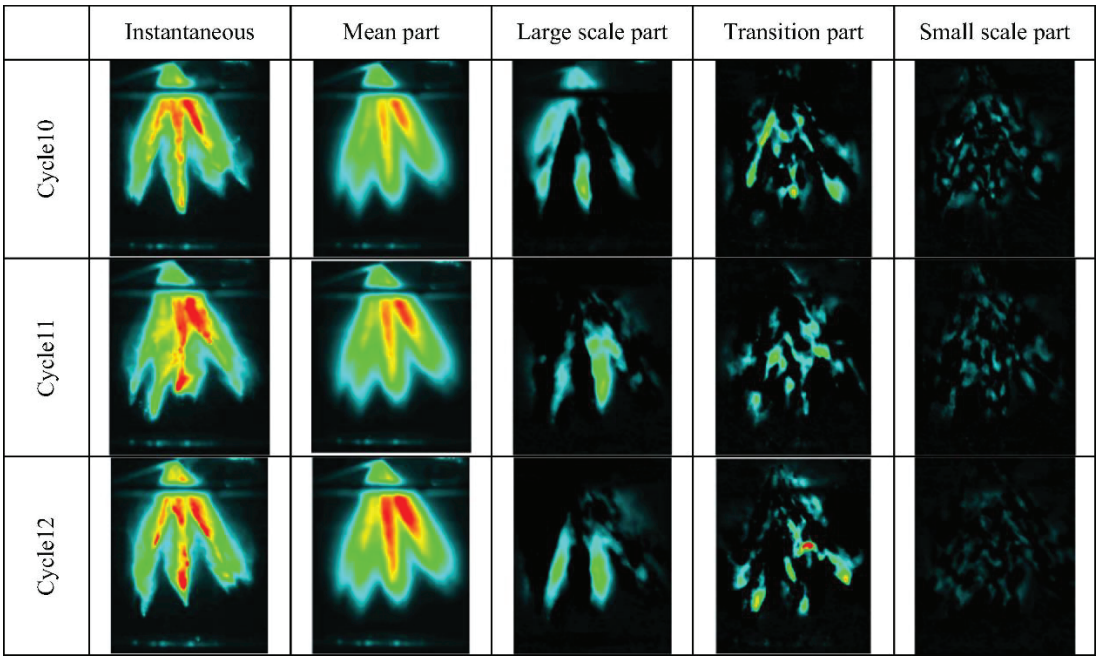

Figure 1.11 Spray fields of 3 individual cycles decomposed into four parts at 3° ASOI by POD [68].

Several studies pertaining to the CCV of fuel spray characteristics have been performed using various techniques. Hung et al. proposed the PPI method to evaluate the CCV of pulsing sprays inside a DISI engine [73]. Subsequently, Hung and Zhong used the PPI technique to investigate the beginning of fuel spray CCV. The results

indicated that if the time delay after the start of injection (ASOI) is nearer to the response time of the needle valve opening, then a significant CCV will be yielded [74]. Marchi et al. evaluated the spray stability of different injector types by analyzing the mean and RMS images of fuel spray. It was discovered that injectors with positive inward seal bands can reduce spray CCVs [75]. Zhou et al. used ultraviolet–visible laser absorption scattering (UV-LAS) technology and Mie scattering optical diagnostic technology, combined with different statistical methods such as PPI, IoU, and EFL, to analyze the CCV of spray characteristics under idle operating conditions of an engine. It turned out that the CCV was quite large after end of injection (EOI). In addition, a higher injection pressure or fuel temperature can result in a significant CCV of spray [76]. Recently, Chen et al. innovatively proposed and developed the POD method, which addressed the limitations of PPI and RMS methods, to analyze the CCV of pulsing spray characteristics [77,78]. In addition, Zhuang et al. decomposed changes in penetration, plume swing, and spray angle into different modes using the POD method, and the results indicated that changes in the spray structure were primarily reflected by changes in the plume swing and spray angle [79]. Wieske et al. utilized laser-induced exciplex fluorescence (LIEF) technology to investigate the causes of periodic variations inside a DISI engine via an air-guided combustion process. It was found that the air–fuel ratio at the spark plug determined the change in each cycle. [80]. Subsequently, Wu et al. also investigated the CCV of a fuel spray using the POD method. It was discovered that a higher fuel temperature enabled more stable spray liquid and vapor phases to be obtained. The vapor phase was more sensitive to air entrainment than the liquid phase, which resulted in a higher fuel spray CCV in the vapor phase. Additionally, it was discovered that a higher ambient pressure resulted in a greater CCV in the fuel spray. Furthermore, the CCV in flash spray was lower than that in non-flash spray, and the symmetrical distribution of injector holes in the space promoted a more stable spray plume [81]. Besides that, previous investigations demonstrated that the CCVs of single- and multi-component fuels were different from each other. As shown in the Figure 1.12, Qi et al proposed a

new prediction equation for the spray vapor distribution area, and it can be used to characterize the vapor-phase behavior when considering cyclic variations [82]. In summary, various research methods and evaluation criteria, such as POD, PPI, IoU, and EFL, have been applied to analyze spray CCVs.

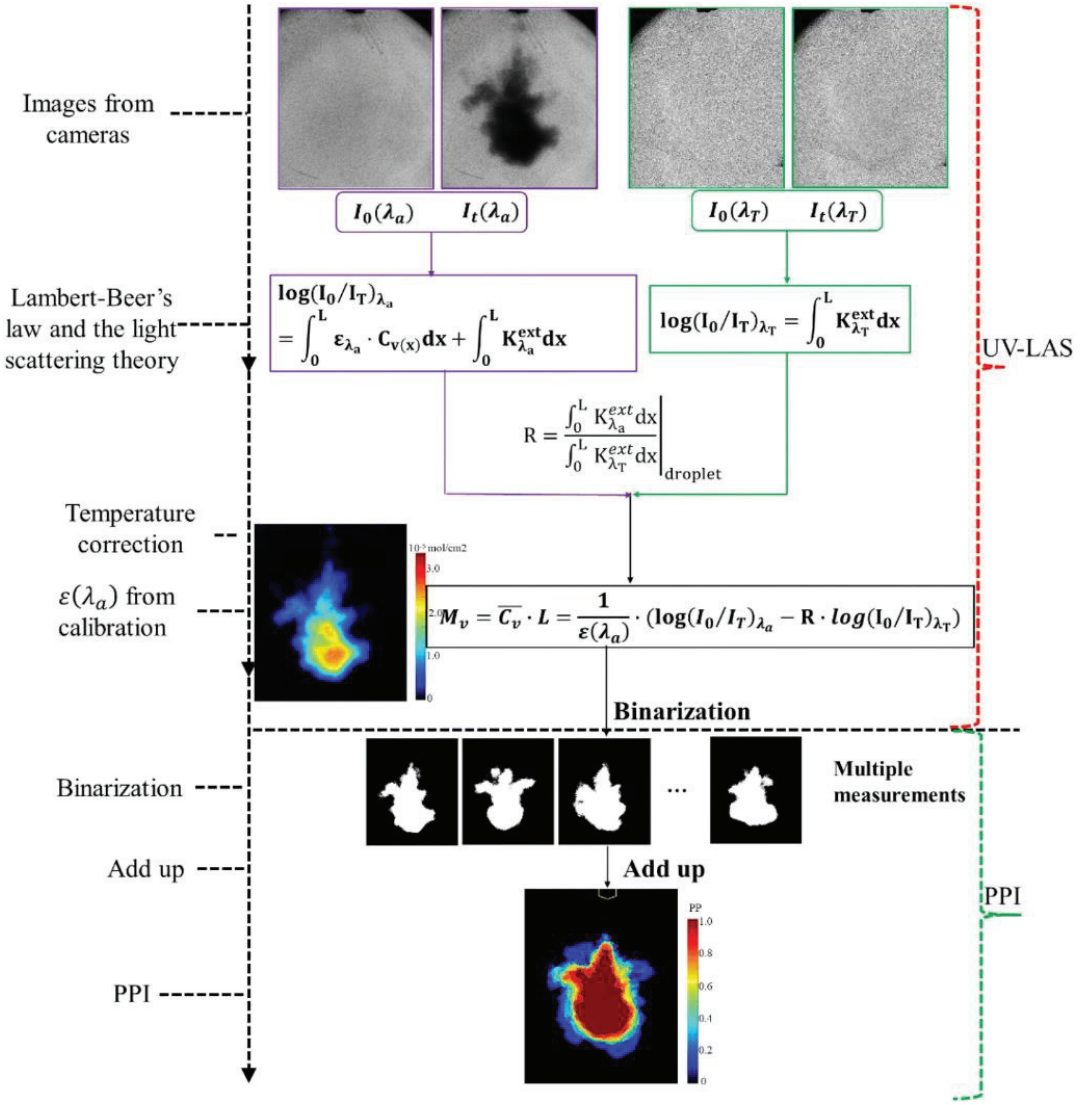

Figure 1.12 Image process flowchart of UV-LAS imaging technique and PPI method [82].

Although the air motion and spray characteristics in combustion chamber have been investigated by many researches, it is hard to directly analyze the CCV mechanism clearly. Because the conditions, such as pressure, velocity of flow, temperature in the combustion chamber, always changes. In that case, to further

understand the processing, some fundamental investigations should be taken in the single conditions. At present, there are few studies that have been performed to investigate the CCV of spray characteristics under cross-flow conditions so far. Therefore, the CCVs of fuel spray characteristics will be further investigated under single condition of cross-flow, which plays a great role at the end of the exhaust period.

1.4.3 Spray/jet in cross-flow

Modern propulsion and power applications, such as gas turbine, ramjet, and scramjet engines, conduct extensive research on the injection of liquid jet/spray into the cross-flow flow field [83]. In practical applications, combustion performance is determined by liquid atomization, spray penetration, and the mixing process. Recent attention has been paid to the effects of cross-flow on spray in DISI engines [84,85]. By the way, the interactions between cross-flow and spray are also studied in agricultural chemical spray [86].

After being injected into a cross-flow flow field, a liquid jet will undergo a series of processes, including breakup and vaporization [87]. The liquid first breaks into droplets, and then the droplets break down into smaller droplets, which is the primary breakup. After that, the smaller droplets dissipate and form clouds of vapor. On the other hand, a low-pressure wake is formed on the windward side. Leeward and windward side pressure differences cause the liquid column to be bent by cross-flow. The liquid column or droplets can break up due to the momentum of the entrained air.

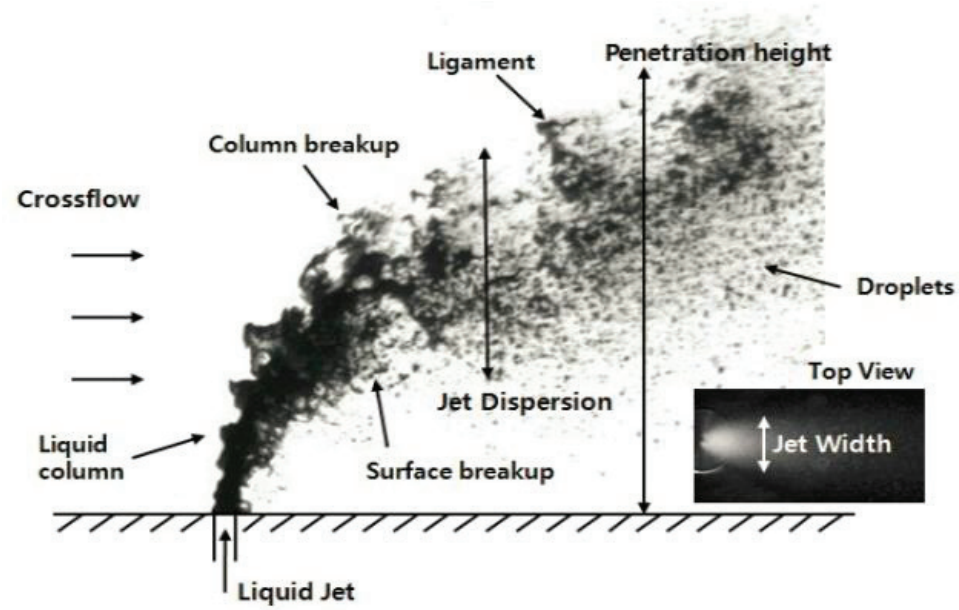

Figure 1.13 Typical parameters of liquid jet in cross-flow [88].

Several parameters, such as column and surface breakup, penetration height, jet width, droplet size, and droplet velocity for the liquid jet in cross-flow are measured, as shown in Fig. 1.13 [88]. These measurements are done so that the mechanism of the interaction between cross-flow and jet can be understood.

Furthermore, plentiful studies pertaining to the interaction between cross-flow and spray are being performed currently. Moon et al., employed a slit injector to investigate the effects of cross-flow on spray profiles; they discovered that the spray profile varied significantly on the downstream spray, whereas it changed slightly near the nozzle [89]. Moriyoshi et al. analyzed the formation of a fuel spray mixture using numerical and experimental methods. They discovered that atomization was affected by the relative velocity between a droplet and ambient gas. In addition, numerous small droplets were transported downstream by the cross-flow [90]. Panão et al. hypothesized that cross-flows can promote secondary atomization and affect secondary droplet diffusion [91]. Guo et al. experimentally investigated the characteristics of fuel spray and its interaction with a cross-flow on vertical/ horizontal sections. The expansion of both sides of the vertical section sprays increased with the cross-flow, and the “Karman vortex street” phenomenon was

observed in the horizontal section (the upper section of the spray). Meanwhile, they considered the effect of ambient pressure and discovered that the curved spray profile became more enhanced as the ambient pressure increased [92-94]. In addition, Sinha and Ravikrishna discovered that certain wave-like structures formed in the near-nozzle region owing to shock–vortex interactions [95].

Although several studies have been conducted on free spray under cross-flow conditions, only a few studies have been conducted on wall-impingement spray, especially for the fuel adhesion characteristics.

1.4.4 Spray/ wall interaction

Another issue is that the fuel spray might impinge on the piston cavity wall before being fully vaporized owing to the high injection pressure and downsized cylinder of DISI engines. Engineers in the automotive industry have discovered that the spray/wall interaction has a significant impact on the formation of mixtures, combustion, and emission levels.

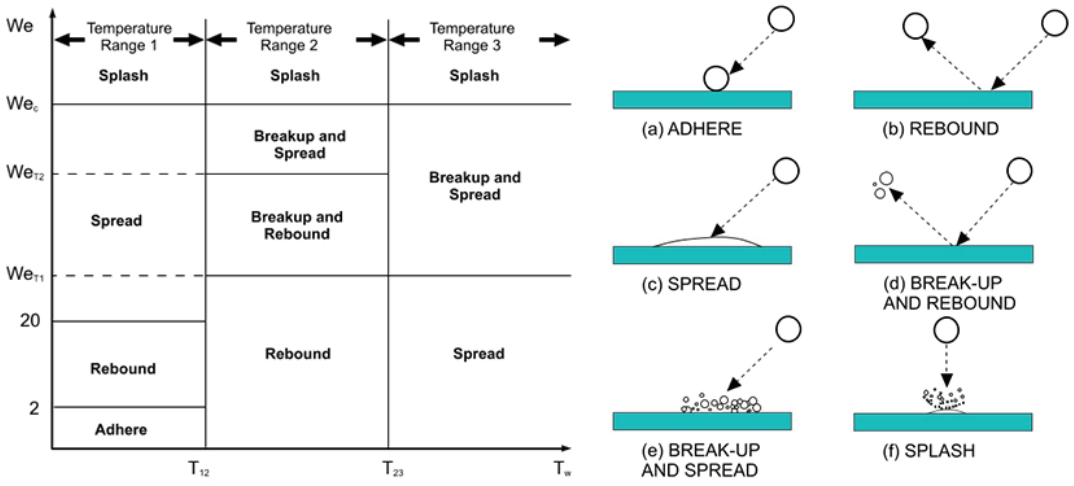

Figure 1.14 Behavior of droplet after impinging on wall [96].

Atomization under impinging conditions differs greatly from free spray atomization. When droplets with large Weber number impinging on the wall, the secondary breakup process improves, which leads to smaller droplets being formed. When droplets with small Weber number impinging on the wall, a liquid film forms,

and this has a negative impact on the amount of unburned hydrocarbons (UHC) and soot emissions. Droplet behavior after impinging on a wall is depicted in Fig. 1.14 [96], which is dependent on the temperature of the wall and the Weber number of impinging droplets.

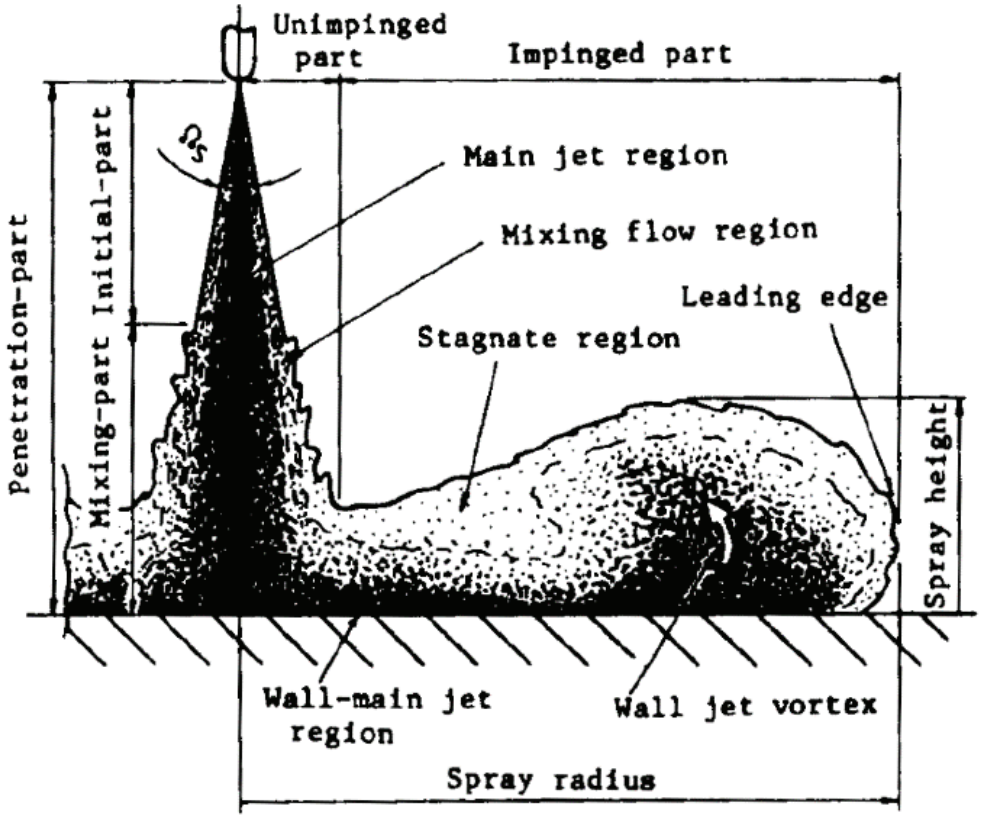

Figure 1.15 Model of a wall-impingement spray [97].

Initially, Fujimoto et al. [97] studied the wall-impingement spray at room temperature, and then Katsura et al. [98] further investigated the wall-impingement spray and proposed a typical model for wall-impingement spray as shown in Fig 1.15. After impingement, the spray is seen to flow along the wall. In the spray tip, a wall-jet vortex region is created cause of the resistance in the ambient gas flow. The droplets are rolled up by the vortex, increasing the volume of the spray. The closer the measuring point is to the wall surface, the greater the density of the droplets. However, droplets concentration is varying according to the spray height along the wall direction, which is dense in the impinging point and wall-jet vortex regions.

Wall-impingement spray was investigated by Senda et al. [99] and Meingast et al. [100] in evaporative conditions. It has been found that the wall-jet vortex enhances evaporation. For the duration of stable injection, the liquid phase penetration is limited to a height of 2 mm, and it does not increase. According to Arcoumanis and Chang [101], the wall-jet vortex becomes more intense when the wall temperature increases, and the droplet size decreases at the leading edge, but increases behind the wall-jet vortex due to the changing competitive effect of droplet collision and coalescence [102].

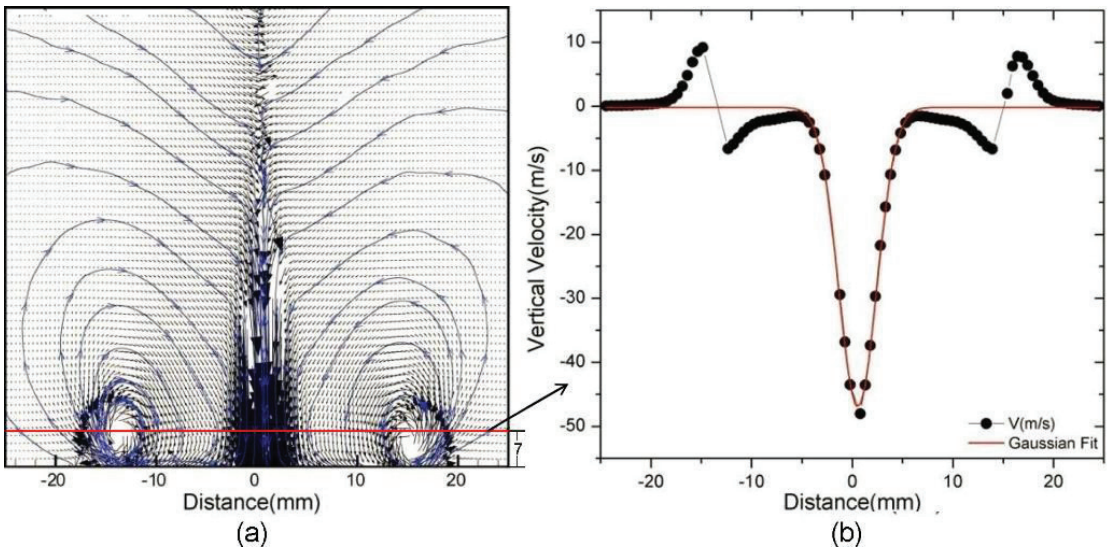

Figure 1.16 Typical velocity field and streamlines of impinging spray (a) and velocity profile at thencenter of wall-jet vortices (b) [105].

Cossali et al. [103] used laser doppler anemometry (LDA) to examine the air entrainment of wall-impingement spray and discovered that spray/wall interaction significantly affects the air entrainment. Laser Sheet Imaging was used by Mohammadi et al. [104] to investigate the ambient air entrained processes in detail. The air entrainment is enhanced by increasing the injection pressure or the orifice diameter under the wall-impinging condition, according to this study. Additionally, reducing the impinging distance also enhances air entrainment. PIV technique was used by Bruneaux et al. [105] to determine the velocities and streamlines of wall-impingement spray (Fig. 1.16). Due to the large normal velocities, the wall-

impingement spray has more air entrainment in the wall-jet vortex region, but the total air mass entrained is less due to the penetration reduction. Numerous studies [106-109] examined the impact of air entrainment on wall-impingement spray concentration and equivalence ratio. According to the results, a dense or rich area of wall-impingement spray appears near wall-impinging points, while the leading edge of wall-impingement spray forms a lean mixture.

To better understand the influence of the wall-jet vortex on the mixture formation, Fujimoto et al. [110] investigated the internal structure of free spray and wall-impinging spray and the diffusion process. The PIV approach was utilized to capture the overall flow characteristics and the wall-jet vortex shape. Subsequently, the internal structure models were created based on the experimental data. Xu and Wang [111] investigated the laminar vortex rings formed by spray wall-impingement using laser-induced fluorescence (LIF) and PIV. A large stroke length prevents the vortex ring from interacting with the vortex clusters near the wall from merging, resulting in a quick reduction in the strength of the vortex near the wall. To investigate the structure of the wall-impingement spray, Yu et al. [112] conducted large-eddy simulations. The findings revealed that the primary vortex structure is generated periodically, which is a significant factor in the generation of secondary vortex in the wall-jet region. Besides that, Yu et al. [113] researched the effects of wall impingement on low pressure ratio (PR) jets using the PLIF technique. It was found that the typical characteristic during the development stage of the wall-impinging jet is that the vortex core gradually grows at the wall-jet tip region and forms a large-scale vortex structure. The surrounding air is entrained into the wall-jet vortex and the wall-jet region along with the large-scale movement. Although fuel accumulates on the wall as a fuel film, the wall-jet vortex can quickly mix with air at the wall-jet tip region, significantly improving the mixing efficiency. The structure of the wall-jet vortex after wall-impingement should be investigated further.

The occurrence of fuel adhesion should be prevented to reduce the soot

emissions. At present, various factors that affect fuel adhesion characteristics, such as temperature and pressure in the cylinder, injection pressure, spray impingement angle and wall temperature, and the fuel type and temperature, have been comprehensively studied by multiple researchers [114-117]. Luo et al. [118-120] studied the effects of injection and ambient pressure, wall surface roughness, ambient temperature, and impingement distance on the distribution of fuel adhesion thickness and area. The results demonstrated that the fuel adhesion was more uniformly distributed under high ambient pressure. The uniformity of the fuel adhesion distribution decreased with an increase in the wall roughness [118]. Additionally, the uniformity of the fuel adhesion thickness can be enhanced by a high ambient temperature. A primary impingement region was formed after the primary droplets impinge on the wall and the splashed droplets were redeposited to form a secondary impingement region [119]. The fuel adhesion mass significantly increased with an increase in the impingement distance [120]. Akop et al. [121, 122] found that the fuel adhesion mass decreased with an increase in the injection pressure and the inclination of the flat-wall. Wang et al. [123] proposed that an increase in the flash boiling and the dwell time between split injections can reduced the fuel concentration deposited on the wall and the lifetime of dense fuel adhesion. Muramatsu et al. [124] measured the distribution and volume of the fuel adhesion after injection. It was stated that the fuel adhesion thickness decreased with an increase in the injection pressure. Meanwhile, the tendency of decrement was higher at small injection angles. Shim et al. [125] combined numerical calculations and experimental research methods and observed that vortex clouds were distributed inside the cavity, and greater fuel adhesion mass can be seen under a high ambient pressure. Yu et al. [126] investigated the effect of impingement distance and degree on the wall-film ratio when different fuels are mixed. The wall-film ratio was mainly affected by the fuel surface tension, viscosity, and saturated vapor pressure of the fuel mixture. The impact momentum significantly affected the wall-film ratio when the injection pressure or impingement distance was changed. As shown in the Figure 1.17, Schulz et al. [127] studied the effect of fuel temperature on fuel adhesion

characteristics under flash boiling conditions. It was found that an increase in the fuel temperature cannot cause a continuous reduction in the fuel adhesion, whereas the flash boiling of the spray can cause the accumulation of the fuel adhesion in a small region. The accumulation delayed the evaporation process, which leads to an increase in the emission of soot particles. It can be noted that most scholars have paid attention to the characteristics of the fuel adhesion produced by the wall-impingement spray to avoid the formation of the fuel adhesion.

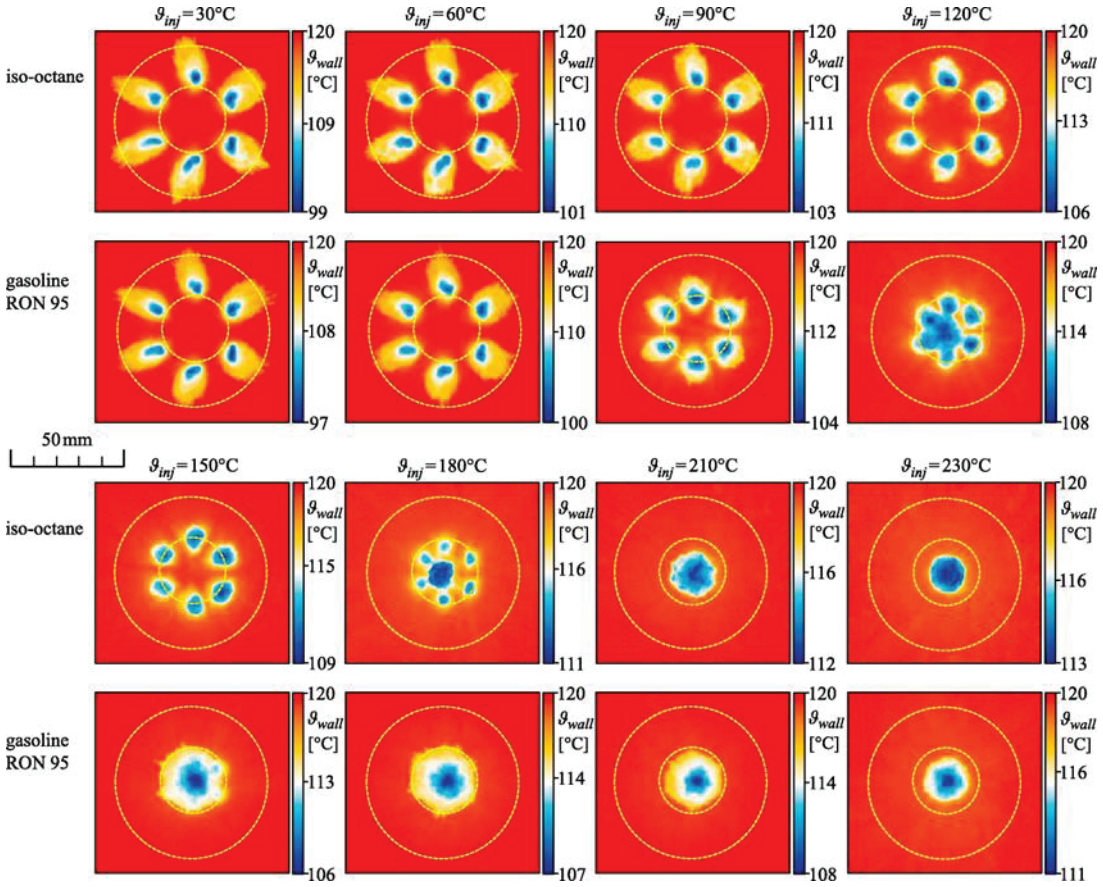

Figure 1.17 Wall temperature distribution 25 ms after the injection of iso-octane and gasoline (RON95) for different initial fuel temperatures [127].

However, the fuel adhesion is inevitably affected by the airflow inside the cylinder [128,129]. Although scholars have studied the effect of various factors on the fuel adhesion characteristics, a fundamental research of fuel adhesion characteristics under cross-flow conditions have not been conducted, which should be given special attention.

1.4.5 Optical diagnostic techniques

It is possible to accurately assess the ICEs' in-cylinder fuel injection, evaporation, and combustion processes by using optical diagnosis technology, which measures a variety of in-cylinder parameters at multiple scales. As a result, optical diagnostic technology provides a reliable test method for advanced engines with high power, high efficiency and low emissions in high temperature and pressure environments. Spray typically occurs from a nozzle within milliseconds, spray droplets move rapidly, and fuels are typically transparent, making direct observation and analysis of spray extremely difficult or impossible. The macroscopic spray evolution can be detected by the various optical diagnostic techniques in spray.

High-speed video photography is commonly used in experiments to observe spray profile and evolution. Spray liquid/ vapor phase development is analyzed using DBI, Mie scattering, Schlieren, and Shadowgraph techniques. [130-132]. DBI measures the liquid phase spray boundary, such as liquid phase penetration and spray structure, using significantly different light extinction capabilities by fuel liquid phase. However, it is difficult to capture the spray vapor phase's boundary due to the spray vapor phase's poor extinction ability. Meanwhile, it is difficult to accurately determine the spray droplet concentration based on the intensity of DBI measurements. Most of the scattering is Rayleigh scattering, which comes from molecules or very small diameters' droplets (smaller than the light wavelength or about the same as 1/10 of the wavelength). Mie scattering occurs when the droplet size is greater than or equal to the light wavelength. Mie scattering dominates spray visualization experiments without evaporation because the light wavelength is smaller than the droplet size. The schlieren method is based on the principle that the light beam will be deflected due to the change of refractive index when the light beam passes through the flow field with changing density. The deflected light is collected and properly shielded by a knife-edge device, and then the light and dark can be formed after the beam diverges. Real image of change. The light and dark areas of the image represent the density variation

of the flow field, and the degree of light and dark is the first derivative of the refractive index (related to density) in the flow field in the test area. The shadowgraph is similar to the schlieren method, except that the knife edge in the light path is eliminated, and the parallel light is directly used to form a light and dark image. However, since the degree of shading of this method is proportional to the second derivative of the density distribution, so its sensitive is poor. In comparison to the Mie scattering / DBI method, the advantage of schlieren and shadowgraph is that they can not only detect liquid phase but also observe vapor phase. Despite this, they were unable to achieve vapor concentration measurements. The primary applications of schlieren and shadowgraph are measuring the structure of spray and shock waves. Figure 1.18 is a schematic representation of a Z-type schlieren setup.

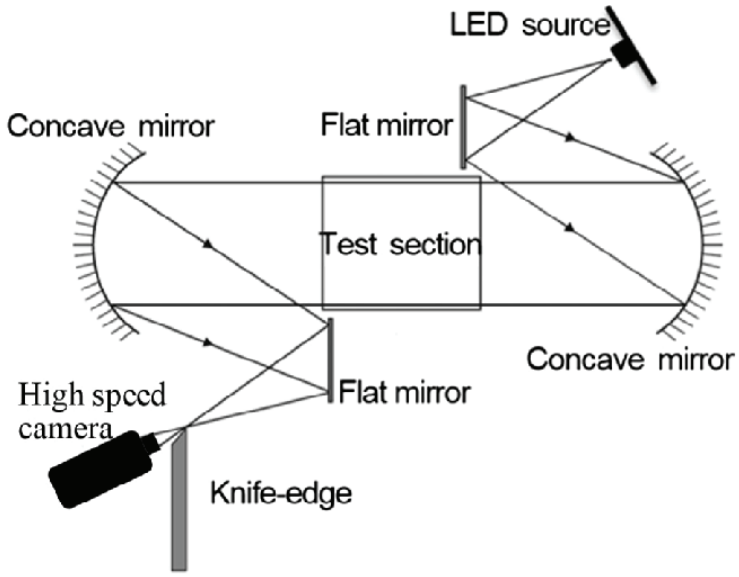

Fig. 1.18 Schematic diagram of schlieren [133].

The single point velocity measurement can be taken by hot-wire anemometry or laser doppler anemometry/velocimety (LDA/LDV), which are used to measure the flow velocity and turbulence [134]. The flow within the engine cylinder is influenced by various of factors, including fuel spray, the flow of intake air, and the movement of the piston. It has a complex structure in space and changes rapidly with time. Traditional flow field measurement methods (eg, anemometers) would interfere with

the flow structure, while laser single-point measurements (eg, LDA/LDV) did not have sufficient spatial resolution. Since the above methods can meet the measurement requirements, so it is necessary to develop a new measurement technology that has no disturbance to the flow field and has a high spatial and temporal resolution. Particle tracking velocimetry (PTV) and PIV are two methods that have been developed to quantify the velocities that are present in complex and unsteady in-cylinder flows [135].

PIV is a flow field laser measurement technique for the spatial distribution of instantaneous velocity, which can perform 2D and 3D measurements [136]. The basic principle of PIV technology is to calculate the velocity and direction of particle movement within this time interval by using two images of particle spatial distribution that are shot continuously in a very short time. However, PIV technology does not track the trajectory of a single particle but divides the particle image captured by the camera into several sub-regions, namely "query windows", and then uses a cross-correlation algorithm to calculate the displacement and direction of all particles in each query window. In recent years, traditional PIV technology [137] has begun to develop towards high dimensions and high temporal resolution, such as the Stereo PIV [138], Biplanar Stereo PIV [139], Chromatography PIV [140], Holographic PIV [141], Rainbow PIV [142].

In addition, it is essential to understand the droplet size distributions in the spray because the droplet size distribution influences the fuel atomization and vaporization processes. Typically, two optical techniques are employed for measuring droplet size: direct imaging techniques and light-scattering techniques. In the former case, the simplest optical droplet sizing technique is direct photographic imaging of fuel droplets. These images reveal the structure of the fuel spray and the droplet size distribution. The droplet size distribution is determined from the recorded images by counting and measuring the droplet diameters. The light source for direct imaging may be either a pulsed or modulated continuous-wave laser. Photography requires

high-resolution images because the camera must be able to capture the image of the smallest droplets. The holographic recordings expand photographic techniques to encompass three-dimensional measurements. Holograms provide three-dimensional images of an object that can be examined similarly to photographs [143].

Phase doppler particle analyzer (PDPA) technology can simultaneously measure droplet velocity and particle size, with high spatial and temporal resolution, and has been widely used in engine research. The principle of PDPA's droplet velocity measurement is the Doppler effect of laser light. Two coherent laser beams with the same wavelength converge at a point to form a measurement body, and interference fringes are generated at the measurement body. When the wavelength and included angle of the two laser beams are known, the spacing of the interference fringes can be obtained. When the droplet passes through the measuring body at a certain speed, due to the existence of interference fringes, the light intensity of its scattered light also changes periodically at a certain frequency. By measuring the frequency of light intensity change, combined with the spacing of the interference fringes, the velocity component of the droplet in the vertical direction of the interference fringes can be obtained. Meanwhile, the principle of PDPA for measuring droplet size is the Lorentz-Mie scattering theory. It can obtain the droplet diameter by measuring the phase difference, and the measurement result does not need to be calibrated.

As mentioned above, the DISI engine in the cylinder can significantly improve the fuel economy. However, it is inevitable that the fuel impinging on the wall in the cylinder and form a fuel adhesion, especially in the current development of lightweight engines and increasing injection pressure. The pool fire effect produced by the combustion of the fuel adhesion can lead to the deterioration of soot emissions, resulting in reduced fuel economy, increased unburned hydrocarbons, and the formation of soot deposits on piston surfaces [144]. Results of previous studies shown that the fuel adhesion thickness is more important than the fuel adhesion mass [145]. Therefore, a transient high-speed quantitative test of the fuel adhesion thickness

distribution should be carried out, which is of great significance for controlling the formation of fuel adhesion. The main testing methods of fuel adhesion characteristics are summarized in Table 1.1.

Table 1.1 Comparison of fuel film test methods.

Method	Principle	Advantage	Shortcoming	Range
Total reflection method [146]	The point light source illuminates the fuel film and transparent medium from the bottom, creating an aperture. Calibrate the aperture radius-fuel film thickness relationship.	Simple test system.	The light's edge is difficult to determine, the liquid's and wall's refractive indices are incorrect, and the experimental uncertainty is high.	0~1000 μm
Interference method [147]	Coherent light passing through oil films of different thicknesses generates light and dark interference fringes. Fringe spacing determines oil film thickness.	No influence on oil film, high precision.	Single point measurement with low time resolution.	0~1000 μm
Laser Induced Fluorescence (LIF) method [148]	Under laser irradiation, a tracer in the fuel emits a fluorescent signal. Calibration of the fluorescence signal intensity and oil film thickness determines its thickness.	Flat and point measurements are possible. High-precision surface measurements.	Tracers have different evaporation characteristics with fuels, making it difficult to reflect heavy component fuel film formation.	0~60 μm
Refractive Index Matching (RIM) [149]	Quartz glass's rough surface diffusely reflects light. Light transmitted through the fuel film reduces diffusely reflected light. Light intensity is correlated with fuel film thickness.	High temporal resolution, accurate results, and optical testing.	Quartz pistons affect heat transfer.	0~5 μm
Diffuse reflection method [150]	Rough metal surfaces reflect light obliquely. In a light-irradiated area, liquid diffusely reflects light is weakened. Light intensity weakening degree and fuel film thickness need be calibrated.	With a metal surface, similar to the real fuel-coated process.	Complex test results require perspective shifts.	0~10 μm

The test system of the RIM technique is simple and easy to implement. It can quantitatively determine the evolution law of the two-dimensional fuel adhesion distribution. It has a high time resolution and test accuracy, and it does not require the use of characterization fuels and tracers, which more accurately reflect real-world fuel adhesion conditions. Presently, it has garnered considerable interest and demonstrated great application potential in fuel adhesion testing.

CHAPTER 2 EXPERIMENTAL APPARATUS AND PROCEDURE

2.1 High-Pressure Wind Tunnel and Observation Chamber

2.1.1 Principles of high-pressure wind tunnel

Tajima et al [151] used a wind tunnel to provide airflow under high ambient pressure. However, the complex structure and high expense of experiments are key issues. The principle schematic of another approach for producing air flow using a pressure tank is shown in Figure 2.1. The air tank can store compressed air. Keeping the valve 2 always full open. When valve 0 is opened and valve 1 remains partially open, the ambient pressure and air-flow velocity in the observation area can be measured simultaneously. Because of the throttling of valve 1 and the air supplement from the pressure tank, the ambient pressure in the observation section will not fast change to atmospheric pressure. In this situation, the observation section's ambient pressure and air-flow velocity conditions can be maintained by adjusting the valves. A quick-response control system can trigger the measurement when the ambient pressure and air-flow velocity reach to the experimental conditions.

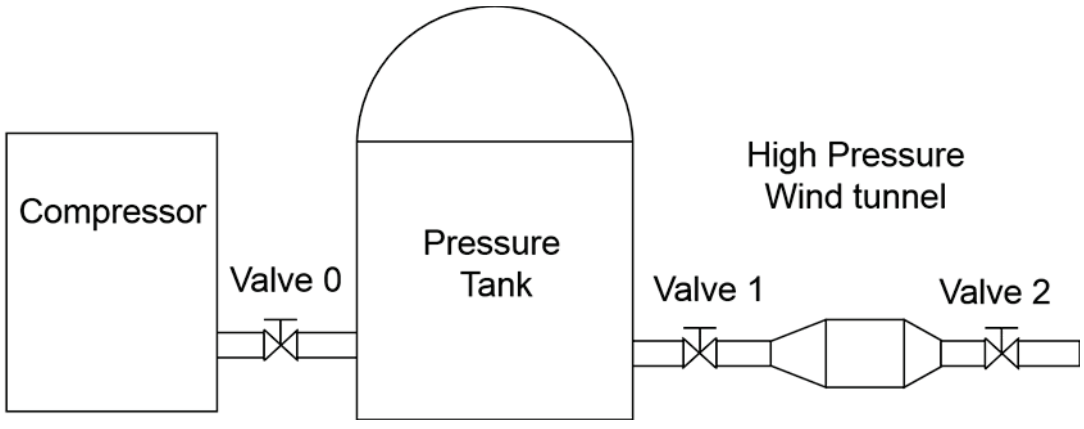

Figure 2.1 Schematic of cross-flow wind tunnel system.

2.1.2 Structure of high-pressure wind tunnel and uniform of cross-flow flow field

The principle of high-pressure wind tunnel already be introduced in above section. Another thing is that the uniform of air-flow flow field is controlled by the structure design of wind tunnel.

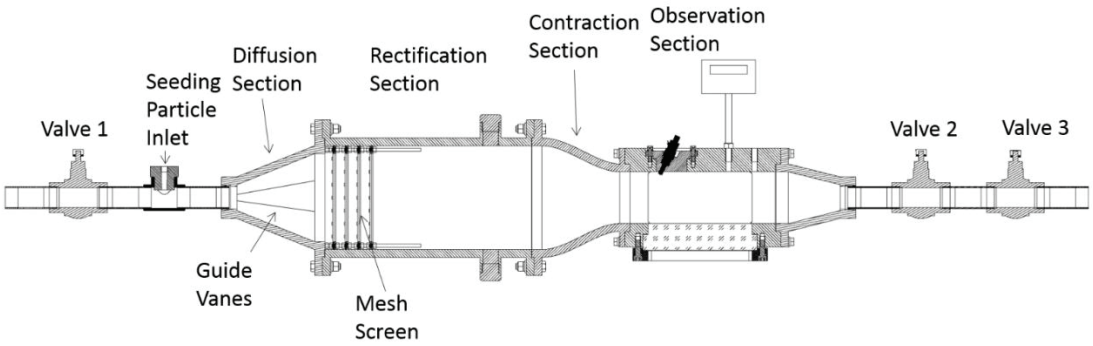

Figure 2.2 Pressure wind tunnel structure.

Figure 2.2 shows the structure of a high-pressure wind tunnel, which is divided into several sections (diffusion, rectification, contraction, and observation) to create a uniform cross-flow field. Upstream of the wind tunnel is the air tank. The air can be blown into the diffusion section, where the section area increases along the direction of the airflow. In the rectification section, five mesh screens with various mesh sizes are positioned, which can limit span-wise fluctuations of surface shear stress in a rational range [152] and decrease turbulence [153]. To unify the velocity distribution in the observation section, the shape curves of the contraction section walls should be sufficiently smooth to reduce turbulence. An observation chamber is connected to the cross-flow wind tunnel downstream, and the observation window (made of Pyrex) measured 200 mm (length) × 100 mm (wide). Observations are permissible from three sides of the observation portion, except the top surface. An adaptor for the injector was attached to the upper surface of the observation chamber. To detect the cross-flow velocity, a hot wire anemometer with a short response time is installed. All joints between the wind tunnel's sections are gastight, and a highly sensitive pressure sensor

is used to monitor the ambient pressure in the chamber. In addition, tracer particles are fed before to the diffusion section during PIV tests; hence, it is vital to maintain clean mesh screens.

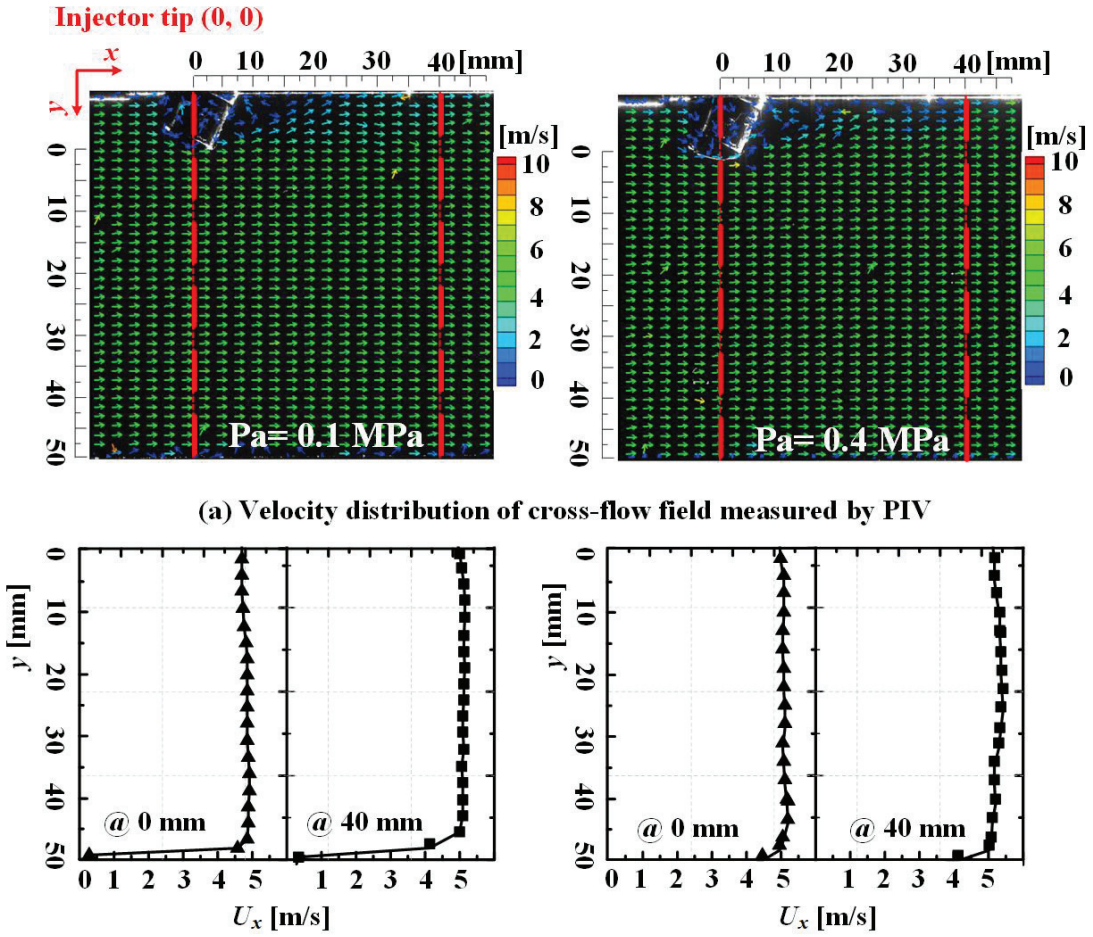

Figure 2.3 Cross-flow velocity distributions in the observation chamber above the wall.

Before the experiment, it was necessary to confirm the uniformity of the cross-flow field. Figure 2.3 (a) shows the velocity distribution of the cross-flow field measured by the PIV method under different ambient pressures. The results show that the overall velocity was stable. The injector nozzle tip position was defined as the origin O of the coordinate system. The cross-flow direction is along the positive x-axis, whereas the injection direction is along the positive y-axis. In addition, the velocity vector of each position was extracted from the PIV data. Figure 2.3 (b) shows the velocity distribution below the nozzle and 40 mm downstream along the cross-

flow. The results show that the velocity distribution under high ambient pressure suggests slight fluctuations. However, the overall spray development region is not affected.

2.2 Trigger Control System

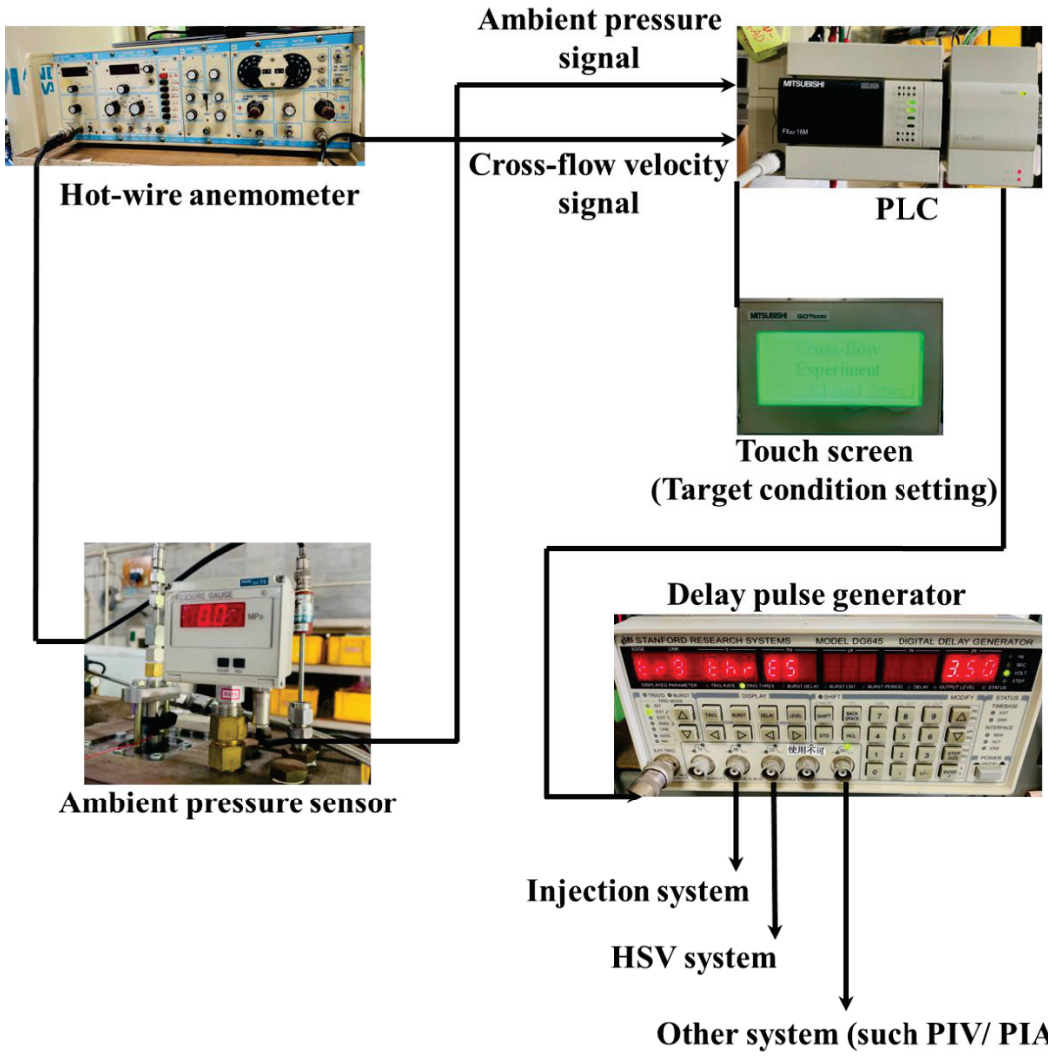

Figure 2.4 Control system for high-pressure wind tunnel.

The high-pressure wind tunnel experiments were triggered by meeting two conditions, ambient pressure and cross-flow velocity, in the observation section. The pressure and velocity were constantly changing in this section. Therefore, the experimental conditions should meet them both at the same time.

As shown in Figure 2.4, a pressure sensor (NSK, GC75243) and a hot-wire anemometer (KANOMAX 0251R-T5) were used to detect the ambient pressure and cross-flow velocity signals simultaneously. They have a quick response time that are less than 1 ms. An analog-digital conversion was used to convert the pressure sensor and anemometer signals from analog to digital (Mitsubishi, FX3U-4AD). The converted signals were loaded into a Mitsubishi FX3U-16MR/ES programmable logic controller (PLC), which could compare the two signals using a written program. The system's interface was a touch screen (Mitsubishi, GT1020-LWD) that displayed ambient pressure and cross-flow velocity values and allowed operations to be performed. The touch screen was programmed with an experimental system for these experiments. PLC would output a pulse when the ambient pressure and cross-flow velocity signals meet the experimental conditions. And then the pulse generator received this pulse, which can control the injection system, high-speed video camera, and PIV system, and so on. Because of the difficulty of velocity measurement in a sealed space with changing ambient pressure, the cross-flow velocity measurement was done in an intrusive manner in this experiment.

Mechanical anemometers, such as cup anemometers and vane anemometers, are commonly used in natural wind measurement. The velocity is converted into electric signals using a set of cups or vane in the principle of them. After measuring, the airflow field would be greatly influenced. The Pitot tube anemometer is a popular type of anemometer in aviation. The Pitot tube anemometer measures velocity based on pressure [154]. A hot-wire anemometer is a type of thermal anemometer that measures velocity and turbulence. The rate at which heat is transferred from a heated filament to the flow in which it is immersed is measured by the hot-wire anemometer [155-157]. The probe's structure is depicted in Figure 2.5, and the hotwire is made of platinum or tungsten.

The vane anemometer was excluded from this investigation due to its effects on airflow and the probe part's structure. The Pitot tube anemometer could be used for

the measurement, but the transferring process was complicated due to the unsteady pressure, and the response time was also an issue. In this study, a hot-wire anemometer was used; its response time is less than 1 ms, and the results were unaffected by pressure changes. The hot-wire probe was teste d in the middle of the observation chamber because the velocity is more stable, and the turbulence is lowest there.

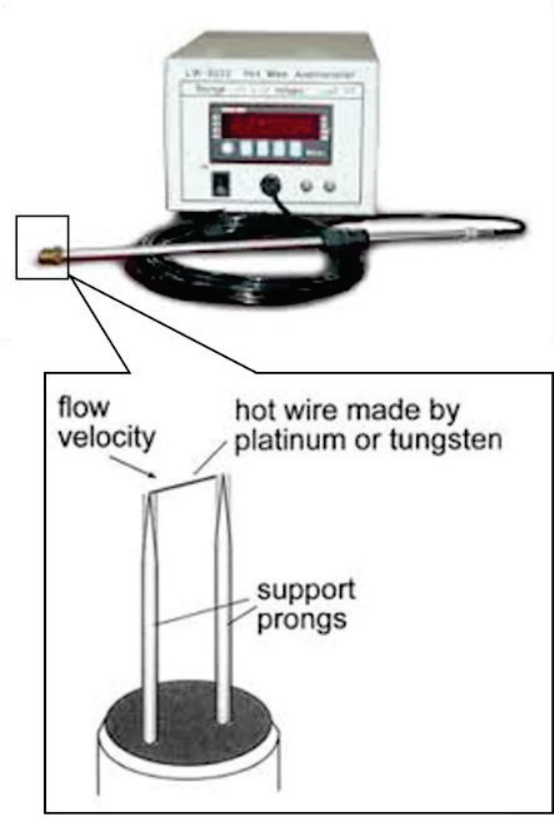

Figure 2.5 Typical Anemometers (hot-wire anemometer was employed).

Cross-flow of various velocities and ambient pressures can be achieved by adjusting the valves before and after the wind tunnel. Figure 2.6 shows the triggering process under the example condition (P_a= 0.4 MPa, U_x= 5 m/s). First, valve 2 maintains a fixed opening degree (61°), and valve 1 is closed. Second, fully open valve 1, the cross-flow is produced. The ambient pressure increases rapidly when valve 1 is opened, and then gradually decreases. Finally, the electronic control unit (ECU) and high-speed video (HSV) camera can be triggered when the cross-flow

velocity and ambient pressure come to the target condition simultaneously. In the previous section, it is already be proven that the cross-flow and ambient pressure could remain stable during the injection duration [158].

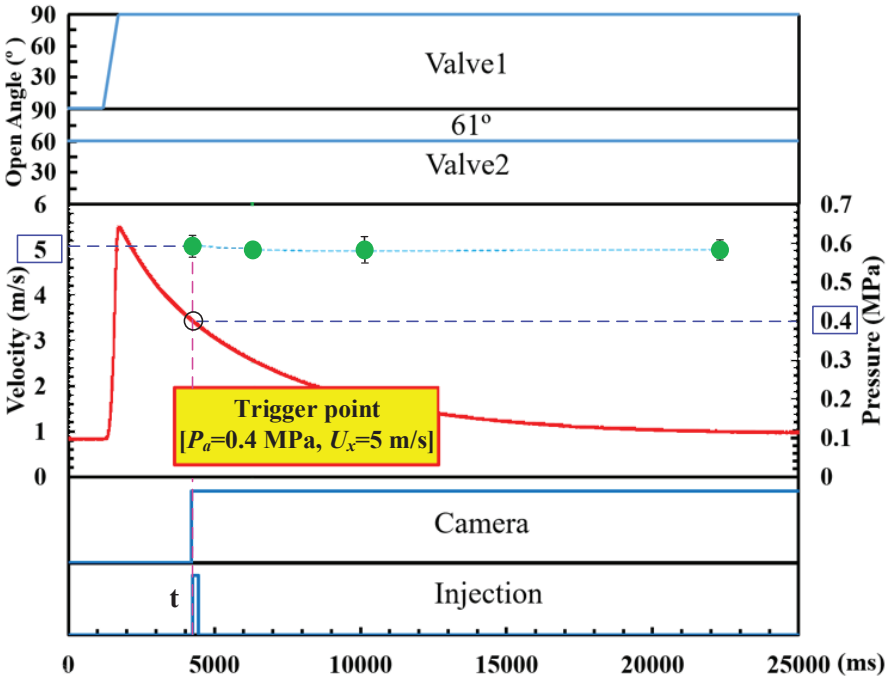

Figure 2.6 Example condition for trigger [P_a= 0.4 MPa, U_x= 5 m/s].

2.3 Fuel Supply System

Figure 2.7 shows the apparatus arrangement diagram of fuel supply system, which was provided by the research association of Automotive Internal Combustion Engines (AICE) project. The fuel supply system mainly consisted of an air compressor, a high-pressure air driven pump, a fuel tank, fuel supply pipeline and the injector. The injection pressure was built by the high-pressure air driven pump (HASKEL), which can be measured using a highly sensitive sensor in real time as well as displayed digitally. The air compressor (MCP-250A) was manufactured by Monotaro Corporation. The volume of this air compressor is 25 liters, and the maximum operating pressure is 0.8MPa. In addition, its rated power is 570 w.

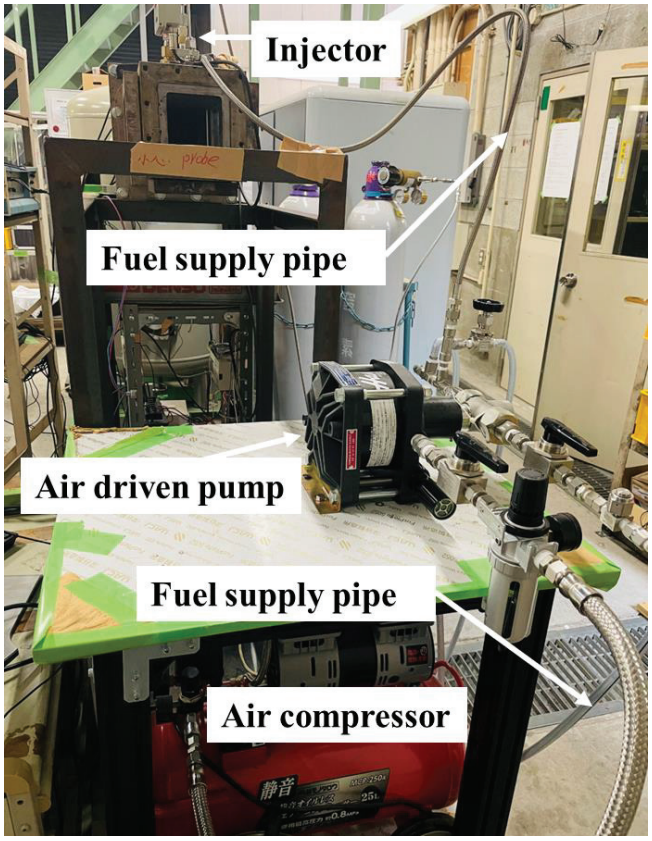

Figure 2.7 Apparatus arrangement diagram of fuel supply system.

2.4 Signal Acquisition System

As shown in Figure 2.8, a complete "signal acquisition system" was included in this experimental system. A vibration acceleration sensor was installed on one side of the fuel injector to collect vibration signals, and the acceleration signal during the needle valve lifting process can be obtained. While sending the trigger signal to the ECU, a breakout line is used to connect the signal to a channel of the oscilloscope for acquiring the trigger signal. We also used a current detection instrument to detect the current signal sent by the ECU to the injector. In addition, the fuel injection pressure, cross-flow velocity and ambient pressure can also be recorded by the oscilloscope during each experiment.

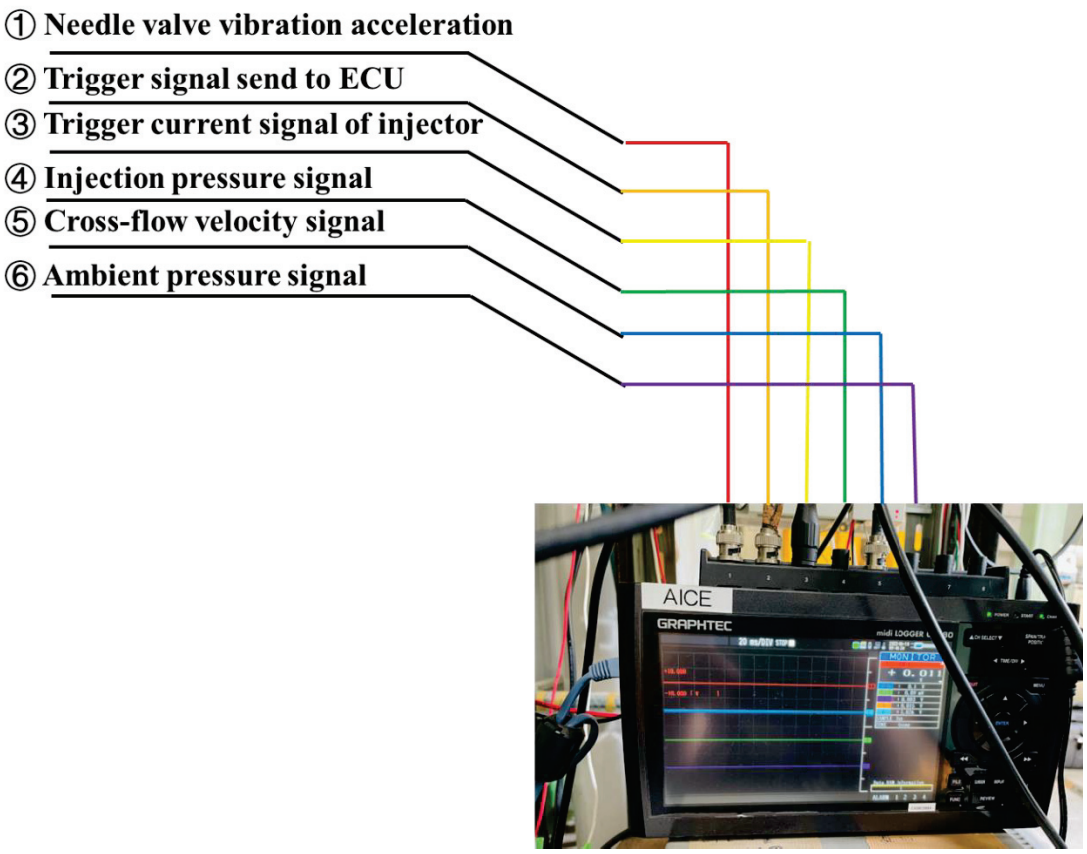

Figure 2.8 Signal acquisition using oscilloscope.

2.5 Image Acquisition System

Figure 2.9 High-speed video camera.

The rapid advancement of high-speed photography technology has facilitated the

use of visualization technology in engineering fields such as spray and combustion. Direct observation is considered to be one of the best observation methods for the research in spray and combustion field. Figure 2.9 depicts the MEMRECAM HX-3 camera provided by Japan's NAC company when using the high-speed camera in this study.

2.6 Injection Rate Measurement System

In the experiment, the fuel injection rate was measured using the Bosch long tube method, which is depicted in Figure 2.10. The examined injector mount, on which the pressure sensor was mounted, the measuring following tube, and an orifice plate separating them are shown in the figure [159]. A check valve was installed at the system's end. The injector mount was the most complex of these structures, as it not only aligned the injector with the measuring tube but also housed the pressure sensor. The length and diameter of the measuring tube were determined by the size of the injector. The longer tube length helps to keep the noise generated by the reflected wave away from the pressure sensor. Meanwhile, the inner diameter of the tube influences the magnitude of the pressure generated by the injection, whereas the length determines the attenuation. The adjustable orifice size determined how much of the reflected pressure wave is reflected. This varies depending on the amount injected. A ball or throttle valve was usually used to meet the quick adjustments. If the orifice diameter is too large, the majority of the pressure wave will enter the next tube, resulting in a negative wave after reflection. A variable check valve was mounted on the end of the following tube to adjust the system's backpressure. This is significant because standard injection pressure can be used while testing an injector in this manner.

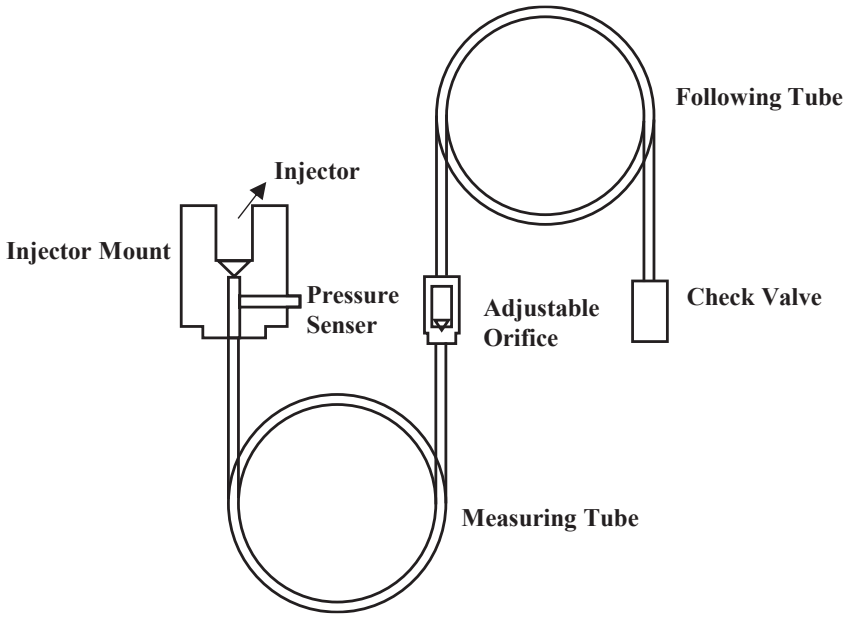

Figure 2.10 Schematic diagram of Bosch long tube method [159].

2.7 Optical Measurement Methods

The following optical diagnostic techniques are used in the experiments described in this paper. High-speed photography was used to capture spray images using the DBI method. CW laser sheet technology is used for high-speed photography in vertical and horizontal planes to obtain images of wall impact spray. Furthermore, the velocity distribution of the wall-impacting spray and the velocity distribution of the cross-flow flow field were obtained using the PIV technique. LDSA was used to determine the SMD of the droplets. To obtain a side view of the fuel spray, high-speed photography was performed on a vertical view using Mie scattering techniques. Meanwhile, the RIM technology was used for high-speed photography at the bottom of the observation section to obtain images of fuel adhesion.

2.7.1 DBI/ Mie scattering using CW laser

DBI is widely used as a visualization research method by various research institutions because of its simple optical layout and is based on the incident light extinction, which is caused by the scattering, absorption, and even reflection when light hits an object. Generally, it includes a light source that provides volume light, a

diffuser, and an HSV as shown in Figure 2.11.

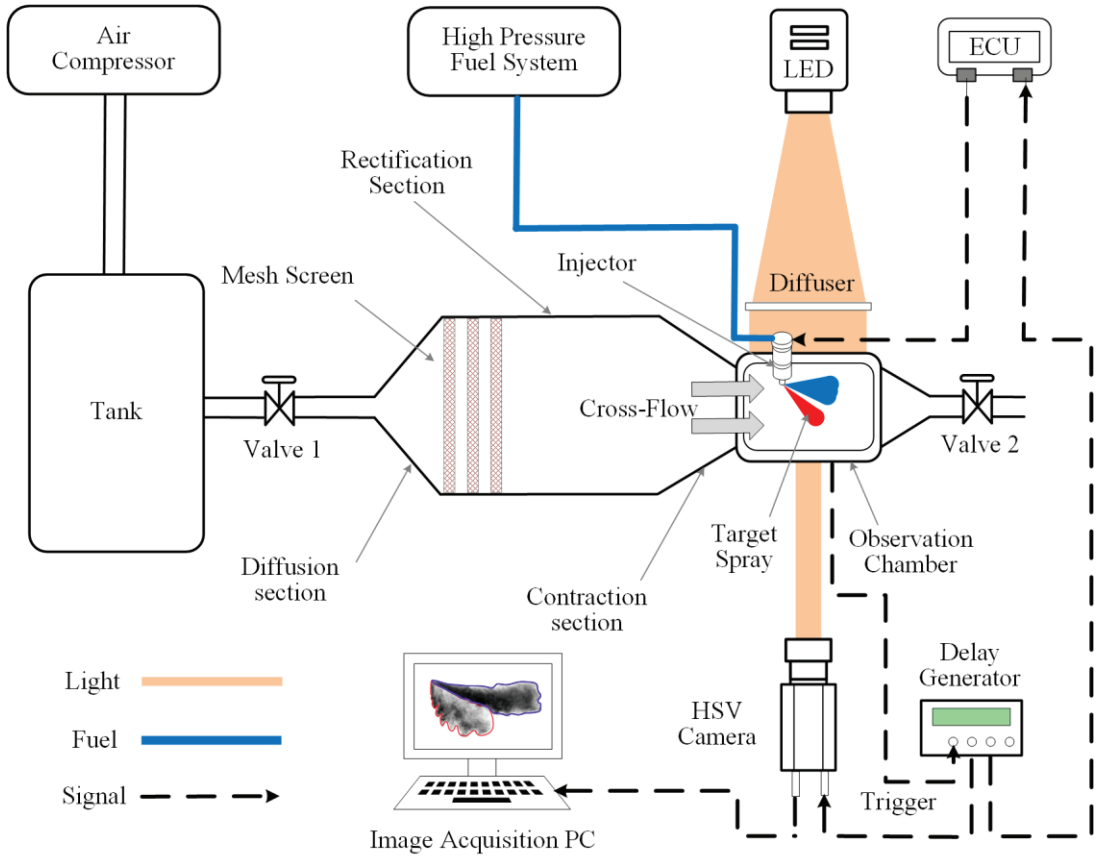

Figure 2.11 Experimental apparatus arrangement for high-speed photography using DBI method.

The experimental system primarily comprised a stable high-pressure fuel supply system, a cross-flow velocity and ambient pressure control system, an injection signal control system, and an image acquisition system. An HSV camera (NAC MEMRECAM HX-3) set at a frame rate of 20000 and a frame size of 768 × 680 pixels was utilized to observe the macroscopic spray; the camera was attached to a long-distance microscope (Nikon, 105 mm, f/ 4.8), and its exposure time was set to 50 μs. Meanwhile, a high-brightness light emitting diode (LED) (Altec, LLBK1-LA-W-0001), which is a stable light source controlled by a constant current, was employed as a light source to provide sufficient uniform brightness. The light passed through the diffuser (acrylic cast board) and was directed into the observation chamber. As shown in Figure 2.11, the HSV camera, light source of the LED, and visual observation

chamber was arranged in a straight line.

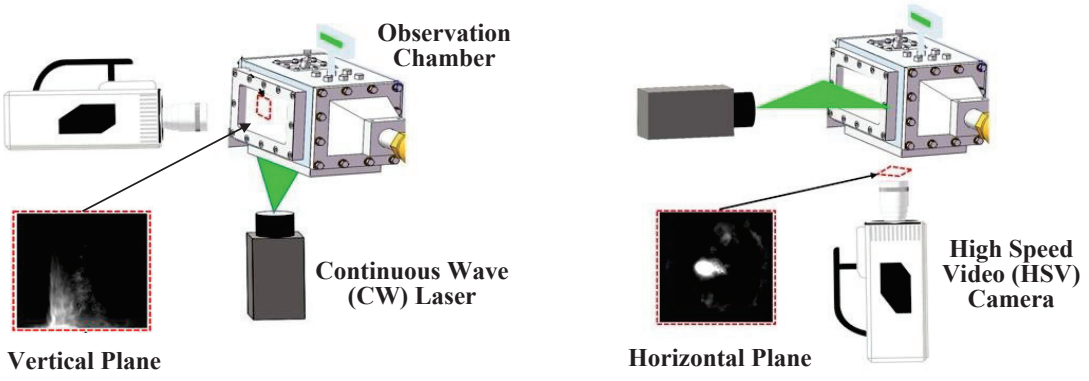

(a) High Speed Video for vertical plane **(b) High Speed Video for horizontal plane**

Figure 2.12 CW laser diagnostic for spray.

Figure 2.12 (a) shows an optical system arrangement scheme for obtaining spray images on the vertical plane. A continuous-wave laser sheet (DPGL-2W, Japan Laser Corp.) was located below the observation chamber with a wavelength of 532 nm. Meanwhile, a HSV camera (Photron FASTCAM SA-Z) was aligned at 90° with the light source. In the optical system arrangement scheme shown in Figure 2.12 (b), the HSV camera and the laser positions are exchanged observing the spray wall-impingement behavior on the horizontal plane.

2.7.2 PIV (Particle Image Velocimetry)

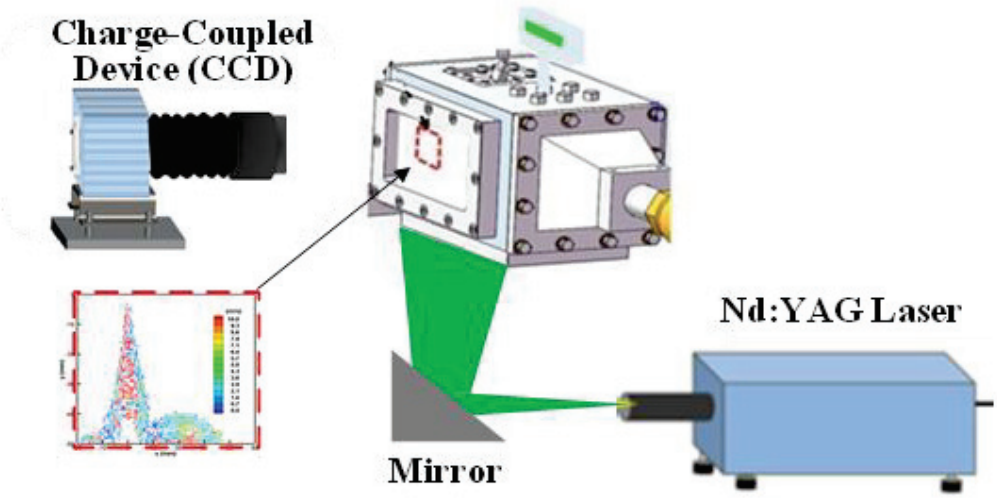

Figure 2.13 Optical arrangement for PIV measurement.

As depicted in Figure 2.13, a PIV system (Seika Corp., 2D PIV system) was used to measure the spray velocity and cross-flow velocity, which included a PIV camera (PCO Inc, PCO1600), a double-pulsed Nd: YAG laser (NEW WAVE RESEARCH Corp., DPIV-N50, a sheet with a wavelength of 532 nm and thickness of 1mm was provided), a host computer, and a synchronizer.

Parallel to the direction of the cross-flow, double-pulsed laser sheets were directed to the observation chamber. The laser sheets were adjusted to illuminate different vertical and horizontal planes while measuring the velocity distributions of the spray droplets and the cross-flow field. The observations were conducted in a plane near the nozzle tip. Olive oil particles, a few microns in diameter, were seeded into the wind tunnel through the tracer particle inlet to measure the velocity of the cross-flow, while the velocity distribution of the spray could be obtained without the additional tracer. By the way, the pulse separation of the double-pulse was 40 μs when measuring the cross-flow field velocity. In comparison, it was shortened to 15 μs when measuring the droplet velocity of wall-impingement spray.

2.7.3 LDSA (Laser Diffraction Size Analyzer)

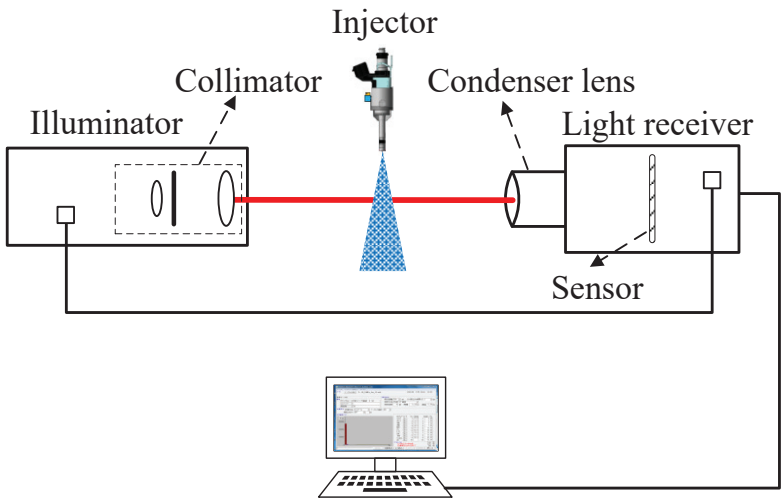

Fig. 2.14 Schematic diagram of droplet size measurement by LDSA.

In order to further analyse the effect of cross-flow on spray atomization, a

droplet size analyser (NIKKISO Corp., LDSA-1400A) was employed to measure the droplet diameter. The device could provide a laser beam of 8 mm diameter (the beam is perpendicular to the vertical plane of spray), which can measure the droplet size ranges from 1.4 μm to 1000 μm with a 300 mm focal length lens. LDSA was triggered by the same pulse generator DG645 that controls the injection duration as well as the sampling time and frequency.

Figure 2.14 shows the schematic diagram of the LDSA device. When the droplet passes through the laser beam, the droplet surface will be diffracted, and the angle Θ of diffraction is inversely proportional to the droplet diameter. In other words, the diffracted light of droplets with different sizes will fall at different positions of the sensor when they pass through the laser beam, that is, the position information reflects the droplet size. Droplets with the same size will fall in the same position, and then the diffraction light intensity at this position will be higher after superposition, so the diffraction light intensity information can reflect the proportion of droplets with the same size in this position.

2.7.4 Mie scattering / RIM (Refractive Index Matching)

To obtain the information of wall-impingement spray and fuel adhesion, Figure 2.15 shows the optical system arrangement for the experiment of Mie scattering and RIM. Figure 2.15 (a) is an optical system arrangement for Mie scattering experiment, which was used to obtain the macroscopic spray images. A HSV camera was located in front of the observation section. Meanwhile, a xenon lamp was located obliquely behind the observation section as the light source. In addition, the optical system arrangement for the RIM experiment is shown in Figure 2.15 (b). The HSV camera was located directly below the observation section, and the xenon lamp was located diagonally below the observation section to observe the microscopic fuel adhesion distribution after spray impinges on the flat-wall. Meanwhile, two sample images are shown in this figure.

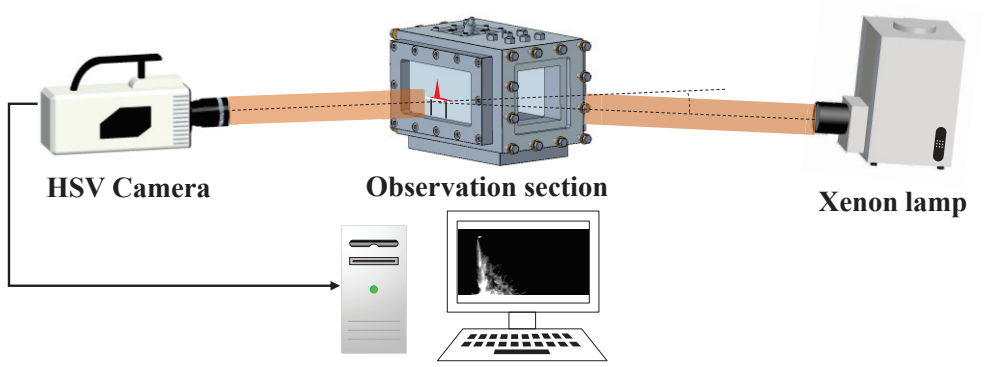

(a) Mie scattering photography

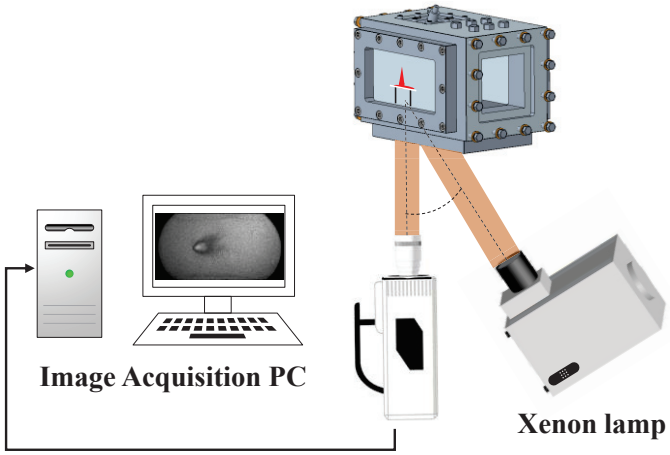

(b) RIM fuel adhesion measurement

Figure 2.15 Optical system arrangement for Mie scattering and RIM experiment.

2.8 Summary

This chapter first introduces the design principles of the high-pressure wind tunnel, and then presents the structural diagram of the cross-flow wind tunnel that can provide a stable cross-flow flow field. In addition, the trigger control process of cross-flow velocity and ambient pressure as external signals was explained in detail. The related signal acquisition system and image acquisition system were also described in detail. Finally, the main optical diagnostic technologies employed in this study and their optical arrangements were introduced.

CHAPTER 3 STATISTICAL VARIATION ANALYSIS OF FREE SPRAY UNDER ATMOSPHERIC PRESSURE

3.1 Introduction

The highly transient characteristics inside ICEs can result in CCVs, which are reflected in various behaviors of fuel spray. All these CCVs are coupled with each other significantly during engine operation, and a significant CCV can results in low thermal efficiency, high fuel consumption, and exhaust emissions. It was discovered in a previous study that if most CCVs can be decreased, then the output power can be enhanced for the same amount of fuel consumed. Therefore, it is of great significance to investigate the spray CCVs inside the ICEs cylinder.

There are few related research works on discussing the CCV of fuel spray characteristics, especially under the cross-flow conditions. The CFD mode that considering the effect of cross-flow on the fuel spray characteristics has not been reported. The objective of present work is to experimentally investigate the effect of cross-flow on the CCV of fuel spray characteristics of multi-hole injector for DISI engine under atmospheric pressure. In this study, the spray images of high-speed photography were obtained by the DBI method. The variations of spray characteristics were evaluated by statistical analysis of 30 times repeated experiments under the atmospheric pressure. Moreover, the coefficient of variation (COV) was used to assess the variation in spray penetrations and area. Finally, the influence of injection pressure and cross-flow velocity on the statistical characteristics of spray were analyzed at the EOI timing, and then the contribution indexes of cross-flow to the spray variation characteristics were evaluated.

3.2 Experimental Conditions and Injector Type

3.2.1 Experimental condition

Details of the experimental conditions are listed in Table 1. Iso-octane was injected into the cross-flow flow field under injection pressures of 18, 30, and 35 MPa and an injection pulse of 1 ms. The cross-flow velocity ranged from 0 to 50 m/s. In addition, the fuel properties of Iso-octane are listed in Table 1. The experiment was performed under atmospheric pressure [160,161].

Table 3.1 Experimental conditions.

Ambient conditions	
Ambient pressure, P_a [MPa]	0.1
Ambient temperature [K]	300
Cross-flow velocity, U_x [m/s]	0, 30, 50
Injection conditions	
Injector type	1+4 holes
Nozzle exit diameter, D [mm]	0.16
Test fuel	Iso-octane
Injection pressure, P_{inj} [MPa]	18, 30, 35
Injection pulse, t_{inj} [ms]	1.0
Fuel properties	
Fuel density, ρ_l [kg/m^3]	691.9
Surface tension, σ [N/m]	0.0188
Viscosity, μ [kg/m s×10^{-4}]	5.04

3.2.2 3D high-pressure wind tunnel, observation chamber, multi-hole injector and trapping device

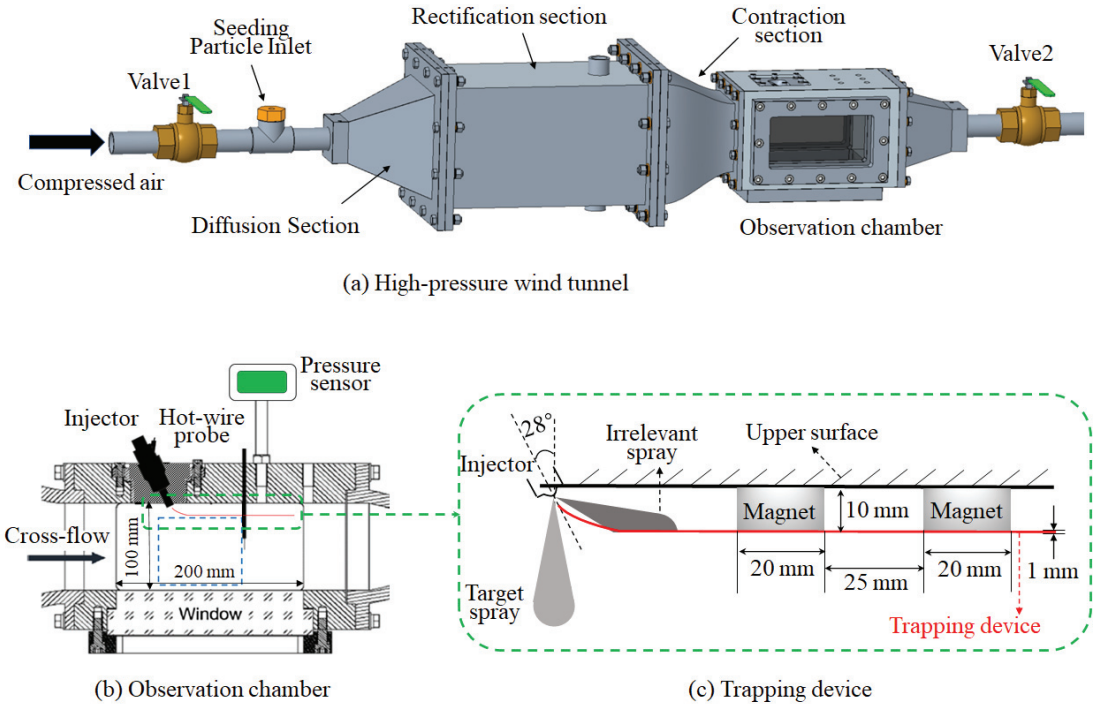

Figure 3.1 Details of experimental apparatus.

Figure 3.1 (a) shows the details of the high-pressure wind tunnel. The side view of the observation chamber (high-speed camera side) is shown in Figure 3.1 (b). From Figure 3.1 (b), an adaptor for the injector was attached to the upper surface of the observation chamber. The nozzle tip was located 5 mm below the inner wall of the adaptor. The injector was installed 62° relative to the upper surface such that the direction of the target spray remained perpendicular to the direction of the cross-flow. In addition, as depicted in the spray images, the irrelevant spray overlapped with the target spray, thereby affecting the target spray measurement. Therefore, a trapping device was designed to lessen the effects of irrelevant spray. The location of the trapping device is shown in Figure 3.1 (c) for clarity. The trapping device comprised a curved iron plate (1 mm thick) and four magnets. The magnet and iron plate were screwed together using bolts. The upper surface of the magnet was attached to the upper surface of the observation chamber. As such, the device can be shifted

conveniently to achieve the best position for target spray visualization.

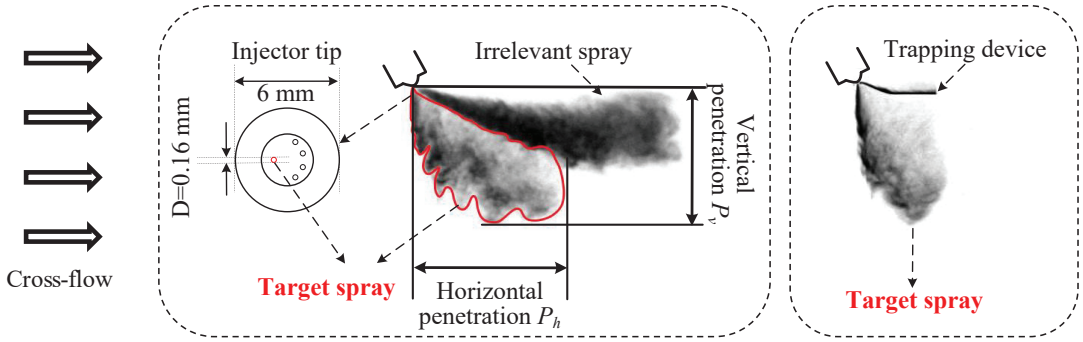

(a) Spray without trapping device (b) Spray with trapping device

Figure 3.2 Target spray captured using trapping device

[U_x = 50 m/s, P_{inj} = 18 MPa, t = EOI].

To reduce HC emissions and the sensitivity of the fuel spray to the in-cylinder flow field, multi-hole injectors are typically used in ICEs. A multi-hole injector provided by Denso was used in the experiment performed in the current study. As shown in Figure 3.2 (a), this study primarily focused on a single hole (red hole) with a diameter of 0.16 mm, whose central axis was situated 28° relative to the injector axis (Figure 3.1 (c)).

In addition to the nozzle structure, the definition of spray penetration is also illustrated in Figure 3.2 (a). Meanwhile, considering the effect of cross-flow, vertical penetration (P_v) and horizontal penetration (P_h) were defined, respectively. Because the present study focused only on the target spray shown in Figure 3.2 (a), the vertical penetration was defined as the distance from the target spray tip (vertical direction) to the nozzle tip, and the horizontal penetration was defined as the distance from the target spray tip (horizontal direction) to the nozzle tip.

As shown in Figures 3.2 (a) and (b), comparing the spray image with and without the trapping device, the irrelevant sprays were obstructed significantly by the trapping device. This study primarily focused on the variations in the target spray characteristics; interactions between the irrelevant spray and the target spray plume will be investigated in a future study.

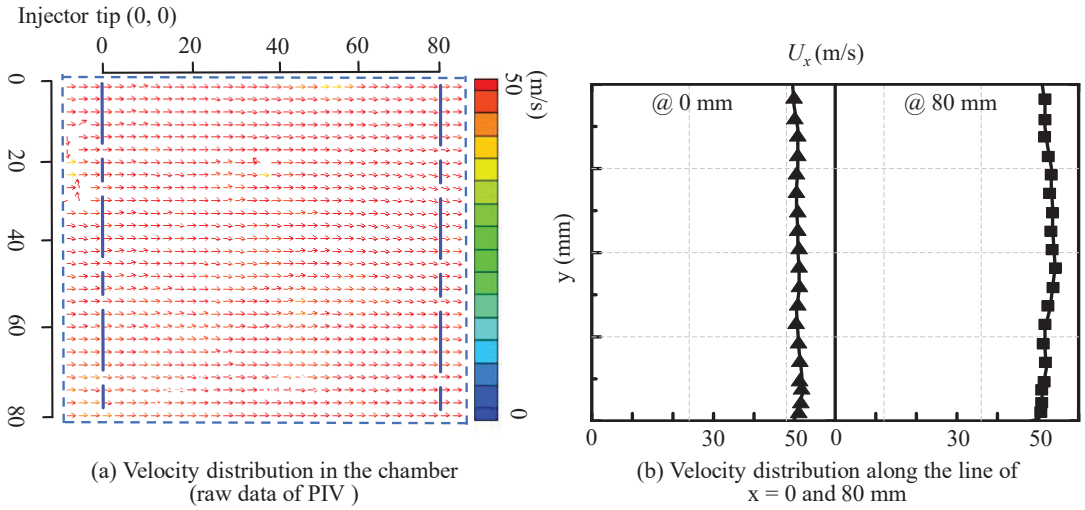

(a) Velocity distribution in the chamber (raw data of PIV)

(b) Velocity distribution along the line of x = 0 and 80 mm

Figure 3.3 Effect of trapping device on cross-flow field.

High-speed videos of the macro spray with/ without the trapping device were added to the manuscript attachment for reference. Additionally, as shown in Figures 3.3 (a) and (b), the trapping device did not affect the uniform cross-flow field distribution when the device was assembled, as evident from PIV data analysis; detailed information pertaining to the PIV measurement is available in Ref. [94]. In addition, the results from our previous study indicate that the turbulence intensity in the boundary layer was large, but the region where the spray had developed was a uniform cross-flow flow field [93]. Therefore, in the subsequent experiment, only the single target spray of the multi-hole injector was analyzed using the trapping device.

3.2.3 Sample numbers' effect and injection rate

Figure 3.4 shows the effect of the sample number on the variation in the spray vertical penetration obtained using a trapping device. The COV was used to evaluate the effect of the sample number on the spray stability, which is defined as the standard deviation P_σ of the penetration divided by the average penetration $\overline{P}$. P_σ can be calculated using Equation (3.1).

$$P_\sigma = \sqrt{\frac{\sum(P_i - \overline{P})^2}{N-1}} \tag{3.1}$$

where P is the penetration, N is the sample number, and P_i is the penetration of

experiment i. As clearly shown in Figure 3.4 (a) and (b), the average vertical penetration converged when N exceeded 25, i.e., approximately 50.38 mm with a standard deviation of ±2.2 mm, approximately 0.7 ms after the start of energization (U_x = 0 m/s, P_{inj} = 35 MPa). Meanwhile, the COV of the penetration reached 4.5% can be seen from Figure 3.4 (c). Thirty shots were performed in this study to evaluate the variations in the spray characteristics.

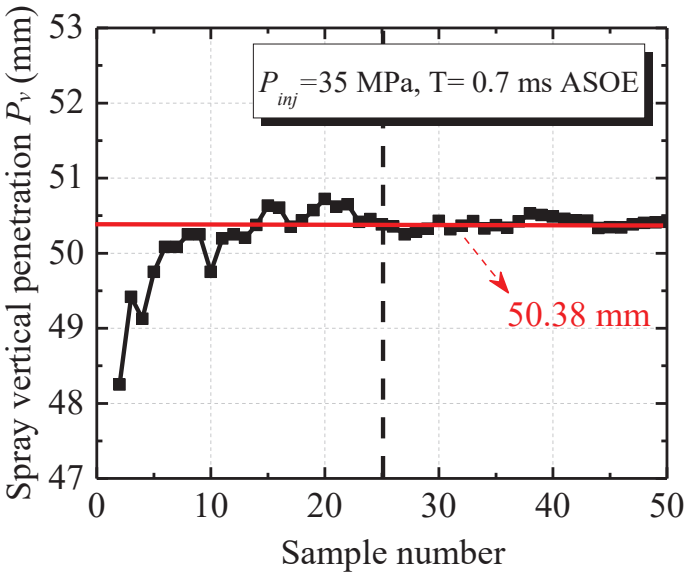

(a) Average vertical penetration

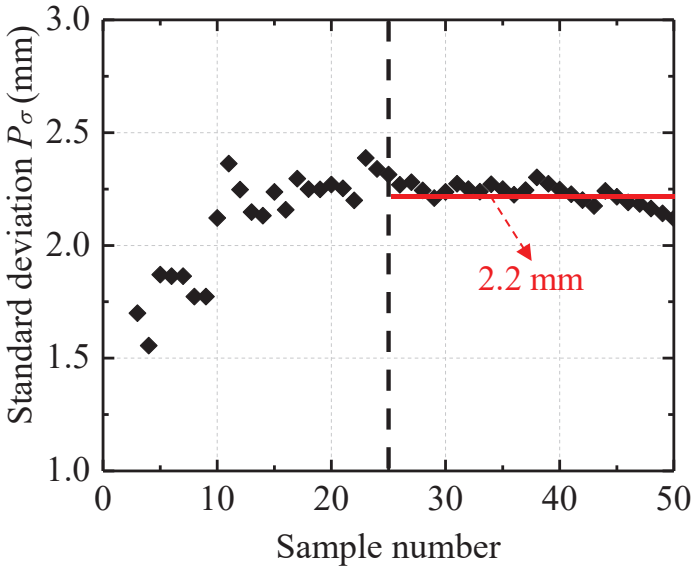

(b) Standard deviation of vertical penetration

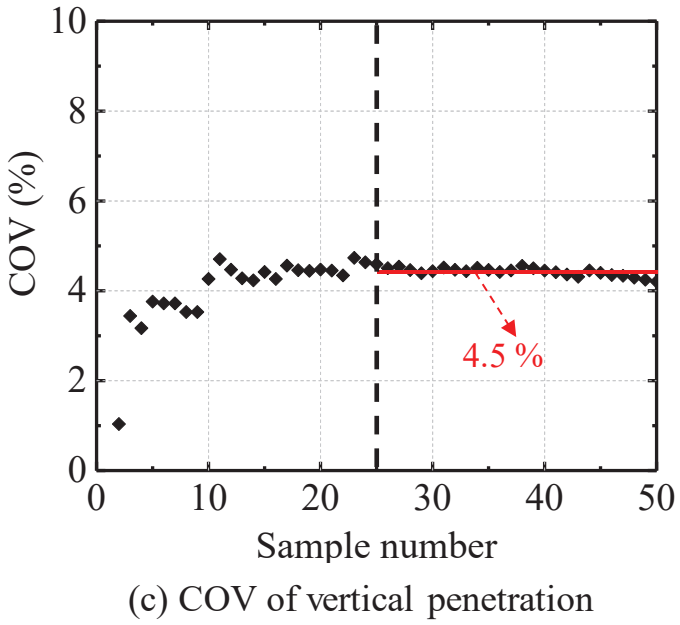

(c) COV of vertical penetration

Figure 3.4 Effect of sample number on variation in spray penetration.

As shown by the results in Figure 3.4 (a), the spray penetration fluctuated, which is attributable to the different times at the actual start of each injection. Therefore, a high-precision acceleration sensor was assembled on the side of the injector to measure the acceleration of the injector needle valve. Meanwhile, the injection delay (the time when the needle valve of the injector began to lift) was used to evaluate the fluctuation at the start of injection. When the needle valve of the injector was elevated, the acceleration generated by the movement was detected as a voltage by the accelerometer.

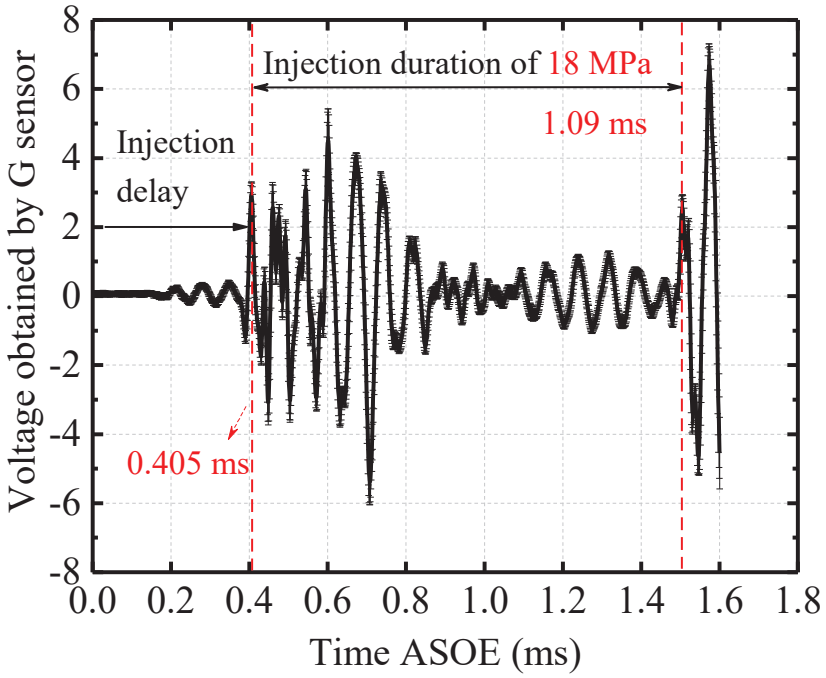

(a) P_{inj} = 18 MPa

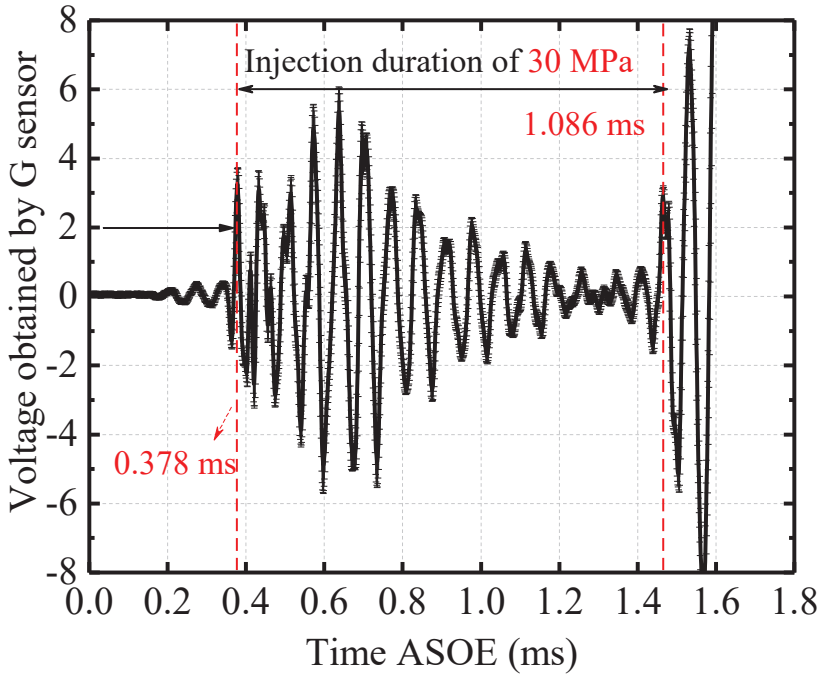

(b) P_{inj} = 30 MPa

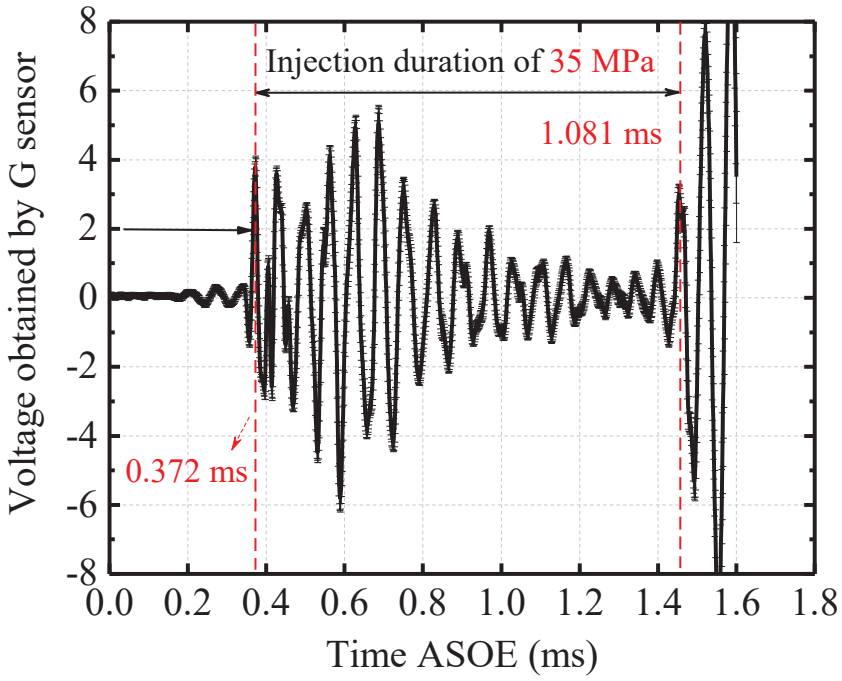

(c) P_{inj} = 35 MPa

Figure 3.5 Vibration signal of injector needle valve during 30 shots under different injection pressure.

Figure 3.5 shows the average voltage of 30 shots detected by the accelerometer over time. The vertical axis represents the acceleration, and the horizontal axis represents the time elapsed since the DG outputs the injection signal. As shown in 3.5 (a), (b), and (c), the average injection delays under injection pressures of 18, 30, and 35 MPa were 0.405, 0.378, and 0.372 ms, respectively. Meanwhile, injection durations of 1.09, 1.086, and 1.081 ms were obtained as well. Next, the variation in the next 30 injection delays was quantitatively evaluated.

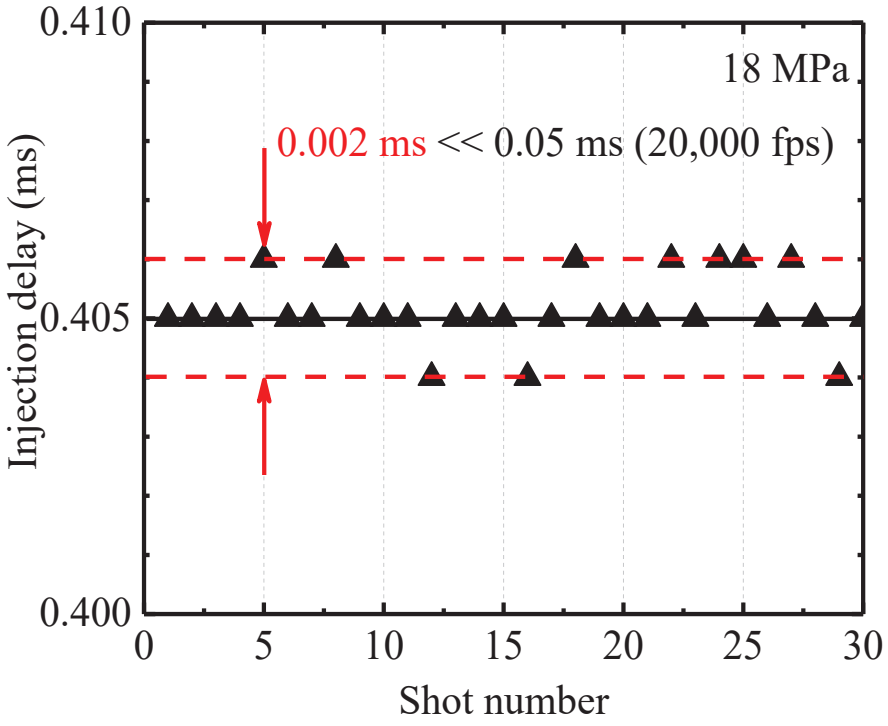

(a) P_{inj} = 18 MPa

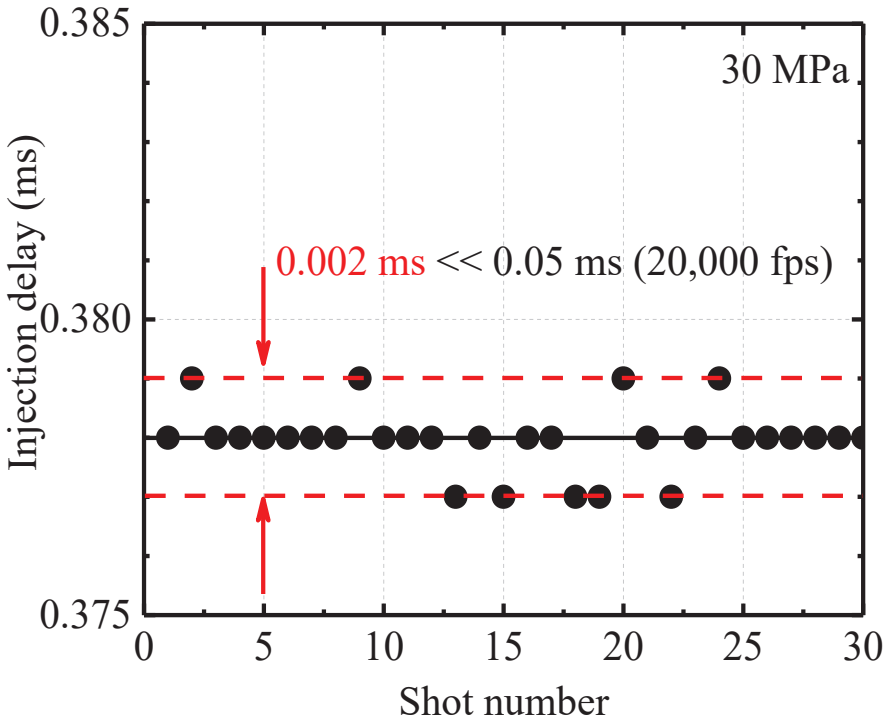

(b) P_{inj} = 30 MPa

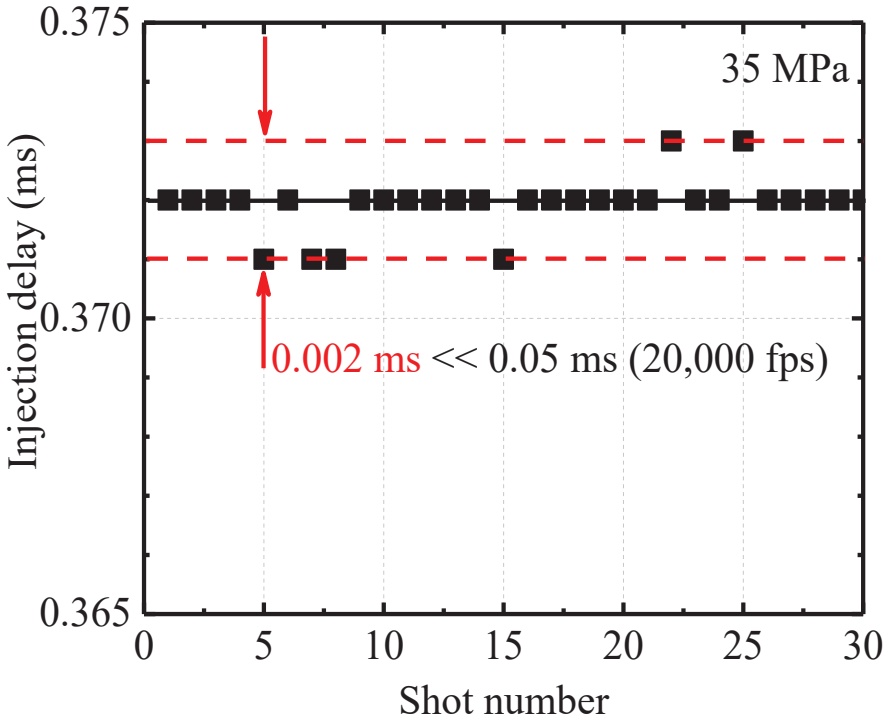

(c) P_{inj} = 35 MPa

Figure 3.6 Injection delay of 30 shots under different injection pressures.

Figure 3.6 shows the injection delay for 30 shots at different injection pressures. As shown in Figure 3.6, the injection delay was relatively stable under each injection pressure (±2 μs). The velocity at the exit of the injection hole was calculated based on the injection pressure and Bernoulli's principle [162]. It was estimated that the spray penetration will change by approximately 0.2 mm in 2 μs under an injection pressure of 35 MPa. The image resolution was set to 0.27 mm/pixel, which implies that the delay time of the valve opening affects the spray penetration by less than 1 pixel. Therefore, it was assumed that the injection delay would not significantly affect the spray variation. The average injection delay shown in Figure 3.5 can be regarded as the actual start of the injection.

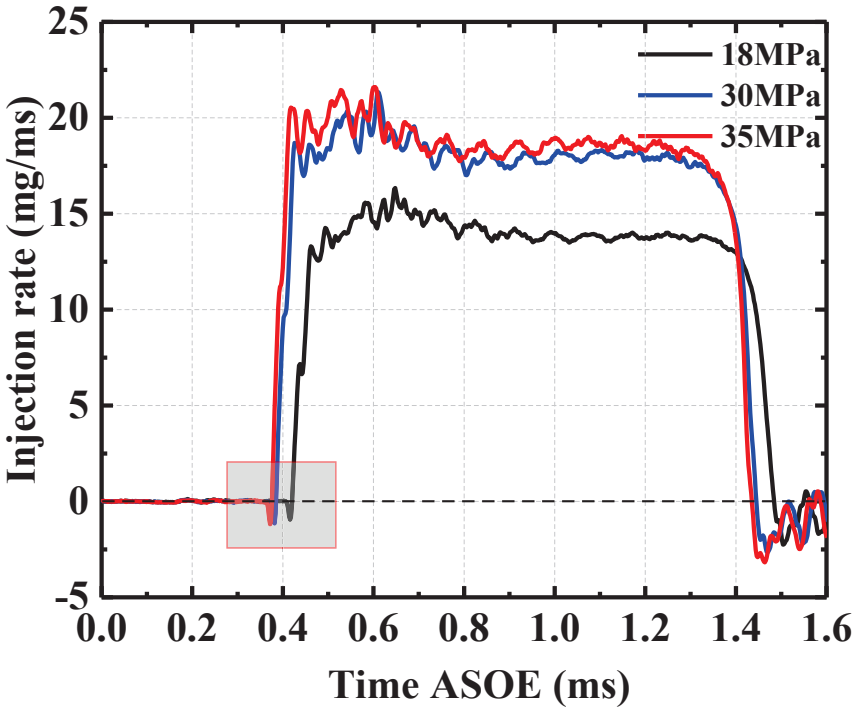
Injection rate (mg/ms)
Time ASOE (ms)
18MPa
30MPa
35MPa
25
20
15
10
5
0
-5
0.0
0.2
0.4
0.6
0.8
1.0
1.2
1.4
1.6

(a)

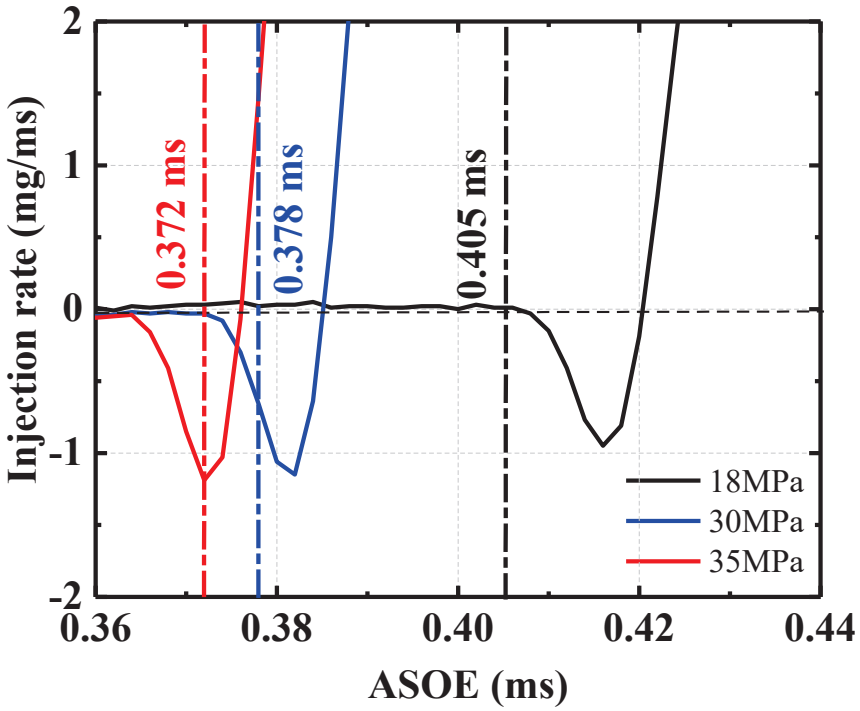
Injection rate (mg/ms)
ASOE (ms)
0.372 ms
0.378 ms
0.405 ms
18MPa
30MPa
35MPa
2
1
0
-1
-2
0.36
0.38
0.40
0.42
0.44

(b)

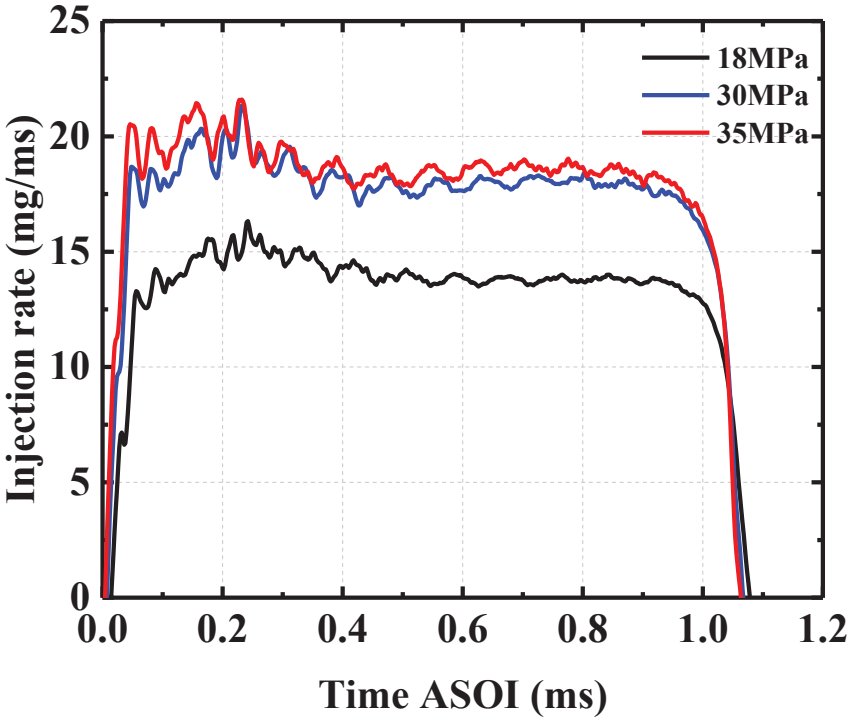

(c)

Figure 3.7 Average fuel injection rate for different injection pressures.

The injection rate is vital to the fuel injection process as it directly affects the spray characteristics [163]. To investigate the spray characteristics under the same injection pulse (1 ms) but different injection pressures, the fuel injection rate must be obtained. In this study, the injection rates were measured by Denso using the Zeuch method. Figure 3.7 shows the fuel injection rate under different injection pressure conditions (provided by Denso). In Figure 3.7 (a), the time after the start of energization (ASOE) is used as the time axis. As shown in Figure 8, a high injection rate can be obtained using a high injection pressure under the same injection pulse. Meanwhile, the injection rate increased faster, and the time to reach a steady stage was shorter under the injection of 35 MPa. As shown in Figure 3.5, the start of injection can be determined, which is enlarged in Figure 3.7 (b). Figure 3.7 (c) shows the injection rate under the time axis of the time ASOI, and it was used to compare the spray characteristics.

3.3 Propagation of Spray

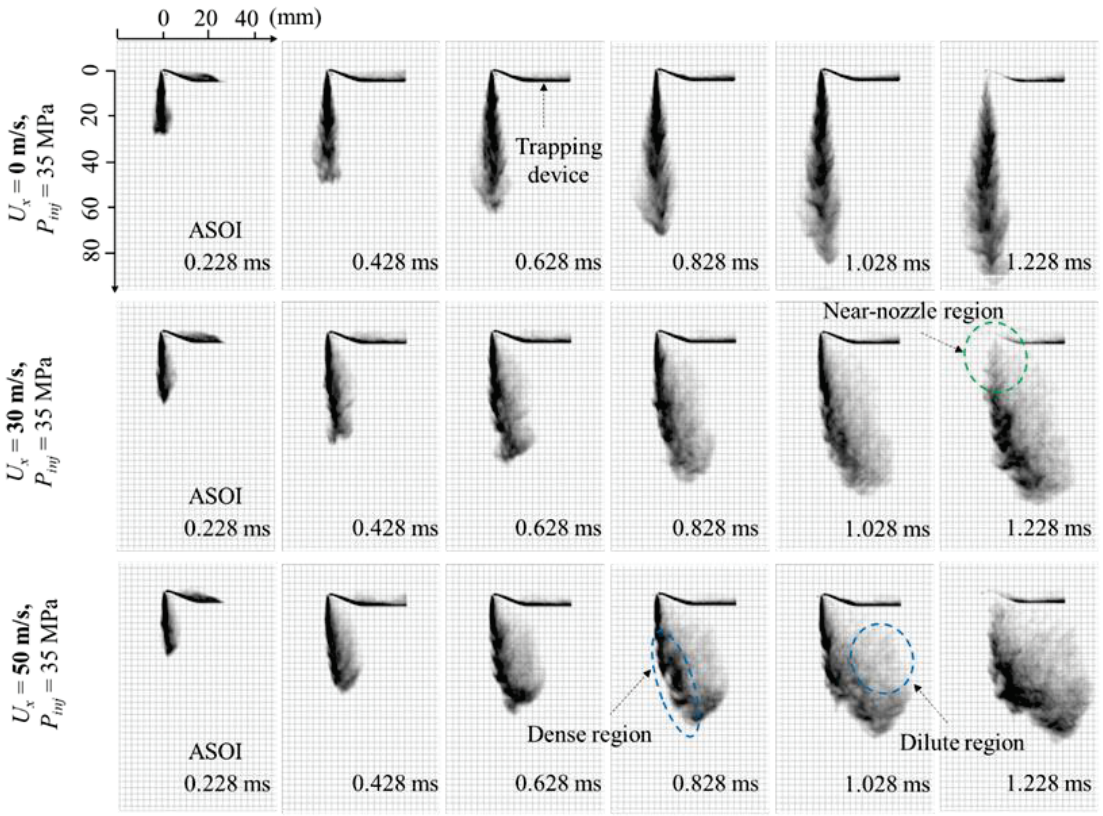

(a) Cross-flow effect

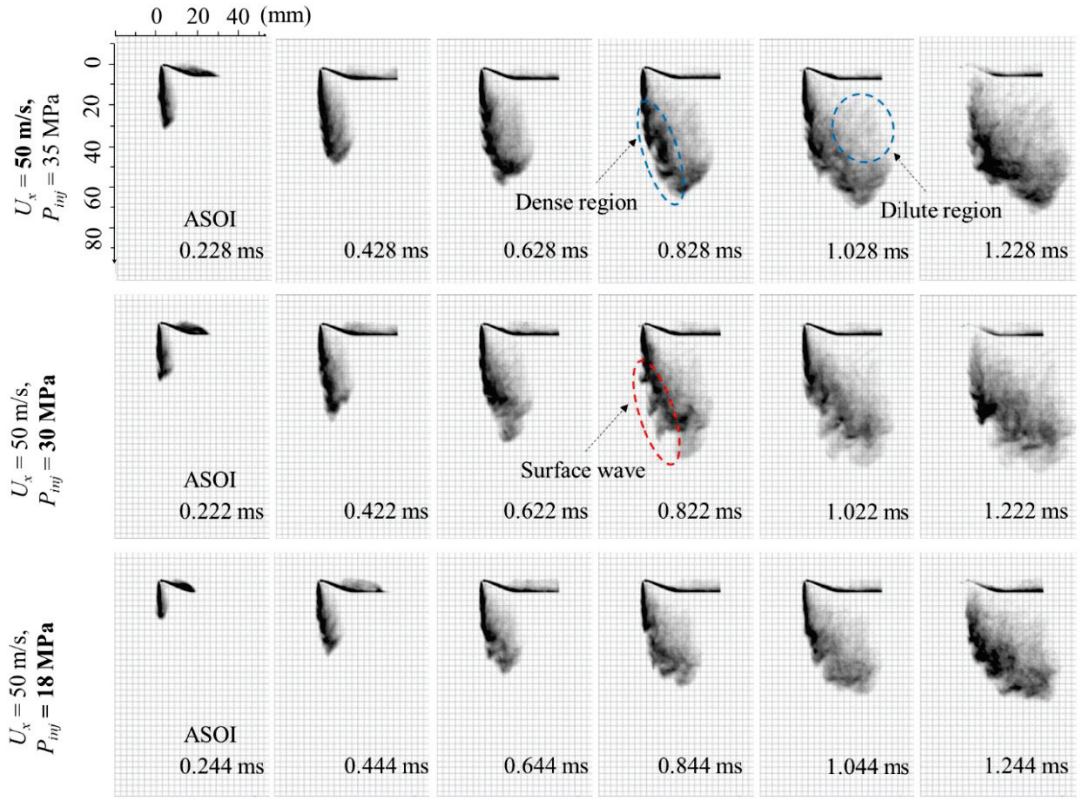

(b) Injection pressure effect

Figure 3.8 Development of spray with trapping device.

Figure 3.8 shows the spray development under the effects of the cross-flow and injection pressure. As depicted in Figure 3.8 (a), the target spray was symmetrical, and the spray tip was inflated with a dilute spray without cross-flow conditions. However, the spray shape became asymmetrical under cross-flow conditions. It was apparent that the bottom part bent more significantly as the cross-flow velocity increased. In addition, under the effect of cross-flow in Figure 3.8 (b), the spray dispersed more considerably in the region around the nozzle. Meanwhile, many droplets were transported downstream of the cross-flow because of the decrease in kinetic energy. Subsequently, the leeward side transformed into a dilute spray region, and the spray area increased. In addition, interesting surface waves are formed on the windward side, this study will not discuss more details due to the complex mechanism.

To obtain more detailed and quantitative spray characteristics, the experimental spray image was processed. First, only the target spray image region was processed;

therefore, this region was selected from the raw images. Second, the background image was subtracted. Finally, a binarized image was obtained via image binarization (the threshold was set to 5% in this study), and it was used to obtain the characteristic parameters of the spray.

3.4 Variation in Spray Penetrations and Spray Area and Optical Thickness（cross-flow velocity/ injection pressure）

3.4.1 Variation in spray penetrations

The tendency of the vertical penetration (left axis) and its COV (right axis) under different cross-flow velocity/ injection pressure conditions are shown in Figure 3.9. The error band was defined as the standard deviation of the spray characteristic parameters. In addition, the zone of time AEOI was colored with light green. As shown in Figure 3.9, the development trend of the vertical penetration with time is similar under different conditions, and both rapidly increased initially. As shown in Figure 3.9 (a), under P_{inj} = 18 MPa, the spray penetration commenced later and developed slower compared with the other injection pressures, which is consistent with the trend of the fuel injection rate. As depicted in Figure 3.9 (b), under different cross-flow velocities, the initial penetration increased rapidly and overlapped, and the penetration was not affected by the cross-flow. Because the initial velocity of the spray was relatively high, the penetration was dominated by the injection pressure. The momentum loss of the spray increased when the secondary droplet occurred, and then the growth rate of the penetration decelerated.

As shown in Figure 3.9, the COV of the vertical penetration can be categorized into two stages. The COV changed significantly in the first stage, and it approached a small value in the second stage, i.e., between 4% and 7%. It is noteworthy that the COV data are not applicable AEOI without cross-flow conditions because the spray impinged on the wall. Compared with the injection pressure, the cross-flow exerted a more significant effect on the variation in the spray vertical penetration.

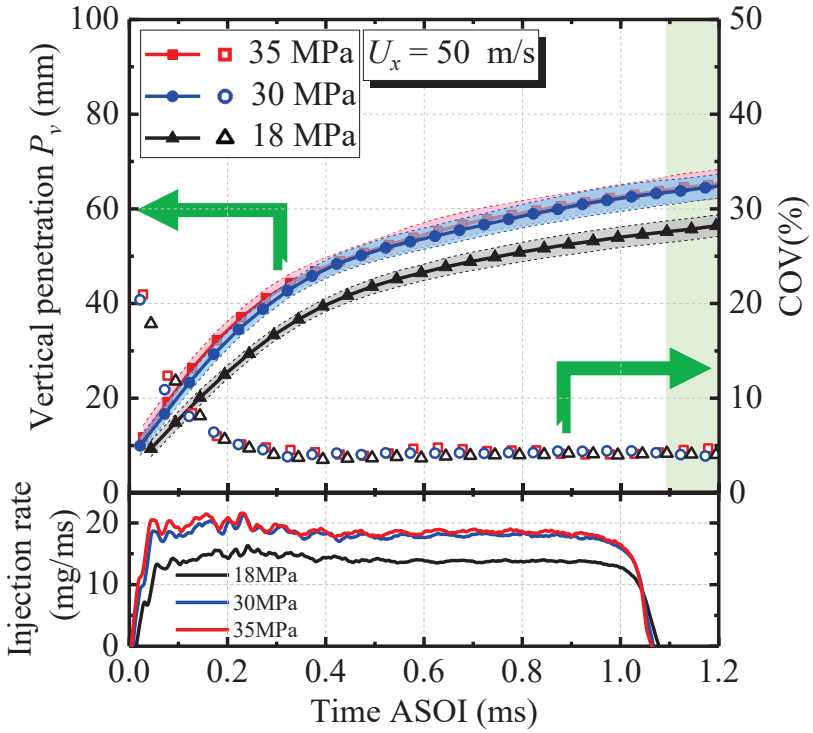

(a) Effect of injection pressure

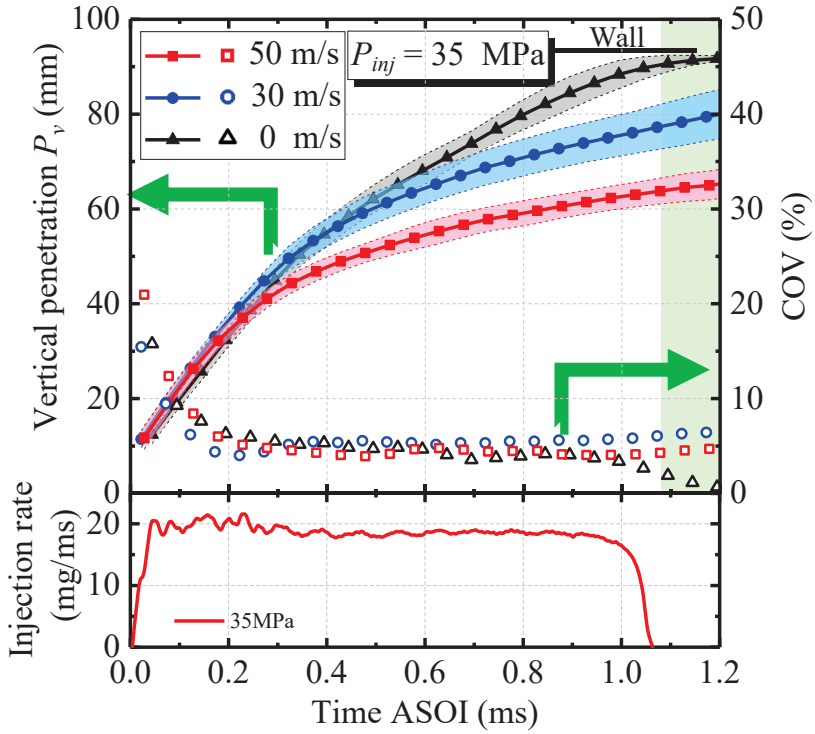

(b) Effect of cross-flow

Figure 3.9 Variation in vertical penetration with trapping device.

The variation in the spray vertical penetration in the initial stage was primarily affected by the internal flow of the nozzle. The rapid movement of the fuel in the nozzle of a multi-hole injector under a high injection pressure can increase the turbulent kinetic energy and turbulence intensity of the fuel. This phenomenon can in fact be validated from the fuel injection rate curve, i.e., the fuel injection volume pulsated before the 0.4 ms ASOI.

The variation in the spray vertical penetration in the second stage was primarily affected by the coupling of the breakup process and the flow field in the chamber. The occurrence of secondary breakup caused the spray liquid beam and ligaments to disperse into smaller droplets. Meanwhile, the breakup process can reduce the kinetic energy of the spray, as confirmed by the development speed of the vertical penetration (the gradually decreasing curvature shown in Figure 3.9. Consequently, numerous small droplets can be transported downstream by the cross-flow [93], resulting in a stable COV of the vertical penetration.

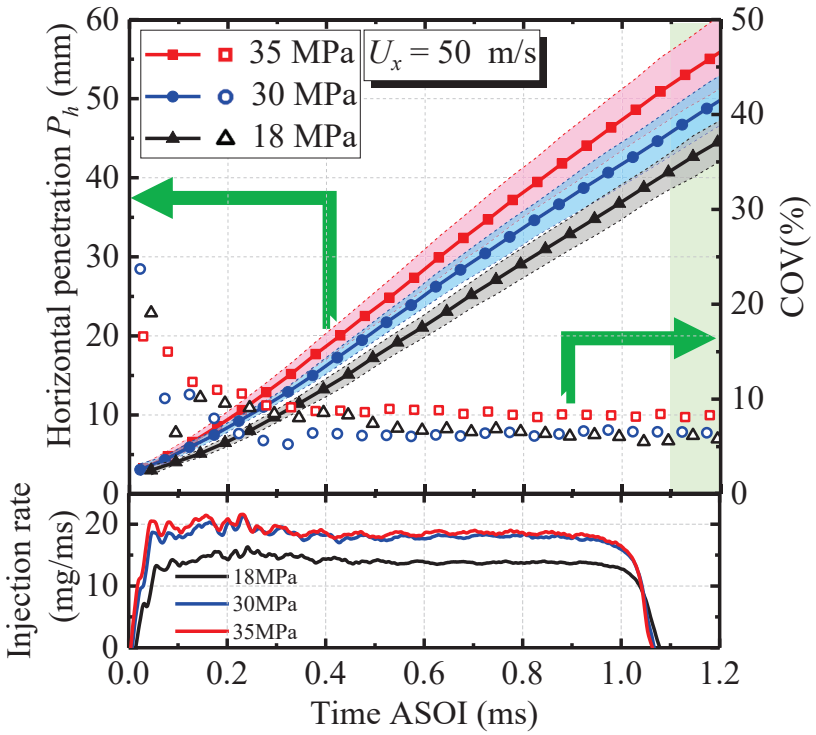

(a) Effect of injection pressure

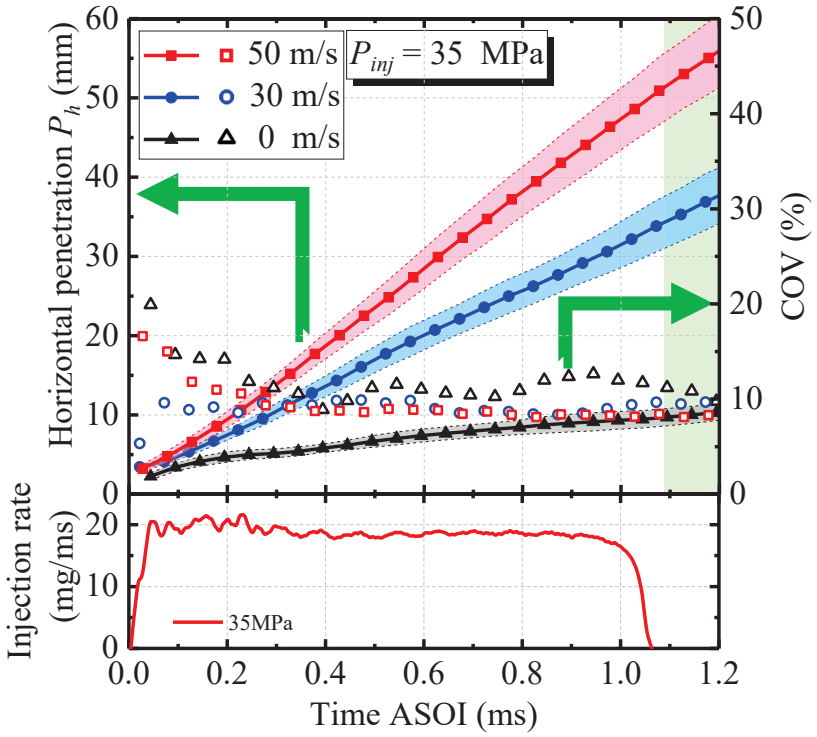

(b) Effect of cross-flow

Figure 3.10 Variation in horizontal penetration with trapping device.

Figure 3.10 shows the tendency of the horizontal penetration and its COV under different cross-flow velocity/ injection pressure conditions; the results can supplement the spray development along the cross-flow direction. The development trend of the horizontal penetration was almost linear, indicating that the uniform cross-flow can dominate the spray development along this direction. As shown in Figure 3.10 (a), the horizontal penetration increased with the injection pressure. Based on the results of a previous study [161], the SMD of the droplets decreased as the injection pressure increased; therefore, the smaller droplets were easier entrained to downstream, resulting in an improved horizontal penetration. In addition, Figure 3.10 (b) shows the effect of the cross-flow velocity on the horizontal penetration under the same P_{inj} = 35 MPa. It was observed that the horizontal penetration increased with the cross-flow velocity. A higher cross-flow velocity can provide more horizontal kinetic energy to the smaller droplets. In addition, the slope was slightly smaller than the cross-flow velocity under atmospheric pressure, thereby confirming that the movement of the

droplets in the horizontal direction was dominated by the cross-flow.

In addition, as shown in Figure 3.10, the COV of the horizontal penetration was significantly larger than that of the vertical penetration, and the two-stage segmentation could not be clearly distinguished. The COV of the horizontal penetration was between 6% and 12% in the late injection stage. Furthermore, it was apparent that the variation mechanisms of spray characteristics in the vertical and horizontal directions were different. The results show almost no correlation between the COVs of the horizontal penetration and the injection pressure/ cross-flow velocity, owing to the dominance of the cross-flow in the spray development. Furthermore, previous studies indicated that some complex movements, such as the movement of the Karman vortex street, occurred downstream, thereby resulting in disordered movements of secondary droplets [164].

3.4.2 Variation in spray area

To comprehensively evaluate the variation in the spray development on a two-dimensional plane, Figure 3.11 shows the tendency of the spray area (left axis) and its COV (right axis) under different cross-flow velocity/ injection pressure conditions. As shown, the spray area increased with the cross-flow and injection pressure. The COV was the highest at the initial stage, but it decreased gradually thereafter. Moreover, the COV of the spray area was the highest under the conditions of U_x = 50 m/s and P_{inj} = 35 MPa. It was clear that the cross-flow can result in a more unstable spray development and then increase the amount of entrained air, thereby promoting the formation of the spray mixture.

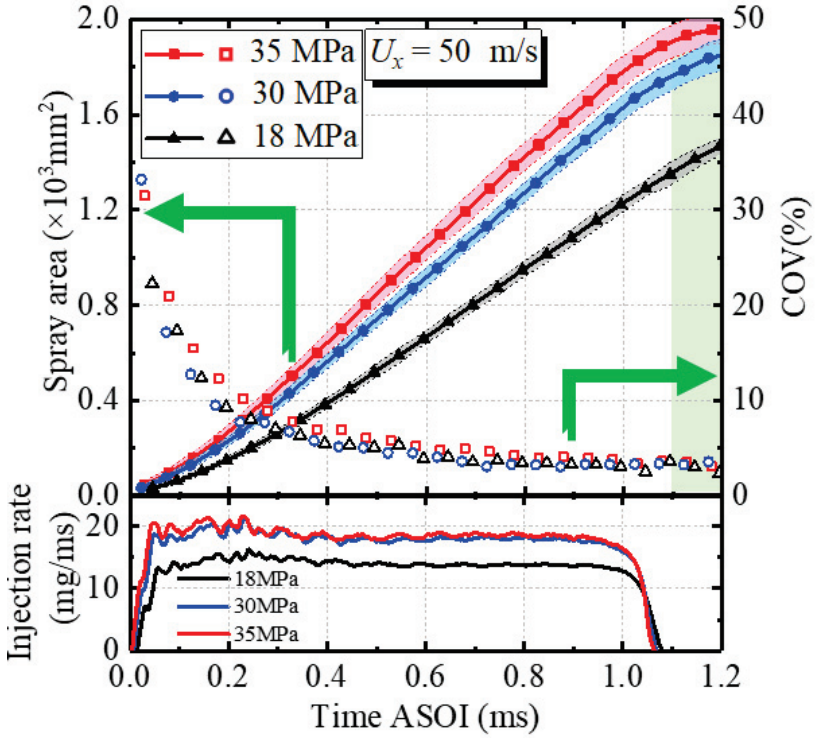

(a) Effect of injection pressure

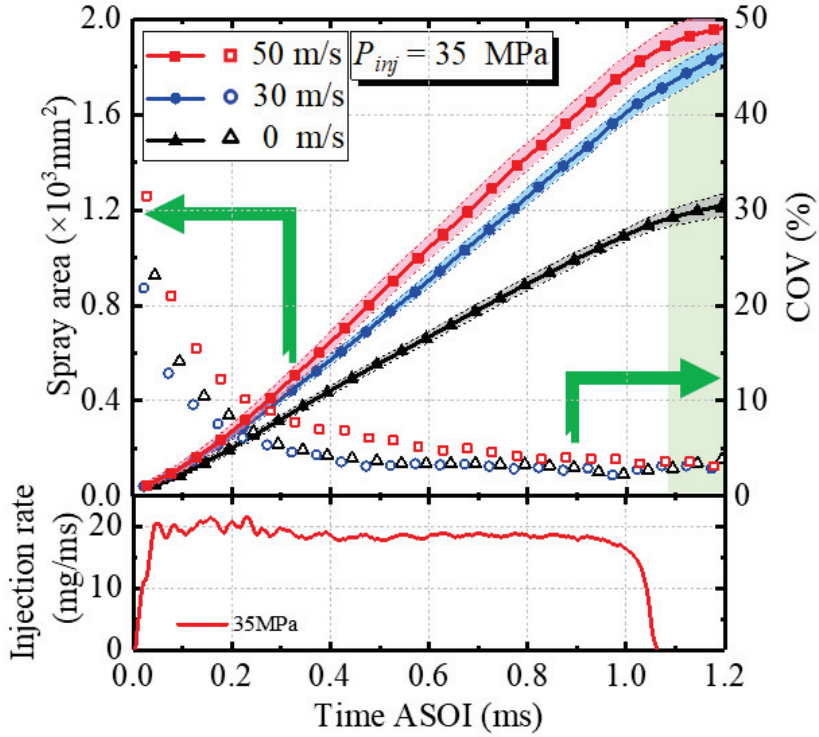

(b) Effect of cross-flow

Figure 3.11 Variation in spray area with trapping device.

3.4.3 Variation in optical thickness

To observe the spray existence probability variation at the same position more intuitively during the spray development under different cross-flow velocity and injection pressure conditions, the optical thickness was used as an evaluation parameter. The optical thickness τ is calculated as the natural logarithm of the original light intensity I_0 divided by the attenuated light intensity I, the optical thickness can be defined by the equation (3.2) [165]:

$$\frac{I}{I_0} = e^{-\tau} \tag{3.2}$$

The COV of the optical thickness τ_{cov} was used to evaluate the change in the mixture concentration; it is defined as the standard deviation τ_σ divided by the average $\bar{\tau}$ at each pixel. The COV of the optical thickness can be calculated using equation (3.3).

$$\tau_{cov} = \frac{\tau_\sigma}{\bar{\tau}} \tag{3.3}$$

Figure 3.12 shows the development of the target spray optical thickness under different cross-flow velocities and injection pressure conditions. The previous analysis showed that setting the upper limit of the color bar to 10% was sufficient for analyzing the distribution of the optical thickness. As shown in the figure, the COV of the optical thickness always decrease with time. In addition, the COV of the optical thickness was low inside, whereas that at the edge was significantly higher. Furthermore, under the effect of cross-flow, the COV on the windward side was significantly greater than that on the leeward side, which may be caused by the surface wave on the windward side. As the injection pressure and cross-flow velocity increased, the variation in the spray tip region intensified.

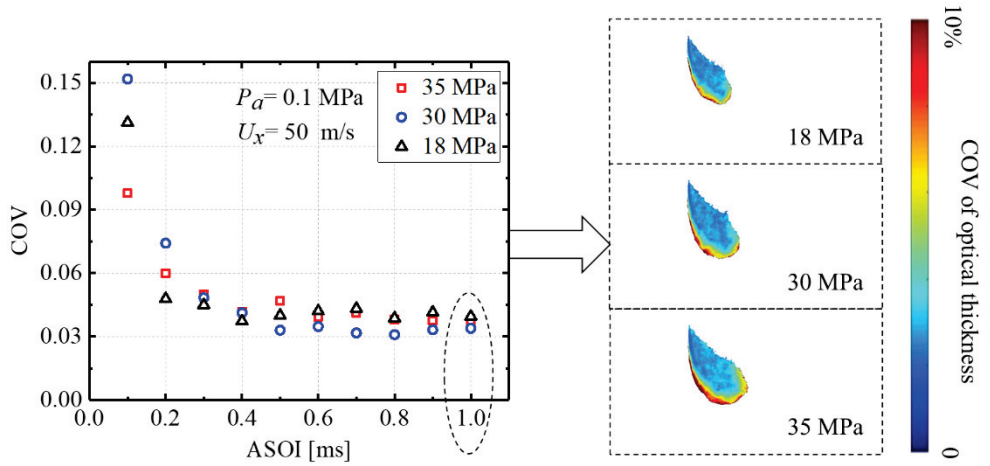

(a) Effect of injection pressure

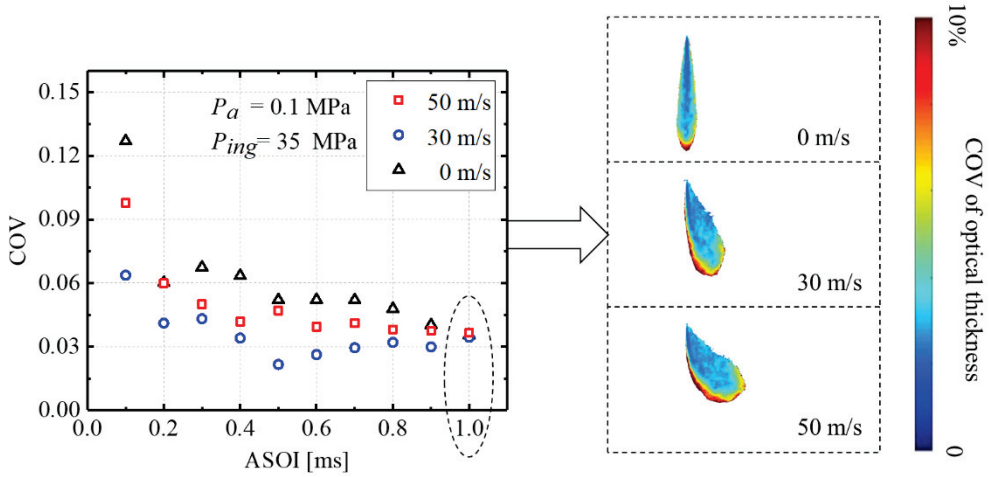

(b) Effect of cross-flow

Figure 3.12 Variation in optical thickness at EOI with trapping device.

3.5 Evaluations of Spray Variation Characteristics in Cross-flow Flow Field

In the sections above, the COVs of the spray characteristic parameters under different conditions were analyzed, and the COV of the optical thickness of the spray images was analyzed visually to clarify the distribution of the higher COV of the spray characteristic parameters. Additionally, the effect of cross-flow on the spray variation characteristics at the EOI was evaluated.

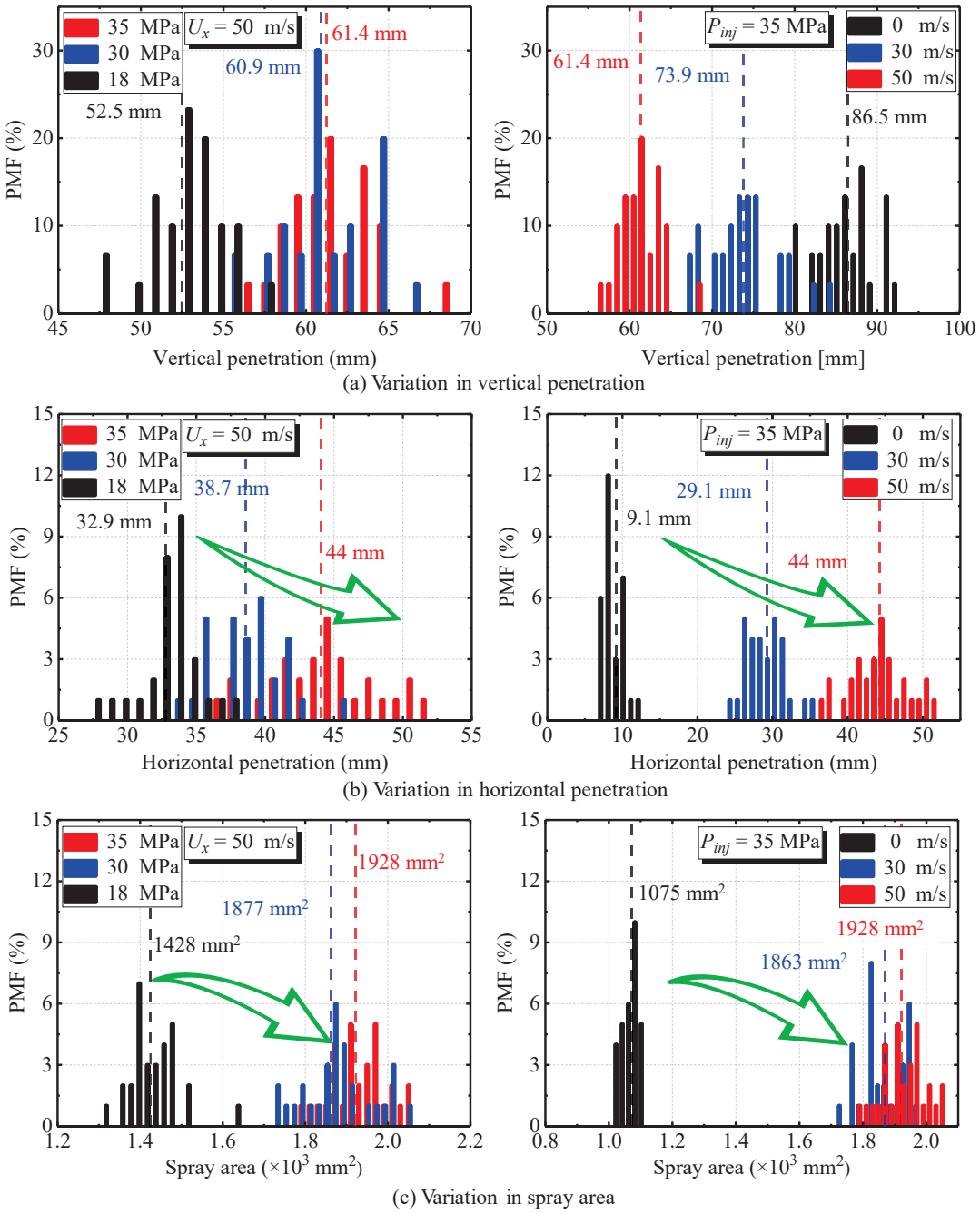

Figure 3.13 Probability mass function (PMF) of spray characteristics at EOI.

Figure 3.13 shows the probability mass function (PMF) of the spray penetration and area. The histogram represents the distribution of each spray characteristic parameter, and the dashed line represents the average value $\overline{P_{ara.}}$. $P_{ara.}$ represents the various spray characteristic parameters (i.e., the vertical penetration, horizontal penetration, and area). An appropriate minimum interval was set to ensure a

reasonable statistical distribution. The distribution interval of both the vertical and horizontal penetrations was 1 mm, and the distribution interval of the spray area was 20 mm^2.

The effects of the cross-flow velocity and injection pressure on the distribution of each spray characteristic parameter can be inferred from Figure 3.13. First, the average value of the spray characteristic parameters was evaluated. In terms of vertical penetration, as shown in Figure 3.13 (a), the injection pressure increased the vertical penetration, whereas the cross-flow restrained it. As shown in Figure 3.13 (b), both the injection pressure and cross-flow enhanced the horizontal penetration. Moreover, Figure 3.13(c) shows that the increase in the spray area was directly proportional to the injection pressure and cross-flow velocity. Meanwhile, it was discovered that the spray area was significantly larger under cross-flow conditions than that of without cross-flow condition, owing to the promotion in spray diffusion by the cross-flow. These results are consistent with those shown in Figure 3.11 (b).

In addition, the CCVs of the spray characteristic parameters at the EOI under different conditions were also evaluated. As shown in Figure 3.13 (a), the variations in the vertical penetration did not show any significant difference, which is consistent with Figure 3.9. The case of EOI was in the second stage of COV propagation. It is noteworthy that the effects of cross-flow and injection pressure on the variations in the spray horizontal penetration and area can be clearly observed at the EOI. Based on the peak distribution shown in Figure 3.13 (b), as the cross-flow velocity and injection pressure increased, the distribution of the horizontal penetration tends to be a flat shape, which indicates a high variation. Similarly, as shown by the peak distribution in Figure 3.13 (c), the spray area was proportional to the cross-flow velocity and injection pressure. This indicates that the cross-flow dominated the variation in the spray horizontal penetration. In summary, the CCV of the spray increased because of the cross-flow and injection pressure at the EOI.

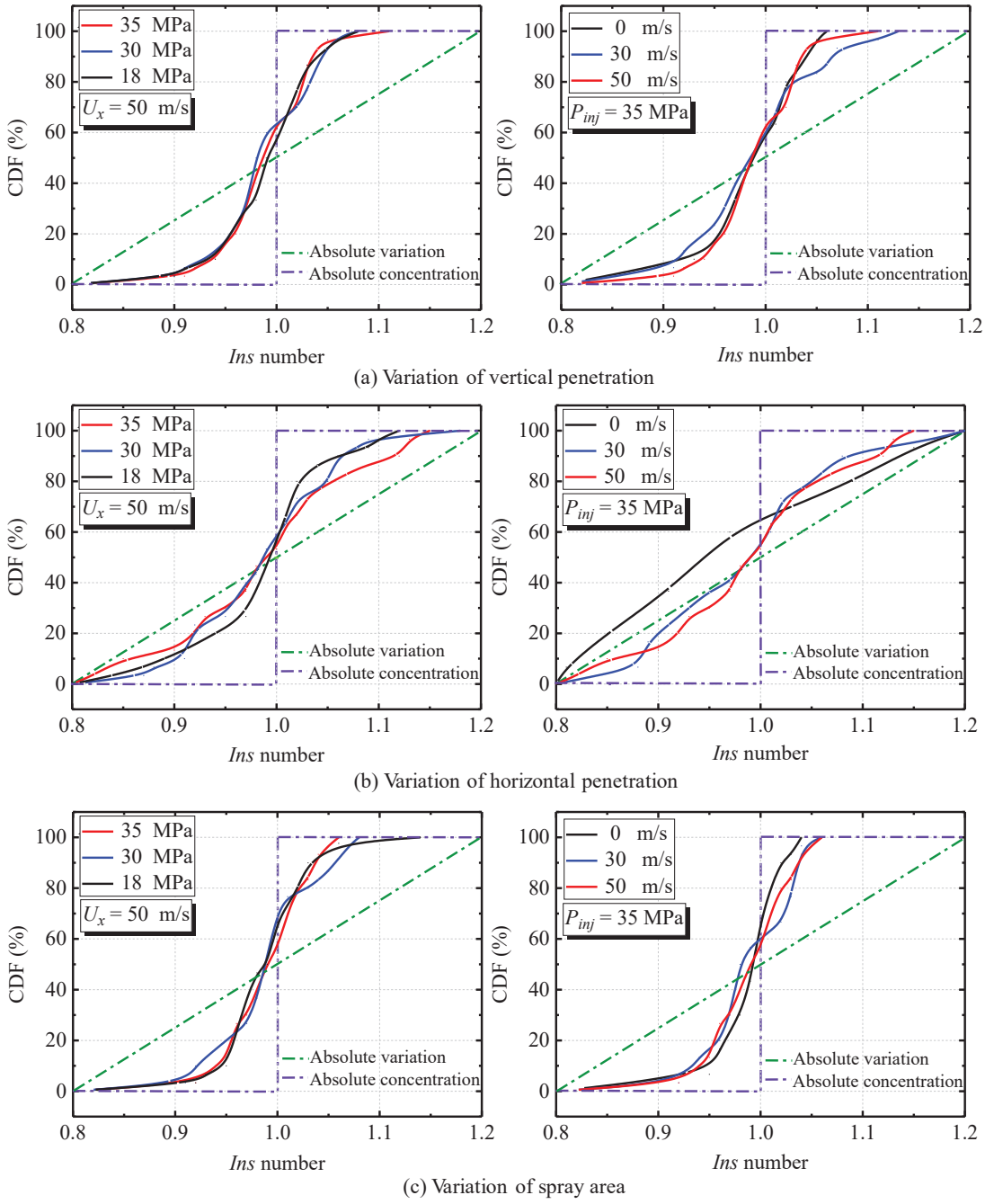

Figure 3.14 Cumulative distribution function (CDF) of spray characteristics at EOI [dimensionless].

Subsequently, the effects of the cross-flow velocity and injection pressure on the distribution of the spray variation characteristics were evaluated quantitatively. In addition, a unified evaluation indicator is required for the variation analysis of various spray characteristics above. Therefore, a dimensionless number, "*Ins* number" is

proposed here to comprehensively evaluate the CCV characteristics of the spray, and it represents the degree of instability of the spray characteristics.

The *Ins* number is defined as the parameter value $P_{ara.i}$ of any spray characteristic at a certain time divided by the average value $\overline{P_{ara.}}$ of the experiment. When the absolute value of the *Ins* number approaches 1 infinitely, it indicates that the CCV of the spray characteristic parameters is low. The mathematical expression for *Ins* is shown in Equation (3.4).

$$Ins = \frac{P_{ara.i}}{\overline{P_{ara.}}} \tag{3.4}$$

Furthermore, the concepts of “absolute variation” and “absolute concentration” are proposed based on the analysis and comparison of the dimensionless spray characteristics, and they can be used as a reference for the analysis of spray characteristics. “Absolute variation” implies that the spray characteristic parameters of each injection from the minimum to the maximum are completely different. “Absolute concentration” implies that the spray characteristic parameters of each injection are exactly the same. Figure 3.14 shows the cumulative distribution function (CDF) of the dimensionless spray characteristics at the EOI. The dash-dotted line represents the absolute concentration trend line, and the dash-dotted green line is called the absolute variation trend line. As shown in Figure 3.14 (b), the CDF of the dimensionless horizontal penetration was almost close to the absolute variation standard under different cross-flow conditions, which is consistent with the results shown in Figure 3.9. Based on the analysis of experimental data in this study, a horizontal penetration with the most significant cyclical variations resulted in *Ins* numbers between 0.8 and 1.2. Furthermore, most of the *Ins* numbers were between 0.9 and 1.1 (±10%), which can be used as data reference for numerical calculations as well as to validate CFD results.

3.6 Distribution of Droplet Size

Mean diameter is one of the most effective methods to express spray quality.

SMD is the most common form of average droplet size. It is widely used because it can better reflect the physical characteristics of droplets， which can be described as:

$$SMD = \int_{d_0}^{d_{max}} d_i^3 dn_i \,/\, \int_{d_0}^{d_{max}} d_i^2 dn_i \tag{3.5}$$

Where n is the number of droplets with a certain size d.

In addition, the dispersion index U is used to characterize the uniformity of droplets size. The uniformity of spray dispersion becomes higher as the value of U becomes larger. D_{10}, D_{50} and D_{90} represent the proportion of droplets size is equal to 10%, 50% and 90%. The expression is as follows:

$$U = \frac{D_{90} - D_{10}}{D_{50}} \tag{3.6}$$

Figure 3.15 a) shows the SMD measurement position without cross-flow condition, the droplet size varying with time at the same position (below the nozzle 50 mm) were measured under different injection pressures by using LDSA equipment. From Figure 3.15 a), the results show that the droplets size ranged from 6 to 12 μm under the injection pressure of 18-35 MPa. Generally, the SMD had a negative correlation with the injection pressure. As the injection pressure increased, the SMD became small. Because the rupture energy of the droplets increased with the injection pressure increased, which resulting in smaller droplet size, that is, a smaller SMD. In addition, it is noted that the droplet size initially decreased slightly with time, but as time goes on, the SMD basically shown an upward trend. The initial large-diameter droplets had higher momentum and reached the measurement position first, but as time progresses, the subsequent small droplets can catch up with the large droplets on the spray tip, meanwhile, the large droplets broke up at this position, which leads to the SMD temporary decreased. Since the measurement position was not far from below the nozzle, as time continues to develop, the slow droplets were caught up by the subsequent droplets and collided here, and then aggregate into droplets with a larger SMD, so the SMD tended to become larger varying with time.

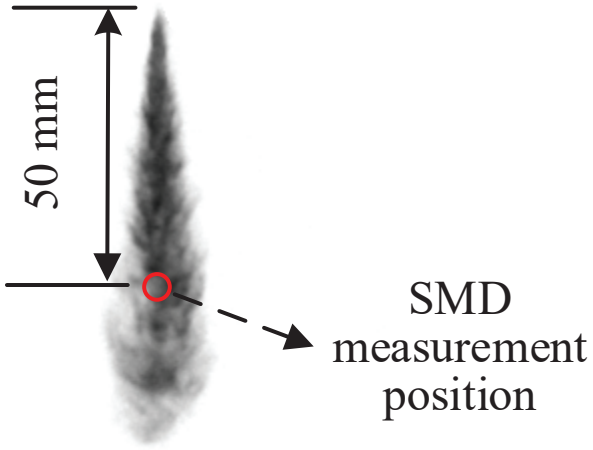

a) SMD measurement position without cross-flow

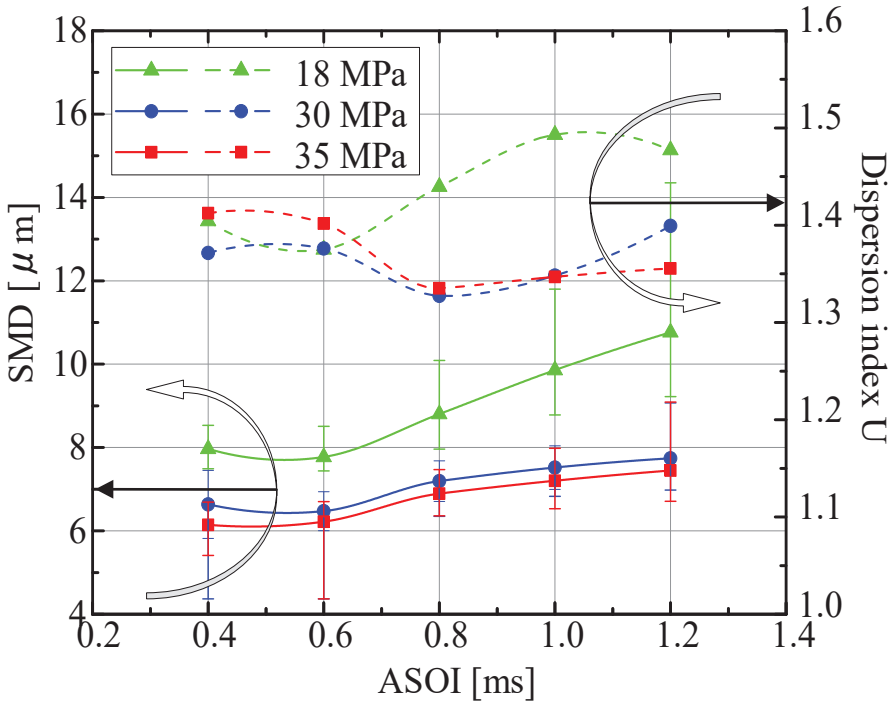

b) SMD and dispersion index under different injection pressure

Figure 3.15 Droplet size and distribution without cross-flow condition.

In addition, Figure 3.15 b) also shows the dispersion index. It is found that the dispersion index of high injection pressure was smaller near EOI, that is, the uniformity of distribution increased, which shows that the lifting injection pressure was feasible to reduce the droplet size and improve the quality of the mixture.

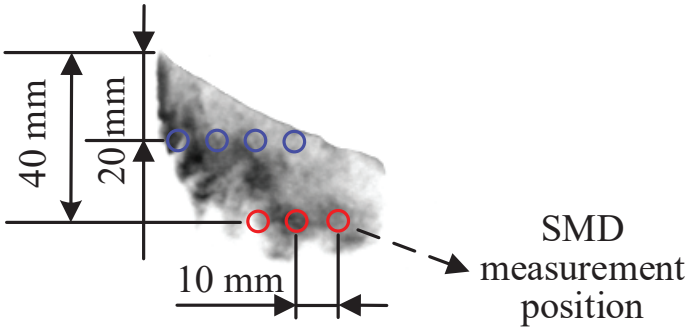

a) SMD measurement position under cross-flow condition

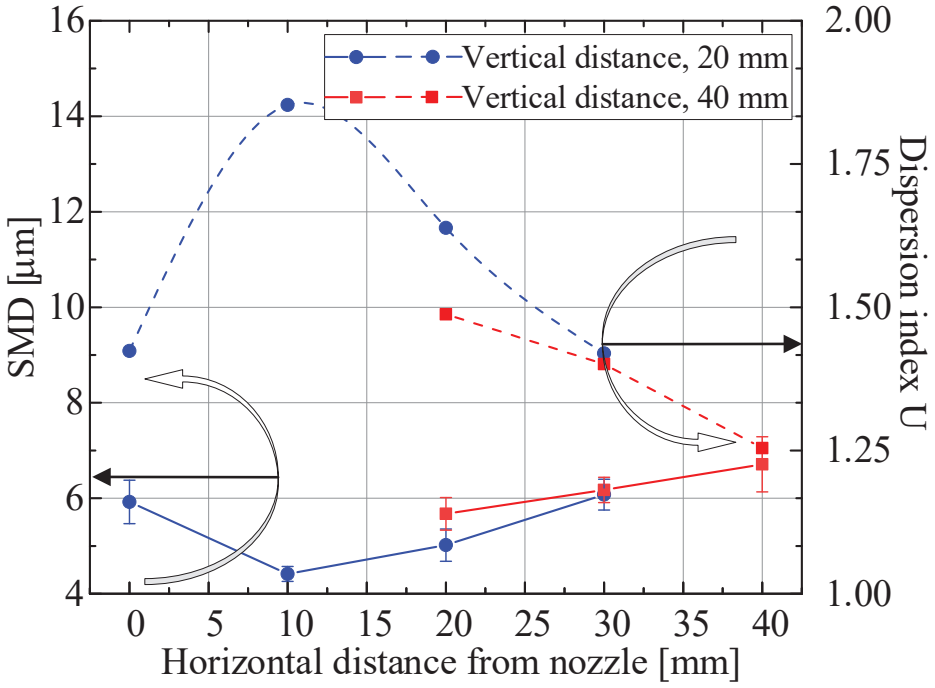

b) SMD and dispersion index under different positions at EOI

Figure 3.16 Droplet size and distribution under cross-flow condition.

[P_{inj}=35MPa, U_x=50m/s, Δt_{ing}=1ms]

Figure 3.16 a) shows the SMD measurement position under cross-flow condition, the droplet size in the different positions at EOI were measured by using LDSA equipment under the same condition. From Figure 3.15 b), the results show that. From the Figure 3.16 b), the results show that the droplets size ranged from 5 to 8 μm under the cross-flow condition, which proved that the cross-flow promoted the atomization of the spray. It is noted that the as the horizontal distance increases, the SMD showed a trend of first decreasing and then increasing. Additionally, the droplet size of

downstream was slightly larger than the upstream, which could be regarded as the result of the droplets collide and gather downstream.

Meanwhile, Figure 3.16 b) also shows the dispersion index. It is found that the dispersion index of downstream was smaller than the upstream, that is, the uniformity of distribution increased.

3.7 Summary

In this study, the statistical variation characteristics of fuel spray were investigated experimentally under cross-flow conditions. To evaluate the spray variation characteristics, a statistical analysis of 30 repeated experiments was conducted. It was discovered that the delay time of the needle valve opening did not significantly affect the spray variation. In addition, the trapping device can capture the target spray and lessen the effects of other overlapping spray plumes. The conclusions of this study are summarized as follows:

(1) The spray plume changed significantly under cross-flow conditions, and the downstream spray was more susceptible to cross-flows. The increase in the cross-flow velocity and spray injection pressure enlarged the spray area. Interestingly, surface waves were observed on the windward side.

(2) The initial stage of the vertical penetration was barely affected by the cross-flow, owing to the high initial kinetic energy. Based on the spray propagation under cross-flow conditions, the COV of the vertical penetration can be categorized into two stages. The COV is the largest in the initial stage of injection, and it approached a small value in the second stage, i.e., between 4% and 7%.

(3) The horizontal penetration changed almost linearly with time, thereby confirming that the movement of the droplets in the horizontal direction was dominated by the cross-flow. Moreover, the COV of the horizontal penetration was significantly higher than that in the vertical direction. The cross-flow significantly affected the spray variation characteristics in the horizontal direction.

(4) The cross-flow significantly intensified the COV of the spray area. Furthermore, the COV of the image optical thickness on the windward side was higher than that on the leeward side, whereas that at the outer side was higher than that on the inner side. The increase in the cross-flow velocity and injection pressure intensified the variation in the spray tip region.

(5) As the cross-flow velocity and injection pressure increased, the distributions of the horizontal penetration and spray area became uniform at the EOI timing, which indicates that the CCV of the spray can be increased by the cross-flow and injection pressure. Under the effect of cross-flow, the *Ins* number for the dimensionless horizontal penetration varied between 0.8 and 1.2, which represents the higher CCV as compared with that of the vertical penetration.

(6) As the injection pressure increased, the SMD became smaller. In addition, it is found that the dispersion index was smaller when close to the EOI timing under high injection pressure, that is, the distribution of the mixture was more uniform. The cross-flow can promote the atomization of the spray, which make the droplets size ranged from 5 to 8 μm. Additionally, the droplet size of downstream was slightly larger than the upstream, which could be regarded as the result of the droplets collide and gather downstream. Meanwhile, it is found that the uniformity of distribution increased in the downstream.

CHAPTER 4 STATISTICAL VARIATION ANALYSIS OF FREE SPRAY UNDER HIGH AMBIENT PRESSURE

4.1 Introduction

In Chapter 3, we discussed the CCV characteristics of free spray of multi-hole injectors under atmospheric pressure. However, for the real operating conditions, the ambient pressure should be much larger than atmospheric pressure. Therefore, the high ambient pressure conditions are considered in this Chapter. The DBI imaging method still used here for study the CCV characteristics under cross-flow conditions. Compared the result of high ambient pressure with the previous atmospheric pressure results in Chapter 3.

4.2 Experimental Conditions

Table 4.1 Experimental conditions.

Ambient conditions	
Ambient pressure, P_a [MPa]	0.1, 0.3
Ambient temperature [K]	300
Cross-flow velocity, U_x [m/s]	0, 5, 10
Injection conditions	
Injector type	1+4 holes
Nozzle exit diameter, D [mm]	0.16
Test fuel	Iso-octane
Injection pressure, P_{inj} [MPa]	18, 30, 35
Injection pulse, t_{inj} [ms]	1.0
Trigger current, I [A]	I_0-, I_0, I_0+
Fuel properties	
Fuel density, ρ_l [kg/m^3]	691.9
Surface tension, σ [N/m]	0.0188
Viscosity, μ [kg/m s×10^{-4}]	5.04

The experimental conditions are listed in Table 1. The experimental fuel was isooctane, as mentioned in the previous section. The same injection duration of 1 ms was used in both experiments. The injection pressures used in the experiment were keep at 18, 30, and 35 MPa. Since of the limited of ambient pressure, the cross-flow velocity was limited to the maximum value of 10 m/s. In addition, the trigger current was considered here. To ensure data accuracy in general, 30 repetitions under the same experimental condition are still required [166].

4.3 Results and Discussions

4.3.1 Variation in spray penetrations

Under the high ambient pressure, the tendency of vertical penetration and its COV with different cross-flow velocity/ injection pressure conditions were shown in Figure 4.1. From the figure, the development trend of vertical penetration with time was similar under different conditions. Under the different cross-flow velocities, the initial penetration length increased rapidly and obviously coincided, where the penetration was not affected by cross-flow, because the initial velocity of spray was quite large. When the droplet began to break up, the momentum loss of the spray increased and the disorder of the droplet movement became larger, and then the growth rate of the penetration distance slowed down obviously. The conclusion mentioned here were consistent with Chapter 3. The development of vertical penetration is significantly inhibited at higher ambient pressure. In addition, the effect of trigger current on vertical penetration distance is not obvious. There is a slight increase in vertical penetration with increasing trigger current at higher ambient pressures.

In terms of the COV of vertical penetrations under the high ambient pressure, it was still very large at the initial stage of injection. As mentioned in the Chapter 3, the inside structure of the nozzle should be the reason, the injection rate at this stage also fluctuated considerably. Then the COV quickly decreased and tend to be stable.

Results show that even if the cross-flow velocity was not so large, the variation of the vertical penetration under high ambient pressure was completely opposite to atmospheric pressure. The COV decreased with the increase of the injection pressure and cross-flow velocity under high ambient pressure at EOI timing. Additionally, the COV increased with the increase of the trigger current under high ambient pressure at EOI timing.

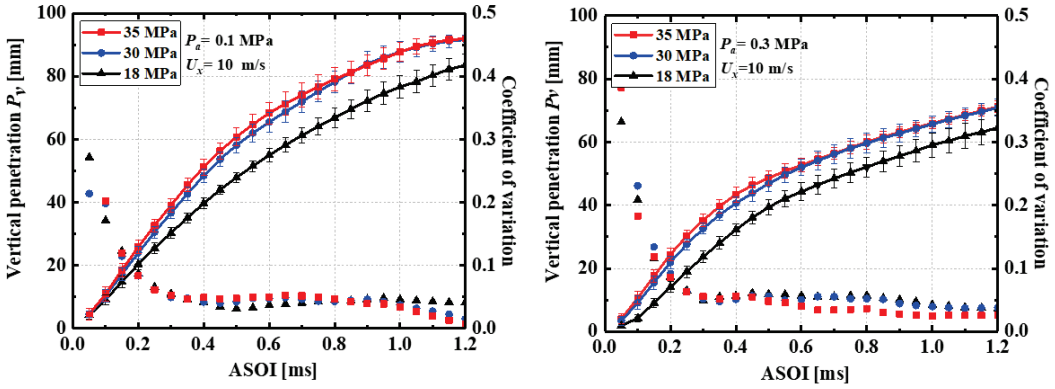

(a) Variation in vertical penetration with various injection pressure

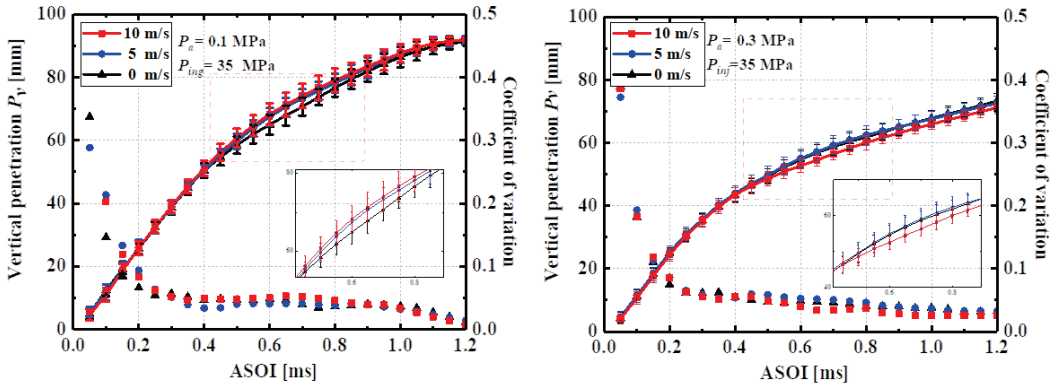

(b) Variation in vertical penetration with various cross-flow velocity

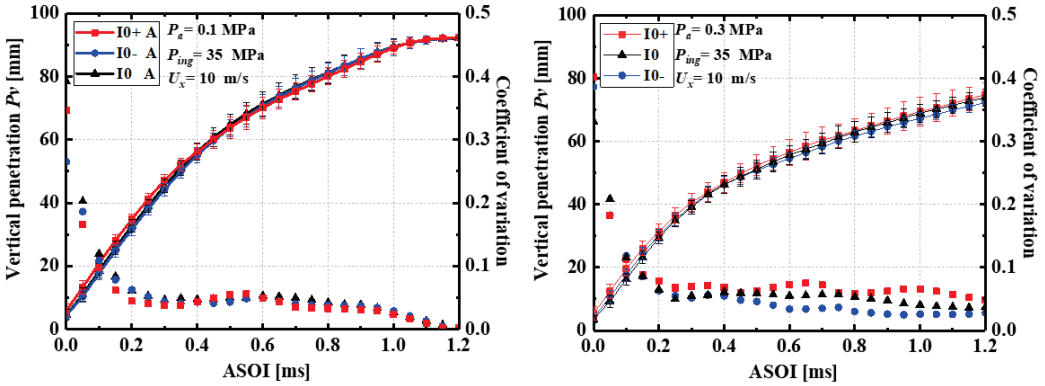

(c) Variation in vertical penetration with various trigger current

Figure 4.1 Variation in vertical penetration with trapping device.

Compared with atmospheric pressure conditions, the variation in the spray vertical penetration in the initial stage was still large, which also primarily affected by the internal flow of the nozzle. Since of the variation in the spray vertical penetration in the second stage was primarily affected by the coupling of the breakup process and the flow field in the chamber, the spray and droplets behaviors must have some difference. Therefore, the difference results can be obtained by the experiment under higher ambient pressure.

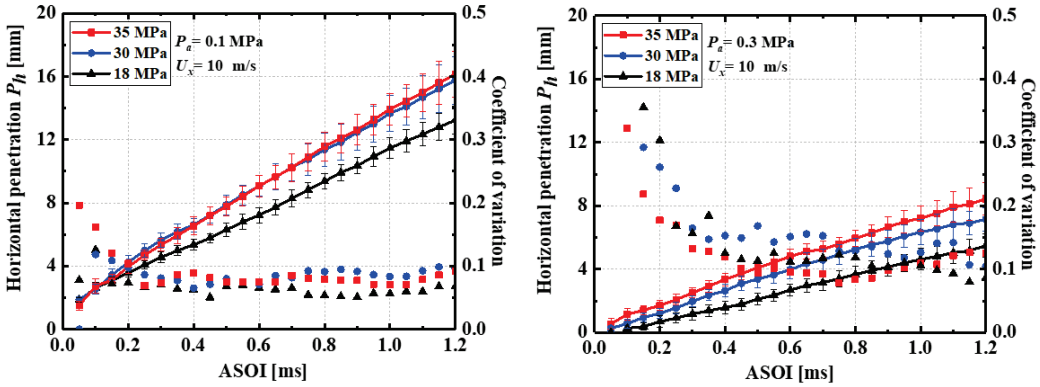

(a) Variation in horizontal penetration with various injection pressure

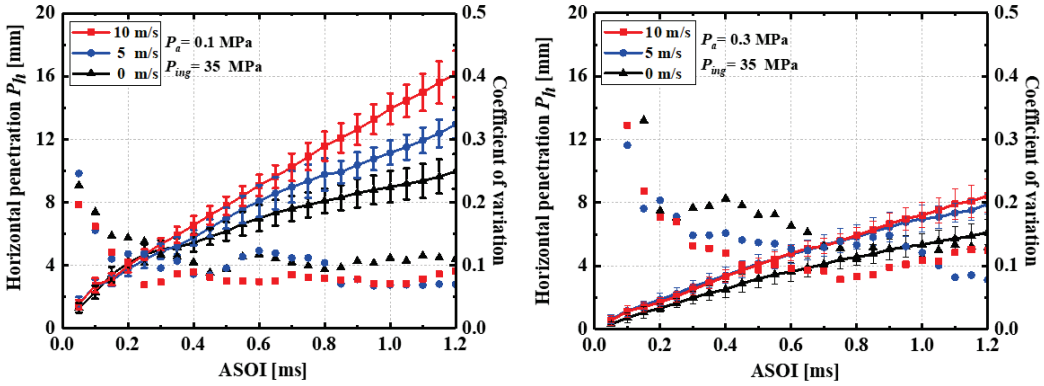

(b) Variation in horizontal penetration with various cross-flow velocity

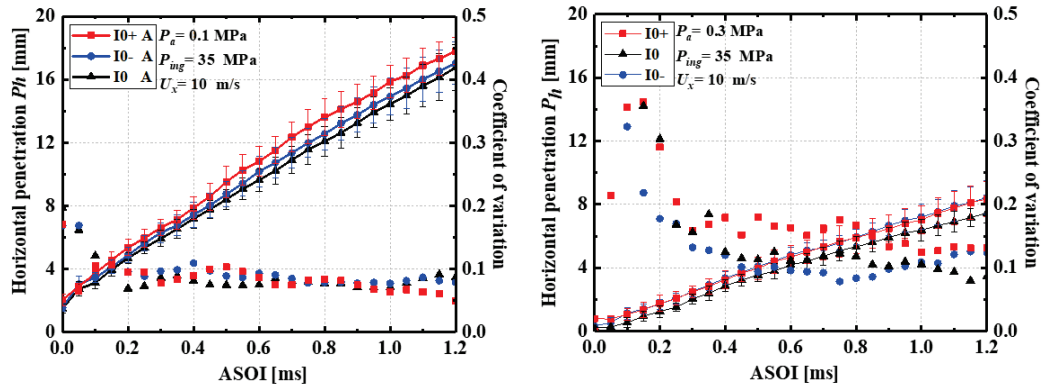

(c) Variation in horizontal penetration with various trigger current

Figure 4.2 Variation in horizontal penetration with trapping device.

It can be seen in Figure 4.2, the development tendency of horizontal penetration with time was still linear even though under the higher ambient pressure. At the same injection pressure, the slope of high cross-flow velocity was large, that was, the horizontal penetration increased with the increase of cross-flow velocity, since the higher cross-flow velocity can provide more kinetic energy for droplets. Through linear fitting, the slope was slightly smaller than that of cross-flow velocity under higher ambient pressure, which should be also attributed to the increases of the ambient density, and then the development of the spray in the horizontal direction was obviously hindered. In addition, the greater the injection pressure, the greater the horizontal kinetic energy of the spray, and then horizontal penetration increased with

the increases of injection pressure. Whether under atmospheric pressure or higher ambient pressure, the trigger current has not obviously influence on the development of horizontal penetration.

Moreover, it also can be seen that the ambient density had a great influence on the COV of the horizontal penetration. In terms of the COV of horizontal penetrations under the high ambient pressure, the COV of horizontal penetration under higher ambient pressure was obviously larger than that under atmospheric pressure. The horizontal penetration changed more obviously under high ambient pressure, which was affected by the interaction of cross-flow and spray.

4.3.2 Variation in spray area

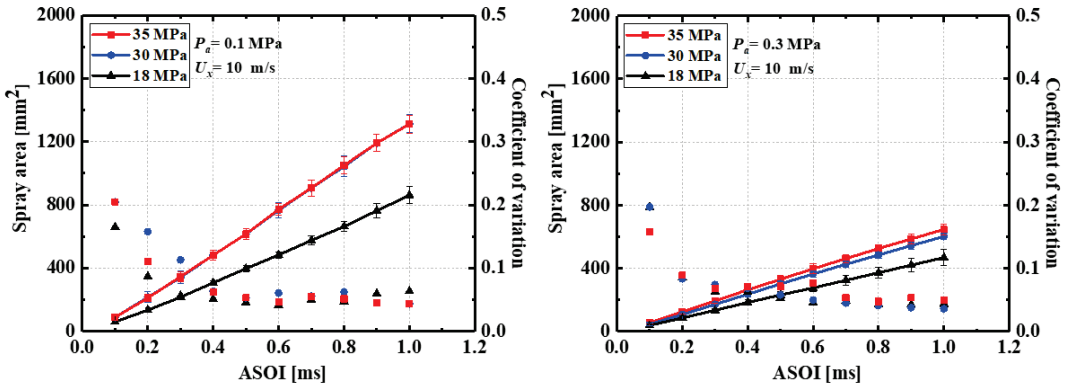

(a) Variation in spray area with various injection pressure

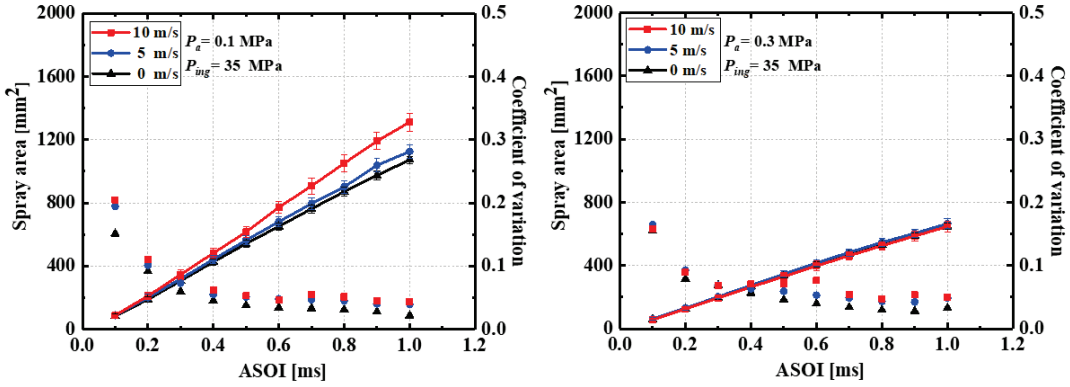

(b) Variation in spray area with various cross-flow velocity

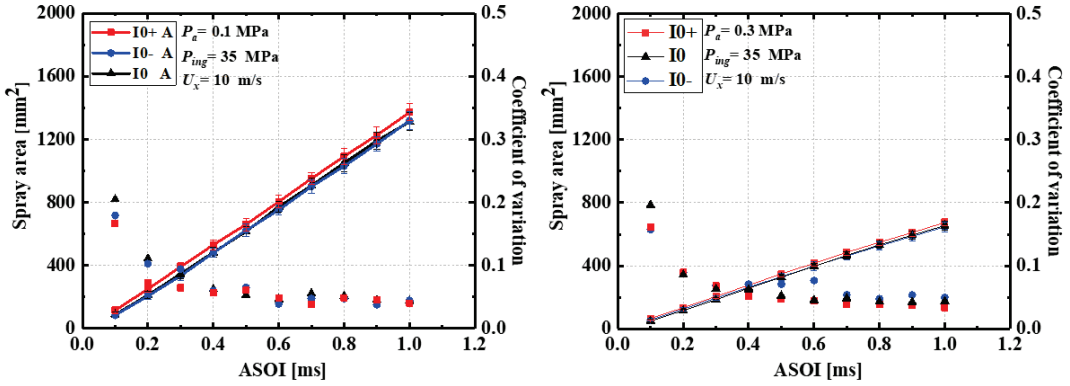

(c) Variation in spray area with various trigger current

Figure 4.3 Variation in spray area with trapping device.

To comprehensively evaluate the variation in the spray development on a two-dimensional plane under the higher ambient pressure, Figure 4.3 shows the variation of spray area under different injection pressure, cross-flow velocity, and trigger current conditions. The effect of ambient pressure on the spray area is quite significant. Results show that the spray area is quite smaller under higher ambient pressure than that under atmospheric pressure, which reduces about 50% when the ambient pressure increases from 0.1 MPa to 0.3 MPa under the effect of other factors (injection pressure, cross-flow velocity, and trigger current).

However, as shown in this Figure, it is difficult to find the effect of environmental factors on the COVs. Only the cross-flow effect can be seen, which was clear that the variation in spray area increases with cross-flow velocity, both at atmospheric pressure and at high ambient pressure. The cross-flow can result in a more unstable spray development and then increase the amount of entrained air, thereby promoting the formation of the spray mixture.

4.3.3 Evaluations of spray variation characteristics in cross-flow flow field under various ambient conditions

The last part mainly evaluates the influence of cross-flow on the spray variation characteristics. Figure 4.4 shows the PMF of spray penetrations. The distribution

interval of vertical penetration was 2 mm, the distribution interval of horizontal penetration was 0.5 mm, then frequency polygons was showed to display the PDFs.

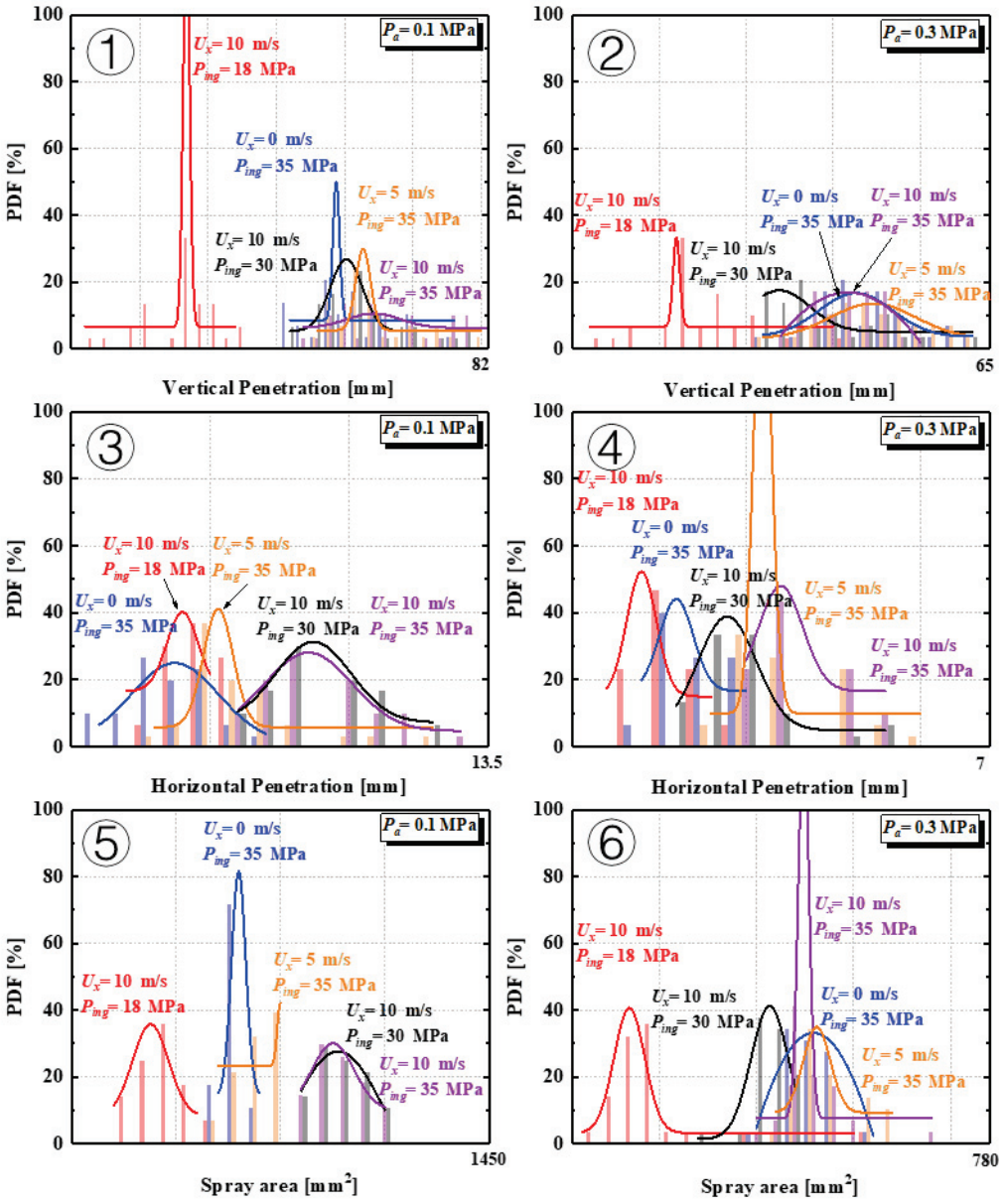

Figure 4.4 Statistical distribution of spray characteristics at EOI.

The results show that the distribution of penetration is asymmetric. The vertical penetration was the smallest under the conditions of 10m/s and 18MPa. Obviously, the spray was easier to be blown downstream by the higher cross-flow velocity when the injection pressure was small, and then the vertical penetration became smaller. In addition, most of the PMFs of horizontal penetration exhibits a left skew distribution.

Under the higher ambient pressure, the horizontal penetration was the largest under the conditions of 10 m/s and 35 MPa. Obviously, the higher cross-flow velocity promotes the movement of the droplets in the horizontal direction, while the high injection pressure provides a greater horizontal initial momentum. In order to compare the influence of ambient pressure on the spray variation characteristics, the range of cross-flow velocity is limited. Therefore, the horizontal penetration does not show a law that is obviously affected by cross-flow velocity.

4.4 Summary

In this study, the CCV characteristics of fuel spray under higher ambient condition are obtained and compared to atmospheric pressure. The conclusions can be summarized as follows:

(1) Higher ambient pressure significantly inhibits the development of vertical penetration. At higher ambient pressures, there is also a slight increase in vertical penetration with increasing trigger current. Even if the cross-flow velocity was not so high, the variation of vertical penetration under high ambient pressure was completely opposite for atmospheric pressure.

(2) Despite the higher ambient pressure, the development tendency of horizontal penetration with time remained linear. The slope was slightly smaller than that of cross-flow velocity under higher ambient pressure, which should also be attributed to increases in ambient density. Furthermore, the ambient density had a significant impact on the COV of the horizontal penetration. Furthermore, the COV of horizontal penetration was clearly greater under higher ambient pressure than under atmospheric pressure.

(3) The spray area is much smaller under higher ambient pressure than it is under atmospheric pressure, which decreases by about half when the ambient pressure rises from 0.1 MPa to 0.3 MPa. The variation in spray area increases with cross-flow velocity, which can lead to more unstable spray development and then increase the amount of entrained air, promoting spray mixture formation.

CHAPTER 5 WALL-IMPINGEMENT SPRAY STRUCTURES

5.1 Introduction

Spray wall-impingement is unavoidable in direct-injection spark-ignition engines, and it affects the formation and combustion process of the mixture, resulting in significant emissions and fuel economy problems. In addition, the airflow in the cylinder inevitably affects spray propagation. Therefore, the influence of cross-flow on the wall-impingement spray behavior was investigated in this work. CW laser sheet technology was applied to obtain the macroscopic structure of the wall-impinging spray, and the wall-jet vortex region was observed in the wall-impinging spray tip. Moreover, PIV technology was employed to obtain the velocity distribution inside the wall-jet vortex region. Under different ambient pressures (0.1 and 0.4 MPa), the structure of the wall-jet vortex was determined at three different cross-flow velocities (0, 2, and 5 m/s) and three wall-impingement distances (25, 50, and 75 mm). In addition, an indicator *Ic* of the "contribution index" is proposed to evaluate the degree of influence of various influencing factors on the wall-jet vortex. These results obtained in this Chapter pertaining to the wall-jet vortex characteristics can provide the necessary guidance and suggestions for better understanding the wall-impingement spray behavior.

5.2 Experimental Conditions and Parameters Definition

5.2.1 Experimental conditions

Detailed experimental conditions are listed in Table 5.1. Dry-solvent was utilized as a test fuel in this study because its physical properties are close to gasoline. In addition, the dry-solvent possesses a higher ignition point for safety experiment. The density and viscosity of the dry-solvent are 770 kg/m3 and 1.3× (10^{-6}) m2/s (at 20 °C), respectively. The surface tension is 23.9 mN/m (at 20 °C). A single-hole injector with

a nozzle diameter of 0.15 mm provided by Mazda was used in the current study. The test fuel was injected under an injection pressure of 10 MPa and an injection pulse of 4 ms, and three shots were performed. The cross-flow velocity ranged from 0 to 5 m/s. The ambient pressure is set as 0.1 MPa and 0.4 MPa. In addition, the impingement distance was adjusted from 25 mm to 75 mm. The experiment was carried out at 300 K. Moreover, the photography conditions are also listed in this Table. In this study, the frame rate of the HSV camera was set to 20,000 fps, and the frame size was 768×640 pixels in the vertical plane/ 896×760 pixels in the horizontal plane [167].

Table 5.1 Experimental conditions.

Ambient conditions	
Ambient pressure, P_a [MPa]	0.1, 0.4
Ambient temperature [K]	300
Cross-flow velocity, U_x [m/s]	0, 2, 5
Impingement distance, L_w [mm]	25, 50, 75
Injection conditions	
Injector type	VCO
Nozzle exit diameter, D [mm]	0.15
Test fuel	Dry solvent
Injection pressure, P_{inj} [MPa]	10
Injection pulse, t_{inj} [ms]	4
Photography conditions	
Frame rate	20,000 fps
Frame size [pixel]	768×640 / 896×760
Image resolution [pixel/ mm]	8.17/ 1.65

5.2.2 Definitions of wall-jet vortex characteristic parameters

Figure 5.1 shows the characteristic parameter definitions of the wall-impingement spray involved in this study. In the figure, the sample image is the wall-impingement spray behaviors under cross-flow conditions. The wall-jet vortex phenomena can be clearly observed, which is surrounded by a red rectangular frame. The wall-impingement distance L_w is the distance from the nozzle exit to the wall-impingement point. The distance from the wall-impingement point to the spray tip downstream is defined as L_x, and the spray tip penetration S is defined as the sum of L_w and L_x. The center of the wall-jet vortex region is defined as the vortex core. Moreover, some parameters are defined as follows to better analyze the propagation of the wall-jet vortex. The distance from the wall-impingement point to the vortex core center is defined as the vortex core distance L_c. The vertical distance from the vortex core center to the wall is defined as the vortex core height H_c. In addition, the vertical distance from the highest point of the upper boundary in the wall-jet vortex region to the wall is defined as the vortex height H.

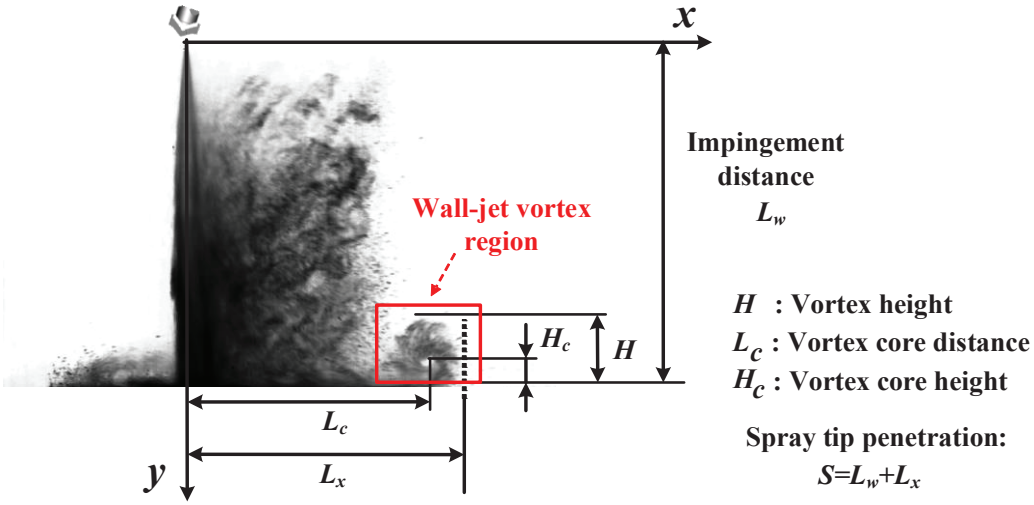

Figure 5.1 Definition of wall-jet vortex characteristic parameters.

5.3 Formation and Propagation of Wall-jet Vortex Phenomenon

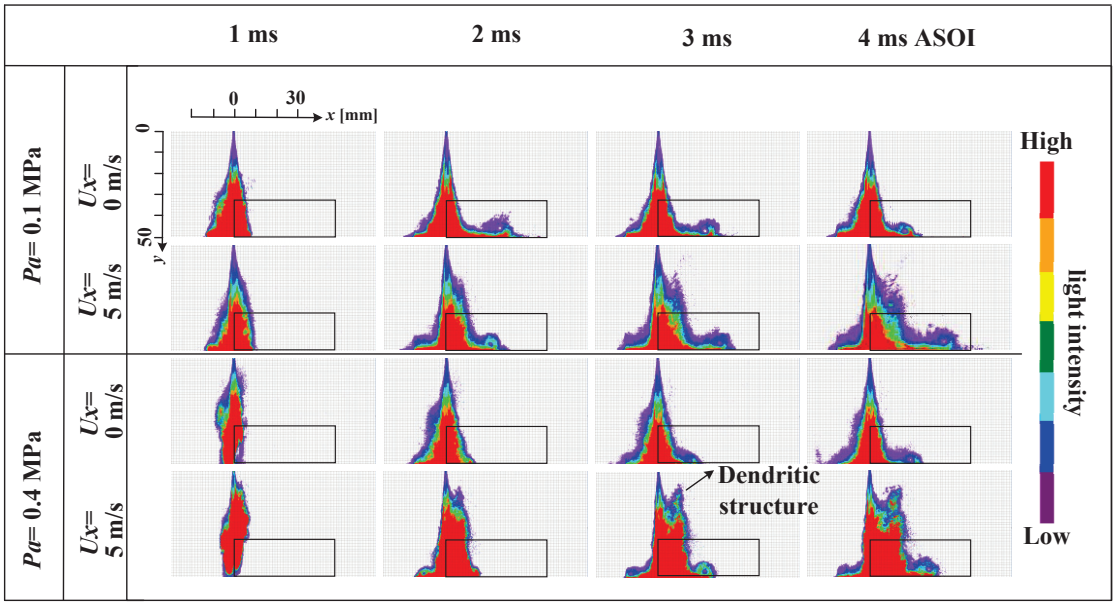

(a)

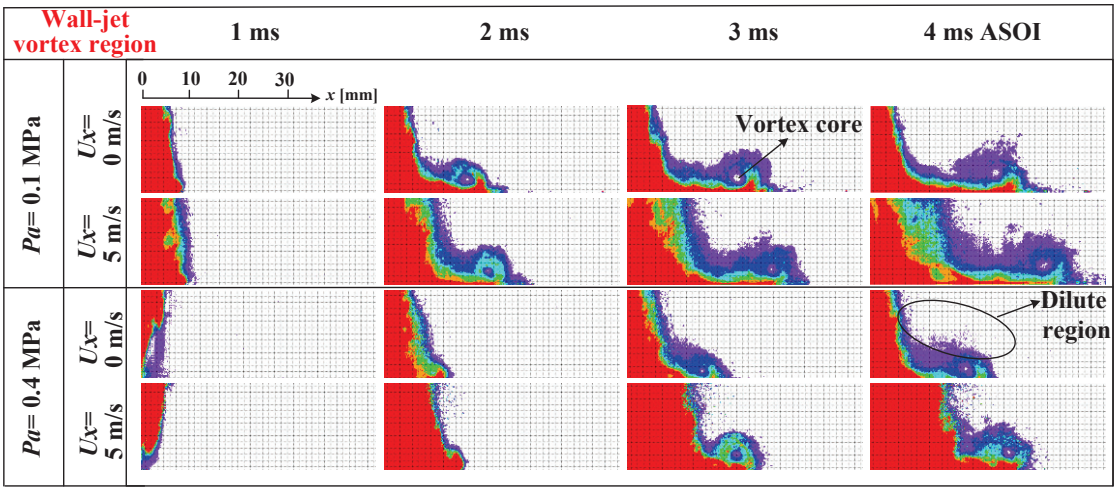

(b)

Figure 5.2 Development of wall-jet vortex under different cross-flow velocities and ambient pressure.

As depicted in Figure 5.2, the Figure 5.2 (a) shows the effect of cross-flow velocity and ambient pressure on the development process of the wall-impingement spray at the same wall-impingement distance of 50 mm. During the experiment, the accuracy of laser sheet imaging was reduced when applied to dense sprays. The inaccuracy can be attributed to three phenomena: laser extinction, signal attenuation and multiple light scattering [168]. However, this is limited by our existing experimental apparatus. The maximum intensity of laser was maintained when

conducting the experiment to decrease the absorption of the scattered light along the direction of the laser sheet to the camera. Different threshold ranges (4%, 8%, 12%, 16%, 20%, 24%, and 28%) were applied in image processing to distinguish the light intensities of the spray images, and rainbow color images were obtained. The wall-impingement spray was basically symmetrical without cross-flow. Under the influence of the cross-flow, the spray moves to the downstream part and then shows an asymmetrical distribution. Also, numerous small droplets can be blown downstream of the cross-flow, which should be the reason for the formation of a dilute region [169]. In addition, the high ambient pressure also promotes the instability of the spray; a dendritic structure appears in the upper right part of the downstream.

Meanwhile, it is interesting that a region of the wall-jet vortex was observed downstream along the wall. To better show the development process of the wall-jet vortex region, the exact location including this region is enlarged, as shown in the Figure 5.2 (b). It can be seen that the cross-flow enhances the movement of the vortex core along the wall, and some droplets can be stripped from the upper surface of the wall-jet vortex region. As a result, the upper surface of the wall-jet vortex becomes a dilute region.

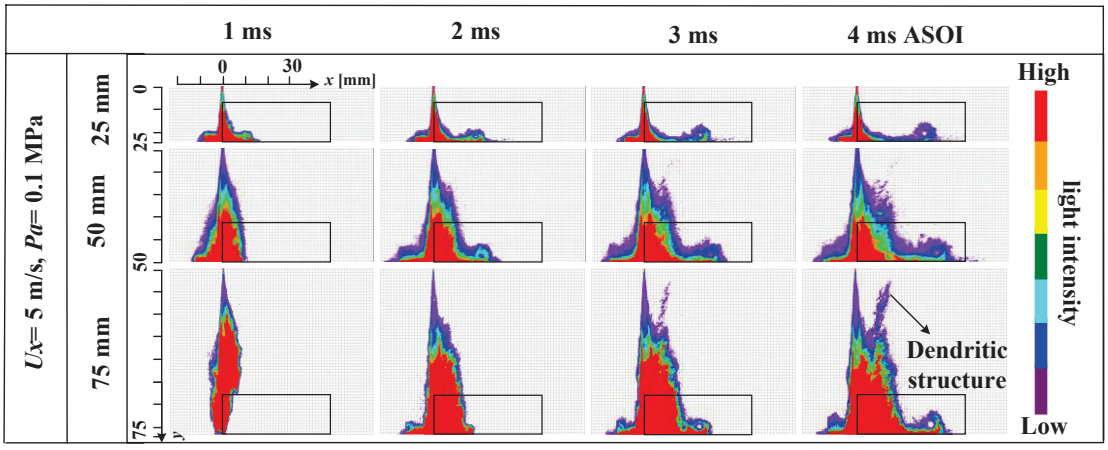

(a)

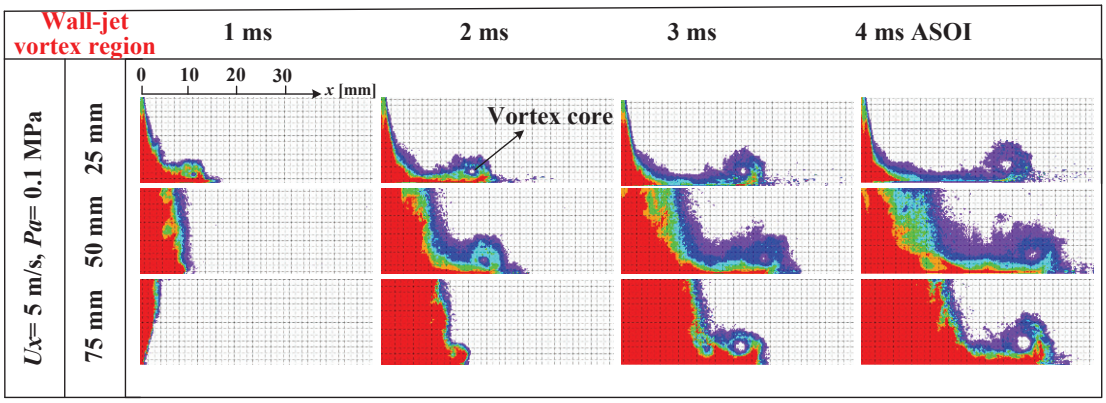

(b)

Figure 5.3 Development of wall-jet vortex under different impingement distances.

It is conceivable that different wall-impingement distances significantly influence on the spray wall-impingement behaviour. To investigate the effect of wall-impingement distances on the propagation of wall-impingement spray, Figure 5.3 shows the different wall-impingement distances at 25, 50, and 75 mm. The spray area increased with an increase in the wall-impingement distances. In addition, the enlarged region shows that the generation time of the wall-jet vortex is delayed after the wall-impingement distances increase. However, it is interesting to find that the moving speed of the vortex core is faster under a larger wall-impingement distance, which suggests that the wall-jet vortex region is more sensitive to the cross-flow with the increase in wall-impingement distances.

5.4 Wall-jet Vortex Characteristics

5.4.1 Wall-jet vortex height and spray tip penetration

Figure 5.4 (a) and (b) show the influence of different cross-flow velocities and ambient pressures on the development process of the average wall-jet vortex height at the same wall-impingement distance of 50 mm. Because the horizontal and vertical axes have errors simultaneously, error bars are not added here (dates are the average of three shots). In this study, only the wall-jet vortex behaviors were investigated here. Under the same wall-impingement distance and atmospheric pressure, it was found

that the cross-flow had almost no effect on the vortex height when the spray tip reached the same position. However, under higher ambient pressure, the vortex height decreases as the cross-flow velocity increased when the spray tip was in the same position. Assuming that the vortex height is the same at an uncertain timing, the wall-jet vortex should move to a farther position along the wall under the condition of higher cross-flow velocity. This is because the wall-impingement point moves downstream when the cross-flow velocity increases, and then the timing of the wall-jet vortex generation is delayed.

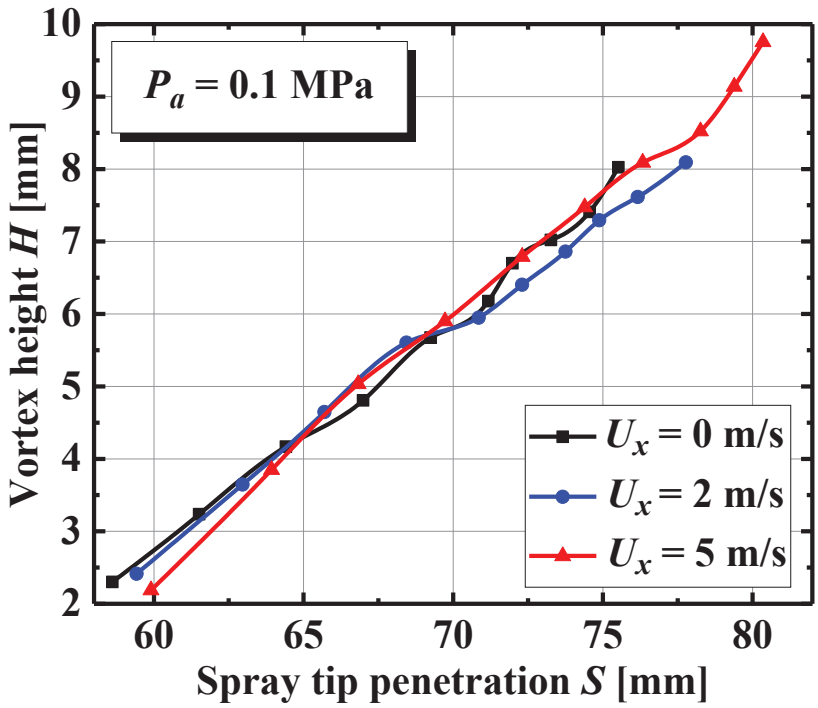

(a)

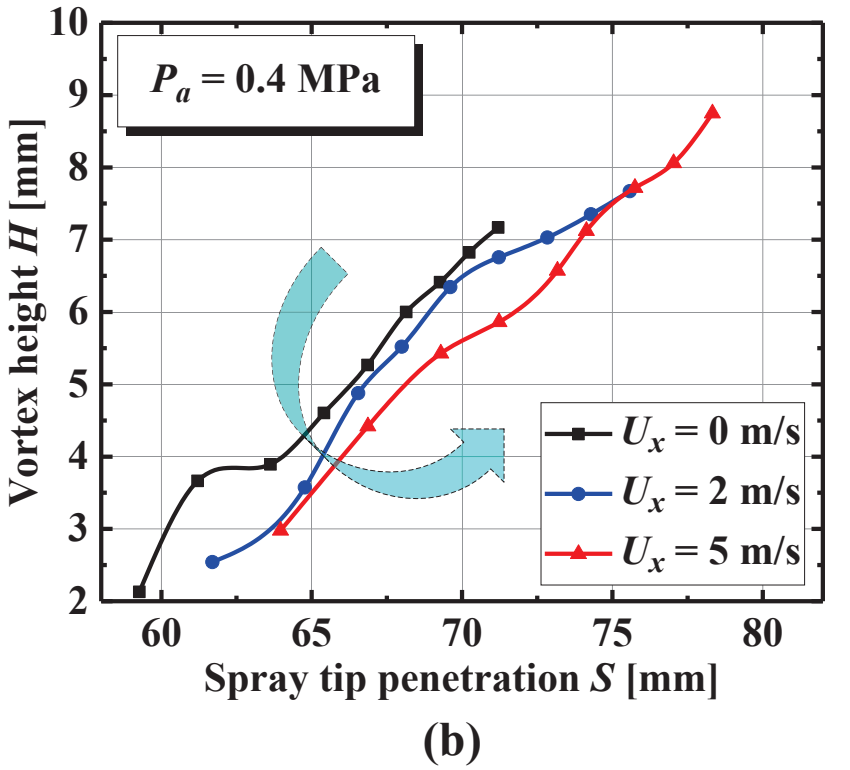

(b)

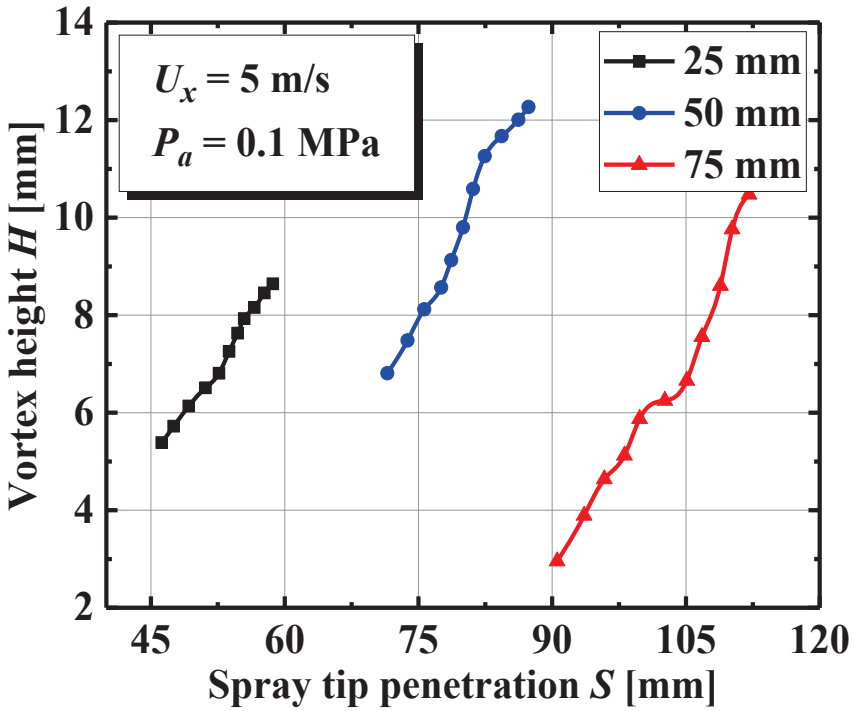

(c)

Figure 5.4 Evolution of wall-jet vortex height *H*.

As shown in Figure 5.4 (c), the generation time of the wall-jet vortex is delayed with an increase in the wall-impingement distance. When the wall-impingement distance was 50 mm, the average vortex height finally reached 13 mm at EOI timing. In addition, the wall-jet vortex requires a longer development time to reach the same vortex height with the increases of wall-impingement distance. It is interesting to note that the minimum value of the vortex height is significantly different under different wall-impingement distances. The spray has considerable kinematic energy when it impinges on the wall with a small wall-impingement distance. Then the wall-jet vortex is submerged by splashed liquid droplets. Therefore, the wall-jet vortex region can only be observed after this region is far away from the wall-impingement point. Moreover, the kinematic energy of the spray is significantly reduced when it impinges on the wall with a larger wall-impingement distance. Then a series of wall-impingement behaviors, including rebound and splash, can be weakened. In this case, the wall-jet vortex behavior can be easily discovered earlier.

5.4.2 Wall-jet vortex core height

As shown in Figures 5.2 and 5.3, the vortex core exists inside the center of the wall-jet vortex region, which can play an essential role in propagating the wall-jet vortex. Therefore, it is necessary to study the development of the vortex cores. Figure 5.5 (a) and (b) show the influence of cross-flow and ambient pressure on the growth of vortex core height Hc. It was also found that the cross-flow had little effect on the development of the vortex core height under atmospheric pressure, reaching approximately 4 mm at EOI. Under higher ambient pressure, it was to find that the cross-flow enhances the vortex core height, which may be caused by two reasons. The growth of the vortex core should be the internal reason, and the changes in the cross-flow velocity and ambient pressure are the external reasons.

Although the vortex core was small, numerous droplets were entrained around the vortex core. The vortex core could grow over time, but the kinetic energy may decrease with an increase in the vortex core size, resulting in poor entrainment ability

of the vortex core. Then the number of surrounding droplets can be decreased. Meanwhile, the internal pressure of the vortex core gradually changes from negative pressure to atmospheric pressure. Eventually, the vortex core can grow into a sphere composed of air and no droplets around it. Therefore, the cross-flow enhances the vortex core height but inhibits the vortex height. The number of droplets around the vortex core is reduced. In addition, the higher ambient pressure suppresses the vortex core height because a more significant ambient density hinders the movement of the wall-jet vortex.

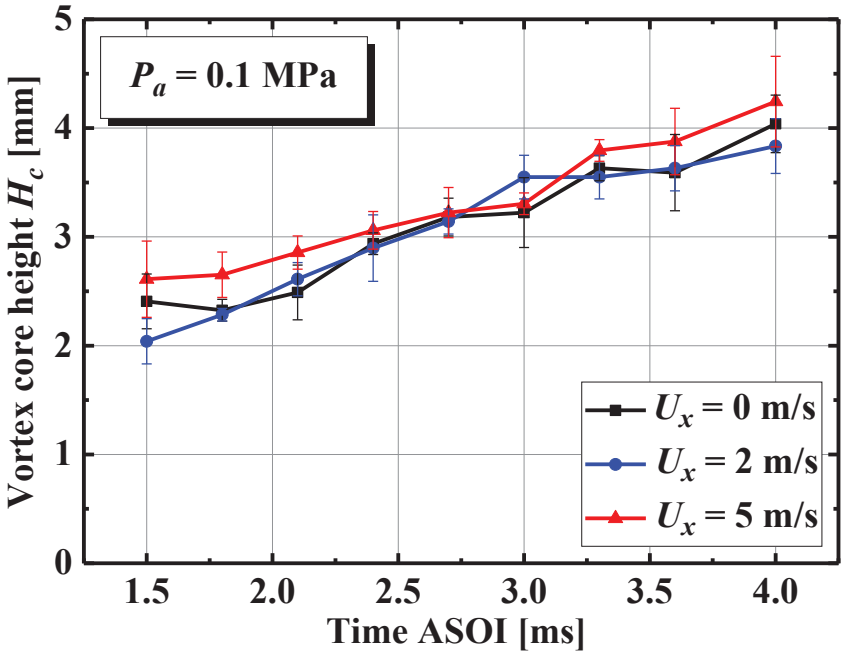

(a)

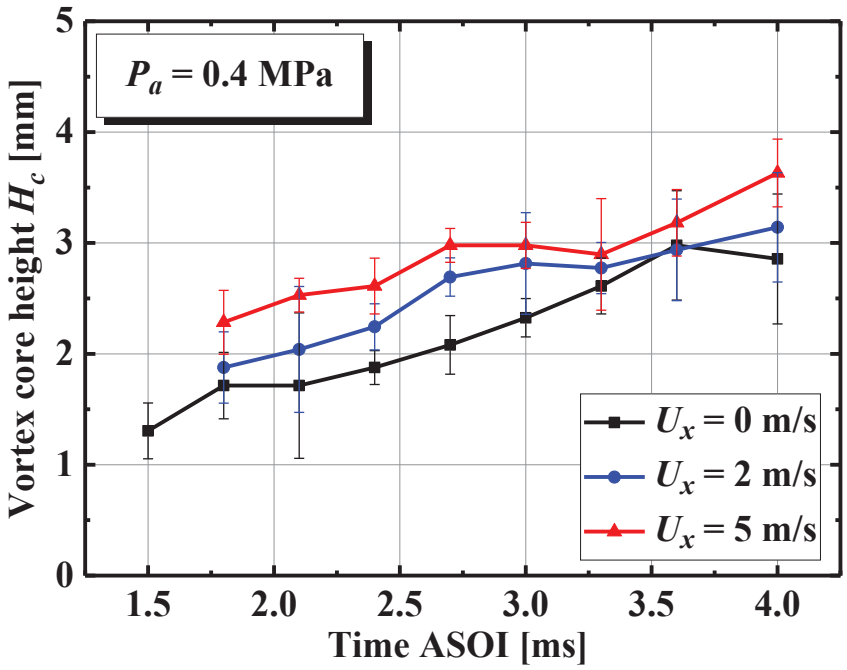

(b)

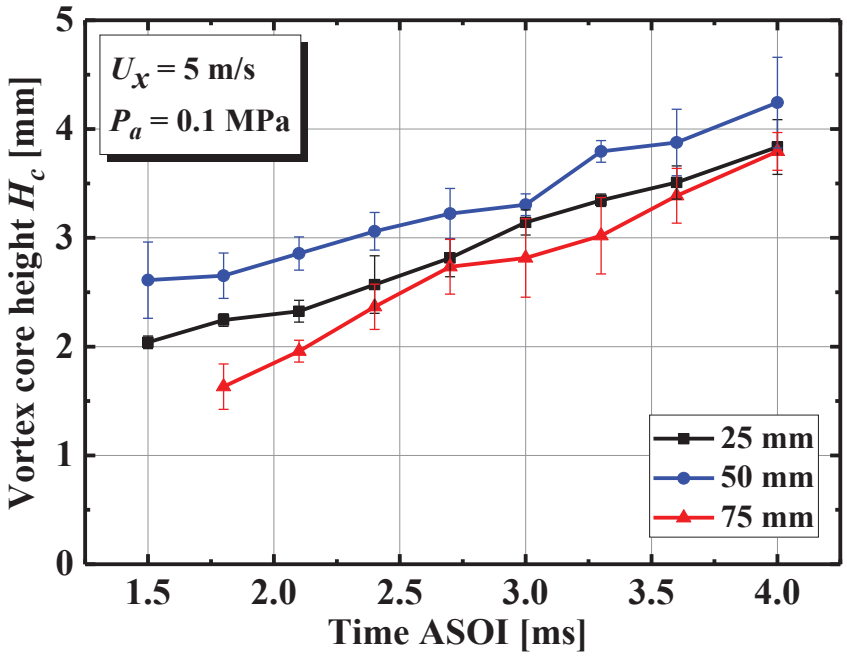

(c)

Figure 5.5 Evolution of wall-jet vortex core height H_c.

In addition, the wall-impingement distance does not positively influence the increases in the vortex core height, as shown in Figure 5.5 (c). The vortex core height

reached the maximum value when the wall-impingement distance was 50 mm. The vortex core height was the smallest when the wall-impingement distance was 75 mm. It is known that the timing of wall-impingement on the wall is delayed, and the other reason is that the kinematic energy of the wall-impingement spray is reduced. It seems that there is a critical impingement distance of approximately 50 mm, which can lead to a higher vortex core height. In the future, the critical impingement distance should be considered.

5.4.3 Wall-jet vortex core distance

As shown in Figure 5.6 (a) and (b), the cross-flow promotes the movement of the vortex core in the horizontal direction. The vortex core distance also increased with an increase in the cross-flow velocity. Meanwhile, it can be found from the slope of the vortex core distance over time that the cross-flow can increase the moving speed of the vortex core. In addition, as the ambient pressure increased, the vortex core distance was also suppressed, which was approximately 20% less than that under atmospheric pressure.

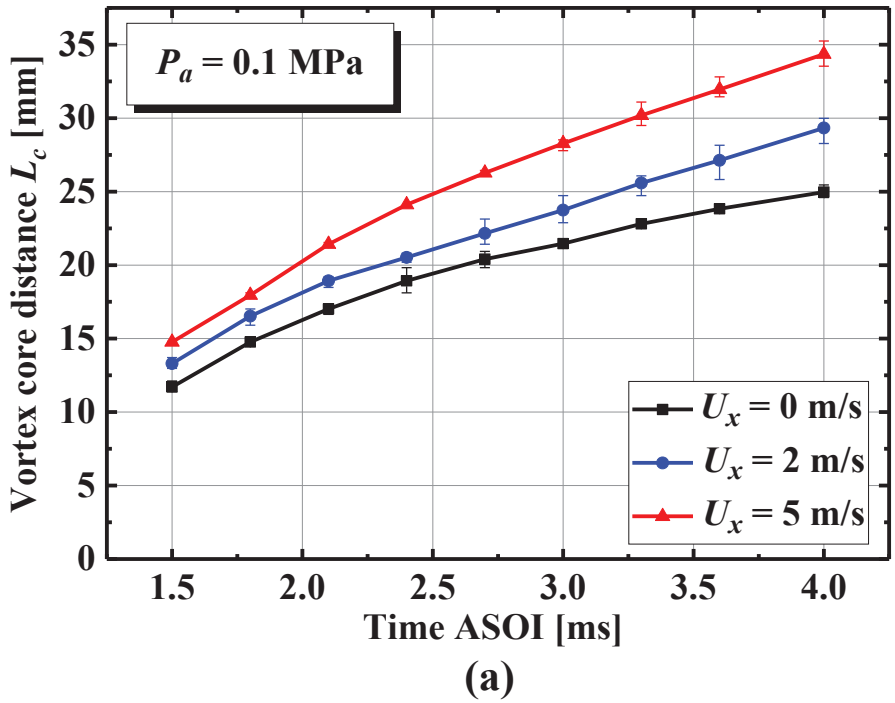

(a)

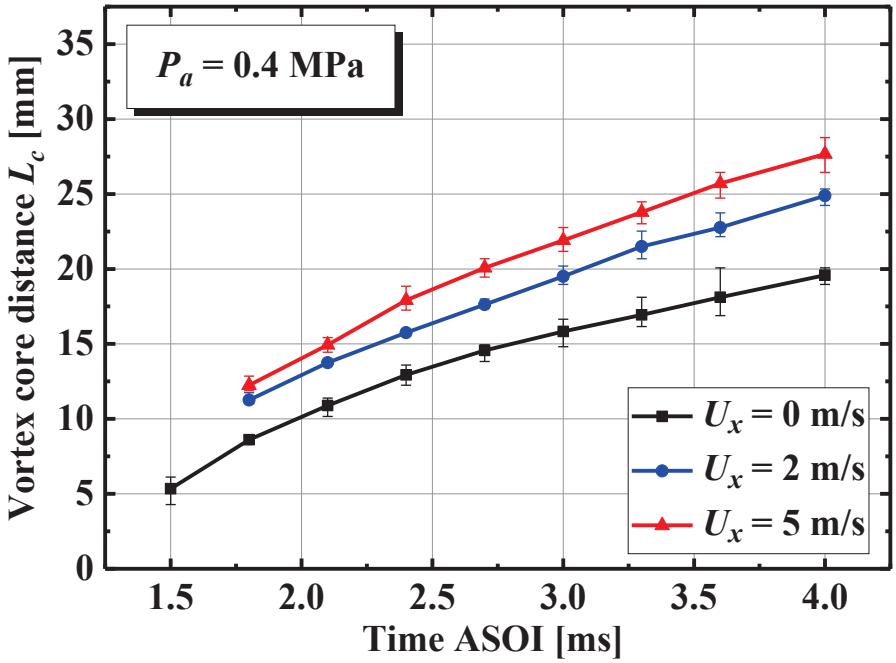

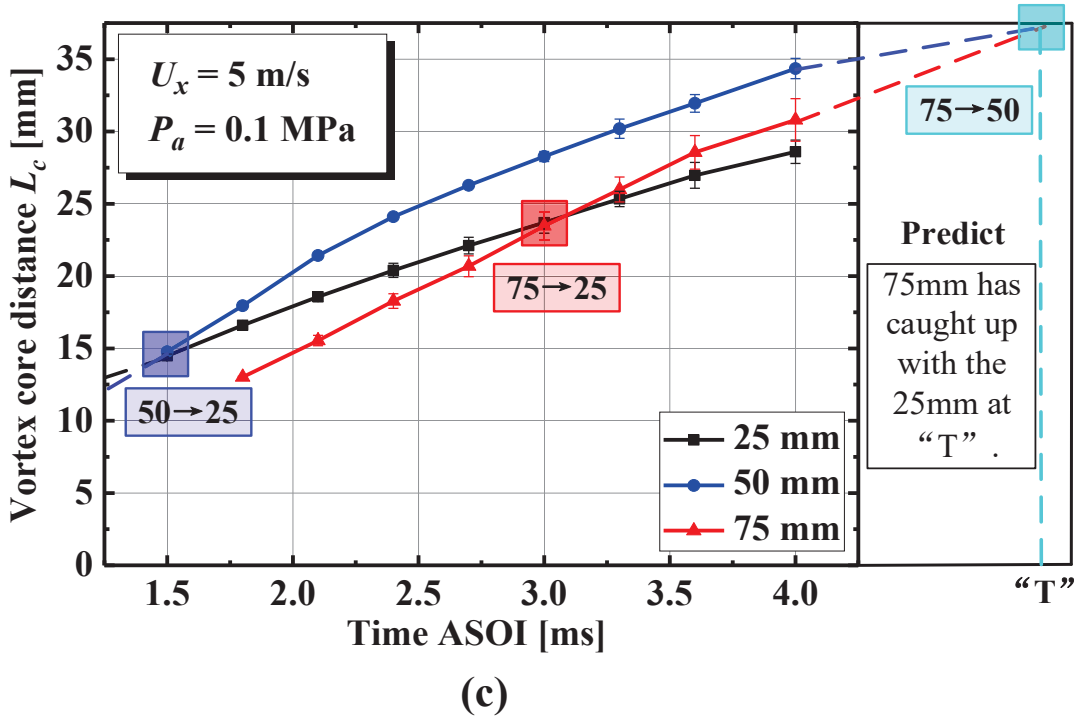

Figure 5.6 Evolution of wall-jet vortex core distance L_c.

Figure 5.6 (c) shows that the vortex core distance at the wall-impingement distance of 50 mm catches up with that of 25 mm at 1.5 ms ASOI. Moreover, at 3 ms

ASOI, the vortex core distance under the wall-impingement distance of 75 mm also catches up to 25 mm. According to the prediction of the development speed on the vortex core distance, the vortex core distance under the wall-impingement distance of 75 mm catches up with that of 50 mm at "*T*" ASOI. The results are consistent with the result in Figure 5.3, where the moving speed of the vortex core increases with an increase in the wall-impingement distance ($v_{75\ mm} > v_{50\ mm} > v_{25\ mm}$). Because the fuel mass of the wall-jet vortex decreases with the increase in the wall-impingement distance, the wall-jet vortex region is more sensitive to the influence of cross-flow and then blown downstream more quickly.

5.4.4 Contribution of each condition to wall-jet vortex

To evaluate the influence of cross-flow, ambient pressure and wall-impingement distance on the wall-jet vortex propagation, an indicator I_c of the "contribution index" is proposed to evaluate the degree of influence of different influencing factors. Figure 5.7 (a) shows the definition of the contribution coefficient. The vertical axis represents the characteristic parameters of the wall-jet vortex, including the vortex core height H_c and vortex core distance L_c, and the horizontal axis represents the time development process ASOI. The mathematical description of the contribution coefficient I_c is given in Equation (5.1).

$$I_c = \left(1 + \frac{S_1 - S_2}{S_2}\right) \times 100\% \tag{5.1}$$

Where the S_1 represent the area enclosed by the horizontal time axis when the vortex core height or distance develops in the different cases, and basic case S_2 is under the reference condition (P_a = 0.1 MPa, U_x = 0 m/s, L_w = 50 mm), S_1 is under the experimental condition after changing a certain variable.

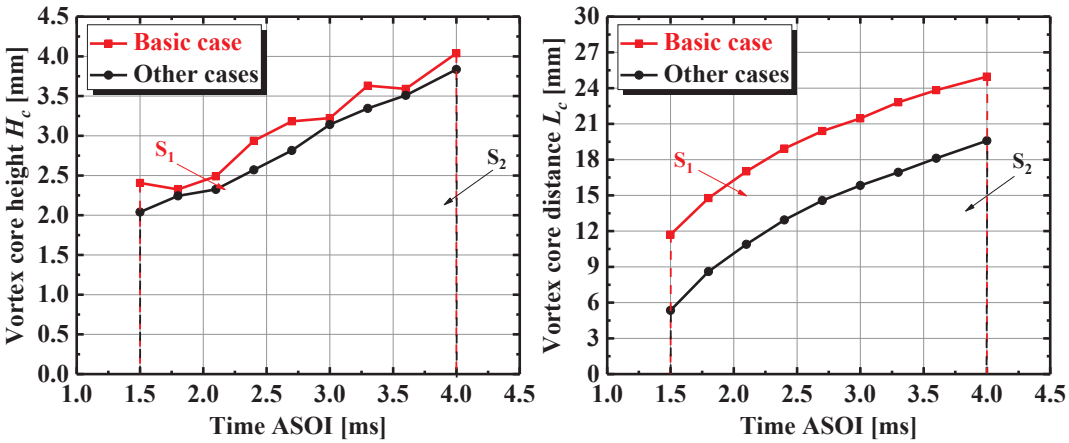

(a) Definition of contribution index

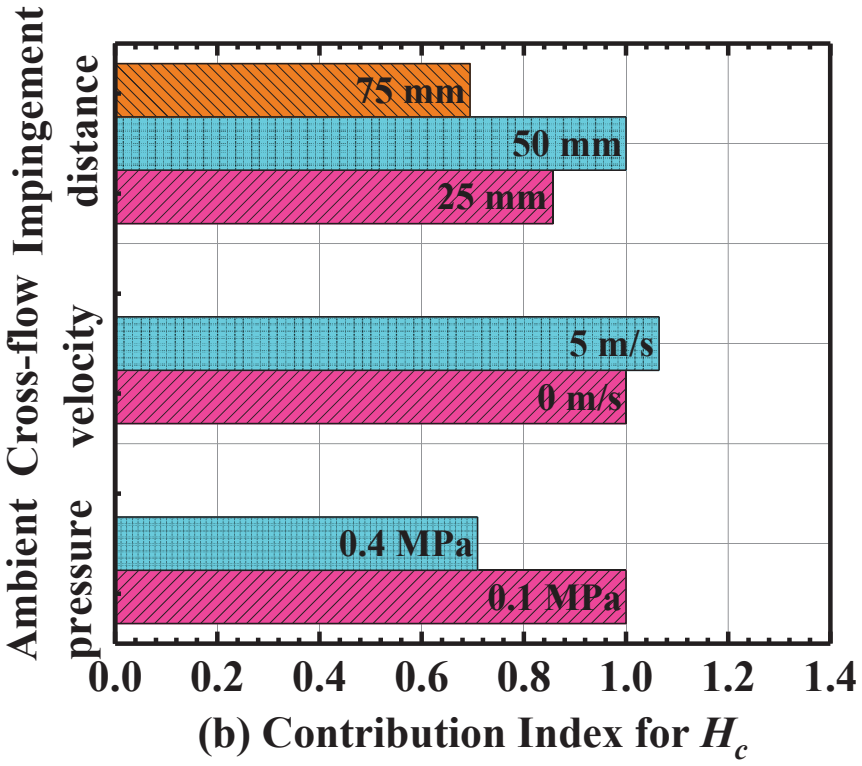

(b) Contribution Index for H_c

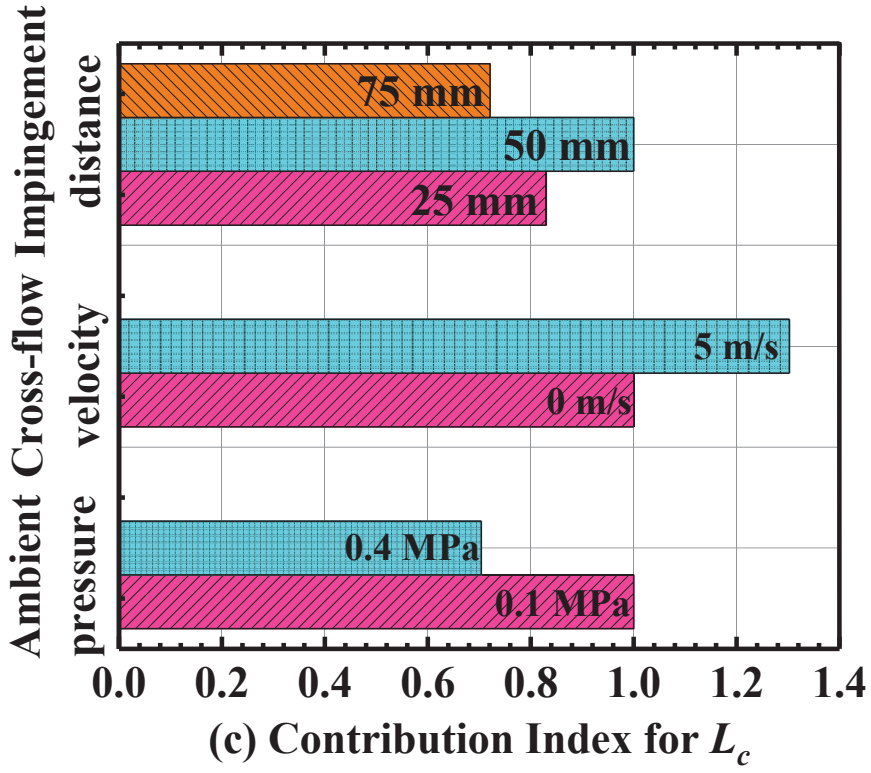

Figure 5.7 Contribution of each condition to H_c and L_c.

As shown in Figure 5.7 (b), the ambient pressure significantly influences the development of the vortex core height. When the ambient pressure increases from 0.1 MPa to 0.4 MPa, the vortex core height is reduced by about 30%. The second is the impact of the wall-impingement distance. When the wall-impingement distance varied from 25 mm to 50 mm, the height of the vortex core increased by 15%. And the vortex core height was reduced by 30% after the distance changed from 50 mm to 75 mm. As depicted in Figure 5.7 (c), it is also noted that the development of the vortex core distance is more sensitive to the cross-flow. The cross-flow velocity of 5 m/s increases the vortex core distance by approximately 30%.

5.5 Velocities Distribution Around a Wall-jet Vortex

Figure 5.8 (a) and (b) shows the PIV results of the wall-impinging spray at 3 ms and 4 ms without cross-flow, respectively. Because the wall-impingement point is the exposed area of the spray, the PIV results cannot be obtained; thus, a blank area is

depicted. Meanwhile, the wall-jet vortex phenomenon was also observed in the PIV results, and this region was enlarged at the upper right corner.

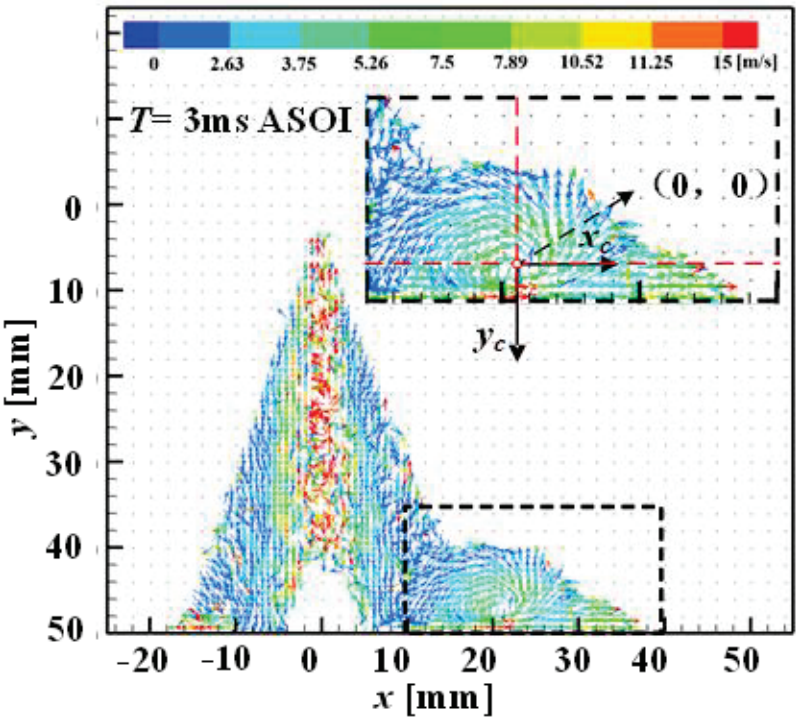

(a) T=3 ms ASOI

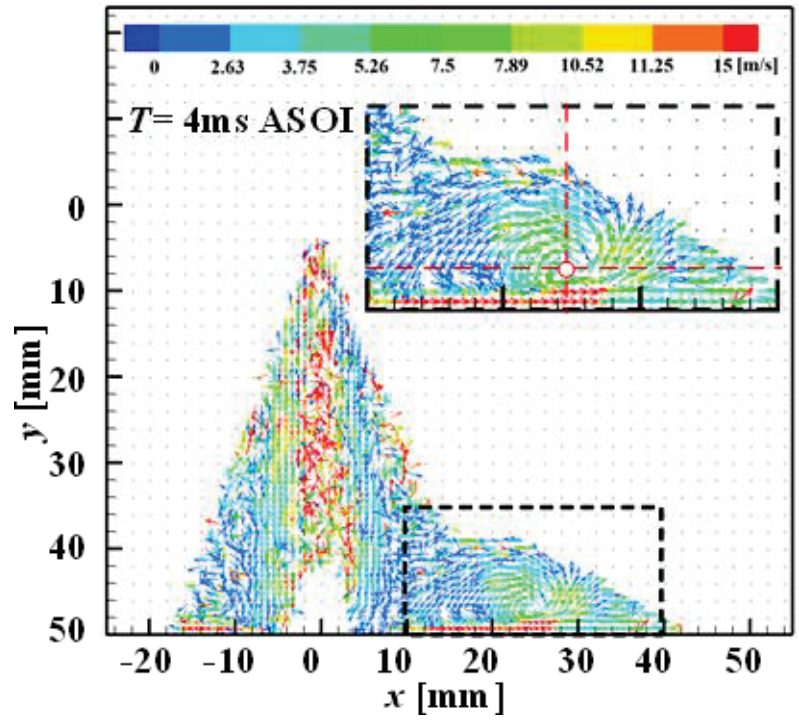

(b) T= 4 ms ASOI

Figure 5.8 Raw data of PIV measurements

To better understand the velocity distribution in the region of the wall-jet vortex, the droplet velocities extracted along the x- and y-axes of the vortex core are shown in Figure 5.9 (a) and (b), respectively.

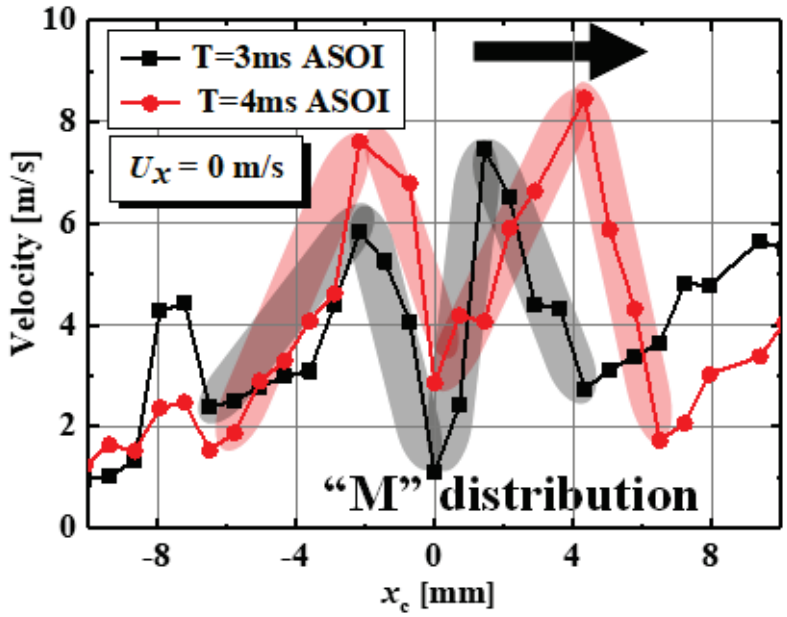

(a) Velocity distribution of droplets along the axis *x*

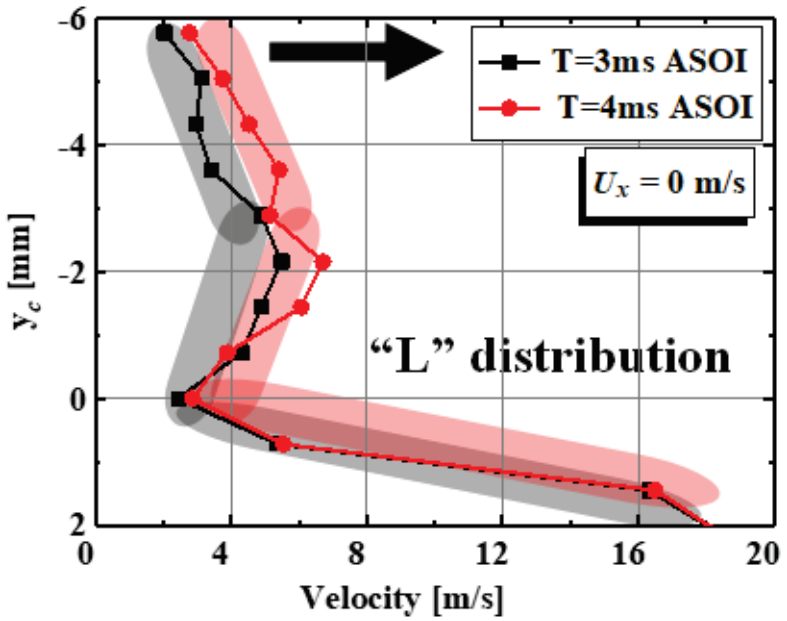

(b) Velocity distribution of droplets along the axis *y*

Figure 5.9 Velocity distribution around wall-jet vortex core without cross-flow.

In the Figure 5.9, the black color represents the velocity distribution at 3ms,

whereas the red color represents the velocity distribution at 4ms. In terms of the velocity distribution along the x-axis of the vortex core, it presents a "*M*" distribution. The velocity is almost 0 m/s at the center of the vortex core, proving that almost no droplets existed inside the vortex core (vacuum zone). Two peaks were observed on both sides of the vortex core, indicating that the droplet velocities on both sides are relatively large. The peak value decreases if continues to extend to both sides. Interestingly, the wall-jet vortex region moves to the right with time, and the peak value of the droplet velocity increases. It is conceivable that a continuous fuel supply can supplement kinetic energy to the wall-jet vortex during fuel injection, and the droplet velocity could increase. It can be predicted that the droplet velocity should decrease after EOI due to energy dissipation.

According to the velocity distribution along the y-axis direction of the vortex core, it is a "*L*" distribution. The velocity near the wall is considerably greater than the far wall velocity by approximately three times. The far wall velocity is smaller because the air entrainment has a significant resistance to the movement of droplets, causing a momentum decrease in the droplets. Meanwhile, the results also show that the droplet velocity increases significantly with time in the far wall region. It was also found that the velocity distribution did not change, which suggests that the vertical component of the droplet velocity along the y-axis direction remains unchanged. However, the horizontal velocity component increases along the wall.

Figure 5.10 shows the PIV results of the wall-impinging spray at 3 ms and 4 ms under the influence of cross-flow, respectively. Compared with the condition without cross-flow, the spray density at the wall-impinging point is reduced because of the spray blown downstream, manifested in the obvious reduction of the block region shown in the PIV results. In addition, since plentiful small droplets can be carried by the cross-flow downstream, PIV can intuitively observe the velocity distribution of the droplets in the upper right corner region, where the droplet velocity is close to the cross-flow velocity.

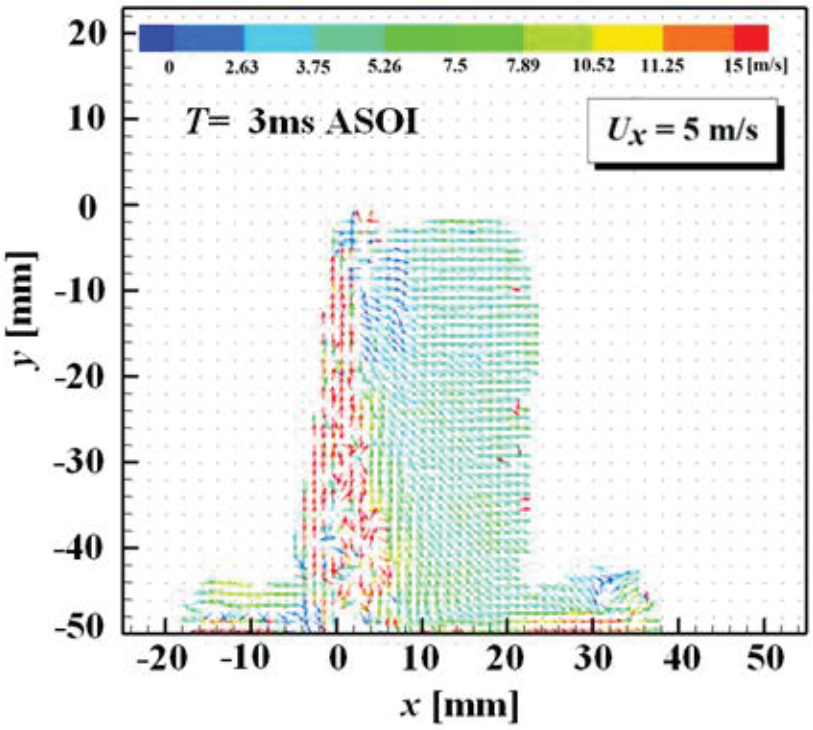

(a) T= 3 ms ASOI

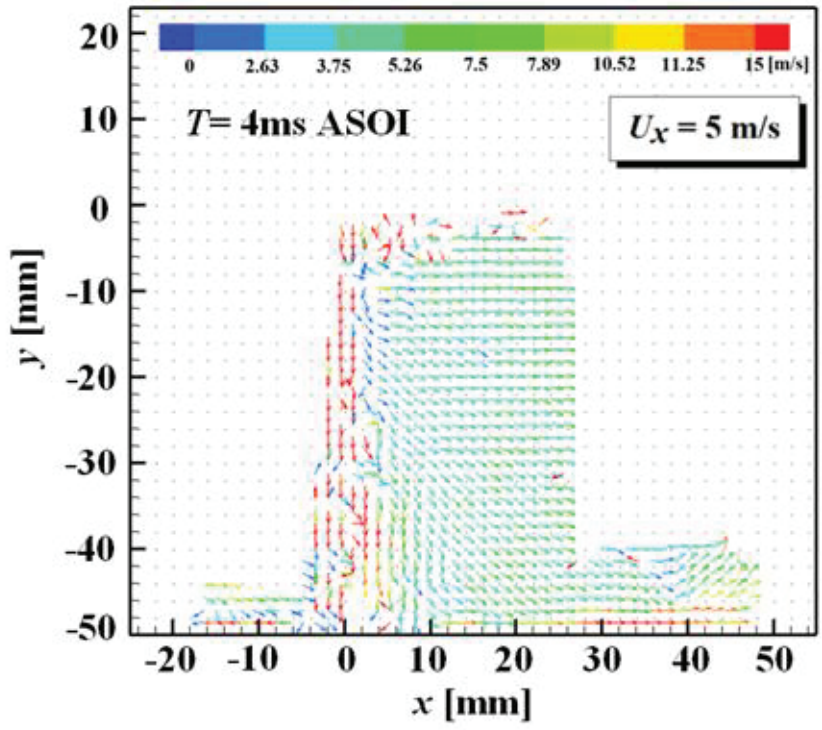

(b) T= 4 ms ASOI

Figure 5.10 Velocity distribution around wall-jet vortex core with a cross-flow velocity of 5 m/s.

Although a wall-jet vortex under cross-flow conditions can be observed in the

previous DBI results, there is no evident vortex structure in the PIV results. The velocity distribution is considerably affected by the cross-flow and is rather messy. It is evident that the area of the wall-jet vortex region increases, the number of droplets increases over time, and a more uniform velocity distribution can be seen. Because the wall-jet vortex region cannot be distinguished, a quantitative velocity analysis around the vortex core has not been performed.

5.6 Wall-jet vortex observed on horizontal plane

Owning to the existence of the wall-jet vortex phenomenon, high-speed horizontal photography near the wall was carried out to further understand its development mechanism. Figure 5.11 shows a series of false-color spray images on the wall-impinging spray with a 50 mm wall-impinging distance; a horizontal plane located 2 mm above the wall surface was selected for shooting. The images only show the horizontal plane photography of spray for observing the vortex core of wall-jet vortex, which are different with the fuel adhesion film. Under the influence of cross-flow, the wall-impinging point is shifted downstream a little, and the spray is distributed asymmetrically. In addition, the whole spray area becomes larger, and the wall-impingement spray is better dispersed, which is consistent with the spray behavior of vertical plane under the cross-flow conditions. Moreover, an obvious vortex core area can be observed under atmospheric pressure, shown as a ring shape. It was also noted that the edge of the spray was corrugated in the horizontal plane.

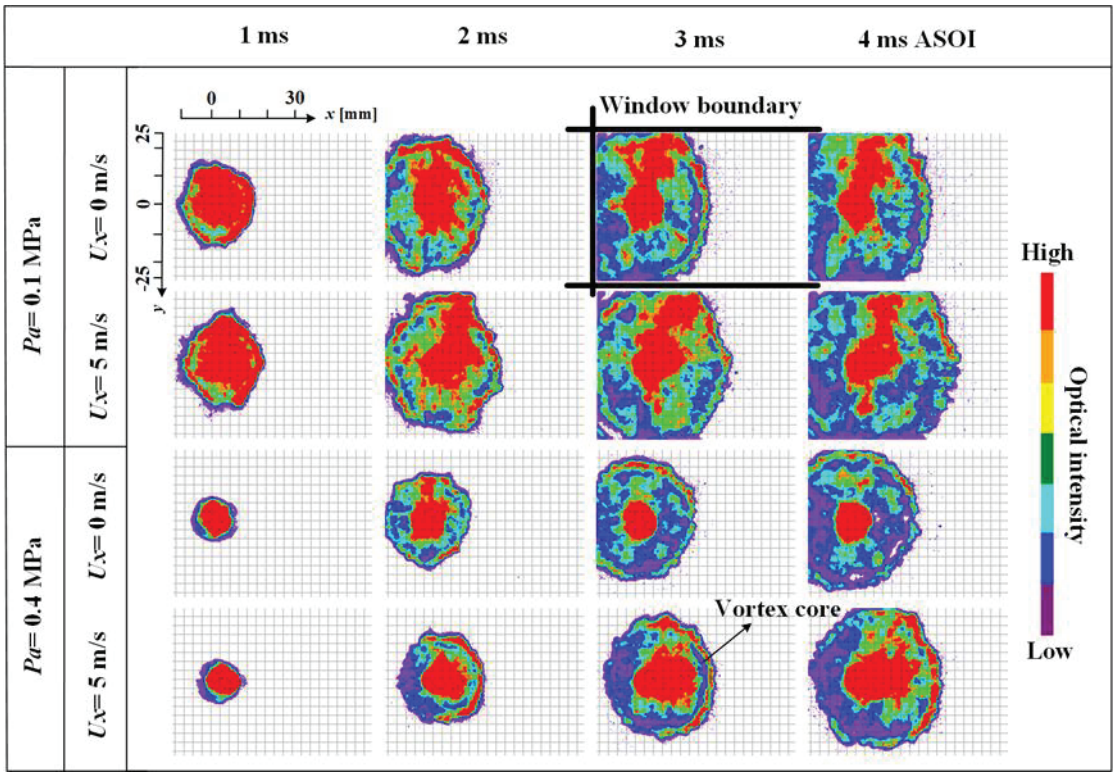

Figure 5.11 High-speed photography of horizontal plane.

(2mm above the wall)

5.7 Wall-impingement Spray Behavior under Cross-flow Conditions

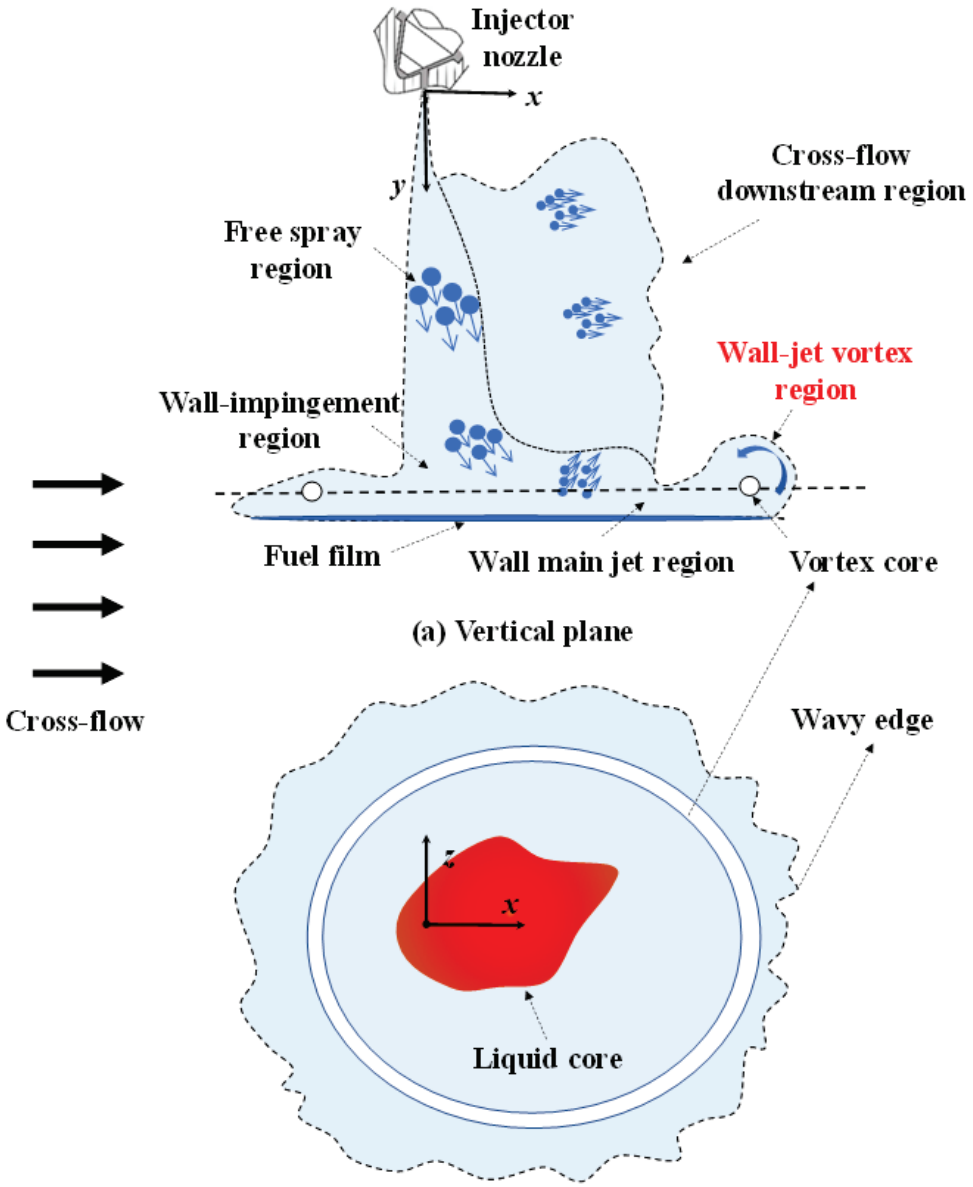

Figure 5.12 The schematic diagram of wall-impingement spray behavior under cross-flow conditions.

The physical phenomenon of wall-impinging spray on the vertical plane is presented in Figure 5.12 (a). According to the findings of this study, the behavior of wall-impinging spray can be divided into five regions: free spray region, wall-

impingement region, cross-flow downstream region, wall main jet region, and wall-jet vortex region. The structure of the free spray region is the same as that of the free spray, the main-jet zone with a high fuel concentration is at its center, and a mixed flow zone with a large concentration gradient is in its periphery. After the fuel enters the wall-impingement region, the concentration quickly dissipates. The fuel concentration in the wall main jet region is relatively thin compared to the free spray region. At the tip of the wall main jet region, wall-jet vortex region is formed by the pressure difference. In addition, cross-flow is conducive to spray dispersion, plentiful droplets can be blown downstream to form a dilute region. As shown in the Figure 5.12 (b), the vortex core can also be observed from the horizontal plane and presents a white ring shape, which indicates that the density of the droplets in this zone is relatively low. Moreover, the edge of the spray structure is distributed in a wave shape.

5.8 Summary

In this study, the wall-jet vortex was characterized under different ambient pressure, cross-flow velocities and wall-impingement distance. An indicator *Ic* of the "contribution index" is proposed to evaluate the degree of influence of different influencing factors. The main conclusions can be summarized as follows.

(1) The wall-impinging spray behaviors can be divided into five regions: free spray region, wall-impingement region, cross-flow downstream region, wall main jet region, and wall-jet vortex region. The cross-flow enhances the kinematic energy of the wall-jet vortex, and the droplets strip from the upper surface of the wall-jet vortex region to form a dilute region.

(2) First, the vortex core height is reduced by approximately 30% when the ambient pressure increases from 0.1 to 0.4 MPa. Because a larger ambient density hinders the movement of the vortex, the vortex core height decreases. However, the cross-flow significantly increases the vortex core height under the higher ambient pressure.

(3) Second, the vortex core distance is more sensitive to cross-flow. The cross-flow

velocity of 5 m/s increased the vortex core distance by approximately 30%. Cross-flow obviously promotes the movement of the vortex core in the horizontal direction, and the moving speed of the vortex core can also be enhanced by cross-flow.

(4) In addition, with an increase in the wall-impingement distance, the timing of spray wall-impingement is delayed, and the spray atomization can be enhanced. Meanwhile, the generation time of the wall-jet vortex was delayed. Moreover, it is predicted that when the wall-impingement distance is 75 mm, the vortex core distance could catch up with that of 50 mm at "*T*".

(5) Finally, the velocity distribution around the vortex core was analyzed. Along the x-axis, the velocity distribution presents a "*M*" distribution. Along the y-axis direction, the velocity near the wall is significantly larger than that of the far wall in the wall-jet vortex region and exhibits a "*L*" distribution.

CHAPTER 6 FUEL ADHESION CHARACTERISTICS OF WALL-IMPINGEMENT SPRAY

6.1 Introduction

As introduced in the Chapter 5, the impingement of fuel spray on the piston surface significantly affects the mixture formation, combustion performance, and emissions of a DISI engine. In this Chapter, the fuel adhesion characteristics of wall-impingement spray were investigated under cross-flow conditions for in-depth understanding the fuel adhesion behavior. Mie scattering and RIM were used to observe the propagation of fuel spray and fuel adhesion, respectively. Subsequently, the area, mass, and thickness of fuel adhesion were evaluated under various cross-flow velocities. Moreover, the formation and propagation mechanism of the fuel adhesion under cross-flow conditions were revealed. The experimental results can provide an insight into the operating conditions of air-flow inside the engine.

6.2 Experimental Conditions

The detailed experimental conditions are listed in Table 6.1. The nozzle outlet diameter of the mini-sac single-hole injector used in the experiment was 0.15 mm and the L/D was 2.2. The nozzle processing method was fluid polishing. Toluene was used as the test fuel. The test fuel was injected into the cross-flow flow field at an injection pressure of 10 MPa and an injection pulse of 2.8 ms. The injection mass was 3.64 mg. Meanwhile, the cross-flow velocity was in the range of 0 ~ 30 m/s. The experiment was carried out at standard atmospheric pressure (0.1 MPa) and room temperature (298 K). The impingement wall was made of quartz glass, the roughness of the wall was 7.7 μm, the area was 125 × 70 mm, and the impingement distance was set to 50mm. In addition, the shooting conditions of Mie scattering and RIM were also provided in this Table. In the Mie scattering experiment, the frame rate of the HSV camera was set to 20,000 fps, the frame size was 1024 × 528 pixels, and the image

resolution was determined by 8.1 pixels/ mm. In the corresponding RIM experiment, the frame rate was set to 10,000 fps, the frame size was 1024 × 688 pixels, and the image resolution was determined by 8.4 pixels/ mm [170].

Table 6.1 Experimental conditions.

Ambient conditions		
Ambient pressure, P_a [MPa]	0.1	
Ambient temperature [K]	298	
Cross-flow velocity, U_x [m/s]	0, 10, 20, 30	
Injection conditions		
Injector type	Mini-sac, Single-hole	
Nozzle exit diameter, D [mm]	0.15	
L/D	2.2	
Nozzle processing	Laser, Fluid Polishing	
Test fuel	Toluene	
Injection pressure, P_{inj} [MPa]	10	
Injection pluse, t_{inj} [ms]	2.8	
Injection mass, m [mg]	3.64	
Impingement conditions		
Impingement plate	Quartz glass	
Shape of impingement plate, [mm]	Rectangle [125*70]	
Impingement distance, L_w [mm]	50	
Surface roughness, R_f [μm]	7.7	
Photography conditions		
Optical methods	Mie	RIM
Frame rate	20,000 fps	10,000 fps
Frame size	1024×528	1024×688
Image resolution	8.1 pixel/ mm	8.4 pixel/ mm

6.3 RIM Principle and Calibration

Drake [145] proposed the RIM method based on the principle that fuel and quartz glass have similar refractive indices. As depicted in Figure 6.1, the principle is that when the upper surface of the quartz glass is dry, the light is refracted and diffusely reflected on the surface of the quartz glass because the refractive index (1.46) of the quartz glass is quite different from that of air (1). This phenomenon can be recorded by the HSV camera. When the fuel adheres to the quartz glass surface to form a fuel adhesion, the light will simultaneously pass through the quartz glass and fuel owing to their similar refractive index indices (1.43~1.49). Consequently, the brightness of the light recorded by the camera will be reduced and the fuel adhesion will appear darker. An increase in fuel adhesion thickness on the wall reduced the brightness of the light recorded. In addition, please reference [171,172] for more information on the RIM principle.

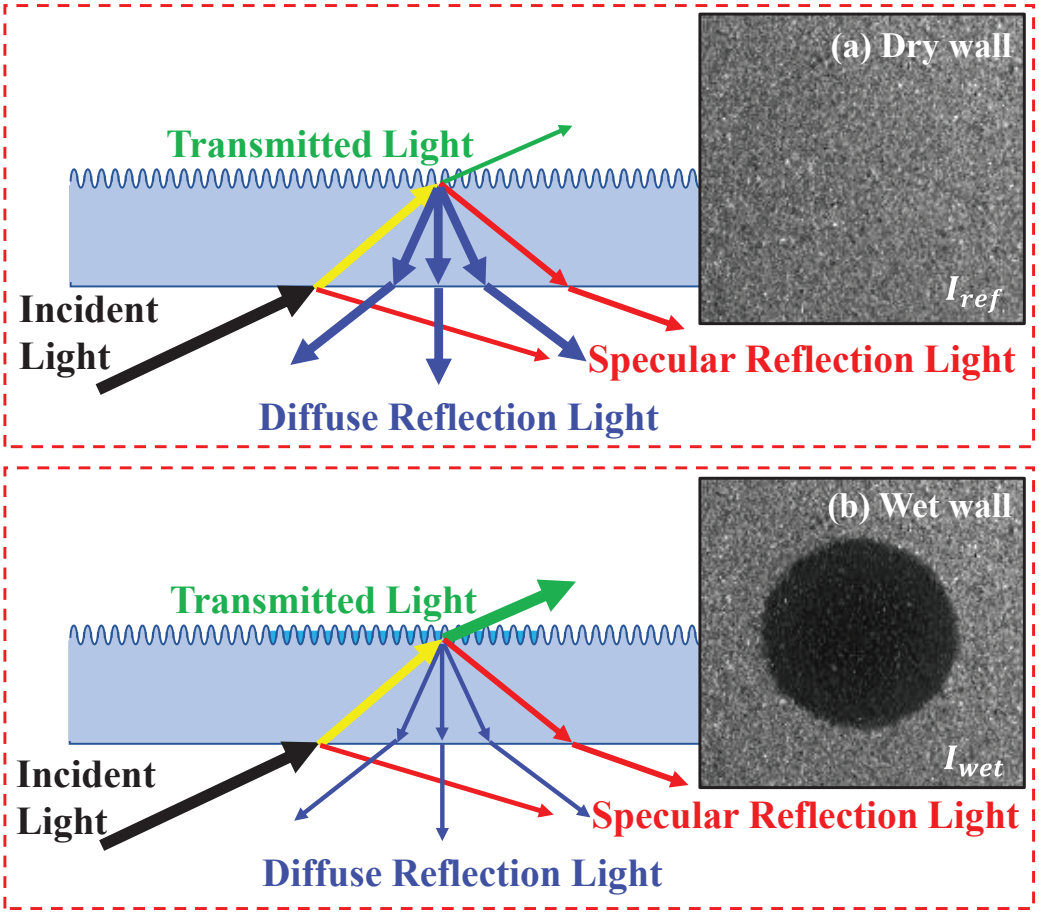

Figure 6.1 RIM principle.

As mentioned above, the spatial distribution of fuel adhesion characteristics can be measured using RIM technology. The surface brightness of the dried quartz is recorded as $I_{ref}(x,y)$, and the surface brightness of the quartz after the fuel adherence to the flat-wall is recorded as $I_{wet}(x,y)$. The change in transmittance $\Delta I(x,y)$ caused by the fuel adhesion can be described as Equation (6.1).

$$\Delta I(x,y) = \left(1 - \frac{I_{wet}(x,y)}{I_{ref}(x,y)}\right) \times 100\% \tag{6.1}$$

According to the principle of RIM, the change in transmittance caused by the fuel adhesion can be regarded as a function "f" of the fuel adhesion thickness $h(x,y)$.

$$\Delta I(x,y) = f[h(x,y)] \tag{6.2}$$

This function "f" is determined by the surface roughness of the quartz glass and the optical system. Therefore, it should be calibrated to establish a relationship between transmittance and fuel adhesion thickness.

Table 6.2 Characteristics of fuels and quartz glass.

Parameter	Refractive index	Density (kg/m^3)	Boiling Point (K)	Kinematic viscosity (10^{-6} m^2/s)	Surface tension (N/m)
Toluene	1.49	866	382 75	0.68	0.0285
Tridecane	1.43	756	507 58	2.35	0.0303
Gasoline	1.42	737	-	0.46	0.022
Quartz glass	1.46	-	-	-	-

To obtain the calibration curve, a calibration experiment was performed under the atmospheric pressure (0.1 MPa) and room temperature (298 K) without the injection system. Two different fuel mixtures of toluene and tridecane (90% by volume of toluene and 10% by volume of tridecane) were impinged on the surface of the quartz glass plate with a microliter injector. A high-speed video camera was used to record the propagation of fuel adhesion. The process of diffusion and evaporation can be found in Figure 6.2. Since tridecane has a low volatility and high viscosity, while toluene has high volatility and low viscosity. In addition, their refractive index

is similar to that of quartz glass. Therefore, a thin fuel adhesion thickness can be achieved using the liquid mixtures of these fuels. The thermophysical and optical properties of fuels and quartz glass are provided in Table 6.2.

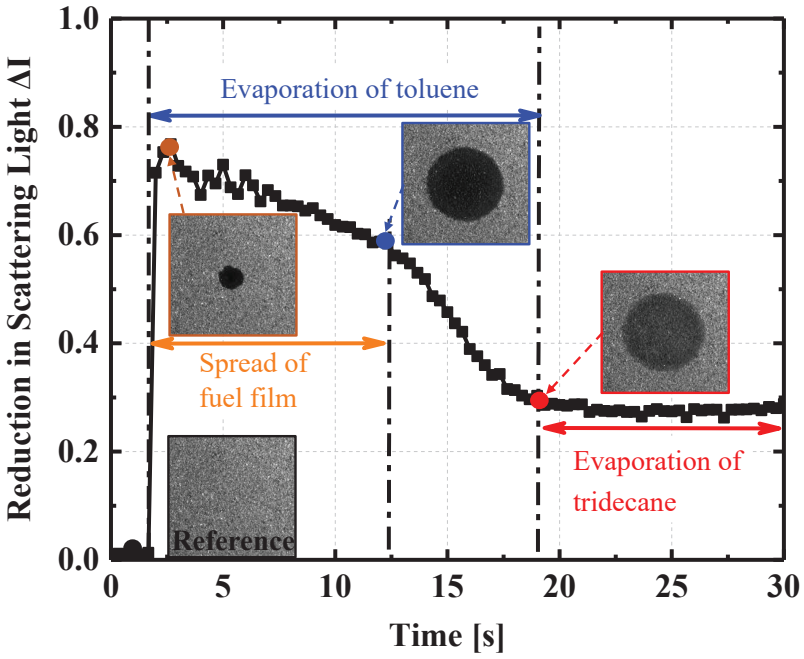

Figure 6.2 Calibration principle.

It can be observed from Figure 6.2 that the average brightness has a stable value when the surface of the flat-wall is dry. The fuel droplets adhere on the surface of the flat-wall and rapidly expands to form a form fuel adhesion under the effect of surface tension. This rapidly reduced the intensity of the scattered light, which dramatically decreases the average brightness. The toluene evaporates first, which is characterized as a light component. And the intensity of the scattered light rapidly increases result in an increase in the average brightness. Then increase rate of average brightness decreases until the droplets are completely evaporated, which represents the evaporation process of the heavy component tridecane. Take the image corresponding to the boundary point of these two different evaporation stages as the calibration point image, and then the Equation (6.1) is used to calculate $\Delta I(x, y)$. Meanwhile, the volume of the corresponding fuel adhesion represents the volume of tridecane. Considering that the thickness of fuel adhesion is uniform, a calibration point of

corresponding $h(x,y)$ and $\Delta I(x,y)$ can be obtained.

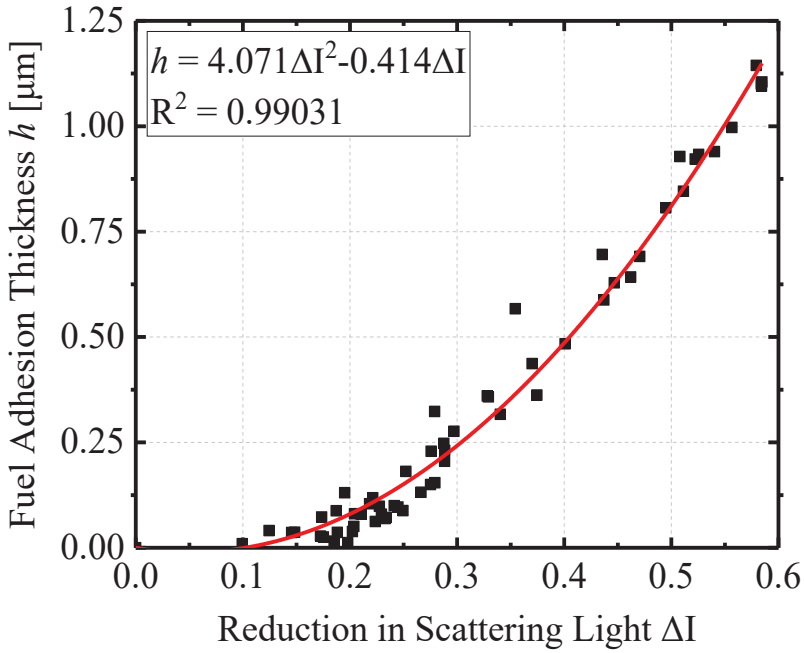

Figure 6.3 Calibration curve for RIM measurement.

Multiple calibration points can be obtained by Equation (6.2) by changing the volume of the fuel mixtures from 0.1 to 10 ml. A quadratic polynomial fitting was performed on the calibration points data, and then a fitting curve was constructed shown in Figure 6.3. The functional relationship between the change in transmittance and the fuel adhesion thickness can be described by Equation (6.3).

$$h(x,y) = 4.071\Delta I(x,y)^2 - 0.414\Delta I(x,y) \tag{6.3}$$

In Figure 6.3, the horizontal axis represents the reduction in the value of scattered light $\Delta I(x,y)$, and the vertical axis represents the fuel adhesion thickness $h(x,y)$. After the calibration calculation, the fuel adhesion thickness can be measured using the RIM method.

6.4 Image Processing

In this study, parameters such as spray penetrations, average fuel adhesion thickness, fuel adhesion mass and area were used to analyze the fuel adhesion

characteristics. The results were calculated by three times under the specific experimental conditions for each group, and the average value was obtained. Figure 5 represents the image processing process, which includes the image analysis of Mie scattering and RIM experiments. The coordinates of the nozzle tip were defined as (0, 0) in the Mie scattering images, and the corresponding theoretical wall-impingement point was marked by a red cross in the RIM images.

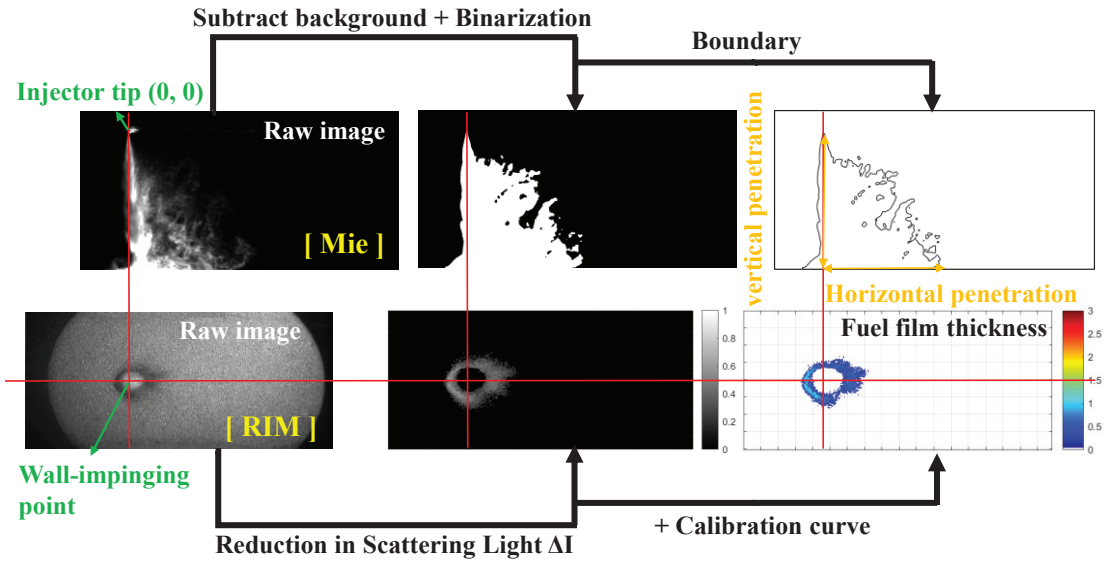

Figure 6.4 Images processing procedures.

In this study, parameters such as spray penetrations, average fuel adhesion thickness, fuel adhesion mass and area were used to analyze the fuel adhesion characteristics. The results were calculated by three times under the specific experimental conditions for each group, and the average value was obtained. Figure 6.4 represents the image processing process, which includes the image analysis of Mie scattering and RIM experiments. The coordinates of the nozzle tip were defined as (0, 0) in the Mie scattering images, and the corresponding theoretical wall-impingement point was marked by a red cross in the RIM images.

The raw image was subtracted from the background image to obtain a binarized image (threshold is set to 5%) during the image processing process of Mie scattering, and then the edge extraction of the binarized image was performed to obtain the macroscopic profile of the wall-impingement spray. Hence, the spray penetration can

be defined. The penetration was divided into vertical penetration and horizontal penetration based on the effect of cross-flow. The maximum distance of spray development along the vertical direction from the nozzle tip was defined as the vertical penetration. Meanwhile, the maximum distance from the theoretical wall-impingement point along the horizontal development was defined as the horizontal penetration.

In the image processing of the RIM experiment, the reduction of scattered light $\Delta I(x, y)$ was calculated according to the image of wet wall surface (raw image) and dry wall surface (background image) using Equation (6.1). The value of $\Delta I(x, y)$ was substituted into the calibration Equation (6.3) to calculate the fuel adhesion thickness $h(x, y)$. In addition, other fuel adhesion characteristics (area and mass) can be determined through image processing and using an internal code developed on MATLAB software.

6.5 Formation and Propagation of Fuel Adhesion

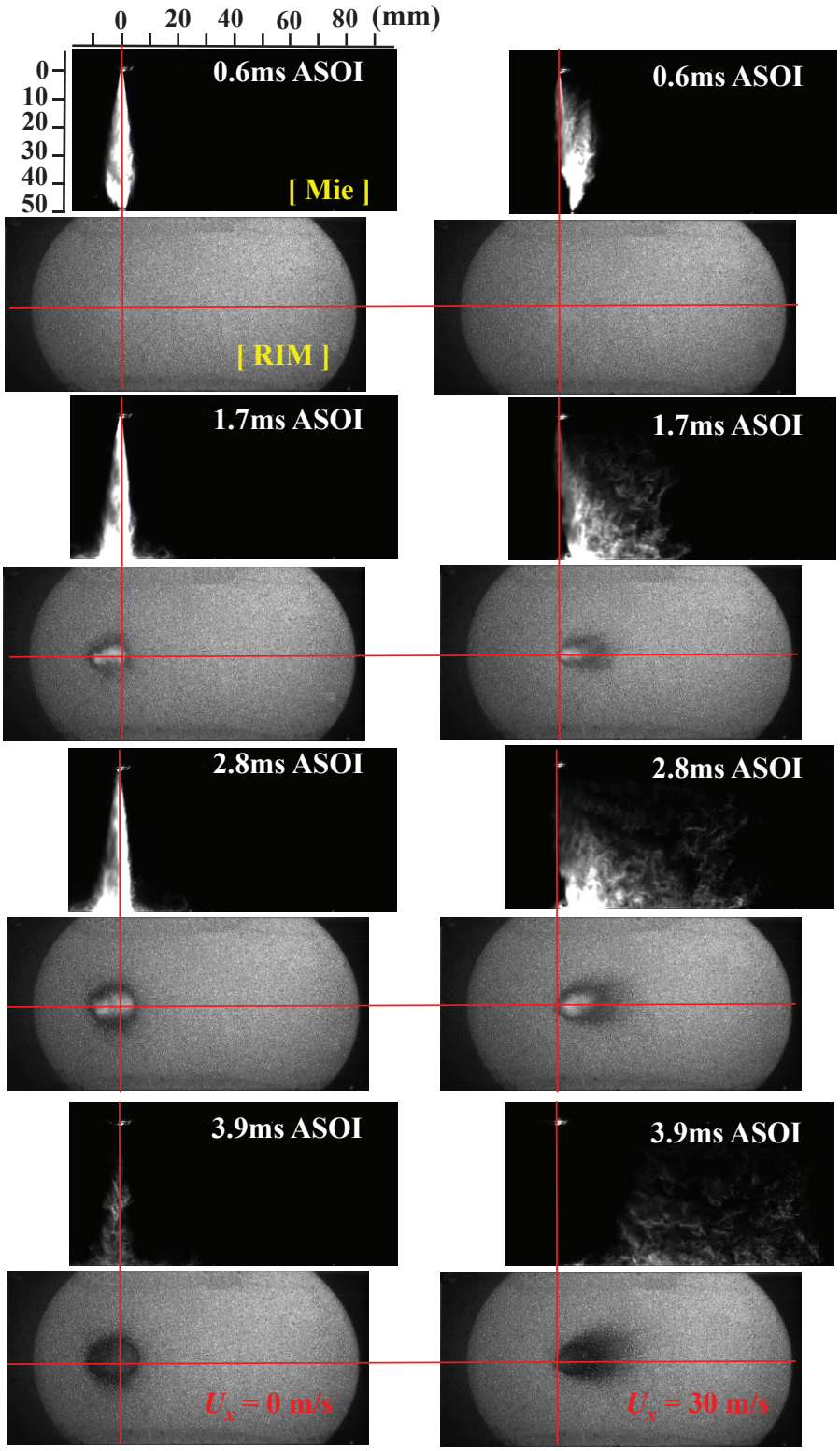

(a) Without cross-flow (b) With cross-flow

Figure 6.5 Spray impinges on flat-wall with and without the cross-flow.

Figure 6.5 (a) and (b) show the process of formation and propagation of macroscopic spray and microscopic fuel adhesion under the conditions of static flow field (U_x = 0 m/s) and cross-flow field (U_x = 10, 20, 30 m/s) before 3.9 ms ASOI. Since the installation of the injector nozzle was not accurately perpendicular to the flat-wall, the impinged fuel spray was not at the injector axis but moved towards the left slightly in the Figure 6.5 (a). It can be observed in the Figure 6.5 (a) that the spray starts impinged on the flat-wall at 0.6 ms ASOI, continuous fuel injection was observed at 1.7 ms ASOI, 2.8 ms ASOI was the end of injection (EOI), and 3.9 ms ASOI was the time after EOI. It was noted that the spray was present above the flat-wall before 3.9 ms ASOI. Since the center of the fuel adhesion exhibited a brighter area on the flat-wall during the continuous fuel supply process, it was not used for the analysis of fuel adhesion characteristics.

In the Figure 6.5 (b), it was observed from the results of Mie scattering that the cross-flow enhanced the dispersion of fuel spray. The profile of the windward side was curved, and the area of leeward side was obviously increased. Correspondingly, the RIM results demonstrated that the location of the wall-impingement point slightly shifted towards the downstream side under cross-flow conditions.

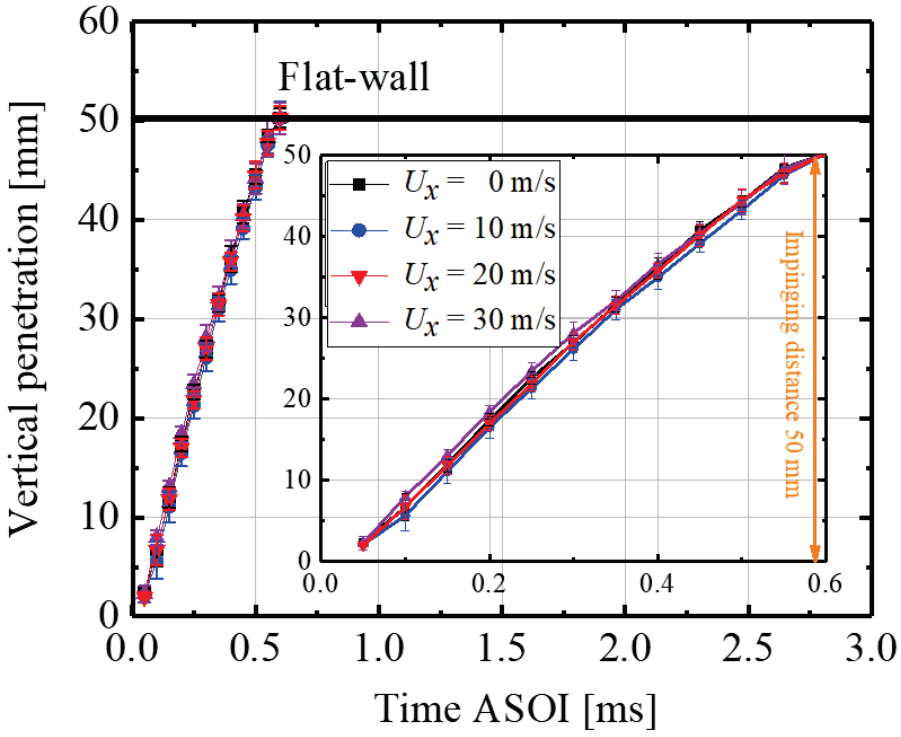

(a) Vertical penetration

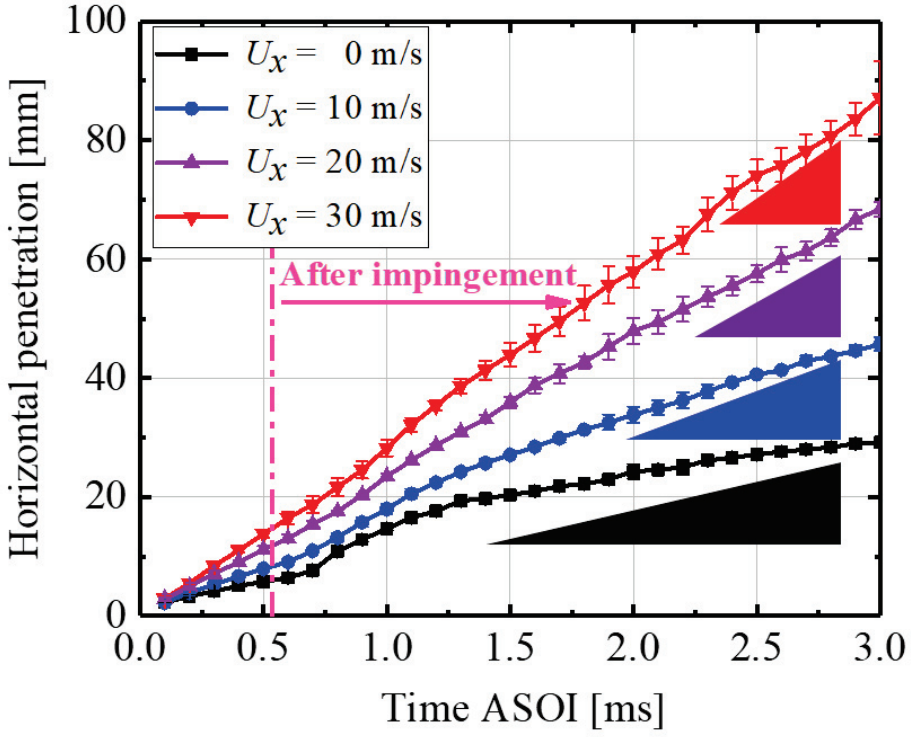

(b) Horizontal penetration

Figure 6.6 Spray penetrations.

Figure 6.6 depicts the variation in spray penetrations over time under different cross-flow velocities. Figure 6.6 (a) and (b) represent the vertical penetration and horizontal penetration, respectively. They were calculated by the definition in Figure 5. In Figure 6.6 (a), the vertical penetration was almost unaffected by the cross-flow due to the short wall-impingement distance and the large initial momentum of the spray. In addition, the maximum value of vertical penetration was 50 mm since the wall-impingement distance was set to 50 mm. The horizontal black solid line represents that the spray impinges on the flat-wall started at approximately 0.6 ms ASOI.

Therefore, the horizontal penetration after 0.6 ms ASOI was mainly discussed in Figure 6.6 (b). It was noted that the cross-flow obviously enhanced the horizontal penetration. Moreover, the increase in the horizontal penetration was approximately linear. The slope obtained after linear fitting was shown by the triangle in the Figure 6.6 (b). The increased speed of the horizontal penetration was slightly higher than the cross-flow velocity, which indicated that a few small droplets obtained the kinetic energy provided by the cross-flow were blown downstream by the cross-flow [173]. Therefore, a thin spray region was formed downstream, which was also observed in our previous research [166].

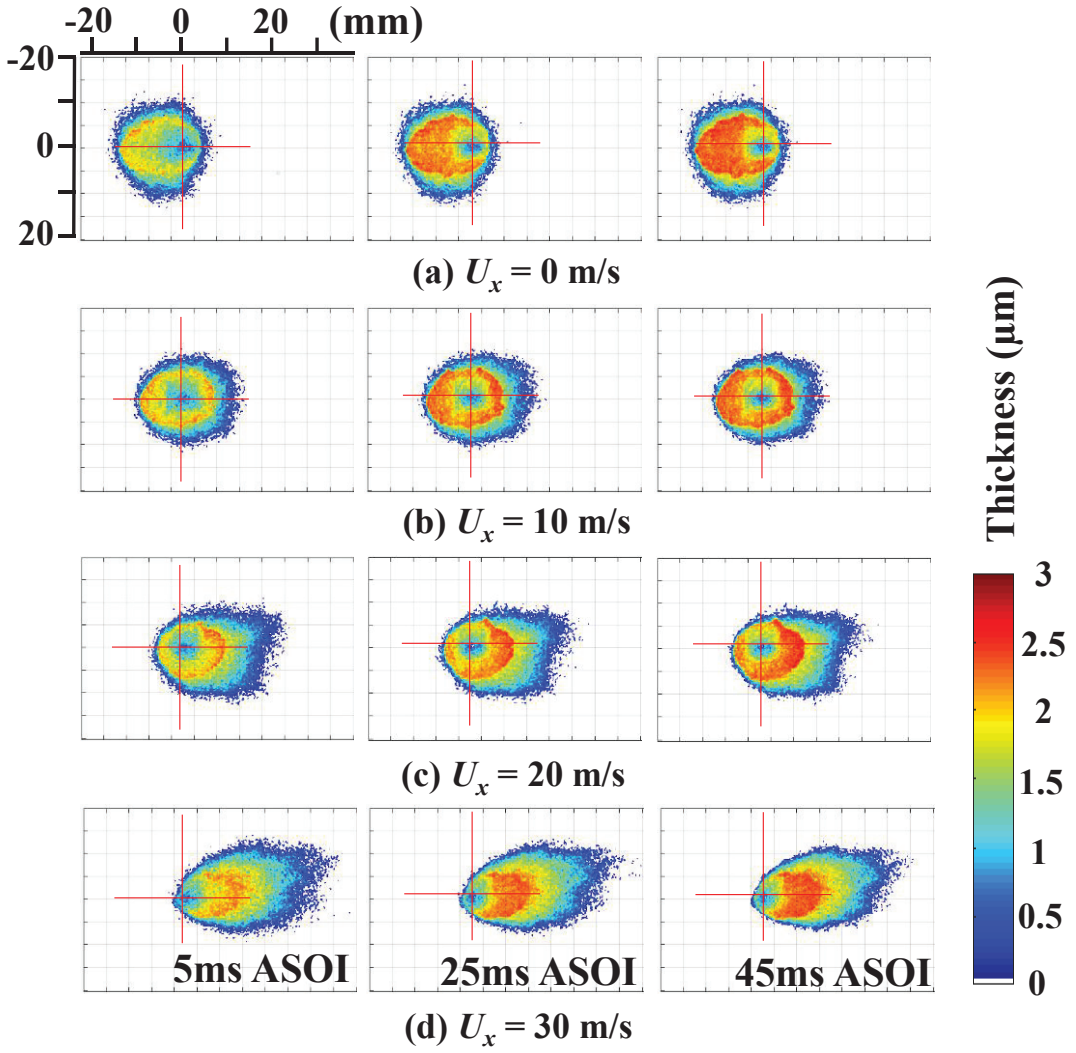

Figure 6.7 Propagation of fuel adhesion after EOI.

Figure 6.7 represents the propagation of fuel adhesion under the conditions of static flow field (U_x = 0 m/s) and cross-flow field (U_x = 10, 20, 30 m/s) after EOI. The image depicts the fuel adhesion thickness in false colors in the range of 0 ~ 3 μm. The "+" indicates the theoretical wall-impingement point. It was noted that the shape of fuel adhesion was spherical under without the cross-flow condition. However, the fuel adhesion changed into an ellipse fuel adhesion under cross-flow conditions. As mentioned in the description of Figure 6.5 (a), since the installation of the injector nozzle was not accurately perpendicular to the flat-wall, it also can be observed in the Figure 6.7 (a) that the fuel adhesion distribution was not symmetrical. Additionally, the fuel adhesion distribution was skewed towards the upper right corner in the Figure

6.7 (b), (c), and (d).

Whether there is a cross-flow effect or not, rebound, splashing and other droplet behaviors occurred due to the greater momentum of fuel droplets at the wall-impingement point of the fuel spray. This reduced the fuel adhesion thickness [169]. The fuel adhesion was thicker around the wall-impingement point, while the fuel adhesion thickness at the edges was thinnest. Meanwhile, compared to the theoretical wall-impingement point, the actual position slightly moved towards downstream side with an increase in the cross-flow velocity. In addition, the distribution area of the fuel adhesion increased with an increase in the cross-flow velocity. It can be seen that the thin fuel adhesion in the edge region slowly disappears with time from the lateral and longitudinal distance of the fuel film adhesion area, which proved that the cross-flow promoted the volatilization of the fuel adhesion at the edge region. Moreover, the lateral reach distance of the fuel adhesion is smaller than the horizontal penetration of the fuel spray as shown in Figure 6.6 (b), indicating that the fuel adhered to the flat-wall surface.

6.6 Fuel Adhesion Characteristics

After the qualitative analysis of the fuel adhesion distribution in Figure 6.7, a quantitative analysis of the fuel adhesion characteristics such as fuel adhesion area, mass, and thickness were conducted to further investigate the propagation mechanism of the fuel adhesion under the cross-flow conditions.

6.6.1 Fuel adhesion area

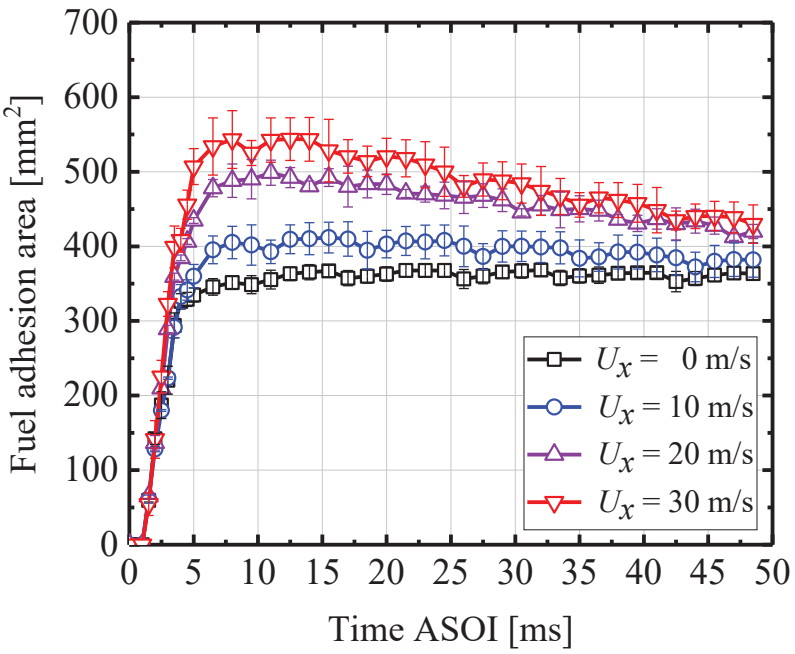

Figure 6.8 Fuel adhesion area.

Figure 6.8 depicts the fuel adhesion area under the conditions of static flow field (U_x = 0 m/s) and cross-flow field (U_x = 10, 20, 30 m/s). The results demonstrated that the fuel adhesion area rapidly increased to a maximum value within 5 ms of ASOI, which owing to the area was significantly increased during the period of continuous fuel supply and the fuel adhered to the flat-wall. This can be verified by the macroscopic spray images shown in Figure 6. The fuel adhesion area under a static flow field remained constant because the fuel adhesion almost did not evaporate at room temperature. However, the fuel adhesion area decreased over time under cross-flow conditions, which was attributed to the fuel volatilization under the effect of cross-flow. It can be observed from the fuel adhesion distribution in Figure 8 that the thin fuel adhesion of edge region slowly disappeared over time under cross-flow conditions. In addition, the cross-flow velocity had a significant effect on the change in the fuel adhesion area. The peak value of fuel adhesion area increased with an increase in the cross-flow velocity, which indicated that the cross-flow enhanced the

spread of the fuel adhesion. Meanwhile, the rate at which the fuel adhesion area decreased was proportional to the cross-flow velocity, which indicated that a stronger cross-flow can decrease the lifetime of fuel adhesion.

6.6.2 Fuel adhesion mass

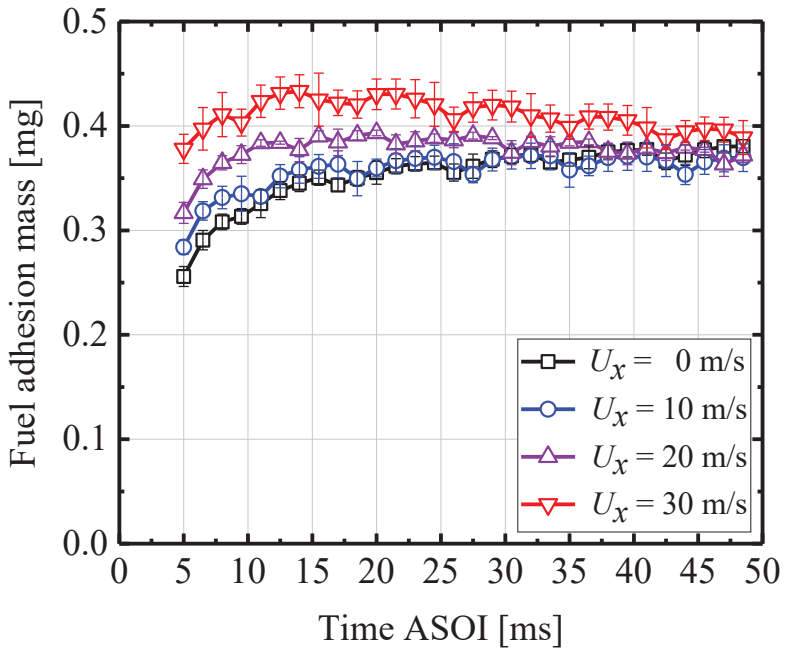

Figure 6.9 Fuel adhesion mass.

Figure 6.9 depicts the fuel adhesion mass under the conditions of static flow field (U_x = 0 m/s) and cross-flow field (U_x = 10, 20, 30 m/s). As represented in Figure 6, since the center of the fuel adhesion exhibited a bright area during the continuous fuel supply process, the analysis of the fuel adhesion mass and thickness will be affected in this stage. Therefore, the data during the initial 5 ms ASOI was neglected here. The results demonstrated that the fuel adhesion mass adhered to the flat-wall initially increased, and droplets entrained by the cross-flow impinged on the flat-wall. However, the fuel adhesion mass significantly decreased with time under cross-flow conditions. This was because the cross-flow increased the fuel adhesion area, which increased the surface area of heat exchange [174]. Therefore, the cross-flow promotes the volatilization of the fuel adhesion, and then the fuel adhesion mass should be

reduced.

6.6.3 Fuel adhesion thickness and maximum thickness

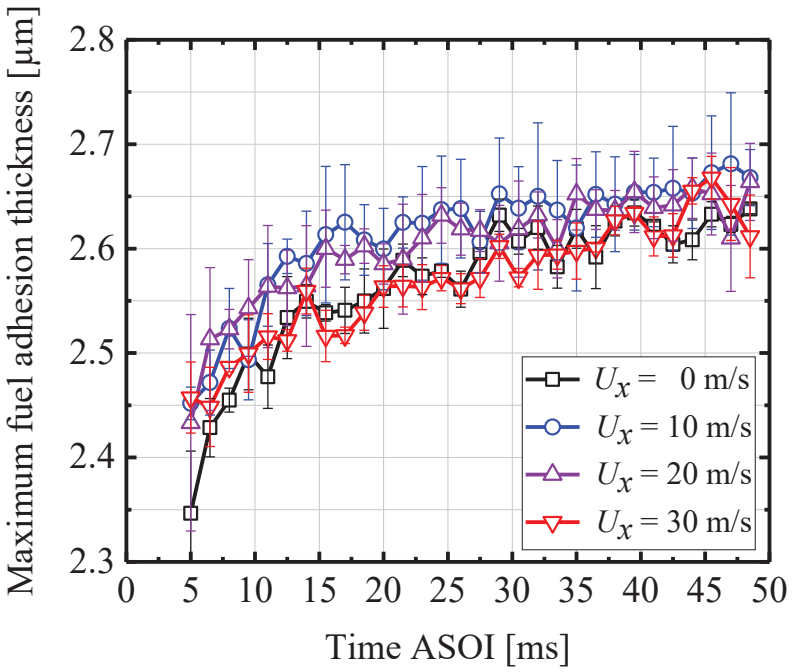

a) Maximum fuel adhesion thickness

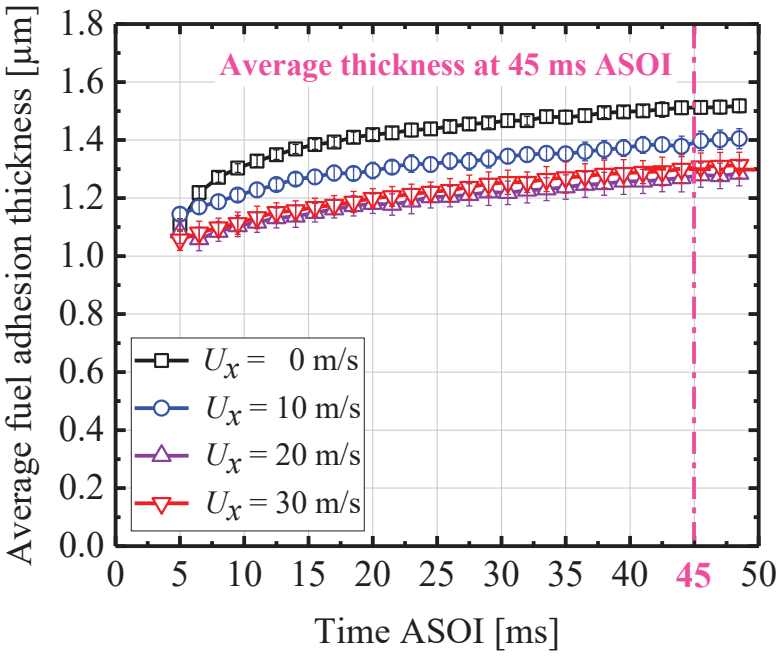

b) Average fuel adhesion thickness

Figure 6.10 Fuel adhesion thickness.

Figure 6.10 depicts the change in the fuel adhesion thickness with respect to time. Figure 6.10 (a) represents the maximum fuel adhesion thickness on the flat-wall. The maximum fuel adhesion thickness increased with time due to the redeposition of droplets. This phenomenon can be observed in Figure 6.7. However, the results demonstrated that there was no exact relationship between the cross-flow and maximum fuel adhesion thickness, although the cross-flow can promote the reduction of the fuel adhesion area and mass. The maximum thickness values under different cross -flow velocities were similar and in the range of 2.4 ~ 2.7 μm.

Figure 6.10 (b) depicts the average fuel adhesion thickness with respect to time. The change in the average thickness with time was similar to that of change in the maximum fuel adhesion thickness, which significantly increased with time. However, the increase rate is decreased over time. The average fuel adhesion thickness obviously decreased under the cross-flow conditions. The results demonstrated that the average fuel adhesion thickness was 1.5 μm at 45 ms ASOI under static flow field conditions. The average fuel adhesion thickness at a velocity of 10 m/s was 1.4 μm. A further increase in the cross-flow velocities resulted in the average fuel adhesion thickness of 1.3 μm under the cross-flow velocities of 20 and 30 m/s.

Figure 6.11 depicts the variation in the fuel adhesion mass distribution with respect to thickness at 5, 25 and 45 ms ASOI. Equation (6.4) was used to calculate the fuel adhesion mass, which is determined by the values of each pixel calculated from the equation below:

$$M(h) = \sum_{i=0}^{\infty} h(i) \tag{6.4}$$

Where $M(h)$ is the sum of fuel adhesion mass in the thickness fraction between $h(i) \pm 0.5\Delta h$ and h, and Δh is 0.1 μm. The condition of static flow field in Figure 6.11 (a) and the cross-flow conditions in Figure 6.11 (b), (c), and (d) represent that the fuel adhesion mass exhibited one large peak value along the thickness, which indicated that the fuel adhesion mass was concentrated on the thicker thickness. In addition, the large peak value significantly increased with time. Considering the

overall distribution, the distribution curve moved toward the right side, which indicated that the thicker fuel adhesion thickness increased. However, it was noted that a stronger cross-flow decreased the fuel adhesion mass, suggesting that the cross-flow promoted the volatilization of the fuel adhesion.

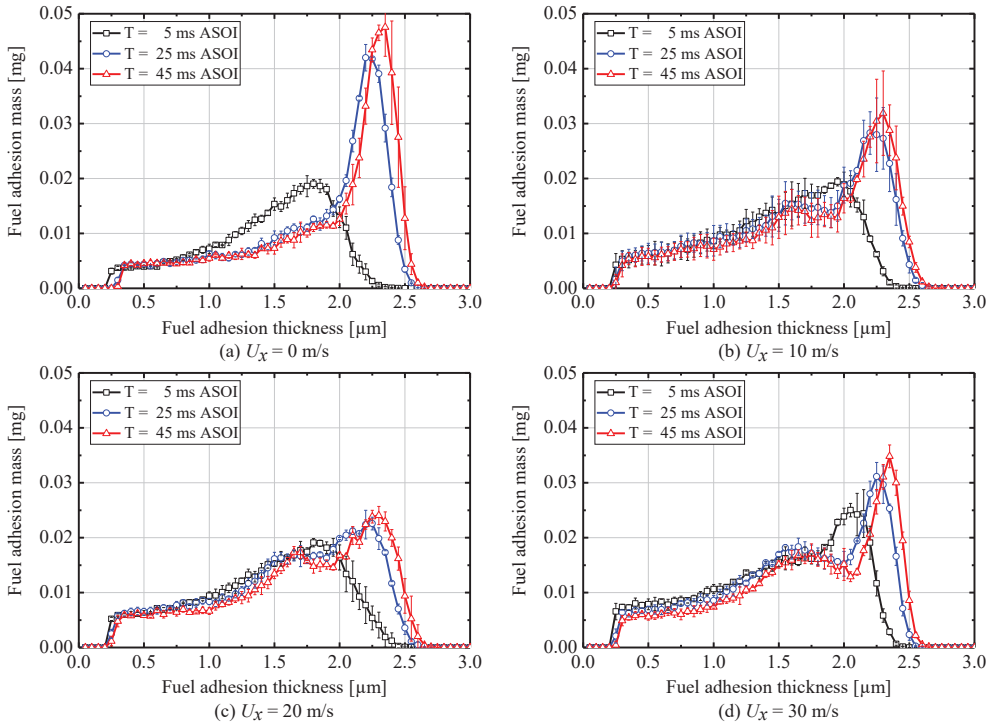

Figure 6.11 Fuel adhesion mass distribution along thickness under different cross-flow condition.

6.6.4 Fuel adhesion mechanism under cross-flow conditions

To better understand and explain the uniformity of fuel adhesion, the probability density function (PDF) of fuel adhesion thickness was calculated. An appropriate minimum interval was set to ensure a reasonable statistical distribution. The distribution interval was set as 0.05 μm, which was based on the thickness value of each pixel.

Figure 6.12 depicts the PDF of fuel adhesion thickness at 5, 25, and 45 ms ASOI. Regardless of static flow field or the cross-flow conditions, the results demonstrated

that the fuel adhesion thickness was concentrated on the thicker thickness value and thinner layer, simultaneously. Two distinct peaks can be observed in the distribution of fuel adhesion thickness. Moreover, the thickness of thinner fuel adhesion decreased, whereas the thickness of thicker layer increased with time. In addition, the fuel adhesion was concentrated in the range of 2.0 ~ 2.5 μm at 45 ms ASOI.

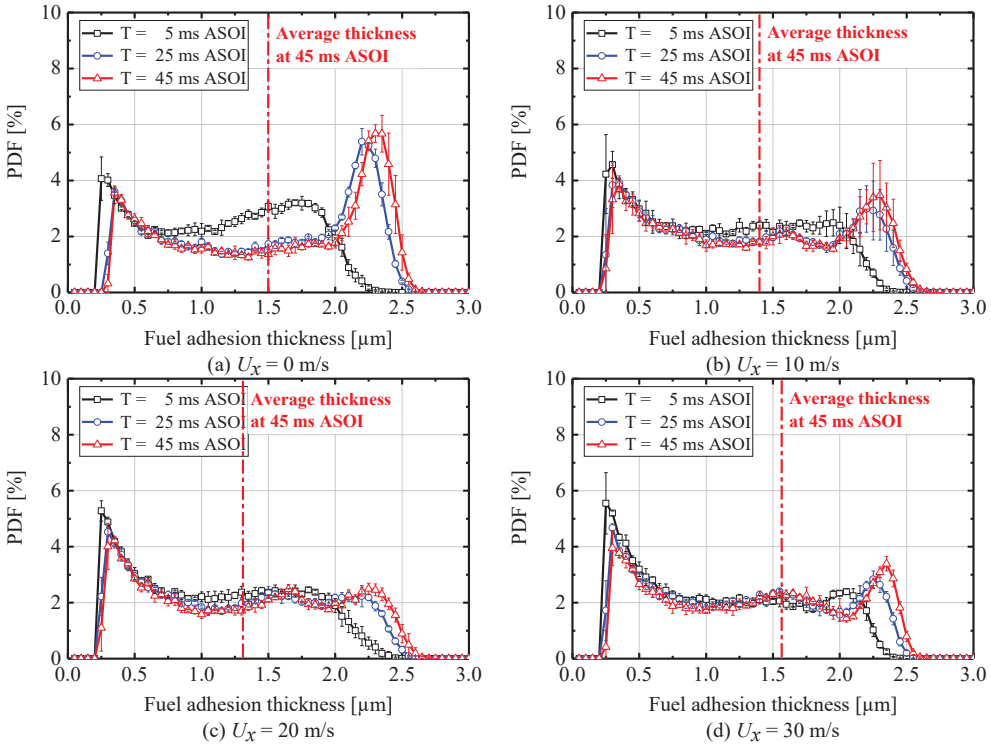

Figure 6.12 Probability of fuel adhesion along thickness.

To better understand the mechanism of the formation and the propagation of fuel adhesion under cross-flow conditions, detailed analysis was conducted as follows. It can be observed in Figure 6.12 that the fuel adhesion thickness distribution was concentrated in the thinner and thicker regions. The fuel adhesion thickness greater than that of the average fuel adhesion thickness at 45 ms ASOI was termed as the thick fuel adhesion region. Conversely, when the fuel adhesion thickness was lower than that of the average fuel adhesion thickness at 45 ms ASOI, it was termed as the thin fuel adhesion region.

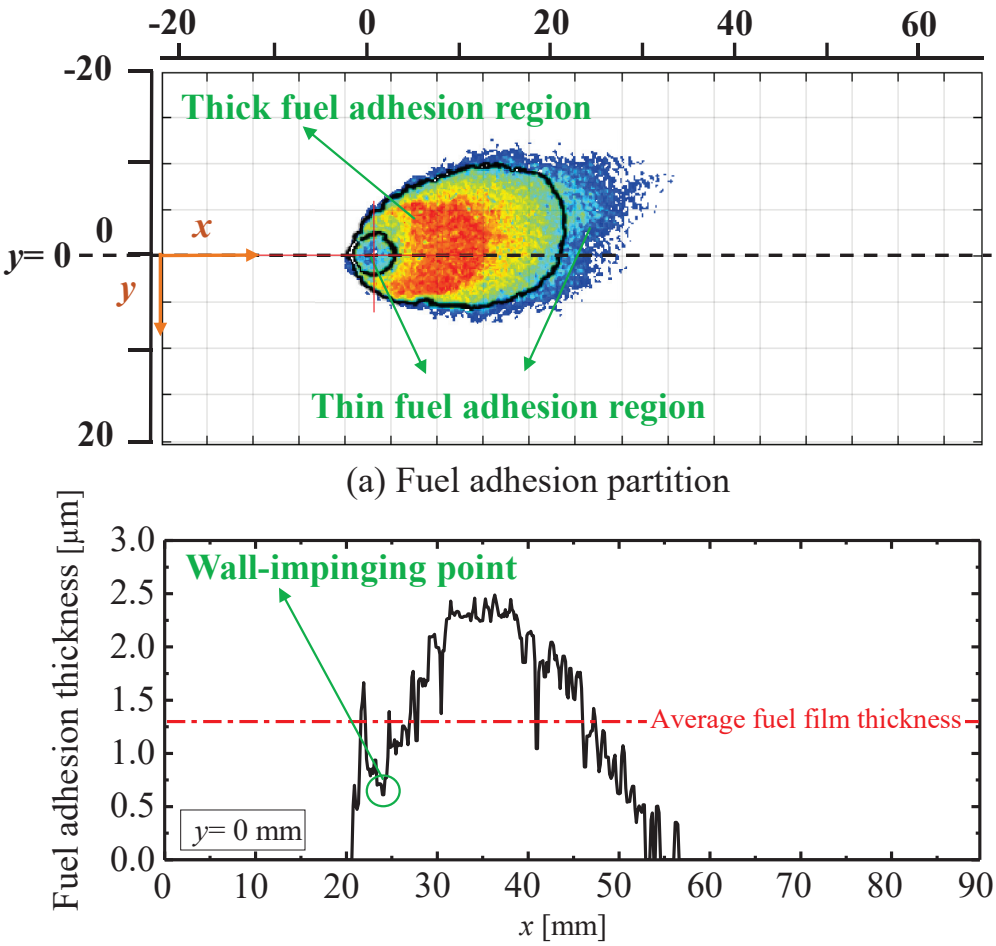

Figure 6.13 Fuel adhesion thickness distribution [U_x = 30 m/s, T = 45 ms ASOI].

Figure 6.13 (a) is a sample of the fuel adhesion distribution at 45 ms ASOI under the cross-flow velocity of 30 m/s. It can be observed from the fuel adhesion thickness distribution in Figure 6.13 (a) that the fuel adhesion around the wall-impingement point was relatively thin. The fuel adhesion was thicker when it spread outside the wall-impingement point, and the fuel adhesion at the edge region was the thinnest. Therefore, the fuel adhesion was divided into two regions after the spray impinged on the flat-wall according to the difference in thickness as mentioned above. The wall-impingement point and the edge region are present in the thin fuel adhesion region. In addition, the distribution law of the fuel adhesion thickness was extracted at the position of the central axis y = 0 in Figure 6.13 (b). The fuel adhesion thickness was quite small at the wall-impingement point in Figure 6.13 (b). Similar conclusion had

also been indicated in Figure 6.5.

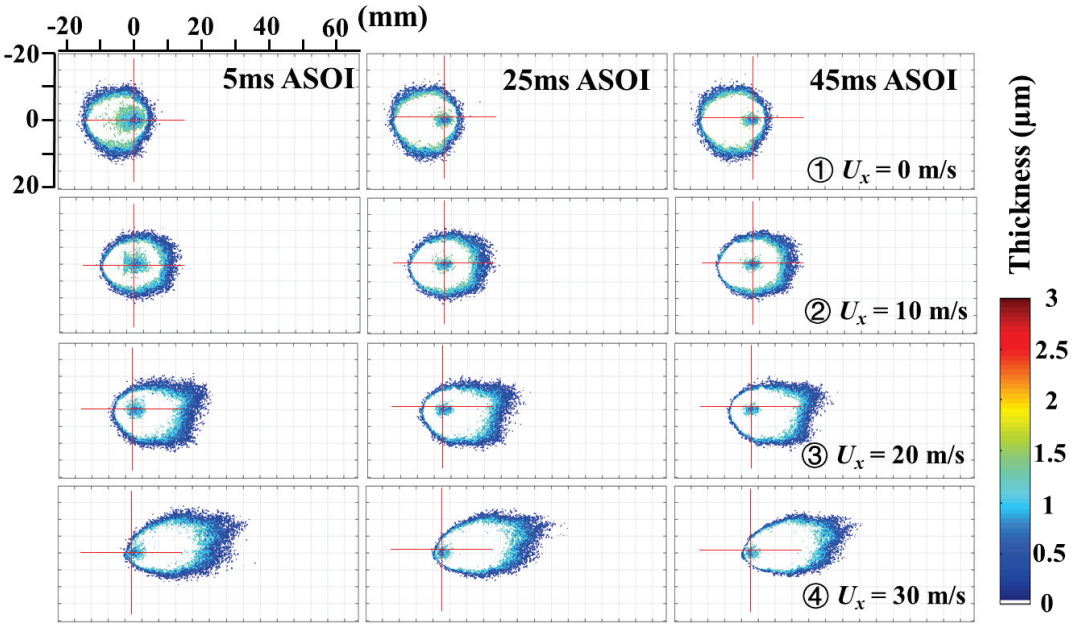

(a)

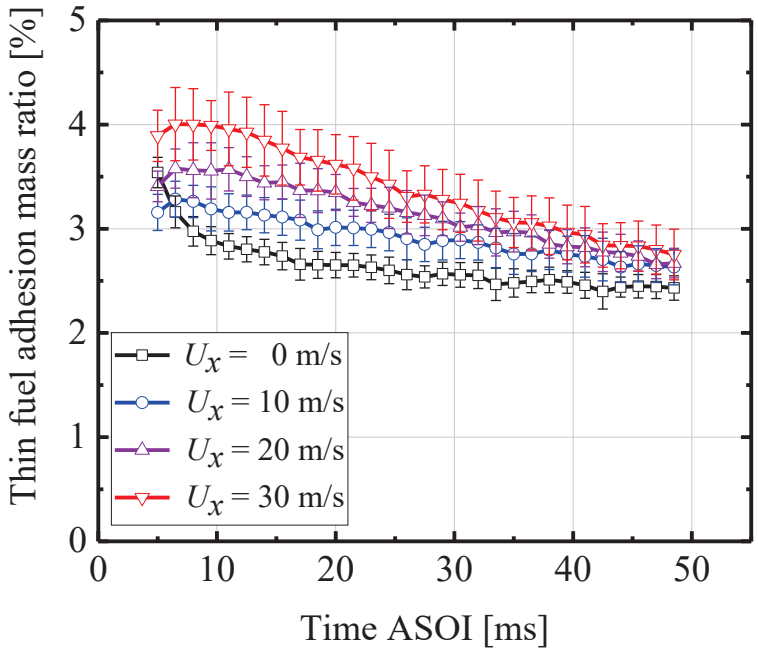

(b)

Figure 6.14 Thin fuel adhesion ratio.

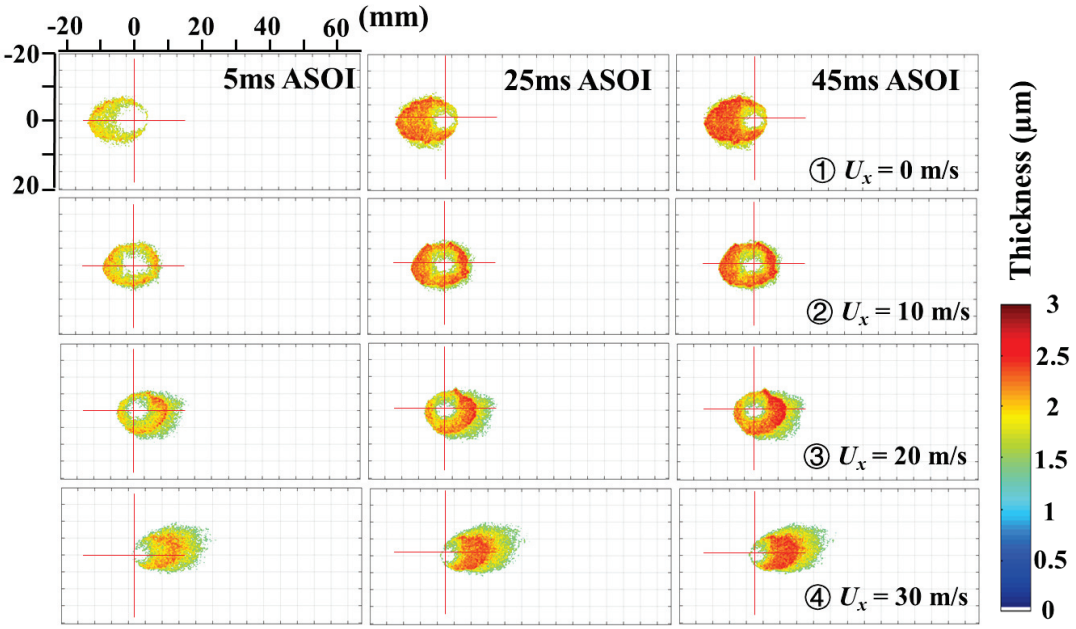

(a)

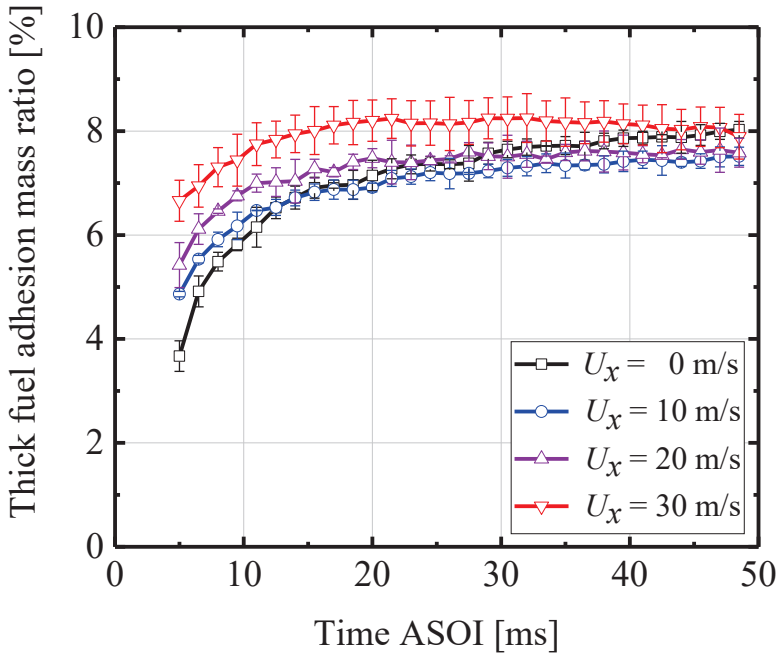

(b)

Figure 6.15 Thick fuel adhesion ratio.

Figure 6.14 and Figure 6.15 represent the variation in the fuel adhesion mass ratio over time in the thin and the thick fuel adhesion region, respectively. The propagation images of fuel adhesion in these two regions can be observed in the PPT of Supplement. The results demonstrated that the thinner fuel adhesion mass ratio

decreased, whereas the thicker region increased with time. The first reason might be that the thin fuel adhesion was converted into a thicker fuel adhesion during the process of continuous impingement of droplets on the flat-wall. The second reason might be that the thin fuel adhesion was volatilized. In addition, the fuel adhesion mass ratio increased with an increase in the cross-flow velocity at the beginning.

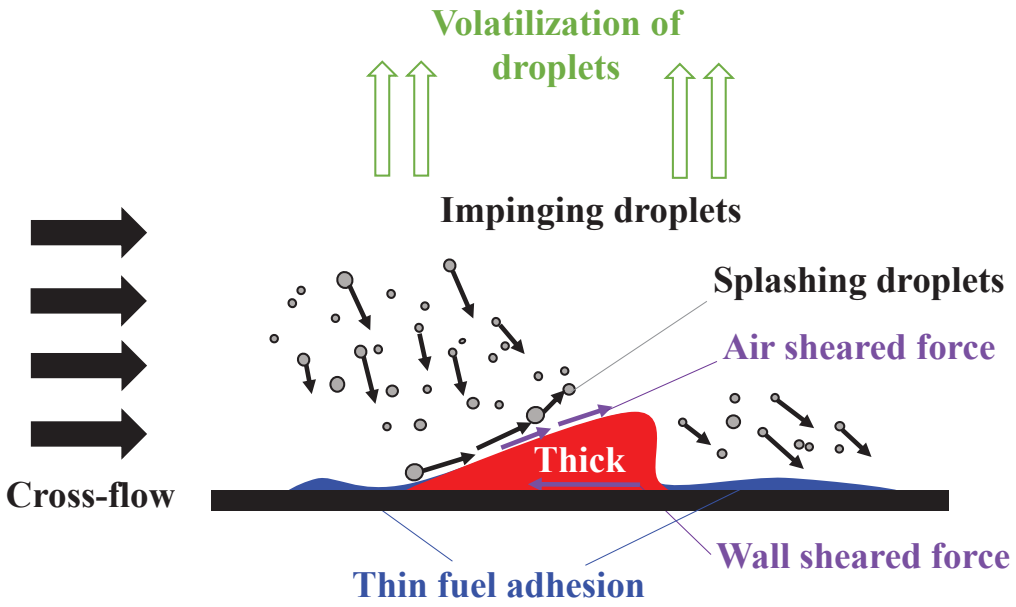

Figure 6.16 Fuel adhesion mechanism under cross-flow conditions after EOI.

Figure 6.16 depicts the fuel adhesion mechanism AEOI under cross-flow conditions. As mentioned above, the formation mechanisms of thin fuel adhesion region and thick region were different. There are two reasons for the formation of a thick fuel adhesion region. First, the effect of wall and air shear force on the fuel adhesion surface which resulted in the aggregation of fuel adhesion into a thick fuel adhesion region [175]. Second, the interaction between the cross-flow and the spray caused the droplets to continuously impinge on the flat-wall. When the fuel adhesion thickness in the thin fuel adhesion region was larger than that of the average fuel adhesion thickness, it can convert into a thick fuel adhesion region.

Additionally, there are two reasons for the formation of thin fuel adhesion region. The first reason is that cross-flow can promote the volatilization of the fuel adhesion,

and the thick fuel adhesion region was converted into a thin fuel adhesion region when the fuel adhesion thickness was less than that of the average value. Second, a few droplets fell on the flat-wall due to the interaction between the cross-flow and spray, which increased the thin fuel adhesion mass ratio. However, while the thick fuel adhesion volatilizes, the thin fuel adhesion should also volatilize. The results indicated that the thin fuel adhesion mass adhered to the flat-wall increased. Therefore, the analysis demonstrated that the main reason should be some small droplets entrained by cross-flow impinging on the wall.

6.7 Summary

The fuel adhesion characteristics have a significant effect on the formation of the mixture, combustion performance, and emission of pollutants. Therefore, the effect of cross-flow on the fuel adhesion characteristics after the spray impinging on the flat-wall was mainly investigated using the RIM method in this work. The main conclusions can be summarized as follows.

(1) The RIM results demonstrated that the cross-flow enhanced the fuel adhesion dispersion downstream, which exhibited an ellipse propagation. In addition, the fuel adhesion at the edge region was the thinnest.

(2) The fuel adhesion area gradually decreased under the cross-flow conditions and remained constant without cross-flow, which can be attributed to the enhancement of volatilization of the fuel adhesion under cross-flow. In addition, it was predicted that a strong cross-flow can decrease the lifetime of fuel adhesion.

(3) The fuel adhesion mass dramatically decreased with time under cross-flow conditions. The increase in fuel adhesion area enhanced the heat exchange area, then the cross-flow promoted the volatilization of the fuel adhesion. Meanwhile, the rate at which the fuel adhesion mass decreased was proportional to the cross-flow velocity.

(4) The average fuel adhesion thickness increased with time. However, the increase rate was decreased over time. The average fuel adhesion thickness obviously

decreased under the cross-flow conditions. Additionally, the thickness of the thinner fuel adhesion region decreased, whereas the thickness of the thicker region increased with time.

(5) The wall and air shear forces on the fuel adhesion surface aggregated the fuel adhesion into a thick fuel adhesion region. The main reason for the formation of thin fuel adhesion region was due to the impingement of a few droplets on the flat-wall entrained by cross-flow. In addition, the thin and thick fuel adhesion regions can transform into each other.

CHAPTER 7 NUMERICAL SIMULATION OF WALL-IMPINGEMENT SPRAY UNDER CROSS-FLOW CONDITIONS

7.1 Introduction

In the previous Chapters, we have discussed the free spray characteristics, wall-impingement spray characteristics, and fuel adhesion characteristics under cross-flow conditions by experimental method. In this Chapter, we would like to combine the numerical simulation method into this research. The 3D model are created and the simulation model are validated by experimental results. We mainly researched on the effect of cross-flow on the fuel adhesion characteristics of wall-impinging spray in the early stage (almost during the fuel injection stage) here, which is difficult to research through the experimental method. Then the droplets size and velocity distribution and the fuel adhesion characteristics are discussed. The realization of this CFD simulation process can be used to study more spray and fuel adhesion characteristics in the cross-flow flow field in the future.

7.2 Basic Equations and Simulation Conditions

7.2.1 Basic equations

The fuel breakup is characterized by two processes: primary breakup and secondary breakup. The primary breakup occurs near the nozzle region with a high Weber number. The secondary breakup generally occurs in the spray outside region, where the effects of air motion are enhanced. Spray modeling involves multiphase flow issues that must simultaneously resolve the conservation equations of the vapor and liquid phases. There are numerous models for atomization processes such as momentum interaction between droplets and gas, turbulent dispersion, evaporation, secondary breakup, and impingement, etc. The typical models include TAB model

[176], GM model, WAVE model [177], KH-RT model [178], Huh-Gosman model [179], and LISA model [180].

The TAB model analyzes droplet vibration and deformation using the analogy of the spring-mass system. Based on this theory, droplet deformation correlations are constructed, and the breakup types are adjusted by the deformations. This model is appropriate for situations with a low Weber number. Reitz and Diwakar (1987) proposed the GM model, which divides spray droplet breakup into two types: bag breakup and stripping breakup. This model is based on a single droplet breakup, which has the benefit of simplifying the application. However, it cannot represent the effects of the flow inside the nozzle on droplet breakup.

Recently, the unstable surface wave theory has been recognized as an important method for investigating droplet breakup and has been widely used in the development of internal combustion engine models. It indicates that increasing the Kelvin-Helmholtz (KH) unstable waves results in droplets being stripped from the liquid column; this model is appropriate for conditions of high relative velocity and high ambient gas density. The disturbance is included in the KH-RT model, which is an improvement over the WAVE model. The LISA model depicts the occurrence of KH unstable waves on the surface of a liquid film. This model includes cavitation effects.

The fuel spray was analyzed in this Chapter using the Lagrangian spray module, which simultaneously solves the conservation equations of the liquid and vapor phases. In the liquid phase simulation using a statistical discrete droplet method, a parcel represents a group of droplets with identical properties [181]. To describe spray vapor, a source item of an additional transport equation for the vapor void fraction in Eulerian formulation was used.

The mass, momentum, and energy conservation equations for multiphase flows are shown in Equations (7.1), (7.2) and (7.3), respectively.

$$\frac{D\rho}{Dt} + \rho\frac{\partial u_i}{\partial x_i} = 0 \tag{7.1}$$

$$\rho\frac{Du_j}{Dt} = \rho\left(\frac{\partial u_j}{\partial t} + u_i\frac{\partial u_j}{\partial t}\right) = -\frac{\partial P}{\partial x_j} + u_i\frac{\partial \tau_{ij}}{\partial x_i} + f_j \tag{7.2}$$

$$\rho\frac{De}{Dt} = \nabla\cdot(\lambda_h\nabla T) - P(\nabla\cdot\vec{u}) + \mu\varphi + \frac{\dot{Q}_s}{dx_1dx_2dx_3} \tag{7.3}$$

where, x_i and x_j are the coordinates in the different directions (m); u_i and u_j are the velocity components in the different axis (m/s); τ_{ij} is stress tensor (N); f_j is the body force (N); e is internal energy (J); λ_h is heat conductivity (w/(m·K)); T is temperature (K); μ is dynamic viscosity (Pa·s); φ is dissipation function; and $\dot{Q}_s$ is heat flux (J). Equation 7.1 is the continuity equation, Equation 7.2 shows the conservation of momentum, and Equation 7.3 describes the conservation of energy.

In this study, the basic RANS governing equations were used to reduce calculation time and simplify the processing. The standard k-ε model was chosen to describe the turbulent kinetic energy and its rate of dissipation [182].

7.2.2 Sub-Models' selection and simulation conditions

In the simulation, a computational domain 200*100*50 mm^3 with the impingement distance of 50 mm was used as shown in Figure 7.1. The left and right sections of this 3D computational domain were set as the inlet and outlet of the cross-flow flow field. In addition, the nozzle was provided at the upper surface of observation chamber.

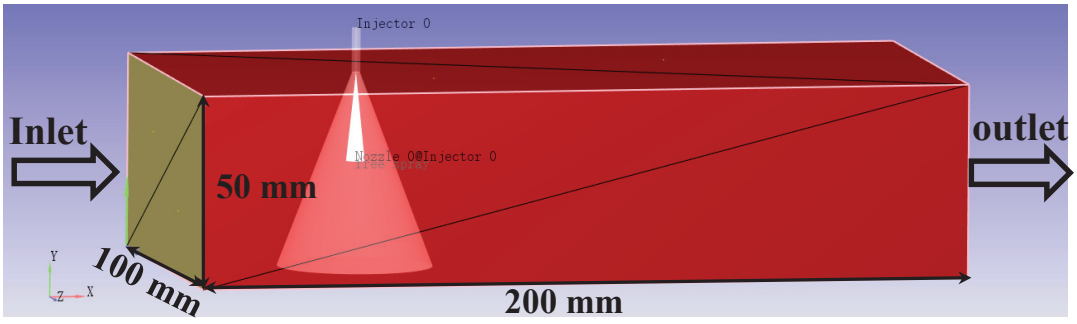

Figure 7.1 Computational domain for impingement spray simulation.

Adaptive mesh refinement (AMR) is a function specific in the Converge

software. As shown in Figure 7.2, the initial mesh is set to 4*4 mm in this calculation, the fixed encryption is level 4, and the adaptive encryption level is level 5, which means the minimum mesh size is 0.125*0.125 mm. The figure shows the meshing of the flat-wall and the vertical center section of spray.

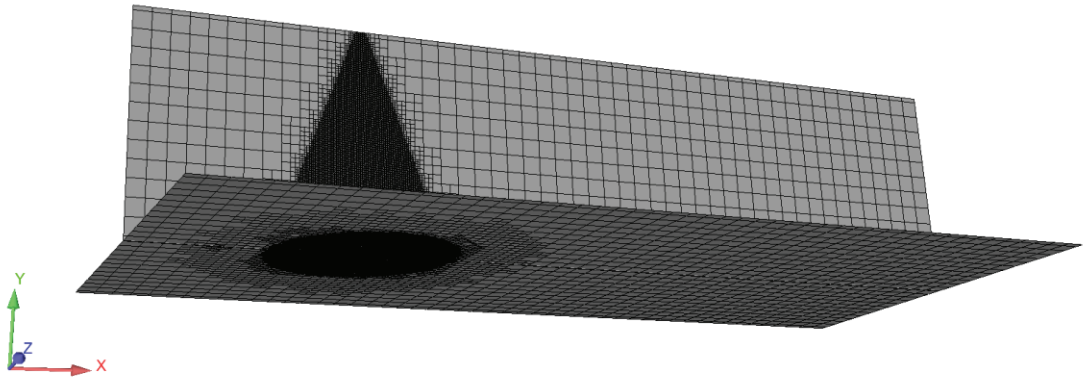

Figure 7.2 AMR meshing.

In this part, some important sub-models were selected in the numerical simulation of spray, such as the sub-models of the spray breakup, evaporation, and wall interaction, etc. The disturbance is included in the KH-RT model, which is an improvement over the WAVE model. Because cross-flow is an important issue in this study, the effects of cross-flow on the spray should be considered in the simulations. Even if under the room temperature, the evaporation should be considered since of the test fuel was toluene. Therefore, the Frossling model was selected as the evaporation model. This simulation focused on observing the effects of the cross-flow on the wall-impingement spray. The impingement issue is important in this work, so the wall-film model was employed, and the Kuhnke film splash model was considered. Some critical parameters setting of sub-models was also shown in the Table 7.1.

Table 7.1 Parameters selection of the main sub-models.

Process	Model	Description of coefficients	Typical value	Selected value
Spray breakup	KH	Model size, B_0	0.61	0.61
		Model breakup time, B_1	5.0-100.0	7
	RT	Model breakup time, C_t	0.1-1.0	1.0
		Model breakup length, C_{bl}	0.0-50.0	1.0
Wall-interaction	Wall-film	Critical value for splashing, E_{crit}^2	3330.0	3330.0
		Fraction splashed, f_{flash}	0.5-1.0	1.0
		Rebound Weber number, We_r	0.0-100.0	5.0

In addition, the detailed simulation conditions were shown in the Table 7.2, which kept consistent with the experimental conditions. It was noted that for keeping the injection pressure at 10 MPa, the injection mass was different value in the simulation. In addition, there is no way to simulate the internal structure of the nozzle in the simulation, which indicates that the spray profile and penetration obtained in the simulation cannot be completely consistent with the experimental results.

Table 7.2 Simulation conditions.

Parameters	Experiment	CFD
Nozzle	Single Hole	Single Hole
Nozzle Hole Diameter [mm]	0.15	0.15
Fuel	Toluene	Toluene
Injection Pressure P_{inj} [MPa]	10	10
Injection Duration d_t [ms]	3	3
Injection Mass [mg]	3.64	5.021
Ambient Pressure P_a [MPa]	0.1	0.1
Ambient Temperature [K]	300	300
Wall Temperature [K]	300	300
Cross-flow Velocity U_x [m/s]	0, 10, 20, 30	0, 10, 20, 30

7.3 Model Validation

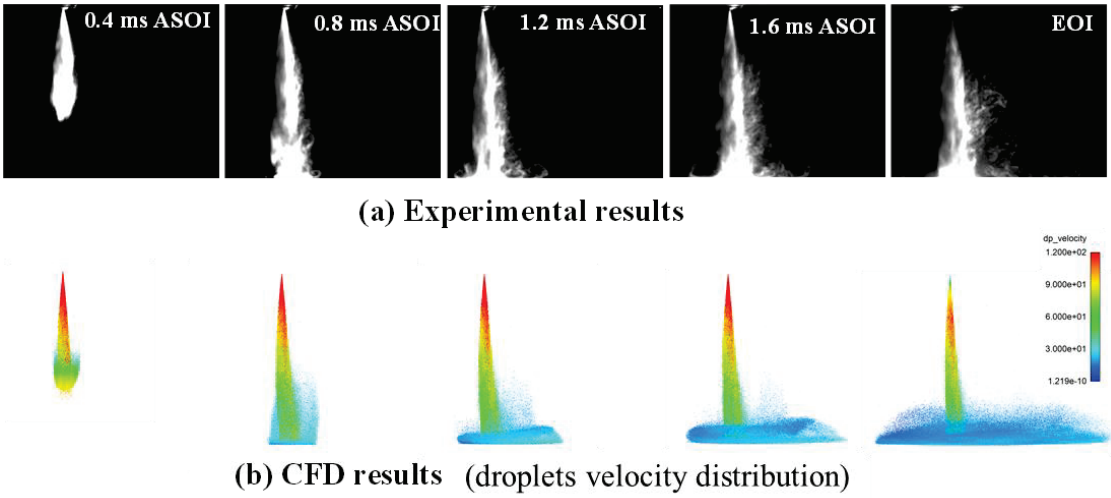

Figure 7.3 Computational Comparisons of the impingement spray evolutions (U_x= 10 m/s, P_{ing}= 10 MPa, P_a= 0.1 MPa).

Figure 7.3 shows the comparation of calculated wall-impinging spray propagation with the experimental results, which show good agreement. The tiny droplets moved downstream of the cross-flow flow field to form a dilution spray

region. In addition, the distribution of droplet velocity is also shown in this Figure. It can be found that the droplets velocity is relatively large along the central axis of the spray and near the nozzle region. In addition, the droplet velocity distribution along the flat-wall is quite small.

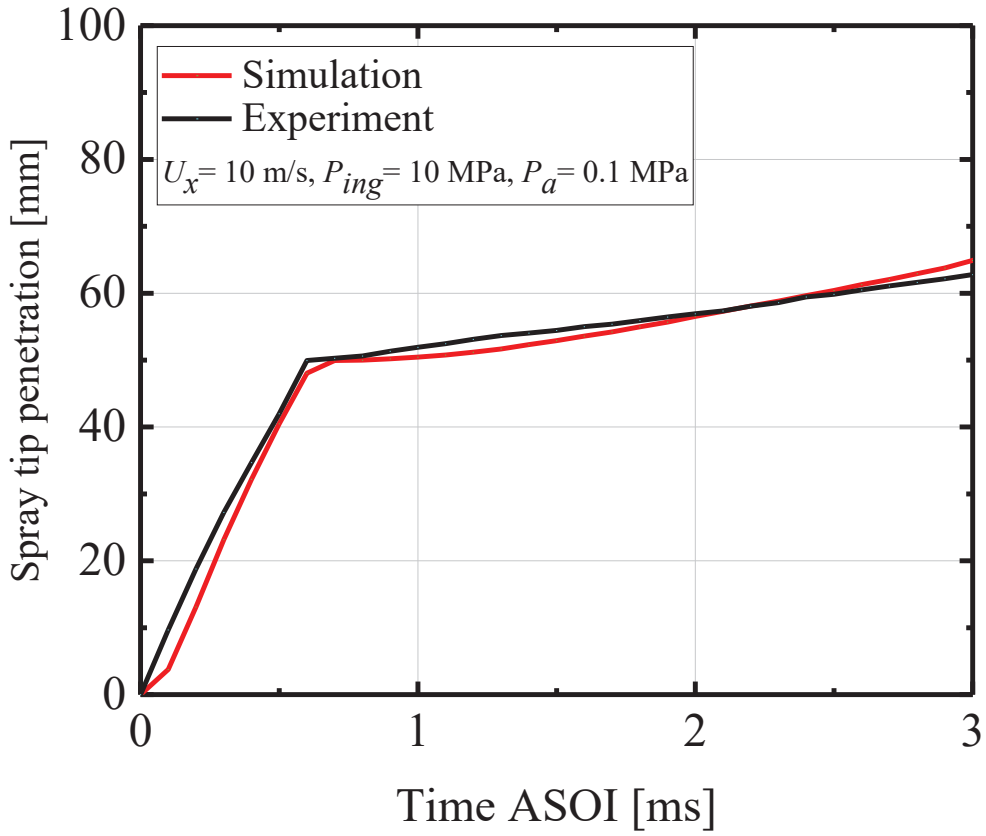

Figure 7.4 Comparative verification of spray tip penetration obtained from simulation and experiments until EOI.

Penetration is an important parameter for the research of spray characteristics. After qualitatively comparing the spray profiles in the cross-flow flow field, we made a quantitative comparison between the spray penetration obtained by experiment and simulation under a certain boundary condition. Figure 7.4 shows that at the cross-flow velocity of 10 m/s, the simulation and experimental penetration development were in a good agreement. Two stages of penetration development can be clearly observed, with both experimental and simulation impinging the flat-wall at the same time of

0.65 ms ASOI. After the spray impinging on the flat-wall, the development speed of spray penetration was significantly inhibited. After completing the model validation, we investigated the fuel adhesion characteristics under different cross-flow velocities. The simulation computation time is set to 5 ms ASOI, which was named the early injection stage here.

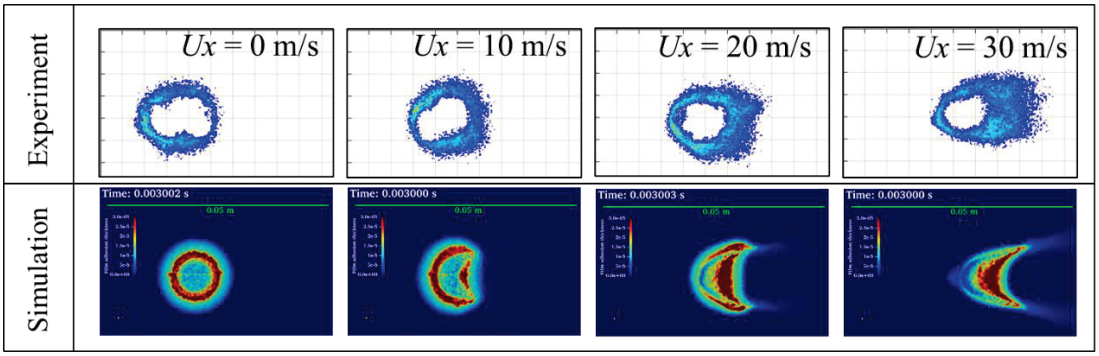

Figure 7.5 Comparison of fuel adhesion characteristics between experiment and simulation results at EOI timing.

Figures 7.5 shows the comparison of fuel adhesion characteristics between experiment and simulation results at EOI timing. Experiment result shows that the white region is existed in the wall-impingement position because of the mie-scattering of spray in the early stage, which is influences the data analysis. Therefore, the fuel adhesion characteristics were calculated using the CFD here. Simulation results show the whole fuel adhesion distribution in the early stage. It can be seen that the effect of cross-flow on the fuel adhesion propagation area is consistent with experimental results. Fuel adhesion was accumulated downstream under cross-flow conditions. However, the fuel adhesion shape of simulation is different with experimental. The wall-film model in the cross-flow flow field should be improved more in the future.

7.4 Droplet Size Distribution

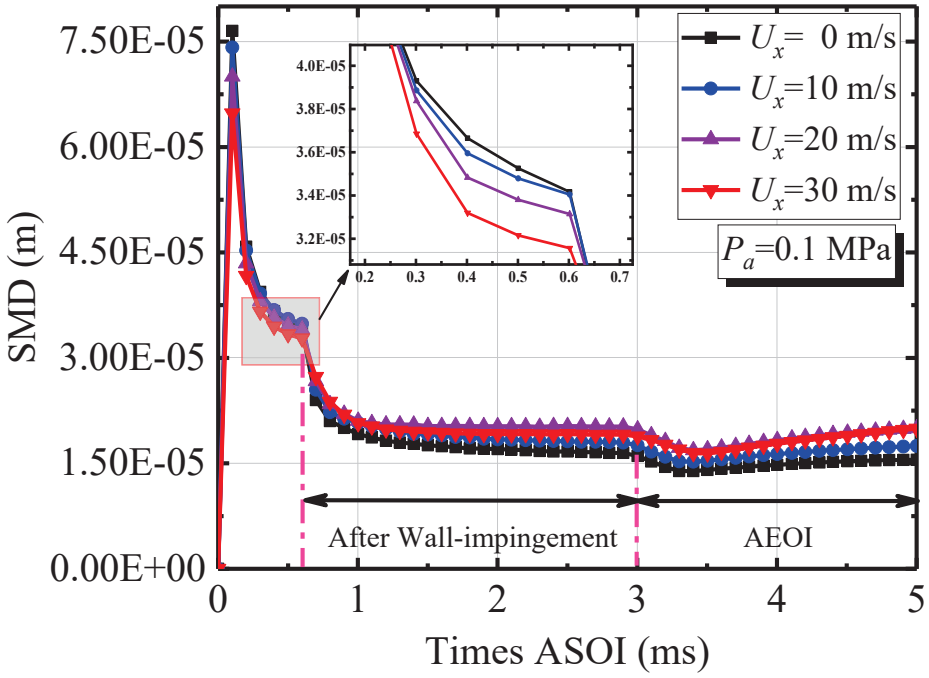

(a)

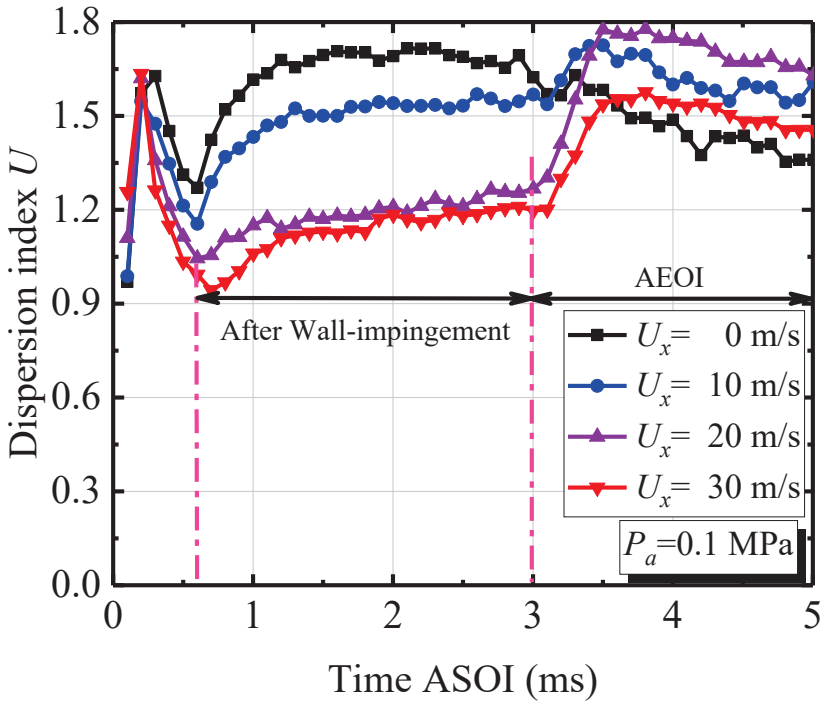

(b)

Figure 7.6 Droplets size distribution under variations cross-flow conditions.

Droplet size is one of the most important parameters on fuel atomization, which significantly affects the formation of the air-fuel mixture. Figure 7.6 shows the time evolution of the global SMD and dispersion index for different cross-flow velocities. The results show that the global SMD decreases significantly with the increase in the cross-flow velocity before impinging on the flat-wall, and the global SMD under different cross-flow velocity after impinging on the flat-wall is basically between 15~20 μm. In addition, the dispersion index of droplets was quite small under cross-flow conditions, and the similar average droplets size indicated that cross-flow promoted droplets breakup and spray atomization. Spray breakup includes two processes: primary breakup and secondary breakup. Aerodynamics have a great impact on breakup, especially in secondary breakup. The cross flow enhances aerodynamics, which improves atomization.

In addition, another important section of the simulation is the analysis of the fuel adhesion characteristics under cross-flow conditions. According to the results obtained in Chapter 6, the center region of the fuel adhesion in the continuous fuel supply process shows a bright area. Due to the limitation of RIM experimental method, it is difficult for us to obtain the fuel adhesion characteristics at this stage. Therefore, data during the initial 5 ms ASOI were ignored in the experimental results. However, the numerical simulation can be used to study the effects of different cross-flow velocities on the fuel adhesion characteristics in the early stages of injection.

7.5 Propagation of fuel adhesion in the early stage

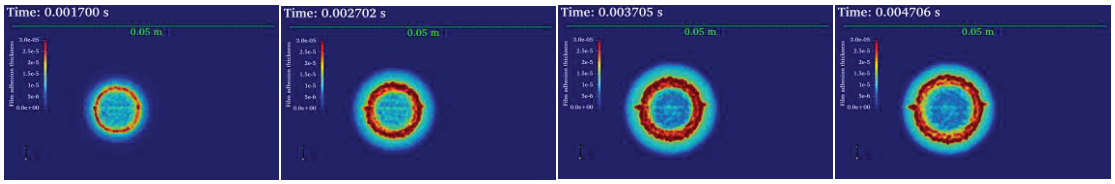

(a) *Ux*= 0 m/s

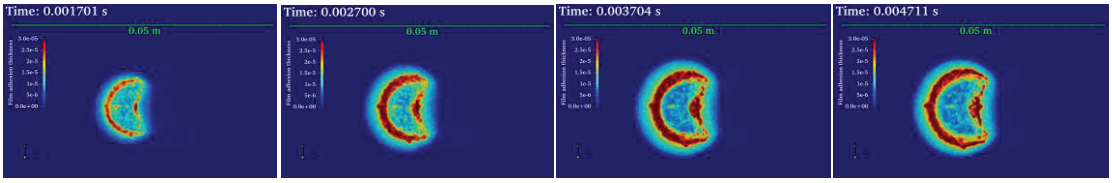

(b) *Ux*= 10 m/s

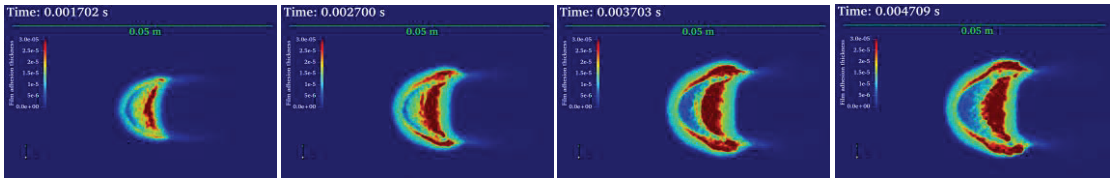

(c) *Ux*= 20 m/s

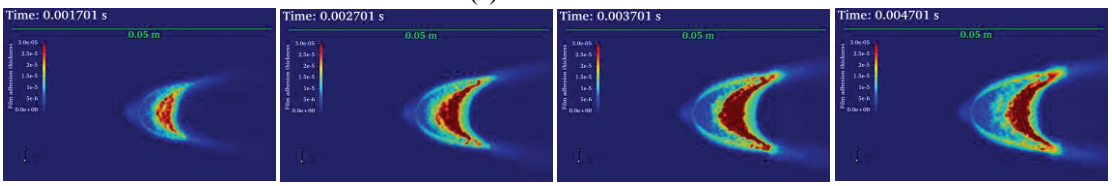

(d) *Ux*= 30 m/s

Figure 7.7 Propagation of fuel adhesion in the early stage under variations cross-flow conditions.

Firstly, the fuel adhesion phenomenon under different cross-flow velocities is discussed. As shown in the Figure 7.7, the fuel adhesion exhibits a circular shape spread without cross-flow condition. It can be clearly seen that the fuel adhesion is quite thin at the wall-impingement point and the edge region. Under the influence of the cross-flow, the fuel adhesion spreads downstream of the cross-flow. In general, the fuel adhesion is relatively long in the direction of the cross-flow, and the fuel adhesion forms the accumulation downstream. It can be seen that the effect of cross-flow on the fuel adhesion propagation behavior is consistent with experimental results. Next, the change of fuel adhesion area, the average fuel adhesion thickness and the fuel adhesion mass ratio with time in the early injection stage under different cross-

flow conditions were quantitatively analyzed.

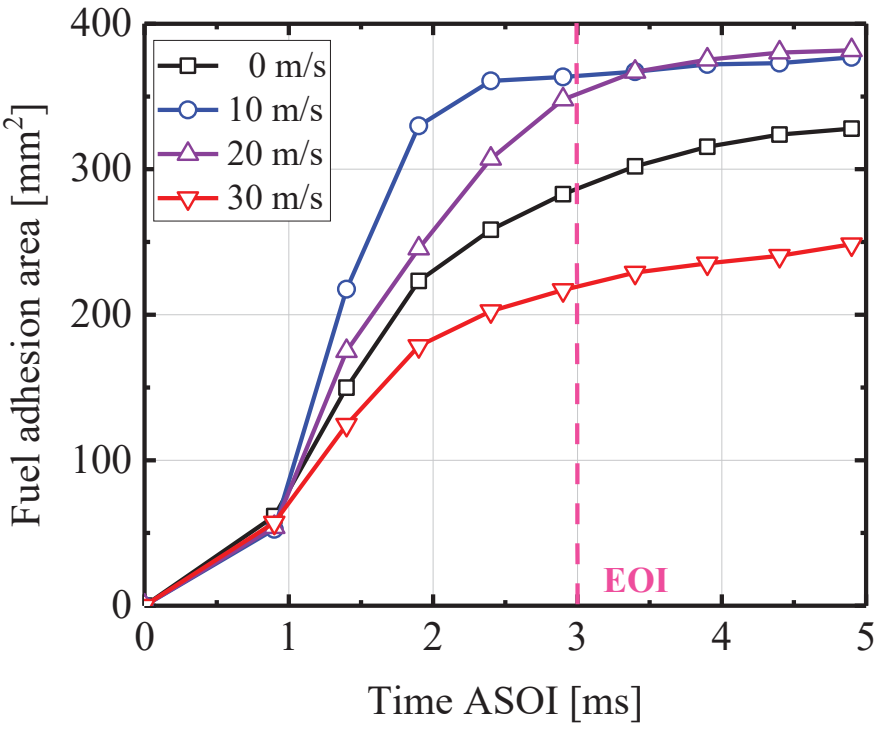

Figure 7.8 Fuel adhesion area under variations cross-flow conditions in the early stage.

Figure 7.8 shows the change of fuel adhesion area with time during the early injection stage under different cross-flow velocities. The results show that the fuel adhesion area becomes smaller under the influence of the cross-flow in the early stage, that's because the cross-flow promotes the spray atomization and makes the spray shape more bend, then less droplets adhere on the wall in the beginning. In addition, the fuel adhesion area gradually increased with time in the early stage, because of the droplets continuously adhered on the flat-wall during this stage. However, the experimental results show that the fuel adhesion area will gradually decrease with time under the influence of the cross-flow in the later stage, and the reduction rate is proportional to the cross-flow velocities.

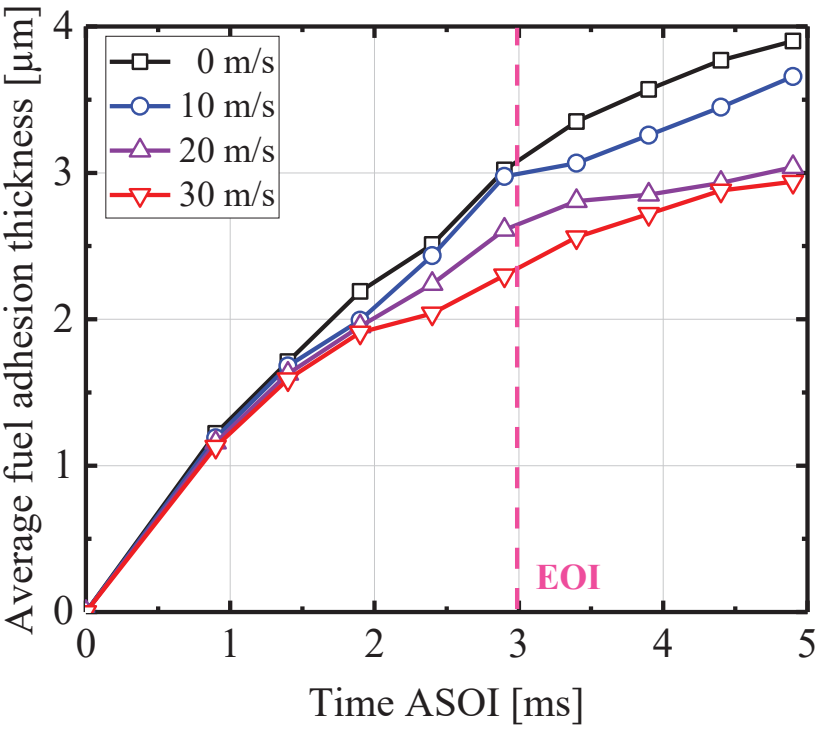

Figure 7.9 Average fuel adhesion thickness under variations cross-flow conditions in the early stage.

Figure 7.9 shows the average fuel adhesion thickness in the early stages under different cross-flow velocities. The results show that the average fuel adhesion thickness increases with time, which is due to the droplets continuously impinging on the flat-wall during this stage. Meanwhile, the cross-flow clearly played a critical role in reducing the average adhesion thickness. The cross-flow can promote the spray atomization, and then more droplets blown downstream, which lead to less droplets adhere on the wall. Therefore, the average fuel adhesion thickness decreases with the increase of cross-flow velocities in the early stage.

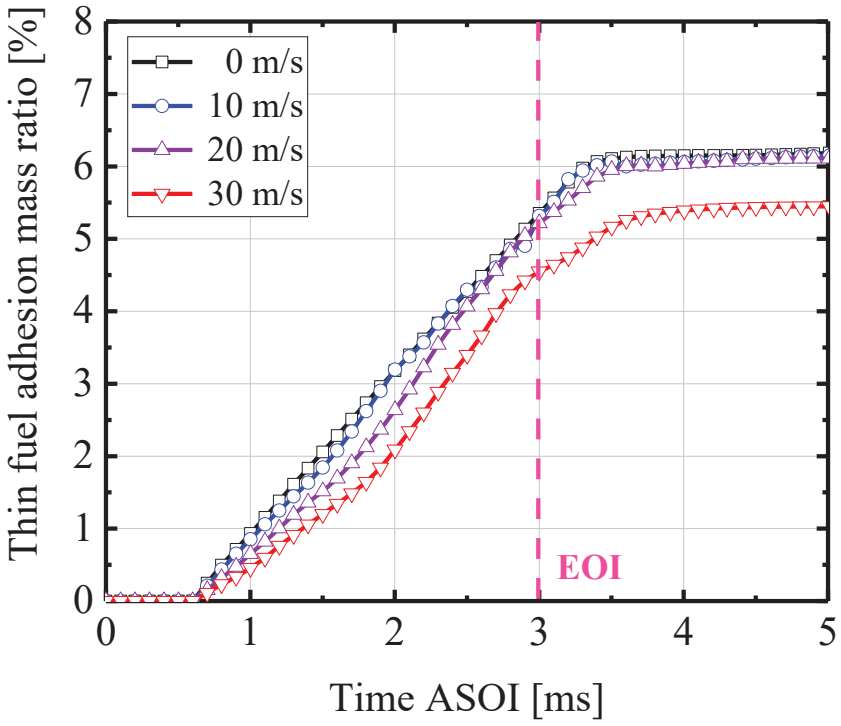

Figure 7.10 Fuel adhesion mass ratio under variations cross-flow conditions in the early stage.

It was mentioned in the simulation conditions that the fuel injection mass is different from the experiment to maintain the same injection pressure of 10 MPa, we only consider the fuel adhesion mass ratio here. Figure 7.10 shows the change of the fuel adhesion mass ratio with time in the early stage under different cross-flow velocities. The results show that the mass of the fuel adhered to the flat wall continues to increase with time after impinging on the flat-wall until it reaches a maximum value, which is because droplets continuously impinging and adhere to the flat-wall during the fuel supply stage. In addition, the fuel adhesion mass ratio decreases significantly with the cross-flow velocity of 30 m/s. This is because the cross-flow promotes the volatilization of the fuel adhesion and then reduces the fuel adhesion mass, which is consistent with the experimental results.

7.6 Summary

Restricted by the RIM experiment method on the fuel adhesion characteristics in the early stage of injection, numerical simulation was used in this chapter to analyze the effect of cross-flow on the fuel adhesion characteristics of wall-impingement spray. Several results are presented, such as spray profile, spray penetration, droplets size and velocity distribution, and fuel adhesion characteristics. Although there are some differences between the simulation results and the experimental results, most of them are in good agreement. The calculation results provided in this chapter can well predict the evolution trend of fuel adhesion characteristics under different conditions. Here we study the effects of different cross-flow velocities on the fuel adhesion characteristics in the early stages of injection. The main conclusions are as follows:

(1) The spray profile variation and penetration obtained by simulation were in good agreement with the experimental results. The increase of the cross-flow velocity obviously promotes the breakup and atomization of the droplets, which leads to the reduction of the global SMD. In addition, results shows that the droplet velocity near the nozzle region is large, and the droplet velocity along the wall surface is small.

(2) The results under different cross-flow velocities show that the fuel adhesion area is smaller under the cross-flow velocity of 30 m/s in the early stage. Meanwhile, the average fuel adhesion thickness decreases with the increase of cross-flow velocities in the early stage. In addition, the fuel adhesion mass ratio decreases significantly with the cross-flow velocity of 30 m/s.

CHAPTER 8 CONCLUSIONS

There are three main research part in the study. First is the CCV characteristics of free spray in the cross-flow flow field. The objectives include to quantitatively the CCV of spray characteristics, to observe the droplet size distribution, and to clarify the effects of cross-flow/ injection and ambient pressure on the CCV of spray characteristics. Second is the characteristics of wall-impingement spray in the cross-flow flow field. The objectives include to quantitatively the wall-jet vortex characteristics, to evaluate the effects of cross-flow/ ambient pressure/ wall-impingement distance on the wall-jet vortex, and to clarify the effects of cross-flow and wall-impingement degree on the fuel adhesion characteristics. Third one is the CFD simulation of wall-impingement spray in the cross-flow flow field. The objective is to validate the CFD results with the detailed measurements and then mainly consider the cross-flow effect. The results obtained in this study can not only provides a technical basis for the optimization of the actual engine but also has important significance for the CFD numerical simulation of the engine.

Spray images were obtained via high-speed photography using the DBI method. The CW laser sheet technology is used to perform high-speed photography on the vertical and horizontal planes to obtain wall-impingement spray images. Additionally, PIV technology was used to demonstrate the velocity distribution of wall-impingement spray. The SMD of spray tip droplets was obtained with LDSA. The Mie scattering technique was used to perform high-speed photography on the vertical observation to obtain a side view of fuel spray. Meanwhile, the RIM technology was used for high-speed photography at the bottom of the observation section to obtain images of fuel adhesion. In addition, Numerical simulations are applied to investigate the characteristics of wall-impingement spray in a cross-flow flow field.

In summary, the CCV characteristics of free spray, structure of wall-impingement spray and the fuel adhesion characteristics of wall-impingement spray were investigated experimentally and by simulation under cross-flow conditions. The

novelty and originalities of this research can be summarized as the following aspects:

8.1 Statistical Variation Analysis of Free Spray

The statistical variation characteristics of fuel spray were investigated experimentally under cross-flow conditions. To evaluate the spray variation characteristics, a statistical analysis of 30 repeated experiments was conducted. The conclusions can be summarized as follows:

The spray plume changed significantly under cross-flow conditions, and the downstream spray was more susceptible to cross-flows. The increase in the cross-flow velocity and spray injection pressure enlarged the spray area. Interestingly, surface waves were observed on the windward side.

The initial stage of the vertical penetration was barely affected by the cross-flow, owing to the high initial kinetic energy. Based on the spray propagation under cross-flow conditions, the COV of the vertical penetration can be categorized into two stages. The COV is the largest in the initial stage of injection, and it approached a small value in the second stage, i.e., between 4% and 7%. In addition, the horizontal penetration changed almost linearly with time, thereby confirming that the movement of the droplets in the horizontal direction was dominated by the cross-flow. The COV of the horizontal penetration was significantly higher than that in the vertical direction. The cross-flow significantly affected the spray variation characteristics in the horizontal direction. Moreover, the cross-flow significantly intensified the COV of the spray area. Furthermore, the COV of the image optical thickness on the windward side was higher than that on the leeward side, whereas that at the outer side was higher than that on the inner side. The increase in the cross-flow velocity and injection pressure intensified the variation in the spray tip region.

As the cross-flow velocity and injection pressure increased, the distributions of the horizontal penetration and spray area became uniform at the EOI timing, which indicates that the CCV of the spray can be increased by the cross-flow and injection

pressure. Under the effect of cross-flow, the *Ins* number for the dimensionless horizontal penetration varied between 0.8 and 1.2, which represents the higher CCV as compared with that of the vertical penetration.

The CCV characteristics of fuel spray under higher ambient condition are obtained and compared to atmospheric pressure. Results show that higher ambient pressure significantly inhibits the development of vertical penetration. At higher ambient pressures, there is also a slight increase in vertical penetration with increasing trigger current. Even if the cross-flow velocity was not so high, the variation of vertical penetration under high ambient pressure was completely opposite for atmospheric pressure. Despite the higher ambient pressure, the development tendency of horizontal penetration with time remained linear. The slope was slightly smaller than that of cross-flow velocity under higher ambient pressure, which should also be attributed to increases in ambient density. Furthermore, the ambient density had a significant impact on the COV of the horizontal penetration. Furthermore, the COV of horizontal penetration was clearly greater under higher ambient pressure than under atmospheric pressure. The spray area is much smaller under higher ambient pressure than it is under atmospheric pressure, which decreases by about half when the ambient pressure rises from 0.1 MPa to 0.3 MPa. The variation in spray area increases with cross-flow velocity, which can lead to more unstable spray development and then increase the amount of entrained air, promoting spray mixture formation.

As the injection pressure increased, the SMD became smaller. In addition, it is found that the dispersion index was smaller when close to the EOI timing under high injection pressure, that is, the distribution of the mixture was more uniform. The cross-flow can promote the atomization of the spray, which make the droplets size ranged from 5 to 8 μm. Additionally, the droplet size of downstream was slightly larger than the upstream, which could be regarded as the result of the droplets collide and gather downstream. Meanwhile, it is found that the uniformity of distribution increased in the downstream.

8.2 Wall-jet Vortex propagation

The wall-jet vortex was characterized under different ambient pressure, cross-flow velocities and wall-impingement distance. An indicator *Ic* of the "contribution index" is proposed to evaluate the degree of influence of different influencing factors. The main conclusions can be summarized as follows:

The wall-impinging spray behaviors can be divided into five regions: free spray region, wall-impingement region, cross-flow downstream region, wall main jet region, and wall-jet vortex region. The cross-flow enhances the kinematic energy of the wall-jet vortex, and the droplets strip from the upper surface of the wall-jet vortex region to form a dilute region.

The vortex core height is reduced by approximately 30% when the ambient pressure increases from 0.1 to 0.4 MPa. Because a larger ambient density hinders the movement of the vortex, the vortex core height decreases. However, the cross-flow significantly increases the vortex core height under the higher ambient pressure. The vortex core distance is more sensitive to cross-flow. The cross-flow velocity of 5 m/s increased the vortex core distance by approximately 30%. Cross-flow obviously promotes the movement of the vortex core in the horizontal direction, and the moving speed of the vortex core can also be enhanced by cross-flow. In addition, with an increase in the wall-impingement distance, the timing of spray wall-impingement is delayed, and the spray atomization can be enhanced. Meanwhile, the generation time of the wall-jet vortex was delayed. Moreover, it is predicted that when the wall-impingement distance is 75 mm, the vortex core distance could catch up with that of 50 mm at time of "*T*".

In addition, the velocity distribution around the vortex core was analyzed. Along the x-axis, the velocity distribution presents a "*M*" distribution. Along the y-axis direction, the velocity near the wall is significantly larger than that of the far wall in the wall-jet vortex region and exhibits a "*L*" distribution.

8.3 Fuel Adhesion Characteristics of Wall-impingement Spray

The fuel adhesion characteristics have a significant effect on the formation of the mixture, combustion performance, and emission of pollutants. Therefore, the effect of cross-flow on the fuel adhesion characteristics after the spray impinging on the flat-wall was mainly investigated using the RIM method in this work. The main conclusions can be summarized as follows:

The cross-flow enhanced the fuel adhesion dispersion downstream, which exhibited an ellipse propagation. In addition, the fuel adhesion at the edge region was the thinnest.

The fuel adhesion area gradually decreased under the cross-flow conditions and remained constant without cross-flow, which can be attributed to the enhancement of volatilization of the fuel adhesion under cross-flow. In addition, it was predicted that a strong cross-flow can decrease the lifetime of fuel adhesion. The fuel adhesion mass dramatically decreased with time under cross-flow conditions. The increase in fuel adhesion area enhanced the heat exchange area, then the cross-flow promoted the volatilization of the fuel adhesion. Meanwhile, the rate at which the fuel adhesion mass decreased was proportional to the cross-flow velocity. The average fuel adhesion thickness increased with time. However, the increase rate was decreased over time. The average fuel adhesion thickness obviously decreased under the cross-flow conditions. Additionally, the thickness of the thinner fuel adhesion region decreased, whereas the thickness of the thicker region increased with time.

The wall and air shear forces on the fuel adhesion surface aggregated the fuel adhesion into a thick fuel adhesion region. The main reason for the formation of thin fuel adhesion region was due to the impingement of a few droplets on the flat-wall entrained by cross-flow. In addition, the thin and thick fuel adhesion regions can transform into each other.

8.4 Numerical Simulation under Cross-flow Conditions

Restricted by the RIM experiment method on the fuel adhesion characteristics in the early stage of injection, numerical simulation was used in this chapter to analyze the effect of cross-flow on the fuel adhesion characteristics of wall-impingement spray. Here we study the effects of different cross-flow velocities on the fuel adhesion characteristics in the early stages of injection. The main conclusions can be summarized as follows:

The spray profile variation and penetration obtained by simulation were in good agreement with the experimental results. Under the cross-flow conditions, the droplets size on the windward side is larger than that on the leeward side, and droplets size is quite large near the nozzle at EOI timing. Meanwhile, the increase of the cross-flow velocity obviously promotes the breakup and atomization of the droplets, which leads to the decrease of the global SMD. In addition, results shows that the droplet velocity near the nozzle region is high, and the droplet velocity along the wall surface is low.

The fuel adhesion area tends to decrease under the strong cross-flow velocity, because the cross-flow promotes the spray atomization and the volatilization of fuel adhesion. In addition, the cross-flow played a criterial role in reducing the average adhesion thickness after EOI timing. The fuel adhesion mass ratio decreases significantly with the cross-flow velocity of 30 m/s.

8.5 Recommendations for Future Works

In order to deal with the problem of global warming, almost all countries have proposed stricter laws and regulations on the emission of internal combustion engines recently. In this study, the variation characteristics of free fuel spray under cross-flow conditions, the spray structure of wall-impingement spray and the fuel adhesion characteristics after impinging on the flat-wall were studied. However, the existing research is still far from enough to understand the interaction mechanism between fuel spray and in-cylinder airflow in a real engine, and the results of this research should

be verified in an optical engine in the future.

In addition, a multi-stage injection strategy has been shown to help improve in-cylinder mixture formation. However, the research on multi-stage injection under the influence of cross-flow has not been reported yet. Future work should focus on the multi-stage injection strategy, especially the research on the influence of the multi-stage injection strategy on the fuel adhesion characteristics under cross-flow conditions is critical, which will help further reduce CO_2 emissions.

Numerical simulation is a useful method to study spray characteristics. However, the correct selection of CFD model and parameters is the fundamental for an ideal simulation, and simplification of the model and incorrect parameters can lead to inaccurate simulations. These models and parameters were chosen based on experimental conditions. Therefore, the simulation model needs to be further improved according to the experimental conditions and results in the near future. In addition, more numerical calculations of boundary conditions should be required, such as changing the fuel to zero-carbon fuels such as hydrogen (H_2), ammonia (NH_3), etc.

REFERENCES

[1] Delworth TL, Zeng F, Vecchi GA, et al. The North Atlantic Oscillation as a driver of rapid climate change in the Northern Hemisphere. Nature Geoscience 2016; 9 (7): 509-512.

[2] Berkeley Earth. Global Temperature Report for 2019. Available at: http://berkeleyearth.org/archive/2019-temperatures/.

[3] The Paris Agreement. https://unfccc.int/process-and-meetings/the-paris-agreement/the-paris-agreement.

[4] Thomas H, Takeshi K, John L, et al. Net Zero Tracker. Energy and Climate Intelligence Unit, Data-Driven EnviroLab, NewClimate Institute, Oxford Net Zero, 2021.

[5] Wang Y, Guo CH, Chen XJ, et al. Carbon peak and carbon neutrality in China: Goals, implementation path and prospects. China Geology 2021; 4 (4): 720-746.

[6] Vaclav S. Energy Transitions: Global and National Perspectives. BP Statistical Review of World Energy, 2017. http://vaclavsmil.com/2016/12/14/energy-transitions-global-and-national-perspectives-second-expanded-and-updated-edition/.

[7] Hannah R, Max R and Pablo R. CO_2 and Greenhouse Gas Emissions. Published online at OurWorldInData.org 2020. Retrieved from: https://ourworldindata.org/co2-and-other-greenhouse-gas-emissions.

[8] WHO. https://wwwwhoint/mediacentre/news/releases/2014/air-pollution/en/.

[9] Lelieveld J, Klingmüller K, Pozzer A, et al. Effects of fossil fuel and total anthropogenic emission removal on public health and climate. Proceedings of the National Academy of Sciences 2019; 116 (15): 7192-7197.

[10] The outlook for energy: A view to 2050. https://corporate.exxonmobil.com/Energy-and-innovation/Outlook-for-Energy/Energy-demand.

[11] Taylor AMKP. Science review of internal combustion engines. Energy Policy 2008; 36: 4657-4667.

[12] Heywood JB. Internal combustion engine fundamentals. Singapore: McGraw-Hill Book Company, 1988.

[13] Tariq M, Irene IG. Electric Vehicles: Prospects and Challenges. 2017.

[14] Alkidas AC. Combustion advancements in gasoline engines. Energy Conversion and Management 2007; 48: 751-2761.

[15] Moon S, Choi J, Abo-Serie E, et al. The effects of injector temperature on spray and combustion characteristics in a single cylinder DISI engine. SAE Technical Paper 2005; 2005-01-0101.

[16] Harada J, Tomita T, Mizuno H, et al. Development of direct injection gasoline engine. SAE Technical Paper 1997; 970540.

[17] Imberdis O, Hartmann M, Bensler H, et al. A numerical and experimental investigation of a DISI-engine intake port generated turbulent flow. SAE Technical Paper 2007; 2007-01-4047.

[18] Tagaki Y, Itoh T, Muranaka S, et al. Simultaneous Attainment of Low Fuel Consumption, High Output Power and Low Exhaust Emissions in Direct Injection SI Engines. SAE Technical Paper 1998; 980149.

[19] Drake MC, Fansler TD, Solomon AS, et al. Piston fuel films as a source of smoke and hydrocarbon emissions from a wall-controlled spark-ignited direct-injection engine. SAE Technical Paper 2003; 2003-01-0547.

[20] Drake MC, Fansler TD, Lippert AM. Stratified-charge combustion: modeling and imaging of a spray-guided direct-injection spark-ignition engine. Proceedings of the Combustion Institute 2005; 30: 2684-2691.

[21] Zhao FQ, Lai MC, and Harrington DL. Automotive spark-ignited direct-injection gasoline engines. Progress in Energy and Combustion Science 1999; 25: 437-562.

[22] Chigier N. Group combustion models and laser diagnostic methods in sprays: A review. Combustion and Flame 1983; 51: 127-139.

[23] Katashiba H, Honda T, Kawamoto M, et al. Improvement of center injection spray guided DISI performance. SAE Technical Paper 2006; 2006-01-1001.

[24] Schwarz C, Schunemann E, Durst B, et al. Potentials of the spray-guided DI combustion system. SAE Technical Paper 2006; 2006-01-1265.

[25] Szekely GA and Alkida A. Combustion characteristics of a spray-guided direction stratified-charge engine with a high-squish piston. SAE Technical Paper 2005; 2005-01-1937.

[26] Koch T, Schanzlin K, Boulouchos K. Characterization and phenomenological modeling of mixture formation and combustion in a direct injection spark ignition engine. SAE Technical Paper 2002; 2002-01-1138.

[27] Schanzlin K, Koch T, Tzannis AP, et al. Characterization of mixture formation in direct injected spark ignition engine. SAE Technical Paper 2001; 2001-01-1909.

[28] VanDerWege BA, Han Z, and Lyer CO. Development and analysis of a spray-guided DISI combustion system concept. SAE Technical Paper 2003; 2003-01-3105.

[29] Boot M, Rijk E, Luijten C, et al. Spray impingement in the early direct injection premixed charge compression ignition regime. SAE Technical Paper 2010; 2010-01-1501.

[30] Gülder ÖL, Smallwood GJ, Snelling DR. Diesel spray structure of transient full cone dense diesel sprays. Commodia 1994; 94: 355-360.

[31] Soteriou C, Andrews R, Smith M, et al. Through the diesel nozzle-a journey of discovery II. ILASS-Europe, Zürich, 2001.

[32] Wu PK and Faethe GM. Onset and end of drop formation along the surface of turbulent liquid jet in still gases. Phys. of Fluids 1995; 7(11): 2915-2917.

[33] Arai M, Shimizu M, Hiroyasu H. Similarity between the breakup lengths of a high speed liquid jet in atmospheric and pressurized conditions. Los Alamos National Laboratory, 1991.

[34] Soteriou C, Andrews R, Smith M. Direct injection diesel sprays and the

effect of cavitation and hydraulic flip on atomization. SAE Technical Paper 1995; 950080.

[35] Tamaki N, Shimizu M, Hiroyasu H. Enhanced Atomization of a liquid jet by cavitation in a nozzle hole. 8th Int. Conf. on Liquid Atomization and Spray Systems, Pasadena, CA, USA, 2000.

[36] Baumgarten C. Mixture Formation in Internal Combustion Engines. Springer: Heidelberg, Germany, 2006.

[37] Hiroyasu H and Arai M. Structures of fuel spray in diesel engines. SAE Technical Paper 1990; 900475.

[38] Dent JC. A basis for the comparison of various experimental methods for studying spray penetration. SAE Technical Paper 1971; 710571.

[39] Fujimoto H, Sugihara H, Tanabe H, et al. Investigation on combustion in medium speed marine diesel engines using model chambers. CIMAC-Congress, Helsinki, 1981.

[40] Heywood JB. Internal combustion engine fundamentals. Singapore: McGraw-Hill Book Company, 1988.

[41] Dan T, Takagishi S, Senda J, et al. Organized structure and motion on diesel spray. SAE Technical Paper 1997; 970641.

[42] Reitz RD and Bracco FV. Mechanisms of breakup of round liquid jets. Encyclopedia of Fluid Mechanics, Gulf Pub, NJ 1986; 3: 233-249.

[43] Hiroyasu H, Arai M, Tabata M. Empirical equations for the Sauter mean diameter of a diesel spray. SAE Technical Paper 1989; 890464.

[44] Hiroyasu H and Nishida K. Fuel spray trajectory and dispersion in a D.I. diesel combustion chamber. SAE Technical Paper 1989; 890462.

[45] Hiroyasu H, Shimizu M, Arai M. Breakup length of a liquid jet and internal flow in a nozzle. ICLASS-91, 1991.

[46] Chehroudi B, Chen SH, Bracco FV, et al. On the intact core of full-cone spray. SAE Technical Paper 1985; 850126.

[47] Youle AJ and Salters DG. A conductivity probe technique for investigating

the breakup of diesel sprays. Atomization and sprays 1994; 4: 253-262.

[48] Chen H, Xu M, Hung DLS, et al. Development of a POD-based Analysis Approach for Quantitative Comparison of Spray Structure Variations in a Spark-Ignition Direct-Injection Engine. SAE Technical Paper 2013; 2013-01-2545.

[49] Müller SHR, Arndt S, Dreizler A. Analysis of the In-Cylinder Flow Field / Spray Injection Interaction within a DISI IC Engine Using High-Speed PIV. SAE Technical Paper 2011; 2011-01-1288.

[50] Koch P, Löffler MG, Wensing M, et al. Study of the mixture formation processes inside a modern direct-injection gasoline engine. International Journal of Engine Research 2010; 11(6): 455-471.

[51] Aleiferis PG, Taylor AMKP, Ishii K, et al. The nature of early flame development in a lean-burn stratified-charge spark-ignition engine. Combustion and Flame 2004; 136 (3): 283-302.

[52] Hung DLS, Chen H, Xu M, et al. Experimental Investigation of the Variations of Early Flame Development in a Spark-Ignition Direct-Injection Optical Engine. Journal of Engineering for Gas Turbines and Power, 2014.

[53] Hill PG, Zhang D. The effects of swirl and tumble on combustion in spark-ignition engines. Prog Energ Combust 1994; 5 (20): 373-429.

[54] Mittal M, Hung DLS, Zhu G, et al. High-Speed Flow and Combustion Visualization to Study the Effects of Charge Motion Control on Fuel Spray Development and Combustion Inside a Direct-Injection Spark-Ignition Engine. SAE International Journal of Engines 2011; 4(1): 1469-1480.

[55] Frieden D, Sick V. Investigation of the fuel injection, mixing and combustion processes in an SIDI engine using quasi-3D LIF imaging. SAE Transactions Journal of Engines 2003; 270-281.

[56] Kang KY, Baek JH. Turbulence characteristics of tumble flow in a four-valve engine. Exp Therm Fluid Sci 1998; 3 (18): 231-243.

[57] Fansler TD. Turbulence Production and Relaxation in Bowl-in-Piston

Engines. SAE Technical Paper 1993; 930479.

[58] Funk CO, Sick V, Reuss DL, et al. Turbulence Properties of high and low swirl in-cylinder flows. SAE Technical Paper 2002; 2002-01-2841.

[59] Holmes P, Lumley JL, Berkooz G. Turbulence, Coherent Structures, Dynamical Systems and Symmetry. Cambridge, UK: Cambridge University Press, 1996.

[60] Kapitza L, Imberdis O, Bensler HP, et al. An experimental analysis of the turbulent structures generated by the intake port of a DISI-engine. Experiments in Fluids 2010; 48 (2): 265-280.

[61] Liu D, Wang T, Jia M, et al. Cycle-to-cycle variation analysis of in-cylinder flow in a gasoline engine with variable valve lift. Experiments in Fluids 2012; 53 (3): 585-602.

[62] Mittal M, Schock HJ. A Study of Cycle-to-Cycle Variations and the Influence of Charge Motion Control on In-Cylinder Flow in an IC Engine. Journal of Fluids Engineering 2010; 132 (5): 051107-051108.

[63] Towers DP, Towers CE. Cyclic Variability Measurements of In-Cylinder Engine Flows Using High-Speed Particle Image Velocimetry. Measurement Science and Technology 2004; 15 (9): 1917-1925.

[64] Voisine M, Thomas L, Borée J, et al. Spatio-temporal structure and cycle to cycle variations of an in-cylinder tumbling flow. Experiments in Fluids 2011; 50 (5): 1393-1407.

[65] Ozdor N, Dulger M, Sher E. Cyclic Variability in Spark Ignition Engines A Literature Survey. SAE Technical Paper 1994; 940987.

[66] Wieske P, Wissel S, Grünefeld G, et al. Experimental investigation of the origin of cyclic fluctuations in a DISI engine by means of advanced laser induced exciplex fluorescence measurements. SAE Paper 2006; 115 (3): 915-924.

[67] Goryntsev D, Sadiki A, Klein M, et al. Large eddy simulation based analysis of the effects of cycle-to-cycle variations on air–fuel mixing in realistic DISI

IC-engines. P Combust Inst 2009; 32:2759-2766.

[68] Qin WJ, Hung DLS, Xu M. Investigation of the temporal evolution and spatial variation of in-cylinder engine fuel spray characteristics. Energ Convers Manage 2015, 98: 430-439.

[69] Stiehl R, Schorr J, Krüger C, et al. In-Cylinder Flow and Fuel Spray Interactions in a Stratified Spray-Guided Gasoline Engine Investigated by High-Speed Laser Imaging Techniques. Flow Turbul Combust 2013; 91 (3):431-450.

[70] Zeng W, Sjöberg M, Reuss DL. PIV examination of spray-enhanced swirl flow for combustion stabilization in a spray-guided stratified-charge direct-injection spark-ignition engine. Int J Engine Res 2014; 16 (3):306-322.

[71] Truffin K, Angelberger C, Richard S, et al. Using large-eddy simulation and multivariate analysis to understand the sources of combustion cyclic variability in a spark-ignition engine. Combust Flame 2015; 162 (12):4731-4390.

[72] Riccardo S, Keith R, Eric P, et al. Cycle-to-Cycle Variations in Multi-Cycle Engine RANS Simulations. 2016 SAE World Congress; 2016-04-01. https://doi.org/10.4271/2016-01-0593.

[73] Hung DLS, Chmiel DM, Markle LE. Application of an imaging-based diagnostic technique to quantify the fuel spray variations in a direct-injection spark-ignition engine. SAE Technical Paper 2003; 2003-01-0062.

[74] Hung DLS and Zhong J. Experimental analysis of the start of fuel cycle-to-cycle variations of solenoid-actuated high pressure fuel injectors. SAE Technical Paper 2011; 2011-01-1882. https://doi.org/10.4271/2011-01-1882.

[75] Marchi A, Nouri J, Yan Y, et al. Spray stability of outwards opening pintle injectors for stratified direct injection spark ignition engine operation. Int J Engine Res 2010; 11 (6): 413–437.

[76] Zhou YF, Qi WY, Zhang YY, et al. Investigation on spray cyclic variations under idle operation of engine using optical diagnostics and statistical methods.

Int J Engine Res 2020. https://doi.org/10.1177/1468087420926015.

[77] Chen H, Hung DLS, Xu M, et al. Analyzing the cycle-to-cycle variations of pulsing spray characteristics by means of the proper orthogonal decomposition. Atomization Spray 2013; 23 (7): 623-641.

[78] Chen H, Hung DLS, Xu M, et al. Proper orthogonal decomposition analysis of fuel spray structure variation in a spark-ignition direct-injection optical engine. Exp Fluids 2014; 55: 1703.

[79] Zhuang H, Hung DLS, Xu M, et al. Analysis of spray structure and penetration variations using proper orthogonal decomposition. The 16th conference of ILASS-Asia 2013.

[80] Wieske P, Wissel S, Grünefeld G, et al. Experimental investigation of the origin of cyclic fluctuations in a DISI engine by means of advanced laser induced exciplex fluorescence measurements. SAE Paper 2006; 115 (3): 915-924.

[81] Wu S, Xu M, Hung DLS, Li T and Pan H. Analyzing the cycle-to-cycle variations of vapor and liquid phases of evaporating SIDI sprays via proper orthogonal decomposition technique. SAE Paper 2016; 9 (1): 193-200.

[82] Qi WY, Zhou YF, Zhang YY. Laser-based measurements and analyses on cycle-to-cycle variations of mixture formation in binary-component fuel sprays. Exp Fluids 2020; 61: 87.

[83] Im KS, Lin KC, Lai MC, et al. Breakup modeling of a liquid jet in cross flow. International Journal of Automotive Technology 2011; 4 (12): 489-496.

[84] Moon S, Bae C, Choi J, et al. The influence of airflow on fuel spray characteristics from a slit injector. Fuel 2007; 86: 400-409.

[85] Nouri JM and Whithelaw JH. Gasoline spray in uniform crossflow. Atomization and Sprays 2007; 17: 621-640.

[86] Ghosh S and Hunt JCR. Spray jets in a cross-flow. Journal of Fluid Mechanics 1998; 365: 109-136.

[87] Sedarsky D, Paciaroni M, Berrocal E, et al. Model validation image data for

breakup of a liquid jet in crossflow: part I. Exp Fluids 2010; 49: 391-408.

[88] No SY. Empirical correlations for penetration height of liquid jet in cross flow-a review. ILASS Europe 2011, 24th Annual Conf. on Liquid Atomization and Spray Systems, Estoril, Portugal.

[89] Moon S, Bae C, Choi J, et al. The influence of airflow on fuel spray characteristics from a slit injector. Fuel 2007; 86 (3): 400-409.

[90] Moriyoshi Y, Uchida R, Takagi M, et al. Numerical and Experimental Analyses of Mixture Formation Process Using a Fan-shaped DI Gasoline Spray: Examinations on Effects of Crosswind and Wall Impingement. SAE Technical Paper 2009; 2009-01-1502. https://doi.org/10.4271/2009-01-1502.

[91] Panão MRO, Moreira ALN, Durão DFG. Effect of a cross-flow on spray impingement with port fuel injection systems for HCCI engines. Fuel 2013, 106: 249-257.

[92] Guo M, Kishi R, Shi B, et al. Cross-Flow Effect on Behavior of Fuel Spray Injected by Hole-Type Nozzle for D.I. Gasoline Engine. SAE Technical Paper 2013; 2013-01-2553. https://doi.org/10.4271/2013-01-2553.

[93] Guo M, Kishi R, Shi B, et al. Effects of Cross-Flow on Fuel Spray Injected by Hole-Type Injector for Direct-Injection Gasoline Engine. Second Report: Spray Pattern, Droplet Size, and Vortex Structure. Atomization Sprays 2016; 26 (1): 53–72.

[94] Guo M, Shimasaki N, Nishida K, et al. Experimental Study on Fuel Spray Characteristics under Atmospheric and Pressurized Cross-Flow Conditions. Fuel 2016; 184: 846–855.

[95] Sinha A and Ravikrishna RV. Experimental studies on structure of airblast spray in crossflow. Indian Academy of Sciences 2019; 44:113.

[96] Bai C and Gosman AD. Development of Methodology for Spray Impingement Simulation. SAE paper 1995; 950283.

[97] Fujimoto H, Saitou M, Monoura A, et al. (1987) Characteristics of a Diesel Spray Impinging on a Flat Wall (1st Report). JSME 1987; 54:2252-2259.

[98] Katsura N, Saito M, Senda J, et al. Characteristics of a Diesel Spray Impinging on a Flat Wall (2nd Report). JSME 1990; 56: 227-234.

[99] Senda J, Tanabe Y, Fujimoto H, et al. Vizualization of Evaporative Diesel Spray Impinging Upon Wall Surface by Exciplex Fluorescence Method. SAE paper 1992; 920578.

[100] Meingast U, Staudt M, Reichelt L, et al. Analysis of Spray/Wall Interaction under Diesel Engine Conditions. SAE paper 2000; 2000-01-0272.

[101] Arcoumanis C and Chang JC. Flow and Heat Transfer Characteristics of Impinging Transient Diesel Sprays. SAE paper 1994; 940678.

[102] Reitz R and Diwakar R. Effect of Drop Breakup on Fuel Sprays. SAE paper 1986; 860469.

[103] Cossali GE, Coghe A, Brunello G. Effect of Spray-Wall Interaction on Air Entrainment in a Transient Diesel Spray. SAE paper 1993; 930920.

[104] Mohammadi A, Kidoguchi Y, Miwa K. Effect of Injection Parameters and Wall-Impingement on Atomization and Gas Entrainment Processes in Diesel Sprays. SAE paper 2002; 2002-01-0497.

[105] Bruneaux G, Causse M, Omrane A. Air Entrainment in Diesel-Like Gas Jet by Simultaneous Flow Velocity and Fuel Concentration Measurements, Comparison of Free and Wall Impinging Jet Configurations. SAE paper 2011; 2011-01-1828.

[106] Fujimoto H, Kusano S, Senda J. Distribution of Vapor Concentration in a Diesel Spray Impinging on a Flat Wall by Means of Exciplex Fluorescence Method -In Case of High Injection Pressure. SAE paper 1997; 972916.

[107] Bruneaux G. Mixing Process in High Pressure Diesel Jets by Normalized Laser Induced Exciplex Fluorescence Part II: Wall Impinging Versus Free Jet. SAE paper 2005; 2005-01-2097.

[108] Egermann J, Göttler A, Leipertz A. Application of Spontaneous Raman Scattering for Studying the Diesel Mixture Formation Process under Near-Wall Conditions. SAE paper 2001; 2001-01-3496.

[109] Senda J, Kanda T, Kobayashi M, et al. Quantitative Analysis of Fuel Vapor Concentration in Diesel Spray by Exciplex Fluorescence Method. SAE paper 1997; 970796.

[110] Fujimoto H, Hyun GS, Nogami M, et al. Characteristics of Free and Impinging Gas Jets by Means of Image Processing. SAE Technical Paper 1997; 970045.

[111] Xu Y, Wang JJ. Flow structure evolution for laminar vortex rings impinging onto a fixed solid wall. Exp Therm Fluid Sci 2016; 75: 211-219.

[112] Yu MZ, Chen LH, Jin HH, et al. Large eddy simulation of coherent structure of impinging jet. Int J Therm Sci 2005; 14: 150-155.

[113] Yu JZ, Vuorinen V, Hillamo H, et al. In-Cylinder Flow and Fuel Spray Interactions in a Stratified Spray-Guided Gasoline Engine Investigated by High-Speed Laser Imaging Techniques. J Nat Gas Sci Eng 2012; 9:1-10.

[114] Schulz F, Schmidt J, Kufferath A and Samenfink W. Gasoline Wall Films and Spray/Wall Interaction Analyzed by Infrared Thermography. SAE Int J Eng 2014 7 (3): 1165-1177.

[115] Schulz F, Schmidt J & Beyrau F. Development of a sensitive experimental set-up for LIF fuel wall film measurements in a pressure vessel. Exp Fluid Sci 2015 56: 98.

[116] Schulz F, Samenfink W, Schmidt J, et al. Systematic LIF fuel wall film investigation. Fuel 2016; 172: 284-292.

[117] Henkel S, Beyrau F, Hardalupas Y, et al. Novel method for the measurement of liquid film thickness during fuel spray impingement on surfaces. Optics Express 2016; 24 (3): 2542-2561.

[118] Luo HL, Nishida K, Uchitomi S, et al. Effect of temperature on fuel adhesion under spray-wall impingement condition. Fuel 2018; 234: 56-65.

[119] Luo HL, Nishida K, Uchitomi S, et al. Effect of spray impingement distance on piston top fuel adhesion in direct injection gasoline engines. Int J Engine Res 2018. https://doi.org/10.1177/1468087418774175

[120] Luo HL, Chang FX, Zhan C, et al. Microscopic characteristics of multiple droplets behaviors at the near-wall region during the quasi-steady state. Fuel 2021; 286: 119431.

[121] Akop MZ, Zama Y, Furuhata T, et al. Characteristics of Adhesion of Diesel Fuel on Impingement Disk Wall. Part 1: Effect of Impingement Area And Inclination Angle Of Disk. Atomization Sprays 2013; 23 (8): 725–744.

[122] Akop MZ, Zama Y, Furuhata T, et al. Characteristics of Adhesion Diesel Fuel on An Impingement Disk Wall Part 2: Droplet Weber Number And Adhered Fuel Mass. Atomization Sprays 2014; 24 (8): 651–671.

[123] Wang ZM, Li YF, Guo HJ, et al. Microscopic and macroscopic characterization of spray impingement under flash boiling conditions with the application of split injection strategy. Fuel 2018; 212: 315-325.

[124] Muramatsu K, Yamamoto K, Jinno K, et al. Measurement of fuel liquid film under the different injection pressure. SAE Technical Paper 2013; 329167. https://doi.org /10.4271/2013-32-9167.

[125] Yu HZN, Liang XY, Shu GQ, et al. Experimental investigation on wall film ratio of diesel, butanol/diesel, DME/diesel and gasoline/diesel blended fuels during the spray wall impingement process. Fuel Process Technol 2017; 156: 9-18.

[126] Shim YS, Choi GM, Kim DJ. Numerical and experimental study on effect of wall geometry on wall impingement process of hollow-cone fuel spray under various ambient conditions. Int J Multiphas Flow 2009; 35: 885-895.

[127] Schulz F, Beyrau F. The influence of flash-boiling on spray-targeting and fuel film formation. Fuel 2017; 208: 587-594.

[128] Lee ZY, Kim DH, Park SW. Effects of spray behavior and wall impingement on particulate matter emissions in a direct injection spark ignition engine equipped with a high pressure injection system. Energ Convers Manage 2020; 213: 112865.

[129] Cheng YS, Deng KY, Li T. The coupling influence of airflow and temperature on the wall-wetted fuel film distribution. Exp Therm Fluid Sci 2010; 34: 227-233.

[130] Padala S, Kook S, Hawkes ER. Effect of ethanol port-fuel-injector position on dual-fuel combustion in an automotive-size diesel engine. Energy Fuels 2014; 1 (28): 340-348.

[131] Settles GS. Schlieren and shadowgraph techniques: visualizing phenomena in transparent media. Springer, Berlin, 2006.

[132] Payri R, Viera JP, Gopalakrishnan V, et al. The effect of nozzle geometry over the evaporative spray formation for three different fuels. Fuel 2017; 188:645-60.

[133] Panigrahi PK, Muralidhar K. Schlieren and shadowgraph methods in heat and mass transfer. Springer 2012.

[134] Auriemma M, Corcione FE, Macchioni R, et al. LDV measurements of integral length scales in an IC engine. SAE Technical Paper 1996; 961161.

[135] Zhao H and Ladommatos N. Engine combustion instrumentation and diagnostics. Society of Automotive Engineers, Inc., 2001.

[136] Raffel M, Willert CE, Scarano F, et al. Techniques for 3D-PIV. Springer 2018.

[137] Stansfield P, Wigley G, Justham T, et al. PIV analysis of in-cylinder flow structures over a range of realistic engine speeds. Experiments in Fluids 2007; 43 (1): 135-146.

[138] Wieneke B. Stereo-PIV using self-calibration on particle images. Experiments in Fluids 2005; 39 (2): 267-280.

[139] Kähler CJ and Kompenhans J. Fundamentals of multiple plane stereo particle image velocimetry. Experiments in Fluids 2000; 29 (1): S070-S077.

[140] Elsinga GE, Scarano F, Wieneke B, et al. Tomographic particle image velocimetry. Experiments in Fluids 2006; 41 (6): 933-947.

[141] Hinsch KD. Holographic particle image velocimetry. Measurement

Science and Technology 2002; 13 (7): R61-R72.

[142] Xiong JH, Idoughi R, Aguirre-pablo AA, et al. Rainbow particle imaging velocimetry for dense 3D fluid velocity imaging. ACM Transactions on Graphics 2017; 36 (4): 1-14.

[143] Tolinger JD. Particle and flow filed holograph. Combustion Measurements 1991; 55-89.

[144] Drake MC, Fansler TD, Rosalik ME. Quantitative high-speed imaging of piston fuel films in direct-injection engines using a refractive-index-matching technique. Proc of the 15th Annual Conference on Liquid Atomization and Spray System 2002.

[145] Drake MC, Fansler TD, Solomon AS, et al. Piston fuel films as a source of smoke and hydrocarbon emissions from a wall-controlled spark-ignited direct-injection engine. SAE transactions 2003; 112 (3): 762-783.

[146] Hurlburt ET, Newell TA. Optical measurement of Liquid film thickness and wave location in liquid film flow. Experiments in Fluids 1996; 21 (5): 357-362.

[147] Ohyma T, Endoh K, Mikami A, et al. Optical interferometry for measuring instantaneous thickness of Transparent solid and liquid films. Review of Scientific Instruments 1988; 59 (9): 2018-2022.

[148] Han Y, Shikazono N, Kasagi N. Measurement of liquid film thickness in a micro parallel channel with interferometer and laser focus displacement meter. International Journal of Multiphase Flow 2011; 37 (1): 36-45.

[149] Schul ZF, Samenfink W, Schmint J, et al. Systematic LIF fuel wall film investigation. Fuel, 2016, 172: 284-292.

[150] He X, Li YK, Sjberg M, et al. Impact of coolant temperature on piston wall-wetting and smoke generation in a Stratified-charge DISI engine operated on E30 fuel. Proceedings of the Combustion Institut 2019; 37 (4): 4955-4963.

[151] Tajima K, Tsuru D, Kawauchi S, et al. Spray model verification via observation of diesel spray propagation in parallel flow field to injection

direction. ILASS-Japan 2011: 194-198.

[152] Bradshaw P. The effect of wind-tunnel screens on nominally two-dimensional boundary layers. J Fluid Mech1965; 4 (22): 679-687.

[153] Groth J and Johansson AV. Turbulence reduction by screens. J Fluid Mech 1988; 197: 139-155.

[154] Klopfenstein R. Air velocity and flow measurement using a Pitot tube. ISA Transactions 1998; 37: 257-263.

[155] Andrews GE, Bradley D, Hundy GF. Hot wire anemometer calibration for measurements of small gas velocities. Int J Heat Mass Transfer 1972; 15: 1765-1786.

[156] Bhatia JC, Durst F, Jovanovic J. Corrections of hot-wire anemometer measurements near walls. J Fluid Mech 1982; 122: 411-431.

[157] Motallebi F. A review of the hot-wire technique in 2-D compressible flows. Prog Aerospace 1994; 30: 267-294.

[158] Welss R, Bornschlegel S, Wensing M. Characterizing Spray Propagation of GDI Injectors under Crossflow Conditions. SAE Technical Paper 2018; 2018-01-1696.

[159] Vass S, Németh H. Sensitivity analysis of instantaneous fuel injection rate determination for detailed Diesel combustion models. Periodica Polytechnica Transportation Engineering 2013; 41 (1): 77-85.

[160] Zhang GX, Luo HL, Kita K, et al. Statistical variation analysis of fuel spray characteristics under cross-flow conditions. Fuel 2022; 307: 121887.

[161] Zhang GX, Luo HL, Kita K, Ogata Y, Nishida K. Experimental Study on Fuel Spray Characteristics of Multi-Hole Injector for DISI Engine under Cross-Flow Conditions. ILASS-Asia 2020.

[162] Leask SB, McDonell VG, Samuelsen S. Critical evaluation of momentum flux ratio relative to a liquid jet in crossflow. Atomization Sprays 2018; 28 (7): 599–620.

[163] Zhai C, Jin Y, Nishida Y, Ogata Y. Diesel spray and combustion of multi-

hole injectors with micro-hole under ultra-high injection pressure – Non-evaporating spray characteristics. Fuel 2021; 283: 119322.

[164] Si ZB, Shimasakia N, Nishida K, Ogata Y, Guo M, Tang CL, Huang ZH. Experimental study on impingement spray and near-field spray characteristics under high-pressure cross-flow conditions. Fuel 2018; 218: 12-22.

[165] Du JG, Mohan B, Sim J, et al. Study of spray collapse phenomenon at flash boiling conditions using simultaneous front and side view imaging. Int J Heat Mass Tran 2020; 147: 118824.

[166] Zhang GX, Luo HL, Kita K, Ogata Y, Nishida K. Statistical Variation Analysis of Spray Injected by a Multi-Hole Injector into Cross-Flow Ambience. ICLASS 2021.

[167] Zhang GX, Si ZB, Zhai C, Luo HL, Ogata Y, Nishida K. Characteristics of wall-jet vortex development during fuel spray impinging on flat-wall under cross-flow conditions. Fuel 2022; 317: 123507.

[168] Kristensson E. Structured Laser Illumination Planar Imaging SLIPI Applications for Spray Diagnostics. Lund University, 2012.

[169] Panão MRO, Moreira ALN. Visualization and Analysis of Spray Impingement Under Cross-Flow Conditions. SAE Technical Paper 2002; 2002-01-2664.

[170] Zhang GX, Shi PH, Luo HL, Ogata Y, Nishida K. Investigation on fuel adhesion characteristics of wall-impingement spray under cross-flow conditions. Fuel 2022; 320: 123925.

[171] He X, Li YK, Sjöberg M, et al. Impact of coolant temperature on piston wall-wetting and smoke generation in a stratified-charge DISI engine operated on E30 fuel. P Combust Inst 2019; 37: 4955-4963.

[172] He X, Li YK, Liu C, et al. Characteristics of spray and wall wetting under flash-boiling and non-flashing conditions at varying ambient pressures. Fuel 2020; 264: 116683.

[173] Guo M, Ogata Y, Nishida K, et al. Experimental study on fuel spray

characteristics under atmospheric and pressurized cross-flow conditions, second report: Spray distortion, spray area, and spray volume. Fuel 2017; 206: 401–408.

[174] Tian J, Lu TJ, Hodson HP, et al. Cross flow heat exchange of textile cellular metal core sandwich panels. Int J Heat Mass Tran 2007; 50: 2521-2536.

[175] Schulz F, Samenfink W, Schmidt J, et al. Systematic LIF fuel wall film investigation. Fuel 2016; 172: 284-292.

[176] O'Rourke PJ and Amsden AA. The TAB method for numerical calculation of spray droplet breakup. SAE Technical Paper 1987; 872089.

[177] Liu AB and Reitz RD. Modeling the effects of drop drag and break-up on fuel spray. SAE Technical Paper 1993; 930072.

[178] Su TF, Patterson MA, Reitz RD, et al. Experimental and Numerical Studies of High Pressure Multiple Injection Sprays. SAE Technical Paper 1996; 960861.

[179] Hun KY, Lee E, Koo JY. Diesel spray atomization model considering nozzle exit turbulence conditions. Atomization and Sprays1998; 8: 453-469.

[180] Schmidt D, Nouar I, Senecal P, et al. Pressure-Swirl Atomization in the Near Field. SAE Technical Paper 1999; 1999-01-0496.

[181] Huethorst JAM and Marra J. Motion of marangeoni-contracted water drops across inclined hydrophilic surface. Langmuir 1991; 7: 2756-2763.

[182] Launder BE and Spalding DB. The numerical computation of turbulent flows. Comp Meth Appl Mech Eng 1974; 3: 269-289.

[183] Cen C, Wu H, Lee C, et al. Experimental investigation on the characteristic of jet break-up for butanol droplet impacting onto a heated surface in the film boiling regime. Int J Heat Mass Transf 2018; 123: 129-136.

[184] Mishra PC, Nayak SK, Pradhan P, et al. Impingement cooling of hot metal strips in runout table− a review. Interfacial Phenom Heat Transf 2015; 3.

LIST OF PUBLICATIONS

International Journals

[1] **Zhang GX**, Luo HL, Kita K, Ogata Y, Nishida K. Statistical variation analysis of fuel spray characteristics under cross-flow conditions. Fuel 2022; 307: 121887. (Q1，IF=6.609)

[2] **Zhang GX**, Si ZB, Zhai C, Luo HL, Ogata Y, Nishida K. Characteristics of wall-jet vortex development during fuel spray impinging on flat-wall under cross-flow conditions. Fuel 2022; 317: 123507. (Q1 ， IF=6.609)

[3] **Zhang GX**, Shi PH, Luo HL, Ogata Y, Nishida K. Investigation on fuel adhesion characteristics of wall-impingement spray under cross-flow conditions. Fuel 2022; 320: 123925. (Q1，IF=6.609)

[4] Luo HL, **Zhang GX**, Chang FX, Jin Y, Ba KX, Ogata Y, Nishida K. Comparisons in spray and atomization characteristics with/without hydro-erosive (HE) grinding in nozzle orifice under non-evaporation and evaporation conditions. Fuel 2021; 297: 120789. (Q1，IF=6.609)

[5] Zhai C, **Zhang GX**, Jin Y, Ogata Y, Nishida K, Luo HL. Characterization of Diesel Spray Combustion Using Two-Color Pyrometry and OH* Chemiluminescence Imaging- Comparison Between Micro-Hole and Ultra-High Injection Pressure Effects. J Energy Inst 2022;103: 104-116. (Q1，IF=6.186)

[6] Luo HL, **Zhang GX**, Dong PP, Nishida K. Macroscopic and Microscopic Characteristics of a Single-hole Spray under Low Ambient Pressure Induced Conditions. Atomization Spray 2022; 32 (8):15–33. (Q3，IF=1.737)

[7] Jin Y, Luo HL, **Zhang GX**, Zhai C, Ogata Y, Matsumura Y, Ichikawa T, Nakashimada Y, Kim W, Nishida Y. Ignition timing effect on the combustion performance of hydrogen addition in methane fermentation gas in a local energy system. Fuel 2022; 324: 124714. (Q1，IF=6.609)

International Conferences

[1] **Zhang GX**, Shi PH, Luo HL, Ogata Y, Nishida K. RIM Experiment on Fuel Adhesion Characteristics of Inclined-Wall-Impinging Spray under Cross-Flow Conditions. COMODIA 2022.

[2] **Zhang GX**, Luo HL, Kita K, Ogata Y, Nishida K. Statistical Variation Analysis of Spray Injected by a Multi-Hole Injector into Cross-Flow Ambience. ICLASS 2021.

[3] **Zhang GX**, Luo HL, Kita K, Ogata Y, Nishida K. Experimental Study on Fuel Spray Characteristics of Multi-Hole Injector for DISI Engine under Cross-Flow Conditions. ILASS-Asia 2020.

ACKNOWLEDGEMENT

This dissertation was accomplished at the Mechanical Power and Motor Systems Laboratory, Mechanical System Engineering, Hiroshima University. I would like to express my gratitude to all those who helped me during the working of this dissertation.

My deepest gratitude goes first and foremost to my supervisors, Prof. Yoichi OGATA and Prof. Keiya NISHIDA, for their guidance and support not only on my research activities but also my daily life throughout the three years while I was studying for Ph.D. in Hiroshima University. Their guidance and encouragement on my academic thoughts deeply affect and will accompany me to explore the unknown in my future life.

Gratefulness is also given to Prof. Hongliang LUO and Prof. Yu JIN for their comment, advice and discussion on my academic activities during their busy work. Fortunately, Prof. Zhanbo SI and Prof. Min GUO also give me many helps on my experiment, many thanks for their help. Also, my sincere appreciation goes to the thesis committee members: Professors Daisuke SHIMOKURI and Yasuhiro SUZUKI.

Thanks also given to Dr. Chang ZHAI, Dr. Guanming GUO, Dr. Chengyuan FAN, Mr. Kouhei KITA, Mr. Kouga NISHI, Mr. Kentaro MIYUKI, Ms. Penghua SHI, for their assistance in the experiment or simulation work. Also, I would like to thank Mr. Feixiang CHANG and Ms. Wenjing XING for the kind help over the past three years. Especially, I want to thank my senior Dr. Kuichun LI, engineering of MAZDA, for the family-like care he given to me in Japan.

I would like to appreciate the China Scholarship Council (CSC) which sponsoring my studies in Hiroshima University by providing scholarship and giving me the opportunity to touch the world outside of China.

The selfless dedication from my parents and little brother inspired me to keep moving forward. Last but not least, I would like to express my highest respect and most sincere gratitude to them here.